Accurate and efficient full-wave modelling for indoor radio wave propagation

Ian Kavanagh

A dissertation submitted in fulfilment of the requirements for the award of
Doctor of Philosophy

School of Electronic Engineering
Dublin City University

Supervisor: Dr. Conor Brennan

August, 2018

Declaration

I hereby certify that this material, which I now submit for assessment on the programme of study leading to the award of Doctor of Philosophy is entirely my own work, and that I have exercised reasonable care to ensure that the work is original, and does not to the best of my knowledge breach any law of copyright, and has not been taken from the work of others save and to the extent that such work has been cited and acknowledged within the text of my work.

Signed: _____ ID No.: _____ Date: _____

Contents

List of Figures

List of Tables

Abstract

Ian Kavanagh

Accurate and efficient full-wave modelling for indoor radio wave propagation

The transition towards next-generation communication technologies has increased the need for accurate knowledge about the wireless channel. Knowledge of radio wave propagation is vital to the continued development of efficient wireless communications systems capable of providing a high data throughput and reliable connection. Thus, there is an increased need for accurate propagation models that can rapidly predict and describe the propagation channel. This is extremely challenging for indoor environments given the large variety of materials encountered and very complex and widely varying geometries.

Currently, empirical or ray optical models are the most common for indoor propagation. Empirical models based on measurement campaigns provide limited accuracy, are very costly and time-consuming but provide rapid predictions. Deterministic models are applied to the geometrical representation of the environment and are based on Maxwell's equations. They can produce more accurate predictions than empirical models. Ray tracing, an approximate model, is the most popular deterministic model for indoor propagation. The current trend of research is focused on improving its accuracy.

Full-wave propagation models are based on the numerical solution of Maxwell's equations. They are able to produce accurate predictions about the wireless channel. However, they are very computationally expensive. Thus, there has been limited attempts at developing indoor propagation models based on full-wave techniques. In this work, the Volume Electric Field Integral Equation (VEFIE) is used as the basis

of a full-wave indoor propagation model. The 2D and 3D formulations of the VEFIE are applied to model the propagation of radio waves indoors. An enhancement to the 2D VEFIE, called 2D to 3D models, is developed to improve its accuracy and utilise its efficiency. It is primarily used for the prediction of time domain characteristics due to its high efficiency whereas the 3D VEFIE is shown to be suitable for frequency domain predictions.

Acknowledgements

I would like to thank my supervisor Dr. Conor Brennan for his help, advice and support during this work. Thanks are also due to my fellow colleagues in DCU, including Sajjad Hussein, Vinh Pham-Xuan, John Monks and Anderson Simiscuka.

I would also like to thank my family for their constant love and support. Special thanks are due to Sarah Connolly for sticking by me through a very stressful and busy time.

Chapter 1

Introduction

The increase in use of mobile devices, in recent times, has put a strain on wireless communications infrastructure. This has led to a move towards decentralised networks. Femto and pico cells served by small telecommunications access nodes are becoming more attractive as a means to provide reliable wireless communications networks with a high capacity [1]. These devices are built to work inside buildings and normally provide a small area of coverage but have to serve very complex environments composed of a large variety of different materials [2]. Knowledge of the propagation characteristics of these environments in the frequency and time domains is vital to the continued development of energy efficient wireless communications systems that can provide the required coverage and performance. A more detailed description of some of the problems faced by wireless communications systems and the need for accurate propagation models that can rapidly describe the propagation channel and serve as tools to optimise the location and configuration of base stations within femto and pico cell environments is presented in Section 2.1. These propagation models should be capable of including as much of the geometrical and material information of the environment as is reasonably possible but also yield predictions rapidly. This is extremely challenging for indoor environments. The study of propagation modelling and the incorporation of geometrical and material information is examined in Sections 2.2 and 2.7. The remainder of Chapter 2 reviews the current state-of-the-art of indoor propagation models.

Empirical models are presently the most common models used for indoor propagation. They provide rapid predictions but lack the accuracy needed for modern applications. In addition, specific models are intended for either frequency or time domain predictions but not for both. A brief survey of some empirical models is presented in Section 2.3. The COST 231 multi-wall model [3] and the Motley-Keenan model

[4], [5] are two quick and theoretically simple empirical[1] models for predicting path loss but their accuracy is restricted by the underlying measurement campaigns used to develop them. The SIRCIM computer simulator [6] produces power delay profiles based on statistical channel impulse response models. Recently, deterministic models have grown in popularity due to advances in compute power and the wide availability of efficient computing resources [7]. In Section 2.4, ray tracing the most popular deterministic model for indoor environments is briefly reviewed. Ray optical methods are built on Geometrical Optics (GO). It is a relatively fast method, although slower than empirical models, that originates from the asymptotic approximation of Maxwell's equations at high frequencies. It is capable of producing predictions in both the frequency and time domains. GO has been augmented with the Geometrical Theory of Diffraction and the Uniform Theory of Diffraction in [8], [9] respectively to include the diffraction phenomenon and increase its accuracy. Lately, diffuse scattering [10] has seen significant investigation in the literature [11]–[18] and is increasingly being included in ray optical models to further augment their accuracy. The current trend towards improving the accuracy of ray optical methods and consequentially their computation time and complexity suggests that it may be beneficial to take a different approach - to start with an accurate full-wave method and attempt to reduce its computational complexity.

Full-wave propagation models are based on the numerical solution of Maxwell's equations. Providing they include all of the information of the propagation environment they should be able to produce accurate predictions. There have been limited attempts in the literature at developing full 3D propagation models based on full-wave techniques because they are very computationally expensive. The most popular of these employed for indoor propagation are surveyed in Section 2.5. For example, the Finite Difference Time Domain method is shown to be slow for relatively small indoor problems [19], [20] in both 2D and 3D with research ongoing to reduce its computational complexity. The boundary integral equation is another full-wave technique that has been used for indoor propagation [21], while the Multi-Resolution Frequency Domain ParFlow (MR-FDPF) method [22]–[24] is based on a full-wave technique but employs approximations to significantly reduce its computational cost. These approximations require the MR-FDPF method to be calibrated with measurements before it can be used as an accurate propagation model, thus,

[1] Empirical models that require some knowledge of the environment are often referred to as semi-empirical models.

calling into question the deterministic nature of the model.

The focus of this thesis is on the use of the Volume Electric Field Integral Equation (VEFIE) as an indoor propagation modelling tool. To the best of this authors knowledge there has only been a single attempt in the literature at developing an indoor propagation model based on the VEFIE [25]. It is reviewed in Section 2.5.2 along with the use of surface integral equations.

Chapter 3 provides a general overview of computational electromagnetics. It presents Maxwell's equations in their differential, integral and time-harmonic forms which underpin the propagation of electromagnetic waves. The two most common methods used to solve Maxwell's equations the finite difference method and the Method of Moments (MoM) are briefly described. The VEFIE which is used extensively throughout the later chapters of this thesis is derived from Maxwell's equations. The MoM is applied to it to discretise it and enable its numerical solution. The application of the MoM results in a set of N linear simultaneous equations that can be formulated as a matrix equation. The N linear equations result from the expansion of the unknown electric field in the VEFIE using N basis functions.

The matrix equation created by the MoM process can be solved by direct matrix inversion. However, for indoor propagation problems this matrix is usually large because the size of the problem is on the order of a few hundred wavelengths. The MoM requires a discretisation rate of $\frac{\lambda}{10}$ in order to accurately model the variations of electromagnetic waves. Thus, iterative solvers are employed to more efficiently solve the matrix equation. The Krylov family of iterative solvers that are employed in this thesis are examined in Chapter 4. The convergence rate of these solvers is based on the spectral properties and condition number of the matrix. Preconditioners are matrices that are used to improve the spectral properties of the system matrix and enhance the convergence rate of the iterative solver. Some of these are described in Section 4.3. The slowest element of the iterative solution is the matrix-vector product that must be performed during each iteration. With specific knowledge of the underlying problem and the composition of the system matrix this computation can be accelerated. The Fast Fourier Transform (FFT) can be used to take advantage of a regular grid pattern in the system matrix to reduce the computational complexity of the matrix-vector product and the storage requirements of the system matrix. The fast multipole method and fast far field approximation are two electromagnetic specific methods that break the problem up into near field and far field regions. Near field interactions are computed exactly whilst those in the far field are approximated. These

techniques are described in Section 4.4. The FFT approach is used to accelerate the solution of the VEFIE in this thesis.

The subsequent chapters describe the work done by the author. The 2D VEFIE discretised with the MoM and solved with the BiCGSTAB method is employed in Chapter 5 to model propagation in buildings. The 2D VEFIE model is accelerated by using the FFT which requires the discretisation of the entire problem domain including free space unknowns. It can be shown that unknowns located in free space are only present to impose a regular grid and enable the use of the FFT and thus don't have any effect on the solution of any other unknown in the problem. Thus, they can be essentially ignored within each iteration, allowing the solver to focus on the fields within the scatterers. This is done using a reduced operator which is described in Section 4.3.3.

Chapter 5 examines the computational efficiency of the VEFIE and its surface counterpart the Surface Electric Field Integral Equation. It validates the 2D VEFIE with the analytical Mie series solution for scattering from a dielectric cylinder. The propagation modelling capabilities of the 2D VEFIE in both the frequency and time domains is examined and it is compared against measurements and contrasted with other indoor propagation models.

In Chapter 6 the 3D VEFIE is presented and used for indoor propagation modelling. The 3D VEFIE is solved similarly to the 2D formulation using the MoM to discretise it and the BiCGSTAB accelerated with the FFT and reduced operator to solve it. The 3D VEFIE is also validated against the analytical Mie series solution for scattering from a dielectric sphere before being applied to model propagation in realistic indoor environments.

In Chapter 7 novel techniques for extending the 2D VEFIE to be able to make accurate 3D predictions are presented. The, so called, 2D to 3D models use the main benefit of the 2D VEFIE, its speed, to develop accurate and efficient indoor propagation modelling tools. The 2D to 3D models are used for frequency and time domain predictions where they are compared against measurements and popular empirical and statistical models.

Lastly, Chapter 8 summarises the thesis and presents some avenues for future research.

1.1 Notation

In this work, matrices and vectors, both linear algebra and those related to position, are represented in bold (e.g. $\mathbf{r}$, $\mathbf{E}$) and $||.||_2$ denotes the Euclidean norm.

Chapter 2

Literature review

2.1 Introduction

Increasingly, it is becoming imperative to be able to accurately model and characterise the wireless channel for several reasons. The demand for wireless data is putting a massive strain on communications networks and exacerbating the global bandwidth shortage and problem of limited spectrum availability for cellular technologies and personal communications systems [26]. Network planning and optimisation tools are critical to the development and operation of communications systems capable of providing a minimum level of signal quality that prevents portable devices from experiencing signal interruptions. The quality of service of a wireless system depends on many factors. Traditionally, the received signal strength has been the most crucial [27] as, historically, planning aimed at pursuing a satisfactory coverage level. However, the development of advanced technical solutions, to solve issues associated with the wireless data boom, more and more depends on the overall nature of the received signal (e.g. time delay, angle of arrival, etc.) and multipath effects (e.g. angle spread and polarimetric properties) than the received signal strength in isolation [28]. In fact, the current 802.11ad and 4G (Long-Term Evolution) standards already make use of Orthogonal Frequency-Division Multiplexing (OFDM) and Multiple Input Multiple Output (MIMO) antenna systems that require knowledge of the spatial and temporal aspects of the channel to operate at maximum capacity and efficiency. Multipath effects, which are very significant in indoor propagation, are a source of attenuation and signal degradation [29] that advanced propagation models can be used to analyse and exploit.

The Internet of Things (IoT) and new wireless communications technologies has necessitated the reuse of frequency spectrum in the unlicensed bands for multiple dif-

ferent and new applications. Frequency reuse causes co-channel interference, which is detrimental to system performance, reducing the coverage area, reliability and throughput of the wireless system [30]. Mitigating co-channel interference in the unlicensed frequency bands remains a major challenge particularly for indoor environments [31]. It is also necessary to consider the best location and optimum number of transmitters for indoor wireless systems in order to maximise performance and reduce costs during deployment and maintenance phases. Propagation models are helpful in complying with safety regulations too [32], [33].

Motivated by the global bandwidth shortage the millimetre wave spectrum is being explored for future 5G communications systems [26]. There is very little knowledge about the propagation of radio waves at the typically underutilised millimetre wave frequencies. Developing channel models and obtaining information about the channel at these frequencies is vital for the efficient design of these systems and the specification of the 5G standard. The next generation of communication systems are expected to use more advanced techniques to provide higher data throughput that will require an in-depth knowledge of the propagation channel [26], [28]. As the frequency increases the size of objects in the environment that need to be modelled decreases and the accurate modelling of surface roughness becomes of greater importance [12]. Dynamic beamforming or beam-switching techniques could possibly require a propagation model assisted algorithm to achieve optimal performance in the future.

The indoor localisation problem is becoming more and more important as IoT expands and for tracking in factories, warehouses, hospitals, smart-homes and high security areas [34] where global positioning systems (GPS) aren't capable of operating. Propagation models are seen as a method to improve the accuracy of real-time location systems and reduce the need for expensive and time-consuming measurement campaigns to characterise the channel for fingerprinting based systems [35]. The ultrawideband (UWB) technology that has emerged as one of the most viable candidates for indoor positioning [34] primarily requires the time of arrival or time difference of arrival to triangulate an object [36]. The development of accurate triangulation algorithms requires knowledge of the multipath effects [37] and ability to adapt due to the time-varying nature unique to the indoor environment [38]. Reviews of UWB technology [34], [39], [40] have outlined the potential benefits associated with it but also the requirements for further development and channel modelling.

2.2 Propagation modelling

The propagation of electromagnetic waves is governed by Maxwell's equations. The study of how these waves propagate and create the wireless channel is called propagation modelling. Propagation analysis helps to determine the characteristics of a signal for a given environment and is a companion to performing expensive and time-consuming measurement campaigns. If accurate, they can reduce the number that need to be undertaken [41]. Propagation modelling includes signal strength analysis, impulse response characterisation and, increasingly, determining the angle of departure and arrival of the received signal [42].

Propagation models can be classified as either statistical or deterministic which can be further classified into empirical, approximate or full-wave methods. Statistical channel models describe the channel in an average sense without requiring knowledge of the underlying geometry of the environment. They are popular in wireless planning tools [24], [43] due to their simplicity and relatively fast computation time. However, they are limited to the scenarios for which they have been characterised and are unable to capture the multipath effects experienced in indoor propagation. To overcome the first issue, site-specific empirical models [44], [45] have been developed that require an underlying knowledge of the environment but they still only describe the channel in an average sense and fail to accurately capture multipath fading effects. For this reason, site-specific deterministic models are seeing increased use in the literature for indoor propagation modelling [28], [41], [46]–[48].

Deterministic channel models are typically based on approximate methods, like ray optics, or full-wave techniques that numerically solve Maxwell's equations. Approximate methods are based on the underlying physics of Maxwell's equations but in the case of ray optical methods employ a high frequency approximation to simplify their solution. Ray optical methods (such as ray tracing or ray launching) approximate electromagnetic waves as rays travelling along infinitesimally thin lines. When a ray impinges on a different medium it undergoes an electromagnetic interaction like reflection, transmission, diffraction or diffuse scattering, which are explained later in Section 2.4. Full-wave techniques, on the other hand, attempt to accurately solve Maxwell's equations without approximations except for those required by their numerical solution. They discretise an environment to enable its solution with a computer. Deterministic site-specific methods require knowledge of the geometry and electrical parameters of materials for the environment of interest. Provided that this

information is available full-wave models should produce accurate results for electromagnetic wave propagation except for numerical inaccuracies. Approximate models require a trade off between the level of accuracy they provide and their complexity and computation time [22], [49], [50]. Full-wave techniques are typically too computationally expensive and require supercomputers to solve them [51], [52]. They are only applicable for electrically small problems unlike those found in indoor propagation [25] or are applied in two dimensions limiting their accuracy [53]. For these reasons, site-specific hybrid models have been proposed, which utilise the accuracy of full-wave techniques and the efficiency of approximate methods, as a viable alternative for indoor propagation modelling [54].

2.3 Statistical and empirical models

The simplest method to predict the wireless channel is with empirical models. They are based on the statistical characterisation of the wireless channel and are determined experimentally from measurement campaigns. The general empirical model [55], [56] that all others are primarily based on expresses the path loss as

$$PL(d) = PL(d_0) + 10n \log_{10}\left(\frac{d}{d_0}\right) + X_\sigma \tag{2.1}$$

where $PL(d)$ is the path loss in dB at a distance d from the transmitter, $PL(d_0)$ is the known path loss at a reference distance d_0, n is a path loss exponent that depends on the propagation environment, and X_σ is a variable that represents uncertainty in the model [57], it could represent slow and/or fast fading. Significant research has focused on determining the parameters of this model for several scenarios [32]. However, its accuracy is limited to the scenarios it has been characterised for and it is unable to provide a high level of accuracy as well as many quantities sought after for indoor propagation modelling. The model above is specific to predicting path loss characteristics of the wireless channel. A model to compute time domain characteristics and estimate the RMS delay spread of the wireless channel was first proposed by Saleh and Valenzuela in 1987 [58]. This was extended to predict angle of arrival information in [59].

Empirical models have been constantly updated, refined and modified since their inception. There is now a wide array of empirical models that have been developed with more and more appearing every year, especially with the move towards next

generation communications technology and millimetre-waves [26]. Some of the most popular empirical models for path loss prediction in indoor propagation today are: the dual-slope model [60], the Cheung model [61], the COST 231 Multi-Wall model [3], the ITU-R Recommendation P.1238-1 model [62] and the Motley-Keenan model [4]. In fact, the popular Motley-Keenan model has recently been adjusted to further enhance its accuracy [5].

A recent development for empirical models is attempting to build in some elements of the underlying physics and geometry into the models to enhance their accuracy. This approach to indoor propagation modelling was previously used for predicting the average power delay profile (PDP) characteristics of a room using reverberation theory [63]. The reverberation theory approach to PDP computation has been enhanced further by considering the locations of transmitters and receivers [64]. Meanwhile, the meaningful indoor path loss model [44] and simple heuristic indoor path loss model [45] are two statistical approaches to predicting path loss based on the environment. They report improved accuracy and portability to different environments without the need for extensive measurement campaigns to characterise their parameters for every scenario.

The choice of which empirical model is best has until yet remained unanswered. Several studies have been performed to analyse the accuracy of different empirical models [60], [65], [66]. In [65] the authors results demonstrate the COST 231 model outperforms the ITU-R model. However, in [66] the COST 231 model produces worse results than the ITU-R model. [66] finds the best model is the partitioned model and proposes a new model based on it that includes the wall penetration factor from the COST 231 multi-wall model. [60], on the other hand, finds that the COST 231 multi-wall model and average walls model (which is based on the COST 231 multi-wall model) produce more accurate results than the partitioned model. These studies and their conflicting results demonstrate some of the issues associated with empirical models and the main reason the propagation community is moving towards deterministic site-specific propagation modelling techniques.

2.4 Ray optical techniques

Initially applied to optical problems ray tracing or ray launching methods are fast becoming the most popular method for electromagnetic wave propagation. The methods by which electromagnetic waves propagate in ray optical models are broken

down into individual components; reflection, refraction, transmission, diffraction, and scattering. A reflected wave occurs when an electromagnetic wave (or ray) impinges on an obstacle whose dimensions are larger than its wavelength [67]. The angles reflected waves take are governed by Snell's law of reflection. Refraction and transmission are linked but are also separate. Electromagnetic waves can refract in the atmosphere due to a changing refractive index but this is less of an issue for indoor propagation modelling and is more seen in tropospheric propagation [68]. Transmission occurs when an electromagnetic wave impinges on an object and instead of all of its energy being reflected some of it passes through the object. The transmitted wave refracts as it traverses the boundary between two different materials [69]. The angle of refraction can be determined from Snell's law of refraction. Typically, because it is difficult to compute and not very significant, the shift due to refraction in transmitted waves through materials, like walls, isn't taken into account in most ray optical models. This simplification can often be satisfactory for computing the magnitude of the transmitted wave but it introduces inaccuracies into the phase calculation. Thus, a simple approximation to slightly correct for this is demonstrated in [69] which shows a good agreement for normal and oblique incident waves. Geometric Optics (GO) is the process used to determine incident, reflected and transmitted fields. It is a high frequency approximation for Maxwell's equations that well captures the propagation of electromagnetic waves when their wavelength is much smaller than the size of the objects being studied.

Very early ray optical models consisted mainly of reflected and transmitted waves but in order to achieve higher levels of accuracy diffracted waves were included [67]. Diffraction occurs at the edges of obstacles and was first introduced in 1962 by Keller as the Geometrical Theory of Diffraction (GTD) [70]. However, it does not produce continuous fields in the incidence and reflection shadow boundaries. In order to overcome these issues Kouyoumjian and Pathak introduced an extension to GTD, the Uniform Theory of Diffraction (UTD) [71], that bounded the diffracted fields across the shadow boundaries. UTD has been approximately extended to consider finite conductivity diffracting edges [72]–[74] which makes it more accurate and viable for indoor propagation problems but it is still shown to produce slight inaccuracies for some complex multipath environments [67]. Advances in computing power over the last few years have helped the development of ray optical methods by making it easier to analyse their accuracy against full-wave approaches and develop more accurate diffraction coefficients [67].

Increasingly, the inclusion of diffuse scattering in ray tracing models has been seen as very important for accurate indoor propagation modelling [11]–[15], [17], [28], [50], [75]. Specular reflections described above are idealised approximations of the interaction that occurs when electromagnetic waves impinge on an object. They consider that the entire ray strikes a single infinitesimally small point and all of the energy in the field reflects in a single direction or is transmitted through the boundary. In reality, the field scatters in many different directions due to the irregular surface or roughness of the object [14], [57]. General GO can't be applied to calculate the effect of this scattering phenomenon so several different models have been developed [11], [14], [17]. In fact the theory dates back to 1953 [10] and has been included in ray tracing models since 1996 [76] but only more recently has it been regularly applied to study indoor propagation [14]–[17] where its importance has been demonstrated [17]. However, the inclusion of diffuse scattering represents a considerable increase of the computational burden of ray optical models [28].

Ray optical models can be categorised as based on either ray tracing which is mostly image theory based, ray launching, also called the shooting and bouncing rays method, or a hybrid approach [77], [78]. Image theory determines the locations where electromagnetic interactions occur by computing images of the transmitter with respect to the faces and edges the interactions occur at and drawing straight lines from the receiver to the image point. Multiple interactions can be computed by utilising visibility algorithms that determine the faces and edges that can see other faces and edges. The path from receiver to transmitter is then traced starting at the receiver. There are many efficient algorithms that can be used. Some of the most popular are binary space partitioning (BSP) [79] and the polar sweep algorithm [80]. The image theory approach can compute all of the interactions for a given receiver point exactly but it is very computationally expensive if a large number of receiver points are required. In [81] image theory coupled with the BSP algorithm and a parallel ray approximation has been shown to reduce the computational time by 66% whilst adding a 10% error in the results. Moreover, the ray launching technique is a brute force approach that is more efficient for computing dense coverage maps. Ray launching algorithms launch a number of rays from the transmitter at a distinct set of angles when the ray interacts with an object the scattered field is computed based on reflection, transmission or diffraction of the launched ray. The process of tracing launched rays continues until their power drops below some threshold level. Ray launching implies an angular/spatial discretisation that limits accuracy and can result in gaps

occurring in the coverage. Thus, it is necessary to construct a reception sphere around receiver points [28], [82]. Any rays which intersect the reception sphere are summed together to produce the field at that point. The coverage issue with ray launching led to the development of the intelligent ray launching algorithm [83] that dynamically accounts for rays to fill the gaps in coverage. Ray splitting [84] is another approach designed to alleviate this problem. The need to launch a large number of rays in ray launching algorithms produces a significant computational burden that has seen a lot of interest in the literature [85]. One very promising approach is based on the use of neural networks [85] whilst [50] found that including diffuse scattering based on an equation of transfer approach is approximately 40% quicker than including diffraction for the same level of accuracy in indoor propagation problems. To further improve upon the image theory and ray launching approaches hybrid methods [77] and approaches based on Gaussian beam tracking [86] have been developed. The use of GPUs has also been investigated [87].

All of the ray optical methods described until now are frequency domain approaches but time domain GO (TDGO) [88] is another approach that can be used. TDGO offers an efficient method for producing frequency sweep information using ray tracing. The approach is very similar to classical (frequency domain) GO except the field strengths are computed in the time domain instead of the frequency domain. TDGO like Finite Difference Time Domain (FDTD) (discussed in Section 2.5.1) can simulate wideband systems in a single run making it much more efficient than frequency domain methods. In fact, TDGO can produce very accurate results in a time frame that is 20 times faster than the full-wave FDTD method [88] but it has still seen very little investigation in the literature compared with its frequency domain counterpart.

2.5 Full-wave methods

2.5.1 Finite Difference Time Domain

FDTD is the most popular full-wave method for indoor propagation modelling [19], [31], [51], [53], [89]–[92]. It is not limited to indoor propagation modelling and has been used in circuit modelling and optics [93]–[95]. It was first introduced by Yee in 1966 [96] and has remained in continuous development and use ever since due to its flexibility and simplicity. It is an explicit finite difference approach that solves Maxwell's curl equations. The Yee algorithm defines a grid for the electric and magnetic

field components. The electric and magnetic fields are then solved in a time-stepping approach which is terminated when the steady-state is reached, i.e. around 3 times the length of time required for the incident field to propagate along the longest direction, or after a predetermined length of time depending on the analysis being performed. The FDTD method requires careful consideration of the boundary of problems to prevent spurious reflections. For indoor propagation problems this requires that all outward propagating waves are simulated as propagating to infinity. For this reason, several absorbing boundary conditions (ABCs) [97]–[104] were developed. The most popular ABC is the perfectly matched layer [105] that was developed by Berenger in 1994, which has been further improved by Berenger [106] and Roden et al. [107].

The FDTD method, like all full-wave methods, has some drawbacks that have prevented its widespread adoption for indoor propagation modelling. Most full-wave methods require a spatial discretisation of $\frac{\lambda}{10}$ where λ is the wavelength of the largest frequency being simulated in the problem. For indoor propagation problems this is a major disadvantage of full-wave methods as it leads to extremely large memory requirements [51]–[53] and can often make it extremely difficult to execute full 3D simulations. The FDTD method is also not unconditionally stable and the Courant-Friedrich-Levy (CFL) limit puts restrictions on the maximum time-step that can be used in FDTD simulations. This requires that in one time-step of the FDTD the incident field must not travel more than the distance of one cell in any direction. These restrictions for a long time limited the use of FDTD to electrically small problems [92] and for indoor propagation limited its use to two-dimensional problems [53]. It was not until the turn of the last decade [19], [31], [51], [91], [92] that three-dimensional FDTD models began to be used for indoor propagation.

The simplicity and popularity of the FDTD method has led to several attempts to reduce its computational burden. Early attempts proposed using multiple independent 2D simulations to generate 3D results in a 2.5D model [89]. Most attempts have focused on reducing the memory requirements of FDTD [90] or attempting to reduce the CFL limit imposed on the time-step to preserve stability [19], [92]. The Multi-Resolution Time Domain (MRTD) method is another improvement to FDTD that attempts to reduce its memory requirements and offer faster solutions, it is reviewed in Section 2.5.5. More recently, advances in computing power, supercomputers and GPUs have been seen as a viable approach to reduce the runtime of FDTD methods.

The reduced FDTD (R-FDTD) [90] method reduces the memory requirements of

FDTD by only requiring four field components to be stored in 3D instead of six. The remaining field components are spatially linked to the stored components by using the divergence-free nature of the electric displacement current and can be computed from the other components when needed. A similar process can be applied in two dimensions where only two components need to be stored instead of three. This results in a 33% reduction in the memory requirements of FDTD (in practical implementations 28.6% because of other elements that need to be stored) but requires 6 extra multiplications per FDTD update due to the need to compute the component that isn't stored. The R-FDTD method exhibits perfect agreement with the full FDTD approach.

Both the locally one-direction FDTD (LOD-FDTD) [92] and alternating-direction implicit FDTD (ADI-FDTD) [19] methods attempt to reduce the CFL limit imposed on the FDTD for stability. The LOD and ADI schemes are similar approaches that solve each time-step in the FDTD method in two steps. The reader is referred to [108], [109] for more information on the LOD scheme and to [110] for more information on the ADI scheme. The one-step ADI scheme is used in [19]. The LOD-FDTD and modified leapfrog ADI-FDTD methods are not exact as in the case of FDTD but applying a limit of 1% on the relative error, which should be sufficient for most indoor propagation problems, they offer a 33% and 60% reduction, respectively, in computational time for typical indoor propagation problems.

In recent years, the use of parallelisation [91], supercomputers [31], [51] and GPUs [43], [111]–[113] has seen significant interest to accelerate FDTD solutions. Simple parallelised indoor propagation FDTD solutions have been shown to experience around a 15 times speed up on a desktop computer [91]. Whilst, the real advantages for accelerating indoor propagation problems have been seen in GPU programming. An off the shelf GPU has been shown to provide a 100 times speed up [43]. However, careful consideration is required in the parallelisation of FDTD on CPUs and GPUs in order to manage memory accesses and achieve the best possible speed up.

2.5.2 Integral equations

The integral form of Maxwell's equations can be formulated as surface or volume integral equations in the frequency or time domain. Surface formulations are primarily used to model piecewise homogeneous dielectrics or metals (perfect conductors) because they discretise only the surface of scatterers, whilst, volume formulations can

be used for inhomogeneous problems as they discretise the entire volume of scatterers. Integral equation methods have seen very limited use in the literature [21], [25], [114] for indoor propagation modelling. Full-wave methods and particularly integral equation methods have primarily been used for low-frequency electrically small problems because of the required $\frac{\lambda}{10}$ discretisation rate.

Integral equation methods can be more complex to solve than ray tracing and FDTD but they provide significant benefits also. Integral equation approaches incorporate all electromagnetic interactions inherently [114] whereas ray optical models must include reflection, transmission, diffraction and diffuse scattering phenomenon individually. Integral equation approaches do not require ABCs and are capable of providing the same propagation information and characteristics as FDTD using both frequency [21], [25] and time [114] domain formulations.

Surface integral formulations are more popular in the literature for indoor propagation modelling. De Backer et al. [115] was one of the first to demonstrate the use of surface integral equations for indoor propagation problems in 1997. De Backer et al. used a surface integral equation discretised with the method of moments (MoM) and demonstrated techniques that can be applied to accelerate the solution of the model. Whilst, the model is only 2D and takes a considerable length of time (10 hours) to produce predictions it is extremely accurate and with modern advances and improvements in computing power this runtime would be expected to fall dramatically. In fact, in 2006, nearly 10 years later, [21] showed that a similar approach using the finite-element boundary-integral (FE-BI) method, a hybrid of the MoM and finite element method applied to surface integral equations, in 3D required less time (7.8 hours) for a problem of a similar size. That same problem can be computed in 6 mins [21] by applying the Array Decomposition-Fast Multipole Method (AD-FMM) [116] to accelerate its solution. The AD-FMM method is good for modelling environments that consist of a large number of repeatable components, like chairs in a classroom, because it only stores each repeatable element once. This part is known as the Array Decomposition Method (ADM). The Fast Multipole Method (FMM) is used to accelerate the computation of interactions between different elements in the problem. The memory requirements and CPU time are reduced by a factor of 10 when the AD-FMM is applied to the FE-BI with the error between the two methods less than 1%. This demonstrates the viability of integral equation methods for indoor propagation modelling and makes them a real alternative to ray tracing and empirical models.

Volume integral equations have seen very little interest in the literature for indoor

propagation modelling. [25] demonstrates the use of the volume electric field integral equation (VEFIE) for indoor propagation problems. The volume integral model is compared against a surface integral formulation and an exact analytic solution where both are shown to produce an excellent agreement. The multilevel Fast Multipole Algorithm (MLFMA) is used in [25] to accelerate the solution of the volume integral model. The MLFMA reduces the complexity of matrix-vector multiplications in the solution of the method from $\mathcal{O}(N^2)$ to $\mathcal{O}(N \log N)$. This is also similar to the benefit provided by the Conjugate Gradient-Fast Fourier Transform (CG-FFT) approach to solving the VEFIE. The authors state in [25] that the CG-FFT approach is not as efficient as the MLFMA because of the significant number of extra unknowns it requires to create a regular grid and fill in free space unknowns but it would be more efficient for problems where most of the problem domain consists of dielectrics as opposed to free space. However, another consideration to make is the accuracy of the model. The FFT approach exactly computes the interactions between different cells in the problem whilst the MLFMA approach is an approximate method with a very small error.

2.5.3 ParFlow

The ParFlow method is a time domain approach for electromagnetic modelling based on the idea of flows. It was first proposed by Chopard et al. in [117] for solving urban propagation problems and is a generalisation of the well-known Transmission Line Matrix (TLM) method (for circuit design) [52], [118]. The ParFlow method is a full-wave approach to propagation modelling. The flows that are introduced to simulate electromagnetic interactions between cells inherently model effects like reflections and diffractions.

Recently, the ParFlow equations have been formulated in the frequency domain and solved using a multi-resolution approach [119], [120]. The frequency domain ParFlow (FDPF) method has been proposed to reduce the computational load of the time domain approach and ensure a faster convergence of the steady-state fields [52]. A multi-resolution scheme has been proposed to solve it. The multi-resolution solution scheme exploits the concept of flows to split the solution into a pre-processing phase and a propagation phase. The pre-processing step creates a cell based tree structure that defines the geometry and interactions between cells in a pyramidal structure, this step is independent of the source location. In the propagation step, a radiating

source is propagated throughout the problem taking advantage of the pre-processed cell based tree structure. The pre-processing step is the most computationally expensive [119], [121] but it only has to be computed once. The coverage due to a source can then be computed efficiently for any location or multiple different locations.

The 3D multi-resolution FDPF (MR-FDPF) method suffers from high memory requirements and computational load [22]. To overcome this drawback of the 3D approach an optimised algorithm [23] has been proposed that ignores propagation modes with a low influence on the resulting coverage predictions using a singular value decomposition approximation. The optimised solution reduces the computational load but introduces approximations. To overcome the large computational time of the 3D MR-FDPF a 2.5D approach [120] has also been proposed for indoor propagation modelling that demonstrates a good agreement with measurements after calibration against those measurements.

As stated previously, the MR-FDPF algorithm is a full-wave method, however, its use as a viable deterministic model without calibration is unclear. In all of the comparisons and validations made with the MR-FDPF method against measurements [22]–[24], [52], [119], [120] the model is simulated at a lower frequency than the physical one. This is an obvious approach to reducing the computational complexity of frequency domain methods as their runtime increases as frequency increases. However, this approach requires that the model is calibrated against measurements, calling into question its deterministic nature. Even with calibration there are errors in predicting the fields due to diffractions [52] in the MR-FDPF method.

2.5.4 Parabolic equation

The parabolic equation is a full-wave method derived from the time-harmonic form of Maxwell's equations using the paraxial approximation. The paraxial approximation assumes an electromagnetic wave propagates mainly along a single direction and significant propagation effects do not occur at angles greater than 15° away from this direction. Thus, it has seen limited interest in the literature for indoor propagation problems [122], [123]. It is primarily suited to cases like long narrow corridors [123] and tunnels [124]. However, there is a wide angle correction [125]–[127] for the parabolic equation that can extend its use for propagation angles within $\pm 90^\circ$ of the paraxial direction which makes it more viable for complex indoor propagation problems.

The parabolic equation can be discretised using a numerical differentiation scheme, like the finite element method, and solved with a time-marching approach. It is a one-way propagation model, similar to FDTD, that can be marched forwards and backwards to account for reflections from end walls and propagation effects in the negative directions as well as the positive direction. For the case of corridors, where the parabolic equation has been designed to work well, it produces reasonable results compared with ray tracing [123] when marched forwards and backwards but its accuracy degrades for more complex indoor scenarios. In [127] the authors compare the 2D parabolic equation with wide-angle approximation in a multi-floor building against measurements and an empirical model. The parabolic equation struggles to accurately capture the fading characteristics present in the measurements and produces very similar RMS error and standard deviation values compared with the empirical model. This suggests the parabolic equation is not sufficient to model complex indoor propagation problems.

The complex geometry of scattering objects in indoor environments produces electromagnetic effects that are not fully captured by the parabolic equation method. Thus, in [29], [128] the parabolic equation has been augmented with an integral equation formulation to capture these complex scattering effects, in two and three dimensions, respectively. This hybrid technique uses the parabolic equation to compute the fields due to an excitation from a transmitting antenna in scattering objects. These fields are then propagated to any free space point of interest using the VEFIE, described in Section 2.5.2, in a simple post-processing step. The volume integral approach assumes scatterers are equivalent sources and because it is used to compute the fields external to scatterers only there is no singularity present. The hybrid technique greatly improves the accuracy of the parabolic equation method with an average improvement to the absolute error of 13.5dB over the standard parabolic equation when compared against measurements [128].

2.5.5 Multi-Resolution Time Domain

The MRTD method is an extension to the FDTD method. There are two variations of it that depend on the type of function used to expand the electromagnetic fields in Maxwell's equations in space, either scaling functions (called S-MRTD) or wavelet functions (called W-MRTD). The electromagnetic fields are also expanded in time and, similarly to the FDTD method, a set of finite difference equations, which can be

solved to determine the field components in a time-stepping approach, are derived. The S-MRTD method, which has been applied to indoor propagation problems [20], [129], uses order-7 Deslauriers-Dubuc biorthogonal interpolating functions to expand the electromagnetic components in space and pulse basis functions to expand them in time.

The S-MRTD method is able to use a coarser discretisation rate than FDTD due to the use of higher order finite differences and expansion functions. This enables it to be able to provide a similar level of accuracy as FDTD with a speed up of around 4 times [20]. Using a FDTD simulation with a discretisation rate of $\frac{\lambda}{20}$ the authors of [20] found that an S-MRTD simulation with a discretisation rate of $\frac{\lambda}{7.5}$ produces an error of 0.8% against it but offers an 8 times speed up. In [129] the S-MRTD method has been accelerated by taking advantage of GPU programming offering a further speed up of 30 times whereas GPU programming is seen to offer only a 10 times speed up for FDTD. In fact for a typical indoor propagation problem the GPU accelerated S-MRTD method is capable of determining PDPs correlated to an accuracy of 90% depending on the simulation frequency in $\frac{1}{134}$ the time. The MRTD method has also been parallelised on a CPU and compared against a similarly parallelised FDTD implementation [49]. The CPU parallelised MRTD implementation is able to produce the same level of accuracy as the parallelised FDTD method 2.4 times quicker with one third less memory requirements. However, currently, only the two-dimensional form of the S-MRTD method has been applied to indoor propagation modelling. In general, the MRTD method has seen very little investigation in the literature despite the speed up it offers over FDTD [20], [49], [129].

2.5.6 Finite integration technique

The finite integration technique (FIT) is a scheme for discretising the integral form of Maxwell's equations. It is applied to the Maxwell Grid Equations (MGE) [130] which can be applied to an open boundary electromagnetic problem. FIT restricts an open boundary problem to a bounded simply connected region[1] that is divided into a number of cells on a regular grid, similarly to FDTD and MoM. The MGE are applied to model discretised fields and produce discrete matrix equations that can be solved by direct inversion or iterative methods.

In [131], the FIT method has been compared against ray tracing and an empirical

[1] A region is simply connected if any simple closed curve can be shrunk into a point while remaining in the region.

model. With adaptive meshing and parallelisation 3D simulations using FIT can be performed in relatively good runtimes of a couple of hours [131]. The main disadvantage of the FIT technique is the large memory requirements [130] that impose a limit on the upper frequency of simulations that can be performed as it uses a spatial discretisation rate of $\frac{\lambda}{5}$. However, it has been shown to produce a much higher level of accuracy (2 - 3.7 dB) than ray tracing (1.4 - 7.5 dB) and the one slope empirical model using average configuration parameters (4 - 8.2 dB) for several different transmitter locations and simulation frequencies [131]. It has also been shown to experience less accuracy degradation (0.3 dB) when detail is removed from the geometrical description of the environment than ray tracing (0.7 - 2.5 dB).

2.6 Hybrid approaches

Due to the high computational burden of full-wave methods and the inaccuracies associated with ray tracing, hybrid approaches have been proposed as a technique to achieve higher accuracies with a lesser computational time. Most hybrid methods involve using a full-wave method to solve the fields in a small region close to complex discontinuities or in the presence of objects comparable in size with the wavelength of the incident field where ray tracing solutions breakdown. This approach has been used with the FDTD [54], [132], [133] and FIT [134] methods for indoor propagation modelling. [54] produced results with a greater accuracy than ray tracing in a shorter runtime because of the large number of receiver locations that were computed. [132] demonstrates a 5 times speed-up over FDTD in 2D with accuracy comparable to it. A trade-off in accuracy can also be made at the expense of a longer or shorter runtime.

Hybrid techniques have seen very little investigation in the literature because it is very difficult to couple the different methods together and it appears a simpler task to either enhance the accuracy of ray optical methods or reduce the computational burden of full-wave methods. [122] employs a novel hybrid approach that uses the parabolic equation to enhance a ray tracing model to compute the coverage over a wide area much more efficiently than ray tracing alone but it is limited in its applicability to general problems. Another issue with hybrid methods is the need for human interaction to define the regions that will be solved with the full-wave technique and ray tracing [25]. Hybrid techniques have also seen very little implementation in three dimensions. The implementation of the Finite Volume Time Domain (FVTD) [54] method in three dimensions [135] demonstrated very little improvement in the

hybrid method over ray tracing and pointed towards the inclusion of diffuse scattering in ray tracing as a larger source of error.

2.7 Parameter uncertainty

Ray tracing approaches are ideally suited to studying the effects of parameter variations [136] or uncertainties in the modelled geometries [137]–[139] and the effects they have on predictions. Polynomial chaos is used in [136] to determine the effect of uncertainties in material properties, building geometry and location of objects, and the difference between real and simulated transmit and receive antennas. The results show that for typical variations that could be considered likely in indoor propagation problems the path loss can vary by around 10 dB for slight changes due to the significant multipath fading found in indoor environments. [137] and [138], [139] studied the effect of uncertainties in material permittivities and geometrical locations of walls separately with respect to the path loss and RMS delay spread. They found that material permittivity uncertainties have a small effect on the path loss but can have a large effect on the RMS delay spread whilst the opposite is true of uncertainties in the building geometry. [140] investigated the level of detail required in geometrical data using point cloud information. The authors constructed an extremely detailed point cloud model and compared simulations using reduced levels of detail against the ultra detailed model. They found very little difference in the field predictions between the ultra detailed point cloud with 0.13 points per square wavelength and the minimal model with 0.2 points per square wavelength. These conclusions appear to suggest that it is not necessary to have ultra detailed models but it is important that the simulated material permittivities and geometries are correct.

2.8 Conclusions

Propagation modelling is needed more and more to keep up with the demands put on wireless communications infrastructure and to aid the development of next generation communications systems and exploitation of millimetre wave bands. Advances in numerical algorithms, computing power and the use of general purpose Graphics Processing Units (GPGPUs) to solve numerical problems has helped change the propagation modelling landscape over the last few years. It will continue to change as 5G systems are developed and deployed with data usage expected to continue to

grow exponentially. The Internet of Things and smart connected devices are expected to dramatically increase the number of applications that require wireless communications to operate placing further demands on the already strained infrastructure.

Of all the methods presented that have been used for indoor propagation modelling there is no consensus on the best method to use or a widely accepted approach. Each of the methods have advantages and disadvantages over each other and in most cases the trade off between desired accuracy and a reasonable runtime plays a huge role in determining the method to use. However, the propagation modelling landscape is changing thanks to the improvements in computational processing power in part due to Moore's law [7] and the development of platforms like Compute Unified Device Architecture (CUDA) by Nvidia which enables the use of GPGPUs to solve numerical problems [141]. The strain on current wireless technologies and systems is leading the development of next generation communications technologies which plan to use advanced technologies and explore the millimetre wave bands to overcome the global bandwidth shortage and keep up with the demands on wireless systems [32]. The future development and operation of these systems requires more accurate knowledge and information about the wireless channel and millimetre wave propagation characteristics. This is pushing the propagation modelling landscape towards the development of more accurate models. However, incorporating these models into algorithms for advanced beamforming techniques and dynamic systems will require that their computational load is kept low, further emphasising the trade off between accuracy and computational complexity that has been a hallmark of the propagation landscape since its early days in the 20th century.

Early attempts of propagation modelling started off with the development of empirical and statistical models based on measurement campaigns. These are the simplest models to implement and have remained under constant investigation since their initial development. There are countless numbers of empirical models that have been developed, some of these are presented in Section 2.3. Unfortunately, most empirical models need to be tuned before they can be used for a specific environment which requires an expensive and time-consuming measurement campaign be carried out beforehand. The large number of empirical models and some studies that compare some for the same scenario [60], [65], [66] demonstrates that there is no widely accepted empirical model that can be used for all scenarios.

In an effort to develop more accurate deterministic site-specific propagation models that don't require calibration with measurements, ray optical methods have seen

significant investigation and use in the literature. However, ray tracing based on GO has been shown to not provide a high enough level of accuracy and has been augmented with the diffraction [67] phenomenon and more recently with diffuse scattering [12], [28] to enhance its accuracy. However, with these additions the complexity of ray optical methods is increasing and tending more towards that of full-wave methods. The choice between a ray tracing and ray launching approach also represents a trade off between accuracy and runtime. Ray tracing has been shown to produce accurate results for particular points but is much slower than ray launching for wide coverage areas [69]. On the other hand, ray launching can suffer from coverage issues, which can effect its accuracy for particular points, depending on the environment and also requires the use of a reception sphere for each point of interest to improve its accuracy [83].

Full-wave methods, on the other hand, can solve the accuracy issues faced by empirical and ray optical models but they are extremely computationally expensive. There are a wide number of full-wave methods available that either solve the differential or integral form of Maxwell's equations. However, they typically require the environment to be discretised at a rate of $\frac{\lambda}{10}$ which makes them very computationally expensive for electrically large problems, like indoor propagation, and even more so for the millimetre wave bands. Whereas, the computational load of empirical models and ray optical methods does not increase appreciably with frequency. There have been attempts to develop full-wave methods that don't require the discretisation rate of $\frac{\lambda}{10}$ [19], [92] but they require a larger number of computations and are typically slower than ray optical methods.

In summary, there is no one size fits all approach to propagation modelling. The choice of which method to use requires a trade off between the desired level of accuracy and an acceptable runtime. The propagation modelling landscape has changed considerably over the early part of the 21st Century and will continue to change for the foreseeable future. Research is tending towards the use of full-wave techniques as they can provide the level of accuracy required but because of their currently slow runtime and large computational load there is still a requirement for ray optical methods and empirical models, particularly those that take into account some facets of the underlying geometry.

Chapter 3

Computational electromagnetics

Computational electromagnetics (CEM) is the study of numerical solutions of Maxwell's equations. It focuses on modelling the interaction of electric and magnetic fields with their surrounding environment. The analytical solution of Maxwell's equations is only possible for a restricted set of problems and the majority of real-world applications, including general scattering problems, must be tackled numerically. CEM is a multi-disciplinary field. Its core disciplines are electromagnetic theory, mathematics and computer science. The advent of computers and numerical algorithms in the 20th century were the beginning of the field that today drives the development of wireless communications technology and devices [142]. CEM is seen by some as a replacement for measurements, which can be very costly and time consuming to carry out, whilst others see it as a companion to measurements [7].

CEM techniques have grown in popularity recently. The improvements in compute power in part thanks to Moore's law but also due to advances in computer science, such as parallelisation and certain key algorithms have been a major contributing factor. CEM is not just a mathematical or electromagnetic analysis but careful consideration also needs to be given to parallelisation, GPU computing, memory and cache issues and other software engineering principles. Efficient numerical algorithms underpinning commercial CEM programs have begun to drive the development of wireless communications technology in recent years. They have been able to reduce the amount of expensive and time consuming measurement campaigns and enable radio communications engineers to optimise and simulate designs before they are manufactured or deployed. However, a criticism of CEM has arisen because numerical techniques are increasingly being applied to problems they have not been designed for by users who are unfamiliar with the underlying electromagnetic theory of the algorithm and problem. The discussion that follows lays out some of the fundamental

ideas of CEM and discusses some of the methods used to solve Maxwell's equations.

3.1 Maxwell's equations

Maxwell's equations are a set of four independent equations that were found through experiments by several scientists but first unified by James Clerk-Maxwell in the 1860s [143]. They are based on Coulomb's law, Ampere's law, Faraday's law and Gauss' laws. These four equations underpin the study of CEM and drive the development of wireless communications technology.

3.1.1 Differential form

The differential form of Maxwell's equations form the basis of CEM analysis. They describe the electric and magnetic field vectors, current densities and charge densities at any point in space and at any given time. They are given by [143]

$$\nabla \times \boldsymbol{\mathcal{E}} = -\boldsymbol{\mathcal{M}} - \frac{\partial \boldsymbol{\mathcal{B}}}{\partial t} \tag{3.1}$$

$$\nabla \times \boldsymbol{\mathcal{H}} = \boldsymbol{\mathcal{J}} + \frac{\partial \boldsymbol{\mathcal{D}}}{\partial t} \tag{3.2}$$

$$\nabla \cdot \boldsymbol{\mathcal{D}} = \rho_e \tag{3.3}$$

$$\nabla \cdot \boldsymbol{\mathcal{B}} = \rho_m \tag{3.4}$$

where the field quantities $\boldsymbol{\mathcal{E}}$, $\boldsymbol{\mathcal{H}}$, $\boldsymbol{\mathcal{J}}$, $\boldsymbol{\mathcal{M}}$, $\boldsymbol{\mathcal{D}}$, $\boldsymbol{\mathcal{B}}$, ρ_e and ρ_m[1] are assumed to be time-varying and a function of space and time, that is $\boldsymbol{\mathcal{E}} = \boldsymbol{\mathcal{E}}(x, y, z; t)$. The definitions and quantities of these field components are

$\boldsymbol{\mathcal{E}}$ is the electric field intensity (volts/meter)

$\boldsymbol{\mathcal{H}}$ is the magnetic field intensity (amperes/meter)

$\boldsymbol{\mathcal{J}}$ is the electric current density (amperes/square meter)

$\boldsymbol{\mathcal{M}}$ is the magnetic current density (volts/square meter)

$\boldsymbol{\mathcal{D}}$ is the electric flux density (coulombs/square meter)

[1] Magnetic current and charge are not physically realisable but have been introduced to balance Maxwell's equations.

$\boldsymbol{\mathcal{B}}$ is the magnetic flux density (webers/square meter)

ρ_e is the electric charge density (coulombs/cubic meter)

ρ_m is the magnetic charge density (webers/cubic meter)

The four equations, (3.1) to (3.4), are known respectively as Faraday's law, the Ampere-Maxwell law, Gauss's law for electric fields and Gauss's law for magnetic fields. Faraday's law, (3.1), states a time-varying magnetic field produces a circulating electric field. (3.2) is commonly referred to as the Maxwell-Ampere law because Maxwell added the electric displacement current density to it. It states that an electric current or a time-varying electric field produces a circulating magnetic field. Gauss's law for electric fields, (3.3), states that an electric charge produces an electric field and similarly for Gauss's law for magnetic fields, (3.4). [144]

A complete description of the electric and magnetic field vectors requires Maxwell's equations and the boundary conditions between different mediums to be considered. The differential form of Maxwell's equations involves derivatives of the field vectors in the space domain which at the boundary between mediums with discontinuous electrical properties have no meaning. The boundary conditions define the behaviour of the field vectors across discontinuous boundaries. The most convenient method for deriving the boundary conditions is to use Maxwell's equations in their integral form [143].

3.1.2 Integral form

The integral form of Maxwell's equations can be derived from the differential form by using Stokes' theorem and the divergence theorem. They describe the electric and magnetic field vectors, current densities and charge densities over a region of space and are analogous to the differential forms. The integral form of Maxwell's equations are given by [143]

$$\oint_C \boldsymbol{\mathcal{E}} \cdot d\mathbf{l} = -\iint_S \boldsymbol{\mathcal{M}} \cdot d\mathbf{s} - \frac{\partial}{\partial t}\iint_S \boldsymbol{\mathcal{B}} \cdot d\mathbf{s} \tag{3.5}$$

$$\oint_C \boldsymbol{\mathcal{H}} \cdot d\mathbf{l} = \iint_S \boldsymbol{\mathcal{J}} \cdot d\mathbf{s} + \frac{\partial}{\partial t}\iint_S \boldsymbol{\mathcal{D}} \cdot d\mathbf{s} \tag{3.6}$$

$$\oiint_S \boldsymbol{\mathcal{D}} \cdot d\mathbf{s} = \varrho_e \tag{3.7}$$

$$\oiint_S \boldsymbol{\mathcal{B}} \cdot d\mathbf{s} = \varrho_m \tag{3.8}$$

where ϱ_e and ϱ_m are the total electric and magnetic charge in a volume V bounded by a surface S, $\iint_S$ denotes integration over a surface S that has the contour C as its boundary and $\oint_C$ is the integral over a closed path C.

3.1.3 Time-harmonic form

The modern form of Maxwell's equations assume the field is time harmonic with a time dependence of e^{jwt}. This will be the format used from here on. Another representation of the time dependence is to use e^{-jwt} where the e^{-jwt} fields are related to the fields obtained assuming e^{jwt} dependence using complex conjugation.

The time-harmonic fields are a major simplification over the instantaneous fields as they are a function of position only. The instantaneous fields are related to the complex time-harmonic spatial form by, in the case of the electric fields,

$$\boldsymbol{\mathcal{E}}(x,y,z;t) = \mathrm{Re}[\mathbf{E}(x,y,z)e^{jwt}] \tag{3.9}$$

where $\boldsymbol{\mathcal{E}}$, $\boldsymbol{\mathcal{H}}$, $\boldsymbol{\mathcal{J}}$, $\boldsymbol{\mathcal{M}}$, $\boldsymbol{\mathcal{D}}$ and $\boldsymbol{\mathcal{B}}$ represent the instantaneous field vectors whilst **E**, **H**, **J**, **M**, **D** and **B** represent the corresponding complex time-harmonic spatial forms that are a function of position only. Thus, the most common format of Maxwell's equations, the time-harmonic differential form, are given by [7], [145], [146]

$$\nabla \times \mathbf{E} = -\mathbf{M} - \jmath\omega\mathbf{B} \tag{3.10}$$

$$\nabla \times \mathbf{H} = \mathbf{J} + \jmath\omega\mathbf{D} \tag{3.11}$$

$$\nabla \cdot \mathbf{D} = \rho_e \tag{3.12}$$

$$\nabla \cdot \mathbf{B} = \rho_m \tag{3.13}$$

and consequently, the time-harmonic integral form of Maxwell's equations can be expressed as [143]

$$\oint_C \mathbf{E} \cdot d\mathbf{l} = -\iint_S \mathbf{M} \cdot d\mathbf{s} - \jmath\omega \iint_S \mathbf{B} \cdot d\mathbf{s} \tag{3.14}$$

$$\oint_C \mathbf{H} \cdot d\mathbf{l} = \iint_S \mathbf{J} \cdot d\mathbf{s} + \jmath\omega \iint_S \mathbf{D} \cdot d\mathbf{s} \tag{3.15}$$

$$\oiint_S \mathbf{D} \cdot d\mathbf{s} = \varrho_e \tag{3.16}$$

$$\oiint_S \mathbf{B} \cdot d\mathbf{s} = \varrho_m \tag{3.17}$$

3.2 Integral equation formulation

The integral equation formulation of scattering problems is derived by considering a general scattering problem and applying the volume or surface equivalence principle. The volume integral equation (VIE) is usually applied to inhomogeneous problems whilst the surface integral equation (SIE) is applied for homogeneous problems as only the boundary of scatterers need be discretised and not the entire volume. The continuous integral equations are then solved using the Method of Moments (MoM) procedure described in Section 3.3.2. The VIE and its derivation is described in detail as it is used throughout the thesis.

3.2.1 General scattering problem

Consider a region of space containing an inhomogeneity with finite volume V illuminated by an electromagnetic field, with a time dependence of e^{jwt} (assumed and suppressed in the following), located outside of the scatterer as shown in Figure 3.1. The inhomogeneous scatterer material is characterised by its relative permittivity $\epsilon_r(x,y,z)$, permeability $\mu_r(x,y,z)$ and conductivity $\sigma(x,y,z)$. The fields external to the scatterer are governed by the equations in Section 3.1.3 and can be split into two components, one associated with the primary source denoted the incident field $\mathbf{E}^i$ and $\mathbf{H}^i$ and the other due to the presence of the scatterer material called the scattered field $\mathbf{E}^s$ and $\mathbf{H}^s$. Both fields radiate in free space and their superposition gives the total field, which is the solution to the scattering problem:

$$\mathbf{E} = \mathbf{E}^i + \mathbf{E}^s \tag{3.18}$$

$$\mathbf{H} = \mathbf{H}^i + \mathbf{H}^s \tag{3.19}$$

where the incident fields in the vicinity of the scatterer must satisfy the vector Helmholtz equations

$$\nabla^2\mathbf{E}^i + k^2\mathbf{E}^i = 0 \tag{3.20}$$

$$\nabla^2\mathbf{H}^i + k^2\mathbf{H}^i = 0 \tag{3.21}$$

The solution of the scattered fields is described in Section 3.2.2.

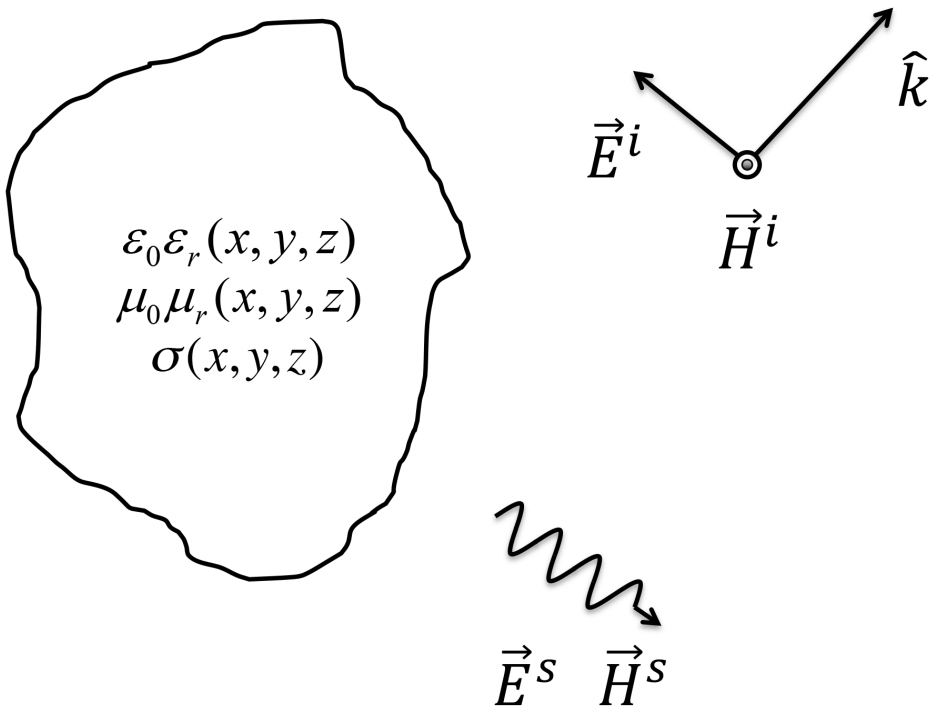

Figure 3.1: An inhomogeneous scatterer illuminated by an incident electromagnetic field that produces a scattered electric field. The fields in the vicinity of the scatterer must satisfy Maxwell's equations.

3.2.1.1 Constitutive parameters

The constitutive parameters of a material are used to characterise its electrical properties. They are called permittivity, permeability and conductivity of a medium and are related to the electromagnetic field vectors. On a macroscopic scale they account for the presence and behaviour of charged particles in materials which when subjected to electromagnetic fields produce currents and alter the propagation of electromagnetic waves to that in free space [143].

The time-varying permittivity of a medium $\hat{\underset{\vee}{\epsilon}}$ (farads/meter) relates the electric flux density $\boldsymbol{\mathcal{D}}$ to the electric field intensity $\boldsymbol{\mathcal{E}}$ in the time domain by

$$\boldsymbol{\mathcal{D}} = \hat{\underset{\vee}{\epsilon}} * \boldsymbol{\mathcal{E}} \tag{3.22}$$

where $*$ denotes convolution, and $\hat{\ }_{\vee}$ represents a time-varying quantity. The time-varying permeability of a medium $\hat{\underset{\vee}{\mu}}$ (henries/meter) relates the magnetic flux density $\boldsymbol{\mathcal{B}}$ to the magnetic field intensity $\boldsymbol{\mathcal{H}}$ in the time domain by

$$\boldsymbol{\mathcal{B}} = \hat{\underset{\vee}{\epsilon}} * \boldsymbol{\mathcal{H}} \tag{3.23}$$

The conduction current density $\boldsymbol{\mathcal{J}}_c$ is related in the time domain to the electric field intensity $\boldsymbol{\mathcal{E}}$ with the time-varying conductivity of a medium $\hat{\underset{\vee}{\sigma}}$ (siemens/meter) by

$$\boldsymbol{\mathcal{J}}_c = \hat{\underset{\vee}{\sigma}} * \boldsymbol{\mathcal{E}} \tag{3.24}$$

For free space

$$\hat{\underset{\vee}{\epsilon}} = \epsilon_0 = 8.854 \times 10^{-12} \text{ (farads/meter)}$$

$$\hat{\underset{\vee}{\mu}} = \mu_0 = 4\pi \times 10^{-7} \text{ (henries/meter)}$$

$$\hat{\underset{\vee}{\sigma}} = \sigma = 0 \text{ (siemens/meter)}$$

and (3.22) to (3.24) reduce to a product.

Materials can be classified as linear versus non-linear, homogeneous versus inhomogeneous, isotropic versus anisotropic, and dispersive versus non-dispersive. A material is linear if its constitutive parameters are not functions of the applied field strength; otherwise it is non-linear. If the constitutive parameters of a material are constant throughout it is homogeneous; otherwise it is referred to as inhomogeneous. An isotropic material has identical values of its constitutive parameters in all

directions - the constitutive parameters are not functions of direction of the applied field; otherwise they are anisotropic materials. A material whose constitutive parameters are functions of frequency is dispersive; otherwise it is non-dispersive and waves of different frequencies all travel at the same speed throughout the material. For linear isotropic non-dispersive materials in the frequency domain the relations (3.22) to (3.24) reduce to products:

$$\mathbf{D} = \epsilon \mathbf{E} \tag{3.25}$$

$$\mathbf{B} = \mu \mathbf{H} \tag{3.26}$$

$$\mathbf{J}_c = \sigma \mathbf{E} \tag{3.27}$$

3.2.2 Volumetric equivalence principle

To simplify the formulation of integral equations it is convenient to replace the inhomogeneous scatterer material in Figure 3.1 by equivalent induced polarisation currents and charges produced by a source located outside the scatterer as shown in Figure 3.2. This leads to an equivalent problem given by [145]

$$\nabla \times \mathbf{E} = -\jmath\omega\mu_0\mathbf{H} - \mathbf{M}_{\text{eq}} \tag{3.28}$$

$$\nabla \times \mathbf{H} = \jmath\omega\epsilon_0\mathbf{E} + \mathbf{J}_{\text{eq}} \tag{3.29}$$

$$\nabla \cdot (\epsilon_0\mathbf{E}) = \rho_e \tag{3.30}$$

$$\nabla \cdot (\mu_0\mathbf{H}) = \rho_m \tag{3.31}$$

where

$$\mathbf{M}_{\text{eq}} = \jmath\omega\mu_0(\mu_r - 1)\mathbf{H} \tag{3.32}$$

$$\mathbf{J}_{\text{eq}} = \jmath\omega\epsilon_0(\epsilon_r - 1)\mathbf{E} \tag{3.33}$$

$$\rho_e = \epsilon_0\epsilon_r\mathbf{E} \cdot \nabla(\frac{1}{\epsilon_r}) \tag{3.34}$$

$$\rho_m = \mu_0\mu_r\mathbf{H} \cdot \nabla(\frac{1}{\mu_r}) \tag{3.35}$$

(3.28) to (3.31) are equivalent to (3.10) to (3.13) thus the procedure of replacing the dielectric or magnetic scatterer material by equivalent induced sources is referred to as the volumetric equivalence principle. The scattered fields described in Section 3.2.1

can now be found from

$$\nabla^2\mathbf{E}^s + k^2\mathbf{E}^s = \jmath\omega\mu_0\mathbf{J}_{\text{eq}} - \frac{\nabla\nabla\cdot\mathbf{J}_{\text{eq}}}{\jmath\omega\epsilon_0} + \nabla\times\mathbf{M}_{\text{eq}} \tag{3.36}$$

$$\nabla^2\mathbf{H}^s + k^2\mathbf{H}^s = -\nabla\times\mathbf{J}_{\text{eq}} + \jmath\omega\epsilon_0\mathbf{M}_{\text{eq}} - \frac{\nabla\nabla\cdot\mathbf{M}_{\text{eq}}}{\jmath\omega\mu_0} \tag{3.37}$$

where $\mathbf{J}_{\text{eq}}$ and $\mathbf{M}_{\text{eq}}$ are the equivalent sources and functions of the total fields $\mathbf{E}$ and $\mathbf{H}$ as given by (3.32) and (3.33).

The sources in (3.32) and (3.33) are assumed to radiate in free space and are much more useful for propagation modelling than solving Maxwell's equations directly in inhomogeneous environments. It is also easier to solve for electromagnetic fields in free space than in inhomogeneous scatterers because explicit integrals can be used to describe the fields produced by sources radiating in free space. These sources are unknown as they depend on the fields which are also unknown. If the relative permeability $\mu_r(x,y,z)$ of the inhomogeneity in Figure 3.1 is assumed constant and equal to that of free space, i.e. $\mu_r(x,y,z) = 1\ \forall\ [x,y,z]$, this has the benefit of removing terms involving magnetic currents and charges from the volume integral equation formulation which will also be used later on to simplify the task of modelling electromagnetic wave propagation.

3.2.3 Electric field integral equations

There are a number of solutions to the Helmholtz equations (3.36) and (3.37). One particular solution is to express the scattered fields as a mixed potential formalisation in terms of the magnetic and electric vector potentials $\mathbf{A}$ and $\mathbf{F}$ as

$$\mathbf{E}^s = -\jmath\omega\mu_0\mathbf{A} - \nabla\Phi_e - \nabla\times\mathbf{F} \tag{3.38}$$

$$\mathbf{H}^s = \nabla\times\mathbf{A} - \jmath\omega\epsilon_0\mathbf{F} - \nabla\Phi_m \tag{3.39}$$

where

$$\Phi_e = \frac{\rho_e}{\epsilon_0} * G \tag{3.40}$$

$$\Phi_m = \frac{\rho_m}{\mu_0} * G \tag{3.41}$$

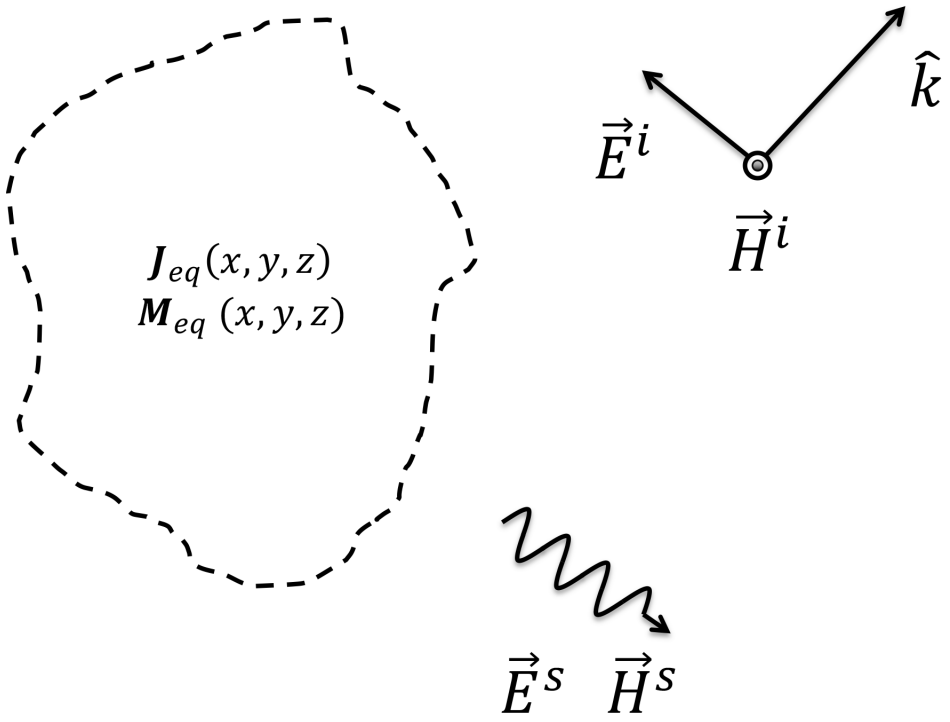

Figure 3.2: Volumetric equivalence problem for the general scattering problem depicted in Figure 3.1.

The vector potentials must satisfy the relationship [145]

$$\nabla^2 \mathbf{A} + k^2 \mathbf{A} = -\mathbf{J}_{\text{eq}} \tag{3.42}$$

$$\nabla^2 \mathbf{F} + k^2 \mathbf{F} = -\mathbf{M}_{\text{eq}} \tag{3.43}$$

where one solution can be written in terms of convolution with the three-dimensional Green's function

$$\mathbf{A} = \mathbf{J}_{\text{eq}} * G \tag{3.44}$$

$$\mathbf{F} = \mathbf{M}_{\text{eq}} * G \tag{3.45}$$

The scalar three-dimensional Green's function is

$$G(\mathbf{r}) = \frac{e^{-\jmath k_0 |\mathbf{r}|}}{4\pi |\mathbf{r}|} \tag{3.46}$$

and the magnetic and electric vector potentials can be expressed as

$$\mathbf{A}(\mathbf{r}) = \iiint \mathbf{J}_{\text{eq}}(\mathbf{r}) \frac{e^{-\jmath k_0 |\mathbf{r}-\mathbf{r}'|}}{4\pi |\mathbf{r}-\mathbf{r}'|} d\mathbf{r} \tag{3.47}$$

$$\mathbf{F}(\mathbf{r}) = \iiint \mathbf{M}_{\text{eq}}(\mathbf{r}) \frac{e^{-\jmath k_0 |\mathbf{r}-\mathbf{r}'|}}{4\pi |\mathbf{r}-\mathbf{r}'|} d\mathbf{r} \tag{3.48}$$

The derivation thus far assumed a three-dimensional problem but for a two-dimensional problem it can be shown that the integration in the third dimension only involves the Green's function. It can be shown that the scalar two-dimensional Green's function is given by [145]

$$G(\mathbf{r}) = \frac{1}{4\jmath} H_0^{(2)}(k_0 |\mathbf{r}|) \tag{3.49}$$

where $H_0^{(2)}(k_0|\mathbf{r}|)$ is the zeroth order Hankel function of the second kind.

Combining the sources described by (3.32) to (3.35) with the source field relationships in (3.38) and (3.39) produces the volume integral equations:

$$\mathbf{E}^i = \mathbf{E}(\mathbf{r}) + \jmath k \eta \mathbf{A} + \nabla \Phi_e + \nabla \times \mathbf{F} \tag{3.50}$$

$$\mathbf{H}^i = \mathbf{H}(\mathbf{r}) - \nabla \times \mathbf{A} + \jmath \frac{k}{\eta} \mathbf{F} + \nabla \Phi_m \tag{3.51}$$

If the scatterer material is composed entirely of dielectric material, i.e. $\mu_r(x, y, z) = 1$

$\forall\,[x,y,z]$, the volume integral equations can be simplified to

$$\mathbf{E}^i = \mathbf{E}(\mathbf{r}) + \jmath k\eta\mathbf{A} + \nabla\Phi_e \tag{3.52}$$

$$\mathbf{H}^i = \mathbf{H}(\mathbf{r}) - \nabla\times\mathbf{A} \tag{3.53}$$

(3.52) is an Electric Field Integral Equation (EFIE) and (3.53) is a Magnetic Field Integral Equation (MFIE).

3.2.4 Volume Electric Field Integral Equation

The Volume Electric Field Integral Equation (VEFIE) is used as the basis for indoor propagation modelling throughout this thesis. It is derived from (3.52) by replacing Φ_e and $\mathbf{A}$ by (3.40) and (3.47) to give

$$\mathbf{E}(\mathbf{r}) = \mathbf{E}^i(\mathbf{r}) + k_0^2\left(1+\frac{1}{k_0^2}\nabla\nabla\cdot\right)\int_V G(\mathbf{r},\mathbf{r}')\chi(\mathbf{r}')\mathbf{E}(\mathbf{r}')d\mathbf{r}' \tag{3.54}$$

where $G(\mathbf{r},\mathbf{r}')$ is the three-dimensional scalar Green's function and

$$\chi(\mathbf{r}') = \frac{k^2(\mathbf{r}')}{k_0^2} - 1 \tag{3.55}$$

is a contrast function, the use of which incorporates the geometry of the problem. k_0 is the background (free space) wave number and $k^2(\mathbf{r}) = \omega^2\mu(\mathbf{r})\epsilon(\mathbf{r}) - \jmath\omega\mu(\mathbf{r})\sigma(\mathbf{r})$. $\int_V$ denotes three-dimensional integration over the entire volume. The three-dimensional form of the VEFIE can be generalised to two dimensions assuming the problem is homogeneous in the z-direction, i.e. infinite scatterers, and invariant fields, and transverse magnetic (TM) polarisation to give

$$E_z(\mathbf{r}) = E_z^i(\mathbf{r}) + k_0^2\int_S G(\mathbf{r},\mathbf{r}')\chi(\mathbf{r}')E_z(\mathbf{r}')d\mathbf{r}' \tag{3.56}$$

where $G(\mathbf{r},\mathbf{r}')$ is the scalar two-dimensional Green's function and $\int_S$ represents integration over the two-dimensional plane. The specific formulations chosen for the VEFIE here use the total electric field $\mathbf{E}$ as the primary unknown as opposed to the volume currents $\mathbf{J}$. This has specific computational benefits in the solution of the VEFIE that will be explained further in Chapter 4. The volume currents are related to

the total electric field by

$$\mathbf{J}(\mathbf{r}) = j\omega\epsilon_0[\epsilon_r(\mathbf{r}) - 1]\mathbf{E}(\mathbf{r}) \tag{3.57}$$

3.3 Numerical solutions of Maxwell's equations

There are various numerical techniques for solving Maxwell's equations that can be classified into two families; full-wave and asymptotic methods. Full-wave methods numerically approximate Maxwell's equations without any physical approximation. Whereas, asymptotic methods make both numerical and physical approximations to Maxwell's equations. The validity of the physical approximations of asymptotic methods increases asymptotically with frequency. Full-wave methods have been typically used for electrically small problems due to their high computational burden. Whilst, asymptotic methods have been developed to study larger problems as they are significantly more efficient. However, with the move towards next generation communications technology asymptotic methods whilst fast, don't provide as high a level of accuracy as full-wave methods. The advancement in numerical algorithms and computing power is making the use of full-wave methods more viable.

Full-wave methods can be further subdivided into those that solve the differential form and the integral form of Maxwell's equations and those that operate in the time and frequency domains. The finite difference (FD) approach and Finite Element Method (FEM) are used to solve the differential form of Maxwell's equations. The MoM is typically used to solve the integral form of Maxwell's equations. The FD approach is most commonly applied in the time domain as the Finite Difference Time Domain (FDTD) whereas the MoM is usually applied to frequency domain integral equations. These are the two most commonly used full-wave techniques [7], [147] and will be described generally below.

The imposition of full-wave methods requires the problem domain to be discretised. Discretising involves subdividing the geometry of the problem into a, typically large, number of small elements. It is also called meshing. There are a large variety of meshes available depending on the technique being used. Some of the more common approaches are a triangular surface mesh, a cuboidal volumetric mesh and a tetrahedral volumetric mesh. The accuracy of full-wave methods is related to the discretisation size and mesh used. The rule of thumb for the discretisation size in the electromagnetic community is ten discrete elements per wavelength, or a mesh size of $\frac{\lambda}{10}$ [7], [145]. Fewer elements per wavelength have been shown to be unable to

capture the variations of the electric and magnetic fields accurately whereas more elements increases the accuracy that can be achieved with the solution and its runtime [142]. The more accurately the environment is modelled and the level of detail that is included, such as modelling small clutter like tables and chairs in indoor environments, also affects the accuracy and runtime of full-wave methods.

Asymptotic methods are primarily based on ray optic methods. Geometric Optics [148]–[150] is the basis of ray tracing [151], [152] and the shooting and bouncing rays method [153]. It originates from the approximation of Maxwell's equations at high frequencies and is currently the most popular method for indoor propagation modelling [46]–[48]. It is used to determine the propagation of incident, reflected and transmitted fields. However, this approach has been deemed not accurate enough for modern applications. Initially, the Geometrical Theory of Diffraction (GTD) [70], [154] was introduced to include the diffraction phenomenon in ray tracing methods. GTD produces infinite fields at shadow boundaries and has been replaced in modern ray tracing models by the Uniform Theory of Diffraction [71], [155], [156] producing accurate diffracted fields across the shadow boundary. Increasingly, the inclusion of diffuse scattering [11]–[13], [18], [75] in ray tracing models has become more popular as a greater level of accuracy is desired. Diffuse scattering considers rays impinging on a surface and scattering in different directions due to the roughness of the surface as opposed to a single specular reflection. Another, less commonly used asymptotic approach is that of Physical Optics [157].

3.3.1 Finite Difference Time Domain

Finite Difference Time Domain (FDTD) is one of the most popular methods in electromagnetic modelling. It has been used in circuit modelling and optics [93]–[95]. It was first introduced by Yee in 1966 [96] and has remained in continuous development and use ever since due to its flexibility and simplicity. Two of its major advantages are; its ability to compute wideband responses in a single computational run and the ease with which it can be parallelised on both CPUs [158], [159] and GPUs [43], [112], [113].

FDTD computes both the electric and magnetic fields, analogous to the Combined Field Integral Equation [160], [161] form of Maxwell's equation. FDTD takes Maxwell's curl equations in the case of linear, isotropic, nondispersive, lossy[2] materials,

[2] Energy of a propagating electromagnetic wave is absorbed in a lossy material.

[94]

$$\frac{\partial \mathbf{H}}{\partial t} = -\frac{1}{\mu}\nabla \times \mathbf{E} - \frac{1}{\mu}(\mathbf{M} + \sigma^* \mathbf{H}) \tag{3.58}$$

$$\frac{\partial \mathbf{E}}{\partial t} = \frac{1}{\epsilon}\nabla \times \mathbf{H} - \frac{1}{\epsilon}(\mathbf{J} + \sigma \mathbf{E}) \tag{3.59}$$

where σ is the electrical conductivity (siemens/meter) and σ^* is the equivalent magnetic conductivity (ohms/meter), and writes them as six coupled partial differential equations (PDEs) where the PDEs for (3.58) are given by

$$\frac{\partial \mathbf{H}_x}{\partial t} = \frac{1}{\mu}\left[\frac{\partial \mathbf{E}_y}{\partial z} - \frac{\partial \mathbf{E}_z}{\partial y} - \frac{1}{\mu}(\mathbf{M}_x + \sigma^* \mathbf{H}_x)\right] \tag{3.60a}$$

$$\frac{\partial \mathbf{H}_y}{\partial t} = \frac{1}{\mu}\left[\frac{\partial \mathbf{E}_z}{\partial x} - \frac{\partial \mathbf{E}_x}{\partial z} - \frac{1}{\mu}(\mathbf{M}_y + \sigma^* \mathbf{H}_y)\right] \tag{3.60b}$$

$$\frac{\partial \mathbf{H}_z}{\partial t} = \frac{1}{\mu}\left[\frac{\partial \mathbf{E}_x}{\partial y} - \frac{\partial \mathbf{E}_y}{\partial x} - \frac{1}{\mu}(\mathbf{M}_z + \sigma^* \mathbf{H}_z)\right] \tag{3.60c}$$

and similar forms can be found for (3.59). The Maxwell curl equations are found by substituting (3.25) and (3.26) into Faraday's law, (3.1), and the Ampere-Maxwell law, (3.2). The six PDEs form the basis of the FDTD method. The FDTD grid, shown in Figure 3.3, must be defined in such a way that Gauss' laws are implicit in the positions of the **H** and **E** field vector components. The finite difference update equations are derived based on Yee's algorithm and for the $\mathbf{E}_x$ component is given by

$$\begin{aligned}
&\frac{E_x|^{n+\frac{1}{2}}_{i,j+\frac{1}{2},k+\frac{1}{2}} - E_x|^{n-\frac{1}{2}}_{i,j+\frac{1}{2},k+\frac{1}{2}}}{\Delta t} = \\
&\frac{1}{\epsilon_{i,j+\frac{1}{2},k+\frac{1}{2}}}\left(\begin{array}{l}\dfrac{H_z|^n_{i,j+1,k+\frac{1}{2}} - H_z|^n_{j,k,l+\frac{1}{2}}}{\Delta y} - \dfrac{H_y|^n_{i,j+\frac{1}{2},k+1} - H_y|^n_{i,j+\frac{1}{2},k}}{\Delta z} \\ - J_x|^n_{i,j+\frac{1}{2},k+\frac{1}{2}} - \sigma_{i,j+\frac{1}{2},k+\frac{1}{2}} E_x|^n_{i,j+\frac{1}{2},k+\frac{1}{2}}\end{array}\right)
\end{aligned} \tag{3.61}$$

for the $n+1$'th time-step. A similar expression can be derived for the $\mathbf{E}_y$, $\mathbf{E}_z$, $\mathbf{H}_x$, $\mathbf{H}_y$ and $\mathbf{H}_z$ update equations. i, j and k refer to the locations in the x, y and z directions. The $n+\frac{1}{2}$ and $n-\frac{1}{2}$ time-steps arise because of the FD approximation of the partial derivative with respect to time.

The Yee algorithm and FDTD method is an explicit FD approach. The set of FD update equations are solved in a leapfrog time-stepping (or time-marching) approach whereby the **E** fields are computed for the next time-step based on the field values at

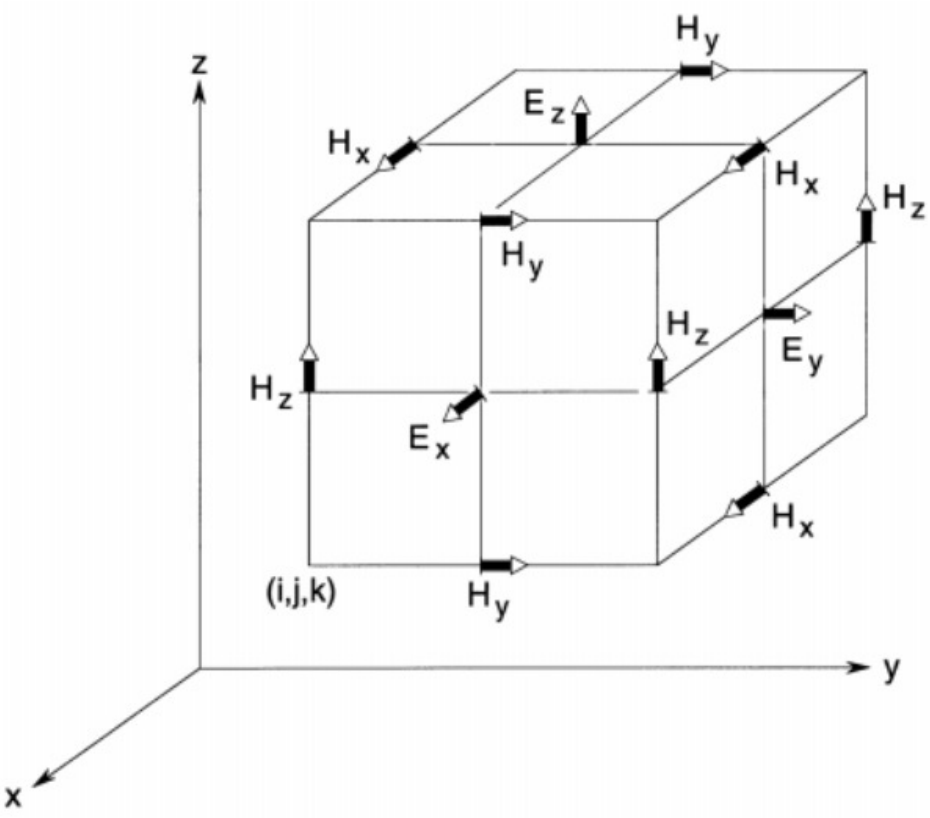

Figure 3.3: Diagram of the Yee cell for the FDTD method.

the current time-step and previous time-steps, then the **H** fields are computed similarly and this process continues until the time-stepping is terminated [96]. The FDTD algorithm is typically stopped when the steady-state is reached, i.e. around 3 times the length of time for the incident field to propagate along the longest direction, or after a predetermined length of time depending on the analysis under consideration [94].

The FDTD method requires careful consideration of the boundary. It is based on differential equations that are approximated by central differences which have no meaning on the boundary of the spatial domain and an open region problem would, therefore, have an infinite computational domain and be impossible to discretise. Thus, the boundary must be terminated appropriately such that the computational domain is finite but the spatial domain is simulated as extending to infinity. For this reason, several absorbing boundary conditions (ABCs) [97]–[104] have been developed which simulate all outward propagating waves propagating to infinity and prevent spurious reflections. The most popular ABC developed by Berenger in 1994 [105] is the perfectly matched layer (PML) that solved the previous issue of mesh termination and led to widespread adoption of the FDTD method [7]. Berenger's PML was revolutionary in that it is completely reflectionless and highly absorbing to plane waves of arbitrary incidence, polarisation and frequency.

The simplicity of the FDTD method stems from the form of the update equations and leapfrog time-stepping algorithm but they do mean that the method is not unconditionally stable. In order to preserve stability an upper limit is placed on the time-step and careful consideration must be given to the discretisation of the computational domain. The time-step restriction was first introduced by Yee but later corrected by Taflove [162] who demonstrated Δt should be chosen according to

$$v_{\max}\Delta t \leq \left(\frac{1}{\Delta x^2} + \frac{1}{\Delta y^2} + \frac{1}{\Delta z^2}\right)^{-\frac{1}{2}} \tag{3.62}$$

where Δx, Δy and Δz are the dimensions of the Yee cube in the x, y and z directions.. A lot of research has been done on non-orthogonal FDTD grids [163]–[165] but this causes the method to lose most of its simplicity.

3.3.2 Method of Moments

The MoM is another extremely popular method in CEM. It was developed by Harrington in 1968 [166] and has been referred to as the method of weighted residuals or boundary element method. It converts a continuous integral equation into a discrete matrix equation that can be solved with linear algebra techniques. It has primarily been used for solving frequency domain integral equation formulations of Maxwell's equations, with an assumed time dependence of e^{jwt}, but can also be applied to time domain integral equation formulations [167], [168].

To describe the MoM procedure, first consider a general inhomogeneous problem of the form

$$L(f) = g \tag{3.63}$$

where L is a continuous operator, f is the unknown function (in the context of EM problems often a current or field quantity) to be determined and g is the excitation (incident field). The unknown function f is expanded into a sum of N weighted basis functions

$$f = \sum_{n=1}^{N} \alpha_n f_n \tag{3.64}$$

where α_n are unknown coefficients and f_n are the basis functions. The basis functions are chosen such that they model the expected behaviour of the unknown function, f, throughout their domain. Substituting (3.64) into (3.63) and using the linearity of L yields

$$\sum_{n=1}^{N} \alpha_n L(f_n) = g \tag{3.65}$$

An inner product (or moment) between a basis function, f_n, and a testing (or weighting) function, w_m, is defined as

$$\langle w, f \rangle = \int w(x) f(x) dx \tag{3.66}$$

and the inner product of (3.65) is taken with the weighting function. This results in

$$\sum_{n=1}^{N} \alpha_n \langle w_m, L(f_n) \rangle = \langle w_m, g \rangle \tag{3.67}$$

which can be written as a matrix equation of the form

$$\mathbf{Za} = \mathbf{b} \tag{3.68}$$

where

$$\mathbf{Z} = \begin{bmatrix} \langle w_1, L(f_1)\rangle & \langle w_1, L(f_2)\rangle & \cdots & \langle w_1, L(f_N)\rangle \\ \langle w_2, L(f_1)\rangle & \langle w_2, L(f_2)\rangle & \cdots & \langle w_2, L(f_N)\rangle \\ \vdots & \vdots & \ddots & \vdots \\ \langle w_N, L(f_1)\rangle & \langle w_N, L(f_2)\rangle & \cdots & \langle w_N, L(f_N)\rangle \end{bmatrix} \tag{3.69}$$

$$\mathbf{a} = \begin{bmatrix} \alpha_1 \\ \alpha_2 \\ \vdots \\ \alpha_N \end{bmatrix} \tag{3.70}$$

$$\mathbf{b} = \begin{bmatrix} \langle w_1, g\rangle \\ \langle w_2, g\rangle \\ \vdots \\ \langle w_N, g\rangle \end{bmatrix} \tag{3.71}$$

(3.68) can be solved by direct matrix inversion or iterative methods.

The choice of basis, f_n, and testing, w_m, functions is important. The basis functions should be linearly independent and chosen such that they can approximate the unknown function, f, reasonably well. The testing functions should similarly be linearly independent. The choice of basis and testing functions is also dependent on the desired accuracy of the solution, the ease of evaluation of the matrix entries and the computational properties of the linear operator L. In two dimensions the simplest and most popular basis function is the pulse basis function [146]. Other basis functions like the piecewise triangular and sinusoidal basis functions exist but they require a slightly higher computational effort. In three dimensions, the most popular basis function for SIE formulations is the Rao-Wilton-Glisson (RWG) basis function [169] whilst for VIE formulations the pulse basis function and Schubert-Wilton-Glisson (SWG) basis function [170] are the most popular. In the MoM the most commonly used testing functions are the Dirac delta function, which is a method referred to as point matching (effectively applying the boundary condition at discrete locations) or using the same basis and testing functions which is known as Galerkin's method [146], [166].

3.4 Method of Moments applied to the volume integral equation

The MoM is used to convert the continuous integral equations (3.54) and (3.56) into linear systems that can be solved by direct matrix inversion or iterative solvers. A weak-form discretisation process will be applied to the 3D VEFIE. It rewrites the integral equation in a different format and uses appropriate basis and testing functions to enable the numerical evaluation of the $\nabla\nabla\cdot$ operation in (3.54) to weaken the singularity. The process of discretising the problem domain and solving the 2D VEFIE with the conventional MoM will be presented first. Then, the weak-form discretisation and MoM will be applied to the 3D VEFIE to solve it.

Considering the general scattering problem in Figure 3.1 the entire problem domain containing scatterer and free space regions is discretised into uniform cubic cells as shown in Figure 3.4. The cells have volume $\Delta v = \Delta x \times \Delta y \times \Delta z$ with cell centres located at $\mathbf{r}_{j,k,l} = (x_j, y_k, z_l)$ where $(j,k,l) \in [1,J]\cdot[1,K]\cdot[1,L]$, in two dimensions their size is $\Delta x \times \Delta y$ with cell centres at $\mathbf{r}_{j,k} = (x_j, y_k)$. The dimensions, Δx, Δy and Δz, of each cell are chosen such that there are at least 10 cells per wavelength.

The unknown total electric field in the VEFIE is expanded with N pulse basis functions represented by

$$p_n(\mathbf{r}) = \begin{cases} 1 & \text{if } \mathbf{r} \in \text{cell } n \\ 0 & \text{if otherwise} \end{cases} \tag{3.72}$$

producing an approximation of

$$E_z(\mathbf{r}) \approx \sum_{n=1}^{N} e_n p_n(\mathbf{r}) \tag{3.73}$$

for the total electric field in two dimensions. Substituting (3.73) into (3.56) produces

$$E_z^i(\mathbf{r}) = \sum_{n=1}^{N} e_n \left(p_n(\mathbf{r}) - k_0^2 \int_{\text{cell } n} G(|\mathbf{r}-\mathbf{r}'|)\chi(\mathbf{r}')d\mathbf{r}' \right) \tag{3.74}$$

Enforcing (3.74) at the cell centres using point matching produces a $N \times N$ system of

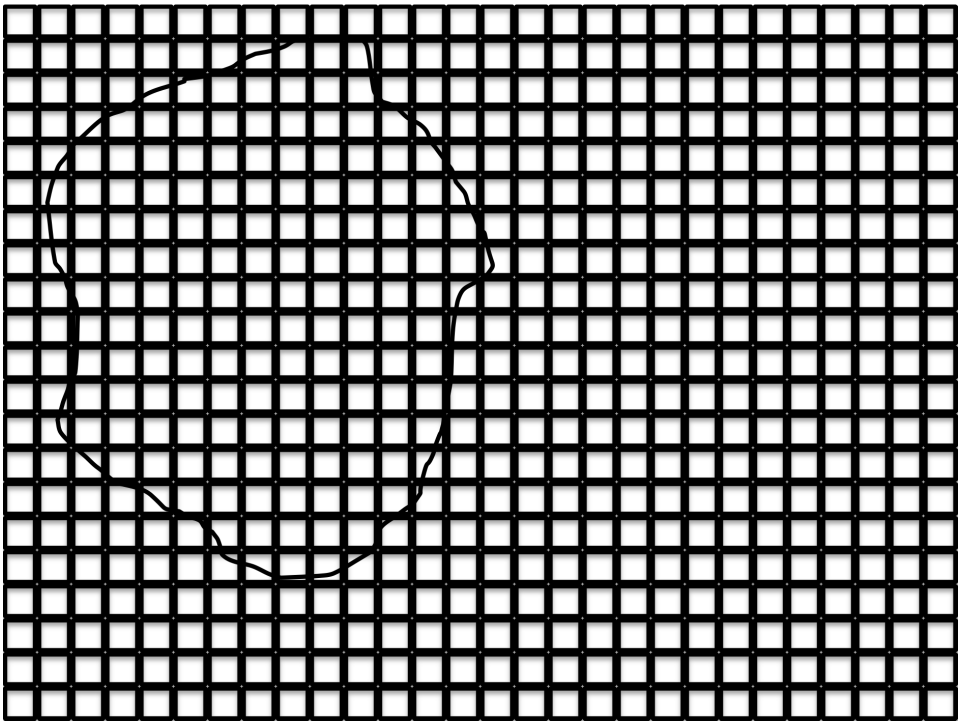

Figure 3.4: Discretised depiction of a general scattering problem.

linearly independent simultaneous equations that can be written as

$$\begin{bmatrix} E_z^i(\mathbf{r}_{1,1}) \\ E_z^i(\mathbf{r}_{2,2}) \\ \vdots \\ E_z^i(\mathbf{r}_{N,N}) \end{bmatrix} = \begin{bmatrix} Z_{11} & Z_{12} & \cdots & Z_{1N} \\ Z_{21} & Z_{22} & \cdots & Z_{2N} \\ \vdots & \vdots & \ddots & \vdots \\ Z_{N1} & Z_{N2} & \cdots & Z_{NN} \end{bmatrix} \begin{bmatrix} e_1 \\ e_2 \\ \vdots \\ e_N \end{bmatrix} \tag{3.75}$$

or more conveniently by

$$\mathbf{v} = \mathbf{Ze} \tag{3.76}$$

where $\mathbf{v}$ is a $N \times 1$ vector containing the discrete values of the incident electric field, $\mathbf{e}$ is a $N \times 1$ vector containing the discrete values of the total electric field and $\mathbf{Z}$ is a $N \times N$ dense matrix given by

$$\mathbf{Z} = \mathbf{I} - \mathbf{GD} \tag{3.77}$$

$$\mathbf{Z}_{mn} = p_n(\mathbf{r}) - k_0^2 \int_{\text{cell } n} G(|\mathbf{r} - \mathbf{r}'|)\chi(\mathbf{r}')d\mathbf{r}' \tag{3.78}$$

The entries of $\mathbf{Z}$ are given by

$$\mathbf{Z}_{mn} = 0 - \frac{1}{4\jmath} \iint_{\text{cell } n} H_0^{(2)}(k_0|\mathbf{r}_m - \mathbf{r}'|)[k^2(\mathbf{r}') - k_0^2]dx'dy' \qquad m \neq n \tag{3.79}$$

for the off-diagonal entries and

$$\mathbf{Z}_{mm} = 1 - \frac{1}{4\jmath} \iint_{\text{cell } m} H_0^{(2)}(k_0|\mathbf{r}_m - \mathbf{r}'|)[k^2(\mathbf{r}') - k_0^2]dx'dy' \tag{3.80}$$

for the diagonal entries. Normally, the integrals in (3.79) and (3.80) would need to be evaluated by numerical quadrature but if the cells are approximated by circles of the same area they can be evaluated analytically using [171]

$$\int_{\phi'=0}^{2\pi} \int_{\rho'=0}^{a} H_0^{(2)}(k_0 R)\rho' \, d\rho' \, d\phi' = \begin{cases} \frac{2\pi a}{k_0} J_0(k_0\rho) H_1^{(2)}(k_0 a) - \frac{\jmath 4}{k_0^2} & \rho < a \\ \frac{2\pi a}{k_0} J_1(k_0 a) H_0^{(2)}(k_0\rho) & \rho > a \end{cases} \tag{3.81}$$

where (ρ, ϕ) represent cylindrical coordinates, a denotes the radius of the equivalent circle, $J_n()$ is the Bessel function of the first kind and order n, $H_n^{(2)}()$ is the Hankel function of the second kind and order n and

$$R = \sqrt{(x - x')^2 + (y - y')^2} \tag{3.82}$$

Using the circular-cell approximation [172] the off-diagonal entries and diagonal entries of $\mathbf{Z}$ can be computed from

$$\mathbf{Z}_{mn} = 0 - \frac{1}{4\jmath}[k^2(\mathbf{r}') - k_0^2]\left(\frac{2\pi a_n}{k_0} J_1(k_0 a_n) H_0^{(2)}(k_0 R_{mn})\right) \qquad m \neq n \tag{3.83}$$

$$\mathbf{Z}_{mm} = 1 - \frac{1}{4\jmath}[k^2(\mathbf{r}') - k_0^2]\left(\frac{2\pi a_m}{k_0} J_0(k_0 R_{mm}) H_1^{(2)}(k_0 a_m) - \frac{\jmath 4}{k_0^2}\right) \tag{3.84}$$

where $|\mathbf{r} - \mathbf{r}'|$ is the distance from the centre of the cell of interest to the integrand point. For the self term, when $m = n$ $R_{mm} = 0$ and $J_0(k_0 R_{mm}) = 1$, therefore, (3.84) reduces to

$$\mathbf{Z}_{mm} = 1 - \frac{1}{4\jmath}[k^2(\mathbf{r}') - k_0^2]\left(\frac{2\pi a_m}{k_0} H_1^{(2)}(k_0 a_m) - \frac{\jmath 4}{k_0^2}\right) \tag{3.85}$$

$\mathbf{I}$, $\mathbf{G}$ and $\mathbf{D}$ from (3.77) are, thus, given by

$$I_{mn} = \begin{cases} 1 & m = n \\ 0 & m \neq n \end{cases} \tag{3.86}$$

$$D_{mn} = \begin{cases} \frac{1}{4\jmath}[k^2(\mathbf{r}') - k_0^2] & m = n \\ 0 & m \neq n \end{cases} \tag{3.87}$$

$$G_{mn} = \begin{cases} \frac{2\pi a_m}{k_0} H_1^{(2)}(k_0 a_m) - \frac{\jmath 4}{k_0^2} & m = n \\ \frac{2\pi a_n}{k_0} J_1(k_0 a_n) H_0^{(2)}(k_0 R_{mn}) & m \neq n \end{cases} \tag{3.88}$$

3.4.1 Weak-form discretisation in three dimensions

The weak-form discretisation reduces the effect of the singularity in the VEFIE [173], [174]. It results in a linear system of N simultaneous equations. The weak-form discretisation defines the magnetic vector potential $\mathbf{A}$ as

$$\mathbf{A}(\mathbf{r}) = -\jmath\omega\mu_0\epsilon_0 \int_V G(|\mathbf{r} - \mathbf{r}'|)\chi(\mathbf{r}')\mathbf{E}(\mathbf{r}')d\mathbf{r}' \tag{3.89}$$

The integral equation, (3.54), can then be rewritten as

$$\mathbf{E}^i(\mathbf{r}) = \mathbf{E}(\mathbf{r}) - \jmath\omega\mathbf{A}(\mathbf{r}) - \mathbf{E}^{irr}(\mathbf{r}) \tag{3.90}$$

where

$$\mathbf{E}^{irr}(\mathbf{r}) = \frac{\jmath\omega}{k_0^2}\nabla\nabla\cdot\mathbf{A}(\mathbf{r}) \tag{3.91}$$

is the irrotational part of the scattered electric field[3].

The problem domain is discretised into N uniform cubic cells. The cell centres are located at $\mathbf{r}_{j,k,l} = (x_j, y_k, z_l)$ where $(j,k,l) \in [1,J]\cdot[1,K]\cdot[1,L]$ and are of size $\Delta x \times \Delta y \times \Delta z$ in the x, y and z directions respectively. Pulse basis functions are used, defined as (3.72), and testing is performed with a Dirac delta function to obtain

$$\mathbf{E}^i_{j,k,l} = \mathbf{E}_{j,k,l} - \jmath\omega\mathbf{A}_{j,k,l} - \mathbf{E}^{irr}_{j,k,l} \tag{3.92}$$

where $\mathbf{E}_{j,k,l} = \mathbf{E}(\mathbf{r}_{j,k,l})$ and $\mathbf{E}^i_{j,k,l}$, $\mathbf{A}_{j,k,l}$ and $\mathbf{E}^{irr}_{j,k,l}$ are defined similarly. The elements of $\mathbf{A}_{j,k,l}$ are obtained from

$$\mathbf{A}_{j,k,l} = C_0 \sum_{j'=1}^{J}\sum_{k'=1}^{K}\sum_{l'=1}^{L} G_{j-j',k-k',l-l'}\chi_{j',k',l'}\mathbf{E}_{j',k',l'} \tag{3.93}$$

where $C_0 = -\jmath\omega\mu_0\epsilon_0\Delta v$. $\mathbf{E}^{irr}_{j,k,l}$ is approximated using a central finite differencing scheme which gives rise to

$$\begin{aligned}
\mathbf{E}^{irr}_{x:j,k,l} &= \frac{\jmath\omega}{k_0^2\Delta x^2}(\mathbf{A}_{x:j-1,k,l} - 2\mathbf{A}_{x:j,k,l} + \mathbf{A}_{x:j+1,k,l}) \\
&\quad + \frac{\jmath\omega}{4k_0^2\Delta x\Delta y}(\mathbf{A}_{y:j-1,k-1,l} - \mathbf{A}_{y:j-1,k+1,l} - \mathbf{A}_{y:j+1,k-1,l} + \mathbf{A}_{y:j+1,k+1,l}) \\
&\quad + \frac{\jmath\omega}{4k_0^2\Delta x\Delta z}(\mathbf{A}_{z:j-1,k,l-1} - \mathbf{A}_{z:j-1,k,l+1} - \mathbf{A}_{z:j+1,k,l-1} + \mathbf{A}_{z:j+1,k,l+1}) \\
\mathbf{E}^{irr}_{y:j,k,l} &= \frac{\jmath\omega}{k_0^2\Delta y^2}(\mathbf{A}_{y:j,k-1,l} - 2\mathbf{A}_{y:j,k,l} + \mathbf{A}_{y:j,k+1,l}) \\
&\quad + \frac{\jmath\omega}{4k_0^2\Delta x\Delta y}(\mathbf{A}_{x:j-1,k-1,l} - \mathbf{A}_{x:j-1,k+1,l} - \mathbf{A}_{x:j+1,k-1,l} + \mathbf{A}_{x:j+1,k+1,l}) \\
&\quad + \frac{\jmath\omega}{4k_0^2\Delta y\Delta z}(\mathbf{A}_{z:j,k-1,l-1} - \mathbf{A}_{z:j,k-1,l+1} - \mathbf{A}_{z:j,k+1,l-1} + \mathbf{A}_{z:j,k+1,l+1}) \\
\mathbf{E}^{irr}_{z:j,k,l} &= \frac{\jmath\omega}{k_0^2\Delta z^2}(\mathbf{A}_{z:j,k,l-1} - 2\mathbf{A}_{z:j,k,l} + \mathbf{A}_{z:j,k,l+1}) \\
&\quad + \frac{\jmath\omega}{4k_0^2\Delta x\Delta z}(\mathbf{A}_{x:j-1,k,l-1} - \mathbf{A}_{x:j-1,k,l+1} - \mathbf{A}_{x:j+1,k,l-1} + \mathbf{A}_{x:j+1,k,l+1}) \\
&\quad + \frac{\jmath\omega}{4k_0^2\Delta y\Delta z}(\mathbf{A}_{y:j,k-1,l-1} - \mathbf{A}_{y:j,k-1,l+1} - \mathbf{A}_{y:j,k+1,l-1} + \mathbf{A}_{y:j,k+1,l+1})
\end{aligned} \tag{3.94}$$

[3] A vector field is irrotational if its curl is zero.

(3.92) can be written as a matrix equation of the form

$$\mathbf{v} = \mathbf{Ze} \tag{3.95}$$

similarly to the 2D case. Here, $\mathbf{Z}$ can be rewritten as

$$\mathbf{Z} = \mathbf{I} - k_0^2 \Delta v \mathbf{GD} - \Delta v \mathbf{HGD} \tag{3.96}$$

$\mathbf{v}$ and $\mathbf{e}$ are column vectors of length $3N$ representing the unknown total electric field and the known incident electric field respectively.

$$\mathbf{v} = \begin{bmatrix} \mathbf{E}_x^i \\ \mathbf{E}_y^i \\ \mathbf{E}_z^i \end{bmatrix}, \mathbf{e} = \begin{bmatrix} \mathbf{E}_x \\ \mathbf{E}_y \\ \mathbf{E}_z \end{bmatrix} \tag{3.97}$$

Each $\mathbf{E}_\mu^i$ and $\mathbf{E}_\mu$, where $\mu = \{x, y, z\}$, in (3.97) are vectors of length N and contain the x, y and z components of the incident and total electric fields at the centre of each cell in the discretised problem. $\mathbf{I}$ is the identity matrix, $\mathbf{G}$ represents the Green's function in (3.46)

$$\mathbf{G} = \begin{bmatrix} \mathbf{G}_\mathrm{T} & 0 & 0 \\ 0 & \mathbf{G}_\mathrm{T} & 0 \\ 0 & 0 & \mathbf{G}_\mathrm{T} \end{bmatrix} \tag{3.98}$$

where each $\mathbf{G}_\mathrm{T}$ has dimensions $N \times N$ and block Toeplitz structure. $\mathbf{D}$ is a diagonal contrast matrix consisting of (3.55) evaluated at the cell centres. $\mathbf{H}$ is a sparse matrix containing a suitable numerical implementation of the $\nabla\nabla\cdot$ operation.

(3.76) and (3.95) can be solved by direct matrix inversion but for very large problems like those encountered in indoor propagation modelling this is very prohibitive. N, the number of linear independent simultaneous equations that must be solved grows as $\frac{\lambda}{10}$ for each of x, y and z. This quickly produces matrix equations in two dimensions of tens of thousand unknown values and in three dimensions millions of unknowns for indoor propagation problems. With a best-case computational complexity of $\mathcal{O}(N^{2.373})$ [175] and a typical complexity of $\mathcal{O}(N^3)$ [176] for matrix inversion and the memory requirements to store the $N \times N$ $\mathbf{Z}$ matrix this becomes very unwieldy quickly. The next chapter investigates iterative methods with a computational complexity of $\mathcal{O}(m\sqrt{k})$ [177], where m is the number of non-zero entries in $\mathbf{Z}$ and k is its condition number, as a means to speed up the solution of (3.76) and (3.95).

Chapter 4

Iterative solvers for the solution of linear systems

4.1 Introduction

The application of the Method of Moments (MoM) produces a large linear system of equations. The resulting $\mathbf{V} = \mathbf{Ze}$ matrix equation is dense and of large order due to the need to discretise the geometry at a rate of at least $\frac{\lambda}{10}$. There are two main approaches that can be used to solve the system; direct matrix inversion or through iterative methods. Direct matrix inversion is only suitable for solving small problems as it requires the storage and inversion of $\mathbf{Z}$ which has $\mathcal{O}(N^2)$ storage requirement and $\mathcal{O}(N^3)$ computational complexity for inversion, where N is the number of unknown values to be computed. Iterative methods on the other hand do not require the explicit storage of $\mathbf{Z}$ and have a computational complexity $\mathcal{O}(N^2)$.

Iterative solvers can't solve all linear systems successfully [178]. The choice of which iterative solver to use has been studied extensively [179], [180] and is dependent on the type of system to be solved. Some factors which affect the choice of iterative solver are whether the matrix is Hermitian[1], the cost of matrix-vector multiplication and the availability of the transpose of the system matrix $\mathbf{Z}$. Iterative solvers are terminated after they satisfy a specific convergence criterion and thus produce a numerically approximate solution. Their efficiency is dependant on various factors such as the geometry and types of materials within the problem which affect the composition of $\mathbf{Z}$.

There are two main types of iterative methods: stationary and non-stationary. West and Sturm [181] have compared various iterative solvers for 2D scattering problems.

[1] A Hermitian matrix is a complex square matrix that is equal to its conjugate transpose.

They concluded stationary methods are more efficient than non-stationary when the problem is well-conditioned. However, non-stationary methods are more robust and are affected less by the geometry of scatterers or for problems where there is a high potential for multipath scattering as in the case of indoor propagation problems [58], [182]–[184]. Greenbaum [179] found the convergence rate of non-stationary methods to be superior to stationary methods for symmetric positive definite systems. Thus, our analysis of iterative methods and use of them in this work will focus on the more robust non-stationary methods, particularly those based on Krylov subspace projection [180], [185].

4.2 Krylov iterative solvers

Non-stationary Krylov iterative solvers are used to solve matrix equations of the form

$$\mathbf{A}\mathbf{x} = \mathbf{b} \tag{4.1}$$

where $\mathbf{A}$ is a $N \times N$ matrix, $\mathbf{x}$ and $\mathbf{b}$ are $N \times 1$ vectors where $\mathbf{x}$ is the unknown to be computed. They are based on projection onto Krylov subspaces and make successive approximations to $\mathbf{x}$. They are currently considered to be the most robust iterative solvers available [145], [179]–[181], [185].

Instead of solving (4.1) they initially solve $\mathbf{K}\mathbf{x}_0 = \mathbf{b}$ where $\mathbf{x}_0$ is an approximation to $\mathbf{x}$. If $\mathbf{x}_0$ is chosen as an initial guess to $\mathbf{x}$ the aim is to find the correction $\mathbf{z}$ that satisfies

$$\mathbf{A}(\mathbf{x}_0 + \mathbf{z}) = \mathbf{b} \tag{4.2}$$

or alternatively written as

$$\mathbf{A}\mathbf{z} = \mathbf{b} - \mathbf{A}\mathbf{x}_0 \tag{4.3}$$

Instead of solving (4.3) it is easier solve

$$\mathbf{K}\mathbf{z}_0 = \mathbf{b} - \mathbf{A}\mathbf{x}_0 \tag{4.4}$$

which leads to a new approximation of $\mathbf{x}_1 = \mathbf{x}_0 + \mathbf{z}_0$. By repeating this procedure for consecutive approximations of $\mathbf{x}_n$ an iterative method for the solution of $\mathbf{x}$ is achieved

$$\begin{aligned} \mathbf{x}_{n+1} &= \mathbf{x}_n + \mathbf{z}_n \\ &= \mathbf{x}_n + \mathbf{K}^{-1}(\mathbf{b} - \mathbf{A}\mathbf{x}_n) \end{aligned} \tag{4.5}$$

It must be noted that $\mathbf{K}^{-1}$ is (almost) never computed explicitly and is only used for notational purposes. If $\mathbf{K}$ is approximated by the identity matrix, $\mathbf{I}$, (4.5) reduces to the Richardson iteration

$$\mathbf{x}_{n+1} = \mathbf{b} + (\mathbf{I} - \mathbf{A})\mathbf{x}_n = \mathbf{x}_n + \mathbf{r}_n \tag{4.6}$$

where $\mathbf{r}_n$ is the residual given by $\mathbf{r}_n = \mathbf{b} - \mathbf{A}\mathbf{x}_n$. (4.6) is the basis for most iterative methods and in particular those discussed here.

Krylov subspace methods aim to make better approximations to the Richardson iteration by projection onto Krylov subspaces. The original idea for Krylov subspaces is based on the Cayley Hamilton theorem [186] which states that the inverse of a $N \times N$ matrix $\mathbf{A}$ can be expressed by a polynomial of degree $(N-1)$ in $\mathbf{A}$

$$\mathbf{A}^{-1} = \alpha_1\mathbf{I} + \alpha_2\mathbf{A} + \alpha_3\mathbf{A}^2 + \cdots + \alpha_N\mathbf{A}^{N-1} \tag{4.7}$$

where α_n are coefficients and $\mathbf{I}$ is the identity matrix. By repeating the Richardson iteration process it can be shown that the approximation to the solution is made up of successive approximations of the previous solutions and thus the residuals

$$\begin{aligned}
\mathbf{x}_{n+1} &= \mathbf{r}_0 + \mathbf{r}_1 + \mathbf{r}_2 + \cdots \mathbf{r}_n \\
&= \sum_{m=0}^{n} (\mathbf{I} - \mathbf{A})^m \mathbf{r}_0 \\
&\in \text{span}\{\mathbf{r}_0, \mathbf{A}\mathbf{r}_0, \mathbf{A}^2\mathbf{r}_0, \cdots, \mathbf{A}^{n-1}\mathbf{r}_0\} \\
&\equiv \mathcal{K}^n(\mathbf{A}; \mathbf{r}_0)
\end{aligned} \tag{4.8}$$

The m-dimensional Krylov subspace, $\mathcal{K}^m(\mathbf{A}; \mathbf{v})$ is defined as the m-dimensional space spanned by a given vector, $\mathbf{v}$, with increasing powers of $\mathbf{A}$ applied to $\mathbf{v}$ up to the $(m-1)^{\text{th}}$ power [180]

$$\mathcal{K}^m(\mathbf{A}; \mathbf{v}) = \text{span}\{\mathbf{v}, \mathbf{A}\mathbf{v}, \mathbf{A}^2\mathbf{v}, \cdots, \mathbf{A}^{m-1}\mathbf{v}\} \tag{4.9}$$

Thus, successive approximations to the solution are contained within the Krylov subspace, where $\mathbf{v} = \mathbf{r}_0$.

Krylov solvers attempt to minimise the residual $\mathbf{r}_n$ at the n^{th} iteration. There are four different classes of Krylov subspace methods that arise from the different approaches used to minimise the residual. The Ritz-Galerkin and Petrov Galerkin ap-

proaches lead to the Conjugate Gradient (CG) and Bi-Conjugate Gradient (BiCG) methods examined here [187]. The CG method is limited to the solution of real, symmetric positive definite matrices[2]. A modification to the CG method known as the Conjugate Gradient applied to the normal equations (CG-NE) will be the variant studied here as it does not require a real, symmetric positive definite system matrix. The minimum norm residual and minimum norm error approaches lead to methods such as the Generalized Minimal Residual (GMRES) and Symmetric LQ (SYMMLQ) [188]. The reader is referred to [189] for more information on these methods. The Bi-Conjugate Gradient Stabilised (BiCGSTAB) [190] method is a hybrid of the Conjugate Gradient Squared (CGS) [191] and BiCG methods. Its aim is to overcome the irregular convergence problem associated with the BiCG method. For a more detailed overview of Krylov subspace methods and iterative solvers the reader is referred to [179], [180], [185], [189].

4.2.1 Conjugate Gradient method

In electromagnetic scattering problems the system matrix often exhibits some symmetry but is not real symmetric positive definite which is required by the CG algorithm. The CG-NE method is suitable for all types of linear systems as it forces the system matrix to be symmetric positive definite by premultiplying by $\mathbf{A}^T$ to produce the normal equations

$$\mathbf{A}^T\mathbf{A}\mathbf{x} = \mathbf{A}^T\mathbf{b} \tag{4.10}$$

where ^{T} denotes the conjugate-transpose operation. The remainder of the CG-NE algorithm is very similar to the conventional CG algorithm.

The CG-NE algorithm seeks an estimate for the solution $\mathbf{x}_n$ with

$$\mathbf{x}_{n+1} = \mathbf{x}_n + \alpha_n \mathbf{p}_n \tag{4.11}$$

where α_n determines how far the algorithm moves along $\mathbf{p}_n$, the search direction in the N-dimensional Krylov subspace, to correct the estimate. It attempts to minimise the least-squares problem

$$||\mathbf{b} - \mathbf{A}\mathbf{x}_n||_2 \tag{4.12}$$

where the α_n that minimises (4.12) along $\mathbf{p}_n$ in N-dimensional space for (4.10) is given

[2] A symmetric $N \times N$ real matrix A is said to be positive definite if the scalar $x^T Ax$ is strictly positive for all nonzero vectors x.

by

$$\alpha_n = \frac{||\mathbf{A}^T\mathbf{r}_n||_2}{||\mathbf{A}\mathbf{p}_n||_2} \tag{4.13}$$

If the minimisation is considered along two directions

$$\mathbf{x}_{n+1} = \mathbf{x}_n + \alpha_n(\mathbf{p}_n + \beta_n\mathbf{q}_n) \tag{4.14}$$

is obtained where $\mathbf{q}_n$, like $\mathbf{p}_n$, is a search direction in N-dimensional space and β_n determines how far along $\mathbf{q}_n$ the CG-NE algorithm moves to minimise (4.12). If $\mathbf{q}_n$ is a direction vector that has been used previously in the iteration process then the best optimisation direction for $\mathbf{p}_n$ is orthogonal to $\mathbf{q}_n$. If $\mathbf{p}_n$ is chosen orthogonal to $\mathbf{q}_n$ the iteration process is minimising the error in a new direction in N-dimensional space, thus, ensuring the best choice possible for subsequent search directions. If the error has already been minimised in one direction with the optimal α_n then minimising it in this direction again would be redundant. Due to the orthogonality of the search directions the residual can be expressed as

$$\mathbf{r}_{n+1} = \mathbf{r}_n - \alpha_n\mathbf{A}\mathbf{p}_n \tag{4.15}$$

where the direction vectors are found from

$$\mathbf{p}_{n+1} = \mathbf{A}^T r_{n+1} + \beta_n\mathbf{p}_n \tag{4.16}$$

β_n is chosen such that $\mathbf{p}_{n+1}$ is orthogonal to $\mathbf{p}_n$

$$\beta_n = \frac{||\mathbf{A}^T\mathbf{r}_{n+1}||_2}{||\mathbf{A}^T\mathbf{r}_n||_2} \tag{4.17}$$

The complete CG-NE algorithm is shown in Algorithm 4.1. An in-depth description of the CG method and its origins can be found in [177].

4.2.2 Bi-Conjugate Gradient method

The BiCG method is another approach for solving non-symmetric systems similar to the CG-NE but it does not guarantee minimisation. It does not try to produce a set of orthogonal residual vectors but instead replaces the residual vector sequence with two mutually orthogonal sequences. One sequence is based on the original system $\mathbf{A}\mathbf{x} = \mathbf{b}$ and the other is derived from the transpose of the original matrix $\mathbf{A}^T\mathbf{x} =$

Algorithm 4.1 Conjugate Gradient method applied to the normal equations

1: $\mathbf{x}_0 =$ initial guess
2: $\mathbf{r}_0 = \mathbf{b} - \mathbf{A}\mathbf{x}_0$
3: $\mathbf{z}_0 = \mathbf{A}^T\mathbf{r}_0$
4: $\mathbf{p}_0 = \mathbf{z}_0$
5: **for** $n = 0, 1, \ldots$ **do**
6: $\quad \mathbf{q}_n = \mathbf{A}\mathbf{p}_n$
7: $\quad \alpha_n = \frac{||\mathbf{z}_n||_2}{||\mathbf{q}_n||_2}$
8: $\quad \mathbf{x}_{n+1} = \mathbf{x}_n + \alpha_n\mathbf{p}_n$
9: $\quad \mathbf{r}_{n+1} = \mathbf{r}_n - \alpha_n\mathbf{q}_n$
10: $\quad \mathbf{z}_{n+1} = \mathbf{A}^T\mathbf{r}_{n+1}$
11: $\quad \beta_n = \frac{||\mathbf{z}_{n+1}||_2}{||\mathbf{z}_n||_2}$
12: $\quad \mathbf{p}_{n+1} = \mathbf{z}_{n+1} + \beta_n\mathbf{p}_n$
13: $\quad$ **if** $\frac{||\mathbf{r}_n||_2}{||\mathbf{b}||_2} <$ tolerance **then**
14: $\quad\quad$ Terminate algorithm
15: $\quad$ **end if**
16: **end for**

b. Hence, the BiCG involves the computation of two different residuals and two different search directions during each iteration. This requires the computation of two matrix-vector products which can increase its computation time.

The residuals in the BiCG are updated similarly to the CG

$$\mathbf{r}_{n+1} = \mathbf{r}_n - \alpha_n \mathbf{A}\mathbf{p}_n \tag{4.18}$$

$$\tilde{\mathbf{r}}_{n+1} = \tilde{\mathbf{r}}_n - \alpha_n \mathbf{A}^T \tilde{\mathbf{p}}_n \tag{4.19}$$

and the direction vectors

$$\mathbf{p}_{n+1} = \mathbf{r}_{n+1} + \beta_n \mathbf{p}_n \tag{4.20}$$

$$\tilde{\mathbf{p}}_{n+1} = \tilde{\mathbf{r}}_{n+1} + \beta_n \tilde{\mathbf{p}}_n \tag{4.21}$$

The coefficients α_n and β_n are chosen to produce orthogonality between the residuals

$$\alpha_n = \frac{(\tilde{\mathbf{r}}_n)^T \mathbf{r}_n}{(\tilde{\mathbf{p}}_n)^T \mathbf{A}\mathbf{p}_n} \tag{4.22}$$

$$\beta_n = \frac{(\tilde{\mathbf{r}}_{n+1})^T \mathbf{r}_{n+1}}{(\tilde{\mathbf{r}}_n)^T \mathbf{r}_n} \tag{4.23}$$

The minimisation process of the CG isn't preserved as the orthogonality of the residuals is not based on previous residuals. Thus, the BiCG has been shown to have irregular convergence [179], [180], [189]. It also requires two matrix-vector products per iteration. The BiCG algorithm is summarised in Algorithm 4.2.

4.2.3 Conjugate Gradient Squared method

The CGS method is a hybrid method developed to avoid the use of $\mathbf{A}^T$ in the BiCG. It can obtain a better convergence rate than the BiCG but suffers from rounding errors that can lead to inaccurate results [189]. It has a similar computational complexity to the BiCG method.

The CGS expresses the residual from the BiCG method as

$$\mathbf{r}_n = \phi_n(\mathbf{A})\mathbf{r}_0 \tag{4.24}$$

where ϕ_n is a polynomial of degree n and $\mathbf{p}_n$, the search direction, is given by

$$\mathbf{p}_n = \psi_n(\mathbf{A})\mathbf{r}_0 \tag{4.25}$$

Algorithm 4.2 Bi-Conjugate Gradient method

$\mathbf{x}_0 =$ initial guess

$\mathbf{r}_0 = \mathbf{b} - \mathbf{A}\mathbf{x}_0$

$\tilde{\mathbf{r}}_0 = \mathbf{r}_0$

$\mathbf{p}_0 = \mathbf{r}_0$

$\tilde{\mathbf{p}}_0 = \tilde{\mathbf{r}}_0$

for $n = 0, 1, \ldots$ **do**

    $\mathbf{q}_n = \mathbf{A}\mathbf{p}_n$

    $\tilde{\mathbf{q}}_n = \mathbf{A}^T\tilde{\mathbf{p}}_n$

    $\alpha_n = \frac{(\tilde{\mathbf{r}}_n)^T\mathbf{r}_n}{(\tilde{\mathbf{p}}_n)^T\mathbf{q}_n}$

    $\mathbf{x}_{n+1} = \mathbf{x}_n + \alpha_n\mathbf{p}_n$

    $\mathbf{r}_{n+1} = \mathbf{r}_n - \alpha_n\mathbf{q}_n$

    $\tilde{\mathbf{r}}_{n+1} = \tilde{\mathbf{r}}_n - \alpha_n\tilde{\mathbf{q}}_n$

    $\beta_n = \frac{(\tilde{\mathbf{r}}_{n+1})^T\mathbf{r}_{n+1}}{(\tilde{\mathbf{r}}_n)^T\mathbf{r}_n}$

    $\mathbf{p}_{n+1} = \mathbf{r}_{n+1} + \beta_n\mathbf{p}_n$

    $\tilde{\mathbf{p}}_{n+1} = \tilde{\mathbf{r}}_{n+1} + \beta_n\tilde{\mathbf{p}}_n$

    if $\frac{||\mathbf{r}_n||_2}{||\mathbf{b}||_2} <$ tolerance **then**

        Terminate algorithm

    end if

end for

where ψ_n is a polynomial of degree n also. $\tilde{\mathbf{r}}_n$ and $\tilde{\mathbf{p}}_n$ are expressed similarly to (4.24) and (4.25)

$$\tilde{\mathbf{r}}_n = \phi_n(\mathbf{A}^T)\tilde{\mathbf{r}}_0 \tag{4.26}$$

$$\tilde{\mathbf{p}}_n = \psi_n(\mathbf{A}^T)\tilde{\mathbf{r}}_0 \tag{4.27}$$

The polynomials ϕ_n and ψ_n are squared forming the basis of the CGS algorithm to give

$$\mathbf{r}_n = \phi_n^2(\mathbf{A})\mathbf{r}_0 \tag{4.28}$$

$$\mathbf{p}_n = \psi_n^2(\mathbf{A})\mathbf{r}_0 \tag{4.29}$$

The CGS algorithm is summarised in Algorithm 4.3. The CGS algorithm still suffers from irregular convergence that can be worse due to the squaring of the polynomials and it introduces significant rounding error too [185].

4.2.4 Bi-Conjugate Gradient Stabilised method

The BiCGSTAB method is a hybrid of the BiCG and CGS methods. It removes the drawbacks of the CGS method and employs a steepest descent update to produce a much smoother convergence. It can be very effective but its performance is quite irregular depending on the problem to be solved [189].

The residual in the BiCGSTAB method is similar to the CGS

$$\mathbf{r}_n = \gamma_n(\mathbf{A})\phi_n(\mathbf{A})\mathbf{r}_0 \tag{4.30}$$

where ϕ_n is the residual polynomial associated with the BiCG algorithm and γ_n is a new polynomial defined recursively at each iteration step for the purpose of 'stabilising' the convergence rate of the original algorithm

$$\gamma_{n+1}(\mathbf{A}) = (1 - \omega_n\mathbf{A})\gamma_n(\mathbf{A}) \tag{4.31}$$

ω_n is chosen, similarly to α_n in the CG, to minimise the error and is given by

$$\omega_n = \frac{(\mathbf{s}_n)^T\mathbf{A}\mathbf{s}_n}{(\mathbf{A}\mathbf{s}_n)^T\mathbf{A}\mathbf{s}_n} \tag{4.32}$$

where

$$\mathbf{s}_n = \mathbf{r}_n - \alpha_n\mathbf{A}\mathbf{p}_n \tag{4.33}$$

Algorithm 4.3 Conjugate Gradient Squared method

$\mathbf{x}_0 =$ initial guess

$\mathbf{r}_0 = \mathbf{b} - \mathbf{A}\mathbf{x}_0$

$\tilde{\mathbf{r}}_0$ arbitrary such that $\tilde{\mathbf{r}}_0^T \mathbf{r}_0 \neq 0$, e.g. $\tilde{\mathbf{r}}_0 = \mathbf{r}_0$

$\mathbf{p}_0 = \mathbf{u}_0 = \mathbf{r}_0$

for $n = 0, 1, \ldots$ **do**

    $\mathbf{w}_n = \mathbf{A}\mathbf{p}_n$

    $\alpha_n = \frac{(\tilde{\mathbf{r}}_0)^T \mathbf{r}_n}{(\tilde{\mathbf{r}}_0)^T \mathbf{w}_n}$

    $\mathbf{q}_n = \mathbf{u}_n - \alpha_n \mathbf{w}_n$

    $\mathbf{x}_{n+1} = \mathbf{x}_n + \alpha_n(\mathbf{u}_n + \mathbf{q}_n)$

    $\mathbf{r}_{n+1} = \mathbf{r}_n - \alpha_n \mathbf{A}(\mathbf{u}_n + \mathbf{q}_n)$

    $\beta_n = \frac{(\tilde{\mathbf{r}}_0)^T \mathbf{r}_{n+1}}{(\tilde{\mathbf{r}}_0)^T \mathbf{r}_n}$

    $\mathbf{u}_{n+1} = \mathbf{r}_{n+1} + \beta_n \mathbf{q}_n$

    $\mathbf{p}_{n+1} = \mathbf{u}_{n+1} + \beta_n(\mathbf{q}_n + \beta_n \mathbf{p}_n)$

    if $\frac{||\mathbf{r}_n||_2}{||\mathbf{b}||_2} <$ tolerance **then**

        Terminate algorithm

    end if

end for

and the residual is given by

$$\mathbf{r}_{n+1} = (I - \omega_n \mathbf{A})\mathbf{s}_n \tag{4.34}$$

Successive approximations to $\mathbf{x}$ are computed from

$$\mathbf{x}_{n+1} = \mathbf{x}_n + \alpha_n \mathbf{p}_n + \omega_n \mathbf{s}_n \tag{4.35}$$

The addition of the 'stabilising' component in the residual of the BiCGSTAB causes it to take a steepest descent step, similar to the CG, to minimise the residual error. This smooths the irregular convergence pattern of the BiCG method. The lack of squaring in the BiCGSTAB method eliminates the rounding errors associated with the CGS method. These improvements lead to a more efficient and stable algorithm that is applied to the matrix equations used in the propagation models investigated here. The BiCGSTAB algorithm is summarised in Algorithm 4.4 and a more complete description of its derivation and that of the CGS and BiCG can be found in [180], [185], [190].

4.3 Preconditioning techniques

A preconditioner transforms a linear system into an equivalent system with the same solution but better spectral properties. This makes its solution via iterative techniques more robust and efficient. The convergence rate of iterative solvers is heavily dependent on the spectral properties of the system matrix [189], [192], [193]. Preconditioners make it possible to improve these properties by more closely clustering the eigenvalues of the system matrix and reducing its condition number[3]. The reliability of iterative methods can depend more heavily on the use of a preconditioner than acceleration techniques [185].

There are three main types of preconditioning techniques: left preconditioning, right preconditioning and left-right preconditioning. If $\mathbf{P}$ is a preconditioner for the system $\mathbf{Ax} = \mathbf{b}$, left preconditioning transforms the system into the equivalent system

$$\mathbf{P}^{-1}\mathbf{Ax} = \mathbf{P}^{-1}\mathbf{b} \tag{4.36}$$

The new system is equivalent to the original and $\mathbf{P}$ is chosen such that $\mathbf{P}^{-1}\mathbf{A}$ has better

[3] The condition number is the ratio of the largest to the smallest singular value of the matrix.

Algorithm 4.4 Bi-Conjugate Gradient Stabilised method

$\mathbf{x}_0 =$ initial guess

$\mathbf{r}_0 = \mathbf{b} - \mathbf{A}\mathbf{x}_0$

$\tilde{\mathbf{r}}_0$ arbitrary such that $\tilde{\mathbf{r}}_0^T \mathbf{r}_0 \neq 0$, e.g. $\tilde{\mathbf{r}}_0 = \mathbf{r}_0$

$\mathbf{p}_0 = \mathbf{r}_0$

for $n = 0, 1, \ldots$ **do**

    $\mathbf{q}_n = \mathbf{A}\mathbf{p}_n$

    $\rho_n = (\tilde{\mathbf{r}}_0)^T \mathbf{r}_n$

    $\alpha_n = \frac{\rho_n}{(\tilde{\mathbf{r}}_0)^T \mathbf{q}_n}$

    $\mathbf{s}_n = \mathbf{r}_n - \alpha_n \mathbf{q}_n$

    $\mathbf{t}_n = \mathbf{A}\mathbf{s}_n$

    $\omega_n = \frac{(\mathbf{s}_n)^T \mathbf{t}_n}{(\mathbf{t}_n)^T \mathbf{t}_n}$

    $\mathbf{x}_{n+1} = \mathbf{x}_n + \alpha_n \mathbf{p}_n + \omega_n \mathbf{s}_n$

    $\mathbf{r}_{n+1} = \mathbf{s}_n - \omega_n \mathbf{t}_n$

    $\beta_n = \left(\frac{(\tilde{\mathbf{r}}_0)^T \mathbf{r}_{n+1}}{\rho_n} \right) \left(\frac{\alpha_n}{\omega_n} \right)$

    $\mathbf{p}_{n+1} = \mathbf{r}_{n+1} + \beta_n (\mathbf{p}_n - \omega \mathbf{q}_n)$

    if $\frac{||\mathbf{r}_n||_2}{||\mathbf{b}||_2} <$ tolerance **then**

        Terminate algorithm

    end if

end for

spectral properties than $\mathbf{A}$. Right preconditioning takes the form

$$\mathbf{A}\mathbf{P}^{-1}\mathbf{y} = \mathbf{b} \qquad \text{where} \qquad \mathbf{x} = \mathbf{P}^{-1}\mathbf{y} \tag{4.37}$$

and right-left preconditioning has the form

$$\mathbf{P}_1^{-1}\mathbf{A}\mathbf{P}_2^{-1}\mathbf{y} = \mathbf{P}_1^{-1}\mathbf{b} \qquad \text{where} \qquad \mathbf{x} = \mathbf{P}_2^{-1}\mathbf{y} \tag{4.38}$$

and $\mathbf{P}_1$ and $\mathbf{P}_2$ are left and right preconditioners, respectively.

The choice of appropriate preconditioner is very complex. The preconditioner should be chosen as a close approximation to $\mathbf{A}$ but it should be relatively easy to construct $\mathbf{P}^{-1}$ and not require excessive computation or storage. It should also be relatively easy to perform multiplication with the preconditioner. The study of preconditioners is quite extensive and also considers their applicability to parallelisation [185], [189], [190], [192], [194]. Preconditioned algorithms for the above iterative solvers can be found in [185], [192].

4.3.1 Diagonal (Jacobi) preconditioner

The simplest and most popular preconditioner is the diagonal or Jacobi preconditioner [189], [195]. The preconditioner $\mathbf{P}$ approximates $\mathbf{A}$ by its diagonal components only

$$\mathbf{P} = \begin{pmatrix} \mathbf{A}_{11} & 0 & \cdots & 0 \\ 0 & \mathbf{A}_{22} & \cdots & 0 \\ \vdots & \vdots & \ddots & \dots \\ 0 & 0 & \cdots & \mathbf{A}_{NN} \end{pmatrix} \tag{4.39}$$

where the inverse of the preconditioner is given by

$$\mathbf{P}^{-1} = \begin{pmatrix} \mathbf{A}_{11}^{-1} & 0 & \cdots & 0 \\ 0 & \mathbf{A}_{22}^{-1} & \cdots & 0 \\ \vdots & \vdots & \ddots & \dots \\ 0 & 0 & \cdots & \mathbf{A}_{NN}^{-1} \end{pmatrix} \tag{4.40}$$

A block variant of the preconditioner is also commonly used where diagonal blocks are used to construct the preconditioner. In the block version the $\mathbf{A}_{nn}$ are blocks, the matrix is block diagonal [189] and its inverse is computed by computing the inverse

of each of the blocks. Due to the simplicity of the preconditioner it is well suited to parallel implementation but it is limited in its effectiveness when compared with more complicated preconditioners.

4.3.2 Sparse approximate inverse preconditioner

A more complicated and popular preconditioner is based on a sparse approximate inverse (SPAI) [196]–[200]. The main advantage of SPAI preconditioners over other methods is the ability to implement them in parallel and memory requirements that can be controlled with a well chosen sparsity pattern. SPAI preconditioners are thus well suited for very large problems.

SPAI preconditioners aim to minimise the following Frobenius norm

$$F(\mathbf{A}) = ||\mathbf{I} - \mathbf{AP}||_F^2 = \sum_{n=1}^{N} ||u_n - \mathbf{A}v_n||_2^2 \tag{4.41}$$

where u_n is the n^{th} column of the identity matrix $\mathbf{I}$, v_n is the n^{th} column of the preconditioner matrix $\mathbf{P}$ and $\mathbf{A}$ is an $N \times N$ matrix. The main advantage of this approach is the ability to express this problem as N independent least-squares problems for each of the N columns of $\mathbf{P}$. Because the n least-squares problems are independent they can be solved in parallel. The difficult task is the selection of the sparsity pattern [201], [202] and the minimisation of the Frobenius norm which GMRES has been used for [203]. The two main approaches for determining the sparsity patterns are based on adaptive and static techniques. Adaptive techniques attempt to dynamically identify the best pattern for $\mathbf{P}$ but they are very complex and expensive. Static techniques determine the sparsity pattern in advance. In electromagnetic scattering problems this can sometimes be based on the physical geometry of the problem [204], [205].

4.3.3 Reduced operator as a preconditioner

A reduced forward operator can be used in conjunction with iterative solvers, similarly to a preconditioner, to force them to ignore certain unknown values when computing successive approximations to the solution. The VEFIE formulation in Chapter 3 uses the total electric field as its primary unknown instead of the volume currents. This form enables the use of the Fast Fourier Transform (FFT) to speed up the matrix-vector multiplication during each iteration of the iterative method but it

also greatly increases the required number of unknown values. The use of the FFT is discussed in Section 4.4.1.

Consider the discretised problems shown in Figure 4.1. If the volume currents are chosen as the unknown in the VEFIE then only the scatterer objects need to be discretised as shown in Figure 4.1a. Contrasting Figure 4.1a with Figure 4.1b, where the electric field is chosen as the unknown in the VEFIE, a much larger number of discretisations is required because the electric field exists everywhere in the problem domain, both within scatterers and free space, whereas the volume currents only exist within scatterers. It can be shown that in the VEFIE formulation electric field values in free space do not contribute to the electric field at any other discretised point within the problem. Consider the cell c in Figure 4.1b which is located in free space. Cell c has an associated row and column in the discretised matrix equation (3.76) and (3.95), $\mathbf{V} = \mathbf{Ze}$;

$$\begin{pmatrix} V_1 \\ \vdots \\ \vdots \\ V_c \\ \vdots \\ \vdots \\ V_N \end{pmatrix} = \begin{pmatrix} Z_{11} & \cdots & \cdots & 0 & \cdots & \cdots & Z_{1N} \\ \vdots & \ddots & & \vdots & & & \vdots \\ \vdots & & \ddots & 0 & & & \vdots \\ Z_{c1} & \cdots & Z_{c(c-1)} & 1 & Z_{c(c+1)} & \cdots & Z_{cN} \\ \vdots & & & 0 & \ddots & \cdots & \vdots \\ \vdots & & & \vdots & & \ddots & \vdots \\ Z_{N1} & \cdots & \cdots & 0 & \cdots & \cdots & Z_{NN} \end{pmatrix} \begin{pmatrix} e_1 \\ \vdots \\ \vdots \\ e_c \\ \vdots \\ \vdots \\ e_N \end{pmatrix} \tag{4.42}$$

The column of (4.42) represents its contribution to other cells and the row represents the contribution of other cells to cell c. It can be seen that all of the elements of the column for cell c are zero except the self term which is one, thus, the free space cell c does not contribute to the field at any other location in the problem. The column associated with cell c is zero because the contrast (3.55) is zero for all free space cells. Consequently, it is beneficial to extract only elements corresponding to unknowns located in scatterers and to focus the iterative solver on solving for these unknowns whilst ignoring all free space unknowns. In the VEFIE formulation the ignored unknowns could be removed if the volume currents were used as the unknown quantity to be computed but this prevents the FFT from being used. They are needed to enforce a regular grid that enables use of the FFT, as explained in Section 4.4.1, but can be ignored as shown here to improve the convergence rate of the iterative solver. The ignored free space unknowns can then be solved for in a simple computation after

the iterative solver has converged. This technique and an analysis of its convergence is presented in more detail in [206].

4.4 Fast matrix-vector multiplication techniques

The main bottleneck of the iterative solvers presented in Section 4.2 is the matrix-vector product of $\mathbf{A}$ with $\mathbf{x}$ and the storage of the $N \times N$ $\mathbf{A}$ matrix. Thus, a significant amount of research has been concerned with accelerating this computation and reducing its storage requirements [7], [25], [142], [145], [146], [207]. Iterative methods, unlike direct solution methods, offer the possibility of reducing the storage bottleneck by exploiting structures and sparsity patterns present in the system. Iterative solvers only require an implicit matrix operator that returns the product of the $N \times N$ system matrix with a vector.

4.4.1 Fast Fourier Transform

The FFT can be used to exploit symmetries in the discrete convolutional kernel of some electromagnetic problems. A general one-dimensional discrete convolution is of the form [7], [145]

$$e_m = \sum_{n=0}^{N-1} f_n g_{m-n} \qquad m = 1, 2, \ldots, N-1 \tag{4.43}$$

or in matrix form

$$\begin{bmatrix} e_0 \\ e_1 \\ e_2 \\ \vdots \\ e_{N-1} \end{bmatrix} = \begin{bmatrix} g_0 & g_{-1} & g_{-2} & \cdots & g_{1-N} \\ g_1 & g_0 & g_{-1} & \cdots & g_{2-N} \\ g_2 & g_1 & g_0 & \cdots & g_{3-N} \\ \vdots & \vdots & \vdots & \ddots & \vdots \\ g_{N-1} & g_{N-2} & g_{N-3} & \cdots & g_0 \end{bmatrix} \begin{bmatrix} f_0 \\ f_1 \\ f_2 \\ \vdots \\ f_{N-1} \end{bmatrix} \tag{4.44}$$

The $N \times N$ matrix shown in (4.44) is a general Toeplitz matrix; all of the elements are contained in the $2N-1$ entries of the first row and column. If the elements repeat with period N so that

$$g_{n-N} = g_n \qquad n = 1, 2, \ldots, N-1 \tag{4.45}$$

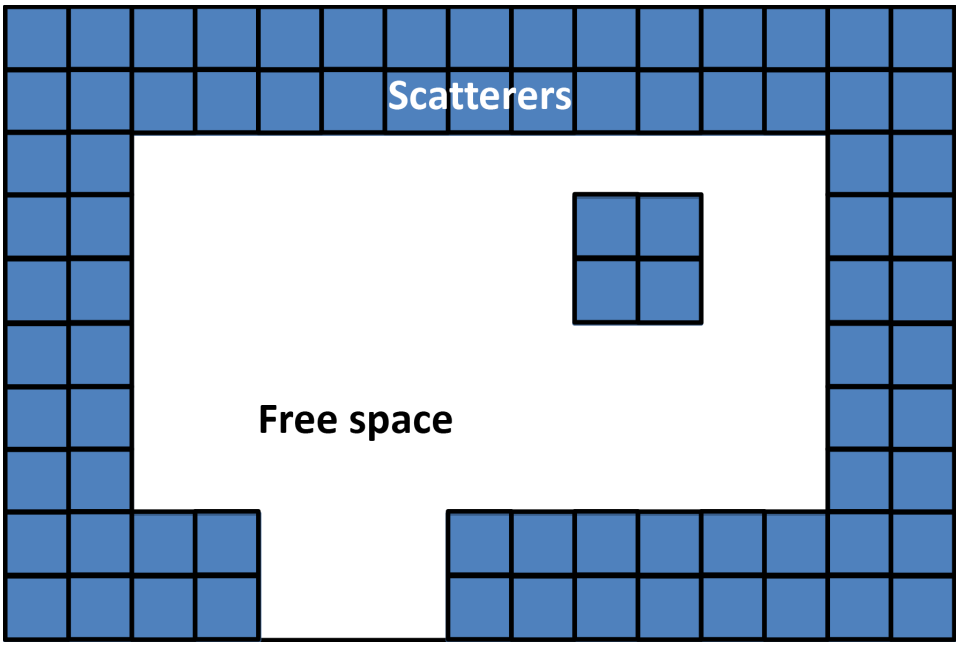

(a) If the volume currents are chosen as the primary unknown then only the scatterers need to be discretised.

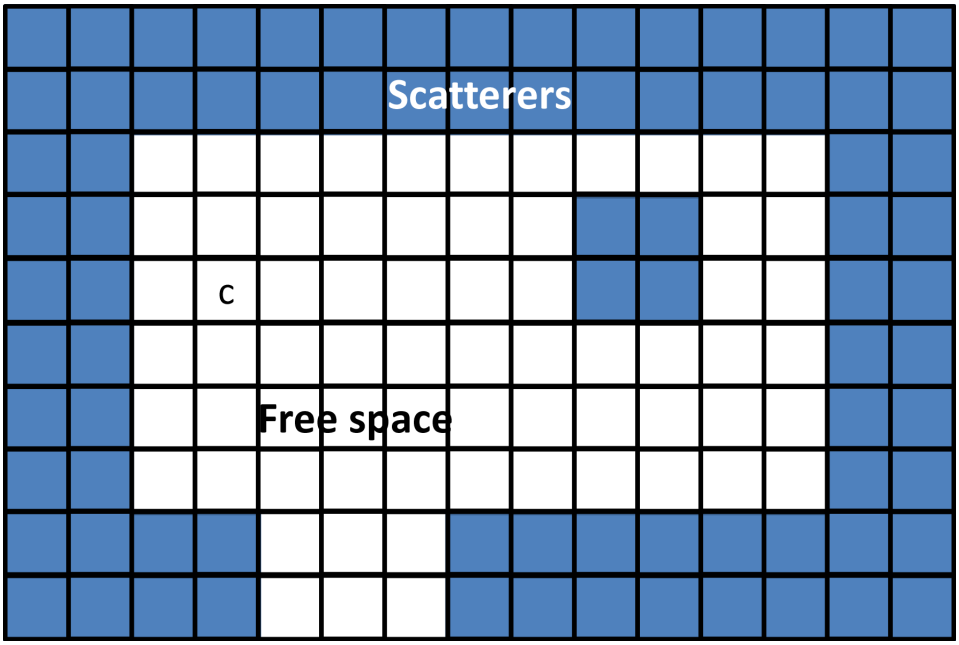

(b) If the primary unknown is the electric field then both scatterers and free space regions need to be discretised. Cell *c* is located in free space.

Figure 4.1: Discretisation of problem domain with the VEFIE depending on the primary unknown.

the $N \times N$ matrix in (4.44) is circulant

$$\begin{bmatrix} g_0 & g_{N-1} & g_{N-2} & \cdots & g_1 \\ g_1 & g_0 & g_{N-1} & \cdots & g_2 \\ g_2 & g_1 & g_0 & \cdots & g_3 \\ \vdots & \vdots & \vdots & \ddots & \vdots \\ g_{N-1} & g_{N-2} & g_{N-3} & \cdots & g_0 \end{bmatrix} \tag{4.46}$$

the operation is known as a circular discrete convolution. Otherwise, it is a linear discrete convolution. Any discrete linear convolution of length N can be embedded into a circular discrete convolution of length $2N-1$ by extending the original sequence $\mathbf{g}$ to repeat with period $2N-1$, padding $\mathbf{f}$ with zeros to length $2N-1$ and changing the summation limit of (4.43) to $2N-2$

$$e_m = \sum_{n=0}^{2N-2} f_n g_{m-n} \tag{4.47}$$

which in matrix form this looks like

$$\begin{bmatrix} e_0 \\ e_1 \\ \vdots \\ e_{N-1} \\ 0 \\ 0 \\ \vdots \\ 0 \end{bmatrix} = \begin{bmatrix} g_0 & g_{-1} & \cdots & g_{1-N} & 0 & g_{N-1} & \cdots & g_1 \\ g_1 & g_0 & \cdots & g_{2-N} & g_{1-N} & 0 & \cdots & g_2 \\ \vdots & \vdots & \ddots & \vdots & \vdots & \vdots & \ddots & \vdots \\ g_{N-1} & g_{N-2} & \cdots & g_0 & g_{-1} & g_{-2} & \cdots & 0 \\ 0 & g_{N-1} & \cdots & g_1 & g_0 & g_{-1} & \cdots & g_{1-N} \\ g_{1-N} & 0 & \cdots & g_2 & g_1 & g_0 & \cdots & g_{2-N} \\ \vdots & \vdots & \ddots & \vdots & \vdots & \vdots & \ddots & \vdots \\ g_1 & g_0 & \cdots & 0 & g_{N-1} & g_{N-2} & \cdots & g_0 \end{bmatrix} \begin{bmatrix} f_0 \\ f_1 \\ \vdots \\ f_{N-1} \\ 0 \\ 0 \\ \vdots \\ 0 \end{bmatrix} \tag{4.48}$$

The discrete convolution theorem states that if (4.43) is a discrete circular convolution it is equivalent to [145]

$$\tilde{e}_m = \tilde{f}_m \tilde{g}_m \qquad n = 0, 1, \ldots, N-1 \tag{4.49}$$

where $\tilde{e}$ is the N-point Discrete Fourier Transform (DFT) of e and similarly $\tilde{f}$ and $\tilde{g}$ are the N-point DFTs of f and g respectively. Hence, the matrix-vector product in (4.43)

and (4.44) can be efficiently computed using the FFT by

$$e = \mathcal{F}_N^{-1}\{\mathcal{F}_N(f)\mathcal{F}_N(g)\} \tag{4.50}$$

where $\mathcal{F}_N$ denotes the N point DFT

$$\tilde{g}_n = \mathcal{F}_N(g) = \sum_{k=0}^{N-1} g_k e^{-j\frac{2\pi nk}{N}} \qquad n = 0, 1, \ldots, N-1 \tag{4.51}$$

and $\mathcal{F}_N^{-1}$ denotes the N point inverse DFT

$$g_k = \mathcal{F}_N^{-1}(g) = \frac{1}{N}\sum_{n=0}^{N-1} \tilde{g}_n e^{j\frac{2\pi nk}{N}} \qquad k = 0, 1, \ldots, N-1 \tag{4.52}$$

If (4.43) is a discrete linear convolution then it must first be embedded in a circular convolution as described above. This process can easily be extended to two and three dimensions as shown in Appendix A.

In the VEFIE formulations in Section 3.2 due to the use of the total electric field as the primary unknown and uniform discretisation with pulse basis functions the FFT can be used to compute the matrix-vector product of $\mathbf{G}$ with $\mathbf{e}$ in (3.76) and (3.95). In (4.44) and (4.48)

$$g_n = g_{-n} \tag{4.53}$$

because the value of the Green's function in two and three dimensions varies with the absolute distance between cells only. Thus, all of the elements are contained in the N entries of the first row or column.

The product of $\mathbf{G}$ with $\mathbf{e}$ in (3.76) and (3.95) is a two and three-dimensional linear discrete convolution for the 2D and 3D VEFIEs respectively. Thus, the FFT can be used to reduce the storage requirements of $\mathbf{G}$ from $\mathcal{O}(N^2)$ to $\mathcal{O}(N)$ and the cost to compute the matrix-vector product from $\mathcal{O}(N^2)$ to $\mathcal{O}(N \log N)$. This represents a significant saving for very large N such as those seen in indoor propagation modelling and greatly improves the efficiency of the volume integral MoM approach for electromagnetic scattering [7]. The Adaptive Integral Method [208]–[210] is an extension of this idea for triangular basis functions. The matrix-vector product of $\mathbf{D}$ with $\mathbf{e}$ can also be performed efficiently because $\mathbf{D}$ is a diagonal matrix. It can be considered as a vector, stored in $\mathcal{O}(N)$ and multiplied with $\mathbf{e}$ with $\mathcal{O}(N)$ computational complexity. However, because of the use of the electric field as the primary unknown the entire

problem domain must now be discretised as opposed to just the scatterers. Thus, the reduced operator explained in Section 4.3.3 is used to further accelerate the iterative solution.

4.4.2 Fast multipole method

The Fast Multipole Method (FMM) [142] is an alternative to the FFT. It can be used to improve the efficiency of the matrix-vector multiplication in iterative solvers applied to integral equation formulations. The FMM separates the computational domain into near-zone and far-zone regions based on the distances between the basis and testing functions:

$$\mathbf{Ze} = \mathbf{Z}^{NF}\mathbf{e} + \mathbf{Z}^{FF}\mathbf{e} \tag{4.54}$$

where $\mathbf{Z}^{NF}$ is a sparse matrix containing information about the basis and testing functions that are close together, i.e. in the near-zone region, and $\mathbf{Z}^{FF}$ is a dense matrix containing information about the far-zone interactions between basis and testing functions. The near-zone computation $\mathbf{Z}^{NF}\mathbf{e}$ is sparse and can be computed exactly from the integral equation and MoM discretisation whilst the far-zone computation $\mathbf{Z}^{FF}\mathbf{e}$ is approximated.

The FMM accelerates the computation of far-zone components. Cells of basis and testing functions are grouped into approximately $\sqrt{N}$ groups of equal size and number of unknown values. Within each group all of the cells are considered to be in the near-field and are calculated exactly. Cells within other groups are considered to be in the far-field and are calculated by an approximation. To calculate the field at a point in group j due to (equivalent) sources in group i three operations are required. First, the sources in group i are expanded into outgoing plane waves centred on $\mathbf{r}_i$. Then, the outgoing plane waves are translated into incoming plane waves centred on $\mathbf{r}_j$. Finally, the incoming plane waves are converted into real contributions for each cell within the group j. More detail and explanation on the FMM can be found in [7], [25], [142], [195]. The approximations made in the FMM and use of $\sqrt{N}$ groups reduces the complexity to compute the matrix-vector product to $\mathcal{O}(N^{1.5})$. The complexity can be further reduced by implementing a multilevel scheme to $\mathcal{O}(N \log N)$ [25], [142], [195] comparable to that of the FFT. However, the main advantage of the FFT is the exact computation of the matrix-vector product as opposed to the relatively accurate approximations used in the FMM.

4.4.3 Fast Far Field Approximation

The Fast Far Field Approximation (FAFFA) [207] is a technique similar to the FMM. It efficiently computes the matrix-vector product in MoM solutions in $\mathcal{O}(N^{1.33})$ complexity with a storage requirement of $\mathcal{O}(N)$. The FAFFA uses the same basic idea as the FMM. Cells of basis and testing functions are grouped together. Near-field interactions are computed exactly while far-field interactions are approximated using the FAFFA in three operations: aggregation, translation and disaggregation.

The FAFFA differs from the FMM by the approximation it applies and in fact the two algorithms can be combined together [211] to provide even higher efficiency. The FAFFA is based on the far-field form of the Hankel function

$$H_{\alpha}^{(2)}(x) \simeq \sqrt{\frac{2}{\pi x}} e^{j(x-\alpha\frac{\pi}{2}-\frac{\pi}{4})} \tag{4.55}$$

However, the main computational advantage arises from the use of interpolation to compute the aggregation of the fields at all points within a group and the disaggregation of the field from the centre of a group to all points within it. Using this approach and choosing the number of groups equal to $N^{\frac{2}{3}}$ leads to a total complexity of $\mathcal{O}(N^{1.33})$. By implementing a multilevel scheme the complexity can be reduced to $\mathcal{O}(N \log N)$. For further information the reader is referred to [207], [212].

4.5 Implementation and parallelisation considerations

The implementation and parallelisation of the algorithms discussed thus far has been of huge importance in recent times. These algorithms are mathematical approaches to reducing the computational cost of solving linear systems and Maxwell's equations but are not the only approach. These algorithms have not been studied in isolation but specific considerations to their implementation and their parallelisation has gone hand in hand with their development [7], [142], [180], [185].

High-performance computing is a major area of study in CEM and has fuelled most of the current use of full-wave methods in CEM. Implementations of iterative solvers and preconditioners have specifically been developed to take advantage of parallel computations [180], [185]. The implementation of iterative solver algorithms needs to take account of vector operations and data memory distribution to ensure optimum performance. The message passing interface (MPI) is one standard for exchanging data on distributed memory systems.

The language of choice to develop software for CEM can often be a trade-off between efficiency and ease of development. MATLAB is a very popular numerical computing environment and programming language. It was developed to aid in solving matrix problems and hides much of the complex memory and implementation details required in CEM. It is extremely easy to learn and complex simulations can be written with great ease. However, its scripts are interpreted and it is less efficient than compiled programs. FORTRAN is a popular compiled language for numerical and scientific computing. Two of the most widely used and robust software libraries in scientific computing BLAS (Basic Linear Algebra Subprograms) and LAPACK are written in FORTRAN and freely available. In fact, most of MATLAB's operations are performed by calls to the BLAS and LAPACK libraries. MATLAB uses the Intel MKL (Math Kernel Library) versions of BLAS and LAPACK which are written in C as the basis for its computations. C and consequently C++ are two further programming languages that see significant use in scientific computing due to their speed. C++ as an object-oriented language can exhibit a higher overhead than C but it can be simpler to write complex programs due to its use of classes and templates. Both C and C++ can call the BLAS and LAPACK libraries or can be built on top of Intel MKL. In recent times, the use of other languages for scientific computing has been increasing, such as Python and Julia.

Of significant investigation recently is the use of graphics processing units (GPUs) for scientific computing. The advent of the OpenCL and CUDA platforms enabled the use of GPUs to perform general purpose calculations in FORTRAN, C and C++. Many of the operations used in the algorithms described here can be computed much more efficiently on GPUs than on CPUs. Specific implementations of the Conjugate Gradient and preconditioning techniques have been developed for GPUs [213]–[220].

4.6 Conclusions

This chapter presented a number of techniques that can be used to efficiently solve the matrix equation resulting from the application of the MoM to the integral equation formulation of Maxwell's equations. The solution of the VEFIE applied to the description of a building forms the basis of an indoor propagation model. The discretised forms of the 2D and 3D VEFIE in Section 3.2 are solved using the BiCGSTAB method preconditioned by a block Jacobi preconditioner. The iterative solver is accelerated by using the FFT and reduced operator.

Chapter 5

2D integral equations for indoor propagation modelling

5.1 Introduction

The Volume Electric Field Integral Equation (VEFIE) was derived from Maxwell's equations in Chapter 3. The discretisation of the VEFIE with the Method of Moments (MoM) was also described in this chapter. In Chapter 4 iterative techniques for the solution of the linear system arising from the MoM discretisation were detailed. In this chapter the Surface Electric Field Integral Equation (SEFIE) and VEFIE are applied in two dimensions to indoor propagation modelling. The VEFIE model is validated against the Mie series solution for scattering from a dielectric cylinder before the two integral equation approaches are compared. The propagation modelling capabilities of the VEFIE is examined and compared against popular empirical models and ray tracing for indoor propagation.

5.2 2D integral equation formulations

Integral equation methods have seen very little interest in the literature for indoor propagation modelling. This is demonstrated in Section 2.5.2. They haven't been used because they are typically very computationally burdensome and can be quite complicated to implement in contrast to a ray tracing solution or empirical model. However, integral equation methods are derived from Maxwell's equations without any approximations and are full-wave in nature as described in Section 3.2. If their computational load can be reduced they could be a very useful tool in analysing indoor propagation.

The VEFIE is well suited to the problem of modelling indoor propagation. It is derived from Maxwell's equations upon applying the volumetric equivalence principle, which is explained in Section 3.2. The SEFIE is derived analogously to the VEFIE using the surface equivalence principle instead of the volume equivalence principle. Volume integral equation (VIE) formulations are typically applied to inhomogeneous problems because they are applied to the entire volume of the problem domain and can thus easily model inhomogeneities within materials. Surface integral equation (SIE) methods are applied to problems involving piecewise homogeneous dielectrics or metals (perfect conductors) where the number of distinct regions is small because they only solve for the fields on the surface or boundary between different materials. The combined Volume Surface Integral Equation (VSIE) [142] can be used to take advantage of the VIEs ability to model inhomogeneous scatterers and the SIEs ability to model metals but it represents a significant increase in complexity over the single volume or surface integral equation methods.

Integral equation methods have a significant advantage over many other full-wave techniques because they do not require the use of absorbing boundary conditions (ABCs). As described in Section 2.5.1, the FDTD method requires the problem domain be extended at the boundaries with an ABC to prevent spurious reflections and to simulate outgoing electromagnetic waves as propagating to infinity. Integral equation methods do not require this because they solve for the fields within scatterers and consider the regions external to these as free space extending to infinity.

5.2.1 Volume electric field integral equation

The 2D VEFIE is derived from Maxwell's equations by considering transverse magnetic (TM) polarisation and scatterers which extend to infinity in one dimension. For convenience, the z dimension is chosen although any dimension can be chosen. The 2D VEFIE is given by (3.56)

$$E_z(\mathbf{r}) = E_z^i(\mathbf{r}) + k_0^2 \int_S G(\mathbf{r}, \mathbf{r}')\chi(\mathbf{r}')E_z(\mathbf{r}')d\mathbf{r}'$$

Section 3.2 presents its derivation. The MoM is applied to discretise the 2D VEFIE in Section 3.4. It results in a linear system of N independent simultaneous equations that can be solved to predict the electric field within the problem. The matrix equation is given by (3.76)

$$\mathbf{V} = \mathbf{Ze}$$

where $\mathbf{Z}$ is (3.77)

$$\mathbf{Z} = \mathbf{I} - \mathbf{GD}$$

(3.76) can be solved by direct matrix inversion but for indoor propagation problems this is infeasible due to the high memory requirements of the VEFIE. Thus, as described in Chapter 4, (3.76) is solved with an iterative technique, namely those from the Krylov family of iterative methods. This enables the use of other techniques to speed up the solution, namely the Fast Fourier Transform (FFT) or Fast Multipole Method (FMM). In this work, the FFT is used, as described in Section 4.4.1, to accelerate the computation of the matrix vector product within each iteration of the iterative solver. The FFT requires a regular grid to operate which forces the use of the electric field as the primary unknown in (3.56). This increases the number of unknown values that need to be specified but by using the reduced operator described in Section 4.3.3 the iterative technique can be focused so that it primarily solves for unknowns in scatterers that have a greater effect on the final solution. The result of this is that the iterative method needs a reduced number of iterations to reach the same error level than without it. The solution can be further accelerated by using preconditioning or parallelisation techniques described in Sections 4.3 and 4.5.

5.2.2 Validation against Mie series

The analytical Mie series solution is ideal for validating the integral equation methods described earlier. The Mie series computes the exact fields at any point interior or exterior to a dielectric sphere illuminated by a plane wave and should agree well with the full-wave integral equation approaches if they have been implemented correctly. The Mie series can only be applied to 2D or 3D spheres [221]. Other analytical solutions exist, for example scattering by wedges [143], but as the VEFIE does not treat these any differently to the Mie series problem it is sufficient to only validate the VEFIE against the Mie series.

To validate the VEFIE, consider a homogeneous dielectric 2D cylinder in a free space region illuminated by a TM^z plane wave propagating in the x direction as shown in Figure 5.1. The cylinder has radius a and is characterised by its permittivity and permeability, ϵ and μ respectively. The total field at a point exterior to the sphere in free space can be expressed as

$$E_z(\mathbf{r}) = E_z^i(\mathbf{r}) + E_z^s(\mathbf{r}) \tag{5.1}$$

where the z subscript will be assumed and omitted from here on. The incident plane wave can be expressed as

$$E^i(\mathbf{r}) = e^{-\jmath k_0 x} \tag{5.2}$$

The Mie series writes (5.2) in expanded form as

$$E^i(\mathbf{r}) = e^{-\jmath k_0 \rho \cos\theta} = \sum_{n=-\infty}^{\infty} \jmath^{-n} J_n(k_0\rho) e^{\jmath n\phi} \tag{5.3}$$

where $J_n()$ is the Bessel function of the first kind and nth order. Analogous to (5.3) the Mie series writes the scattered field external to the cylinder as

$$E^s(\mathbf{r}) = \sum_{n=-\infty}^{\infty} \jmath^{-n} A_n H_n^{(2)}(k_0\rho) e^{\jmath n\phi} \tag{5.4}$$

where

$$A_n = \frac{\frac{\eta_0}{\eta_d} J_n(k_0 a) J_n'(k_d a) - J_n'(k_0 a) J_n(k_d a)}{J_n(k_d a) H_n^{(2)\prime}(k_0 a) - \frac{\eta_0}{\eta_d} J_n'(k_d a) H_n^{(2)}(k_0 a)} \tag{5.5}$$

where k_d and η_d are the wave number and wave impedance of the dielectric cylinder. The total field interior to the sphere in the Mie series is given by

$$E^t(\mathbf{r}) = \sum_{n=-\infty}^{\infty} \jmath^{-n} B_n J_n(k_d\rho) e^{\jmath n\phi} \tag{5.6}$$

where

$$B_n = \frac{\frac{-2\jmath}{\pi k_0 a}}{J_n(k_d a) H_n^{(2)\prime}(k_0 a) - \frac{\eta_0}{\eta_d} J_n'(k_d a) H_n^{(2)}(k_0 a)} \tag{5.7}$$

$J_n'()$ and $H_n^{(2)\prime}()$ are the derivatives of the Bessel function of the first kind and the Hankel function of the second kind. They can be expressed as

$$J_n'(\psi) = \frac{1}{2}\left[J_{n-1}(\psi) - J_{n+1}(\psi)\right] \tag{5.8}$$

$$H_n^{(2)\prime}(\psi) = \frac{1}{2}\left[H_{n-1}^{(2)}(\psi) - H_{n+1}^{(2)}(\psi)\right] \tag{5.9}$$

The Mie series and VEFIE are compared for a 2D cylinder of radius $r = 1.25$m, with $\epsilon_r = 4$, $\mu_r = 1$ and $\sigma = 0.01$ at 700MHz. The VEFIE discretises a 5m $\times$ 5m region centred around the cylinder at a rate of $\frac{\lambda}{40}$ leading to $N = 230,400$ unknowns to be solved. The discretisation rate of $\frac{\lambda}{40}$ is used to accurately capture the curvature of the

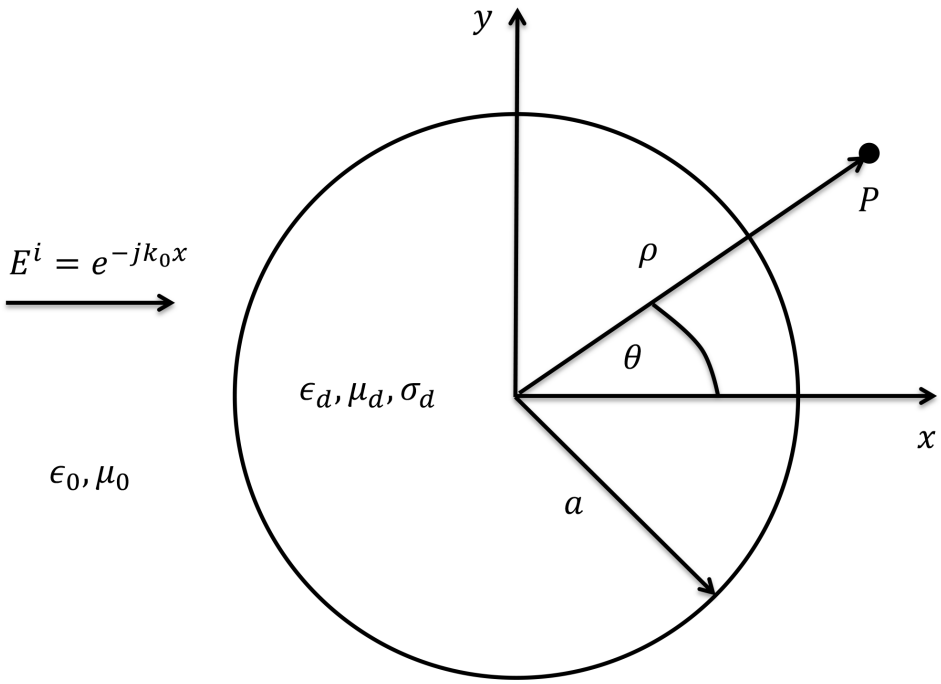

Figure 5.1: Incident plane wave illuminating dielectric sphere for Mie series problem.

cylinder because pulse basis functions are used in the discretisation process which results in a structure like that shown in Figure 3.4 and also to reduce numerical inaccuracies so an accurate validation can be performed. It is solved using the BiCGSTAB method with the reduced operator and block Jacobi preconditioner. The infinite Mie series is truncated to 501 terms where $n \in [-250, +250]$. The total electric field along a line of points external to the sphere is computed by the VEFIE and Mie series. A very good agreement is achieved between both the real and imaginary parts shown in Figure 5.2. The VEFIE and Mie series have been compared for several different cases all producing a good agreement.

5.2.3 Surface electric field integral equation

The 2D SEFIE is derived analogously to the 2D VEFIE by considering TM polarisation and scatterers which extend to infinity in one dimension. For convenience, again the z dimension is chosen. The 2D SEFIE is given by

$$\begin{aligned} E_z^i(\mathbf{r}) &= M_t(\mathbf{r}) + \jmath k_0 \eta_0 A_z^{(0)}(\mathbf{r}) + \left\{ \frac{\partial F_y^{(0)}(\mathbf{r})}{\partial x} - \frac{\partial F_x^{(0)}(\mathbf{r})}{\partial y} \right\}_{S^+} \\ 0 &= -M_t(\mathbf{r}) + \jmath k_d \eta_d A_z^{(d)}(\mathbf{r}) + \left\{ \frac{\partial F_y^{(d)}(\mathbf{r})}{\partial x} - \frac{\partial F_x^{(d)}(\mathbf{r})}{\partial y} \right\}_{S^-} \end{aligned} \tag{5.10}$$

where $\mathbf{r}$ describes the cylinder surface,

$$A_z^{(\alpha)}(\mathbf{r}) = \int J_z(\mathbf{r}') \frac{1}{4\jmath} H_0^{(2)}(k_\alpha |\mathbf{r} - \mathbf{r}'|) dl' \tag{5.11}$$

$$\bar{F}_t^{(\alpha)}(\mathbf{r}) = \int \hat{t}(\mathbf{r}') M_t(\mathbf{r}') \frac{1}{4\jmath} H_0^{(2)}(k_\alpha |\mathbf{r} - \mathbf{r}'|) dl' \tag{5.12}$$

and $\hat{t}$ is a unit vector tangent to the scatterer surface. k_0 is the free space wave number for the medium external to the scatterer and k_d represents the wave number of the scatterer material. The impedances of the media are represented by η_0 and η_d, respectively. The expressions in brackets in (5.10) depend on the side of the surface the observer is located. The first equation should be evaluated with the observer an infinitesimal distance outside the surface of the scatterer, while the second equation should be evaluated with the observer an infinitesimal distance inside the surface. For the complete derivation of the SEFIE the reader is referred to [145]. In this work, the 2D SEFIE is discretised using the MoM and N pulse basis functions, similarly to

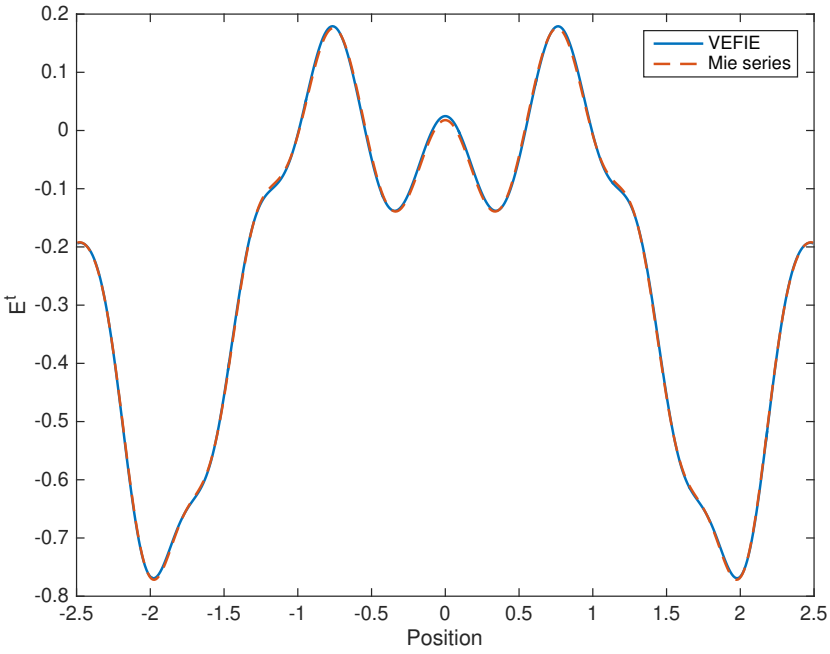

(a) Comparison of real component.

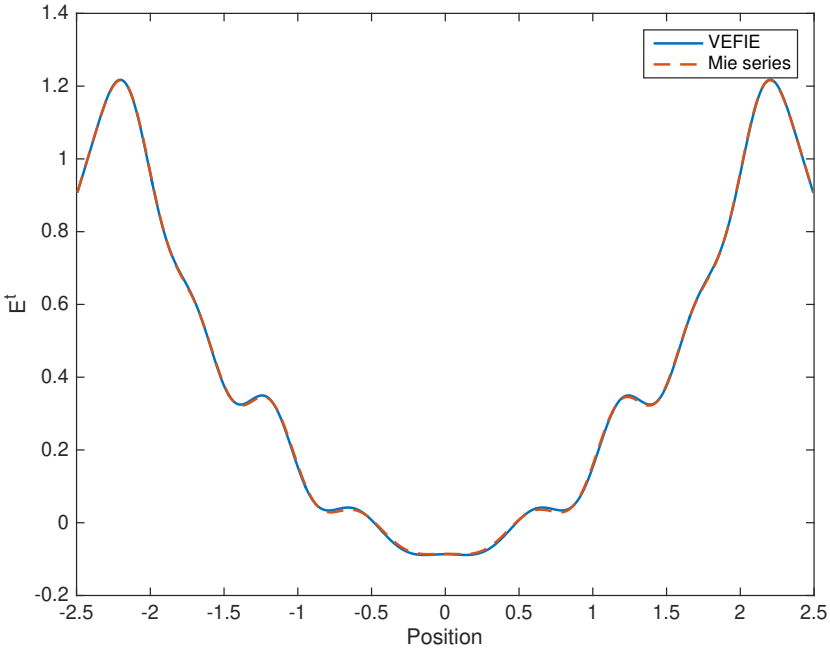

(b) Comparison of imaginary component.

Figure 5.2: Comparison of real and imaginary components of VEFIE and Mie series for the problem in Figure 5.1.

the 2D VEFIE. The N pulse basis functions are defined on the scatterer surface so that the nth segment has centre $\mathbf{r}_n$, normal vector $\hat{\mathbf{n}}_n$ and is of length Δ_n. This yields a $2N \times 2N$ linear system, as opposed to the $N \times N$ system for the VEFIE,

$$\begin{pmatrix} \mathbf{e}^i \\ 0 \end{pmatrix} = \begin{pmatrix} \mathbf{Z}^a & \mathbf{Z}^b \\ \mathbf{Z}^c & \mathbf{Z}^d \end{pmatrix} \begin{pmatrix} \mathbf{j} \\ \mathbf{m} \end{pmatrix} \tag{5.13}$$

where $\mathbf{e}^i$ is a known $N \times 1$ vector containing information about the incident field impinging on the scatterer surface and $\mathbf{j}$ and $\mathbf{m}$ are unknown $N \times 1$ vectors containing information about the electric and magnetic currents, J_z and M_t, on the surface of the scatterer. Each $\mathbf{Z}^\beta$ is a $N \times N$ matrix whose elements are given by

$$Z^a_{mn} = \begin{cases} \frac{k_0\eta_0}{4} H_0^{(2)}(k_0 r_{mn})\Delta_n & m \neq n \\ \frac{k_0\eta_0}{4}\{1 - \jmath\frac{2}{\pi}[\ln(\frac{\gamma k_0 \Delta_n}{4} - 1)]\}\Delta_n & m = n \end{cases} \tag{5.14}$$

$$Z^b_{mn} = \begin{cases} \frac{-k_0}{4\jmath}\hat{\mathbf{n}}_n \cdot \hat{\mathbf{r}}_{nm} H_1^{(2)}(k_0 r_{mn})\Delta_n & m \neq n \\ \frac{1}{2} & m = n \end{cases} \tag{5.15}$$

$$Z^c_{mn} = \begin{cases} \frac{k_d\eta_d}{4} H_0^{(2)}(k_d r_{mn})\Delta_n & m \neq n \\ \frac{k_d\eta_d}{4}\{1 - \jmath\frac{2}{\pi}[\ln(\frac{\gamma k_d \Delta_n}{4} - 1)]\}\Delta_n & m = n \end{cases} \tag{5.16}$$

$$Z^d_{mn} = \begin{cases} \frac{-k_d}{4\jmath}\hat{\mathbf{n}}_n \cdot \hat{\mathbf{r}}_{nm} H_1^{(2)}(k_d r_{mn})\Delta_n & m \neq n \\ -\frac{1}{2} & m = n \end{cases} \tag{5.17}$$

where $\ln()$ is the natural logarithm, $H_n^{(2)}()$ is the Hankel function of the second kind and order n, $\gamma \approx 1.781$, $\hat{\mathbf{r}}_{nm}$ and r_{nm} are the unit vector and length of $\mathbf{r}_{nm}$ which is defined as

$$\mathbf{r}_{nm} = \mathbf{r}_n - \mathbf{r}_m \tag{5.18}$$

Again, as with the VEFIE, the matrix equation resulting from the application of the MoM is solved with an iterative technique. The FFT isn't applicable to the SEFIE to efficiently compute the matrix vector product because there is no regular grid as is present in the VEFIE but the FMM or Fast Far Field Approximation (FAFFA) can be used. Here, the FAFFA, which is briefly described in Section 4.4.3, is applied to efficiently compute the matrix vector product during each iteration of the iterative method to speed up its solution. As with the VEFIE, the solution can be further accelerated by using preconditioning and parallelisation techniques.

5.2.4 Integral equation comparison

The SEFIE and VEFIE approaches described above are applied to a typical 2D indoor propagation scenario. Further numerical results are examined in Section 5.3. Both methods are solved using the BiCGSTAB method preconditioned with a block Jacobi preconditioner. The SEFIE is enhanced with the FAFFA, whilst the VEFIE uses the FFT and reduced operator to accelerate its solution. The two formulations are applied to the 15m $\times$ 15m indoor environment shown in Figure 5.3 which is characterised by the parameters in Table 5.1. A line source producing electric fields given by $H_0^{(2)}(k_0 R)$ radiating at 1GHz is positioned at $(0, 0)$. The fields computed by the VEFIE are shown in Figure 5.4. The SEFIE produces a similar result. It is not shown but a comparison of the fields computed by both methods can be seen in Figures 5.5 and 5.6 for two different lines through Figure 5.3. A very good agreement between the two models is achieved as expected. It is not exact for several reasons. The two methods are not solved exactly, the BiCGSTAB solver is terminated when it reaches a tolerance level which introduces slight inaccuracies into the solution. The tolerance level between the VEFIE and SEFIE differ also, the BiCGSTAB solves the VEFIE to an error tolerance of 0.001 and the SEFIE to an error tolerance of 0.02. Inaccuracies are introduced into the two methods due to the numerical discretisation with the MoM. For the SEFIE, the FAFFA is an approximate method for efficiently computing the interaction between basis functions that are far away, while the FFT used in the VEFIE is an exact approach except for numerical inaccuracies.

Table 5.1: Material parameters used to characterise the indoor environment in Figure 5.3.

Material	ϵ_r	μ_r	σ
Concrete	3.5	1	0.0334
Glass	7.0	1	0
Wood	1.8	1	0

Having shown the SEFIE and VEFIE methods produce similar results their computational efficiency will be analysed here. Table 5.2 compares the runtime of the SEFIE and VEFIE methods. The discretised SEFIE solution requires 40,952 basis functions to describe the problem. The VEFIE requires 1,440,000 basis functions but only 141,472 of these describe scatterers. The other 1,298,528 are in free space and ignored by the reduced operator. The SEFIE is solved to an error tolerance of 0.02 in 388 it-

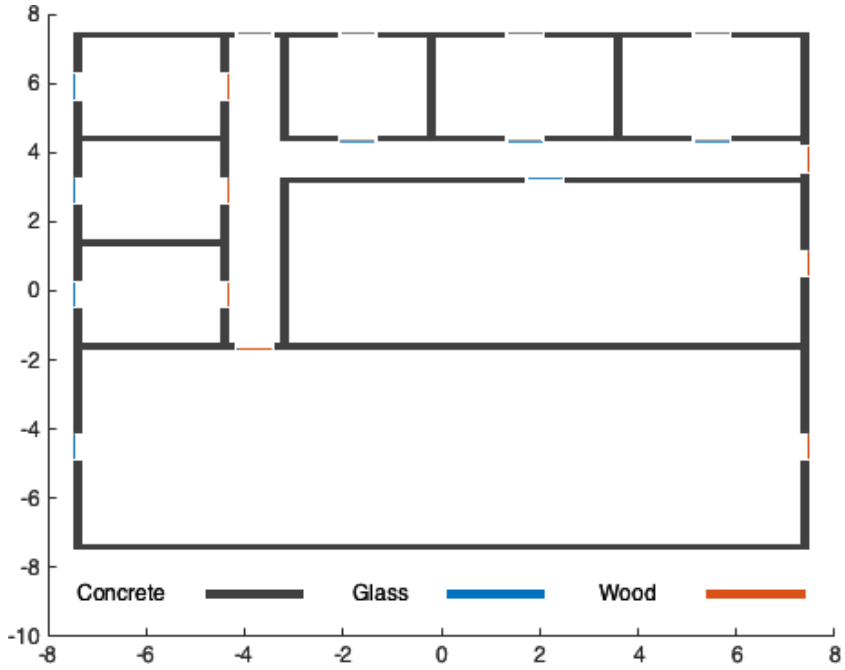

Figure 5.3: 15m $\times$ 15m indoor environment consisting of concrete, glass and wood used to compare the SEFIE and VEFIE methods.

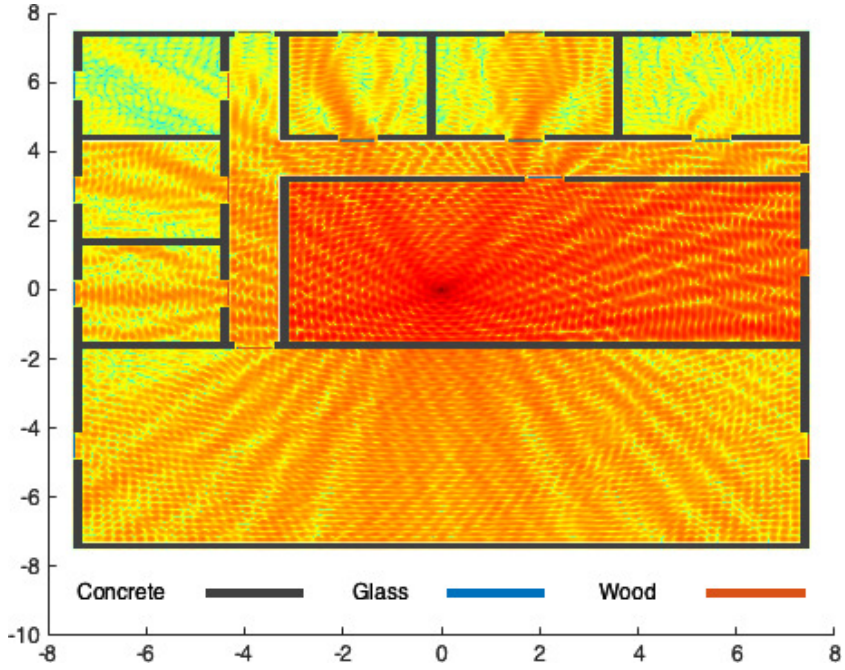

Figure 5.4: Total electric field computed within the indoor test environment.

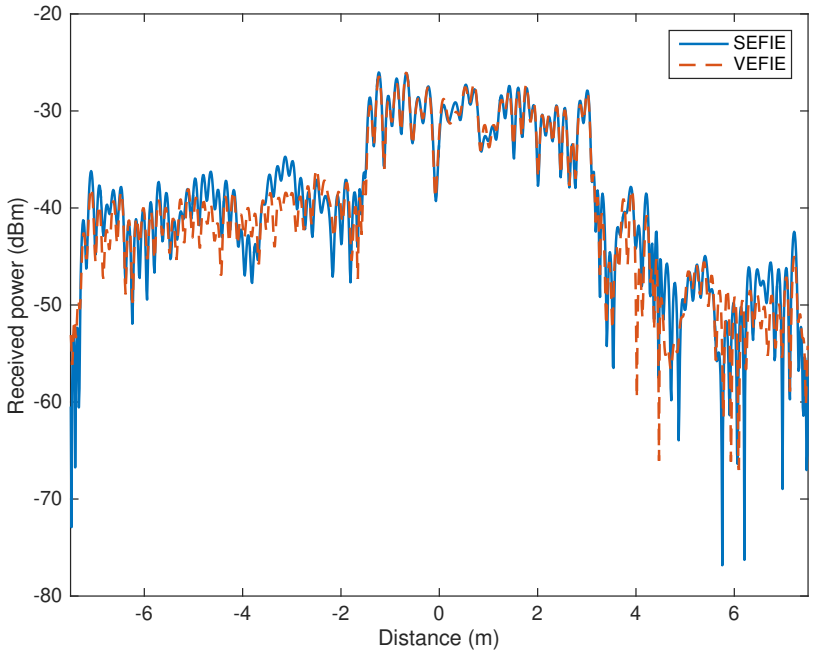

Figure 5.5: Comparison of the received power computed with the SEFIE and VEFIE along the line $x = -1$ in Figure 5.3.

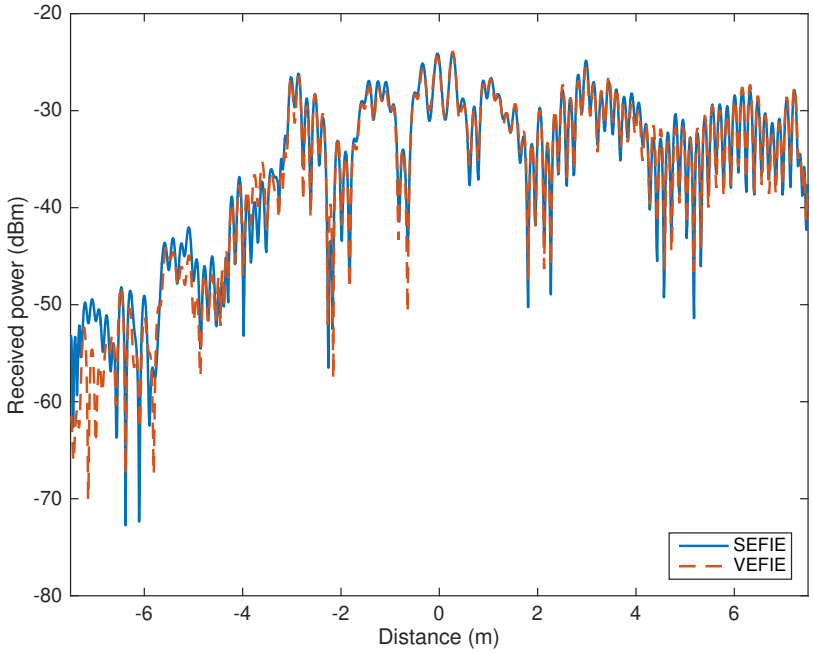

Figure 5.6: Comparison of the received power computed with the SEFIE and VEFIE along the line $y = -1$ in Figure 5.3.

erations and a time of 21,064s. However, the VEFIE is much more efficient as it can be solved to a lower error tolerance of 0.001 in 54 iterations and 43s. The SEFIE also suffers from a very long post-processing time of 8,183s. This is the time it takes to compute the fields everywhere in the problem domain from the surface currents, J_z and M_t. Overall, the SEFIE solution takes 29,370s whilst the VEFIE only takes 69s. This can be attributed to several different reasons. The use of the FFT reduces the storage requirements of the VEFIE from $\mathcal{O}(N^2)$ to $\mathcal{O}(N)$ whereas the FAFFA requires extra information to be computed and stored about the problem which results in the longer setup time than the VEFIE. The FFT is an easily parallelisable operation built in to MATLAB whilst the FAFFA is more computationally intensive. This is the primary reason why each iteration of the VEFIE solution is nearly two orders of magnitude quicker than the SEFIE iterations. The block diagonal preconditioner used is more efficient for the VEFIE solution as it assumes the interaction between basis functions is only dependant on their distance. This assumption holds true for the VEFIE where the mutual interaction between basis functions only depends on the argument of the Green's function, $|\mathbf{r} - \mathbf{r}'|$. In the SEFIE, the mutual interaction between basis functions depends on the distance between them and their orientation. This leads to a worse performance of the preconditioner for the SEFIE than the VEFIE. However, despite these issues some of which could be alleviated the main issue with the SEFIE method for indoor propagation modelling is the long processing time. The solution of the VEFIE produces the fields everywhere in the problem domain as shown in Figure 5.4, particularly when the electric field is chosen as the primary unknown. The SEFIE requires a significant processing time to compute the electric field everywhere in the problem domain from the surface currents which ultimately makes it the less optimal integral equation method for indoor propagation modelling. Thus, in the next section the 2D VEFIE will be examined for its use as an indoor propagation model and in the next chapter the 3D VEFIE will be investigated.

5.3 Numerical results

The propagation modelling capabilities of the VEFIE are examined and compared against measurements. The efficiency of the iterative solvers described in Chapter 4 and some of the acceleration techniques is investigated also. All the following simulations, unless otherwise stated, are executed through MATLAB on a laptop with a Core *i*7-4720HQ CPU and 16GB RAM.

Table 5.2: Comparison of runtime for SEFIE and VEFIE

	SEFIE	**VEFIE**
Error tolerance	0.02	0.001
Required number of iterations	388	54
Iterative solution time (s)	21,064	43
Initialisation time (s)	123	26
Post-processing time (s)	8,183	0
Total runtime (s)	**29,370**	**69**

5.3.1 Propagation modelling

The VEFIE is an efficient method for indoor propagation modelling. Its ability to model inhomogeneous scatterers and the lack of a need for absorbing boundary conditions make it a very convenient method to use. It is known that the VEFIE can produce accurate results when the simulation environment can be controlled exactly, as demonstrated in Section 5.2.2. However, its applicability to real world scenarios is not known and must be considered. Thus, a measurement campaign was performed to further validate it and analyse its accuracy in real world scenarios. The results presented here are intermediary results for the 2D VEFIE. Full 3D results with the 3D VEFIE and 2D to 3D model are presented in Chapters 6 and 7.

5.3.1.1 Measurement campaign

The measurement campaign was performed in the 6.95m $\times$ 8.2m $\times$ 2.95m portion of the house depicted in Figure 5.7. In the 2D slice shown and for the purposes of applying the 2D integral equations to the problem the only materials present are those shown in Figure 5.7, i.e. concrete, glass and wood. The floors in the house are wood, stone and tile for the living room, hall and bathroom respectively. The ceiling is a thin layer of plaster in each room. The electrical parameters used to model these materials can be found in Table 5.3. They are based on averaged values from the literature around 915MHz. Small clutter such as a coffee table, book cabinet and chairs have been neglected in the model but are present in the measurement environment. The stairs located on the left hand side of the building, as seen in Figure 5.7, are modelled as a solid block of wood. These discrepancies between the model and measurement environment will introduce a source of error in the results.

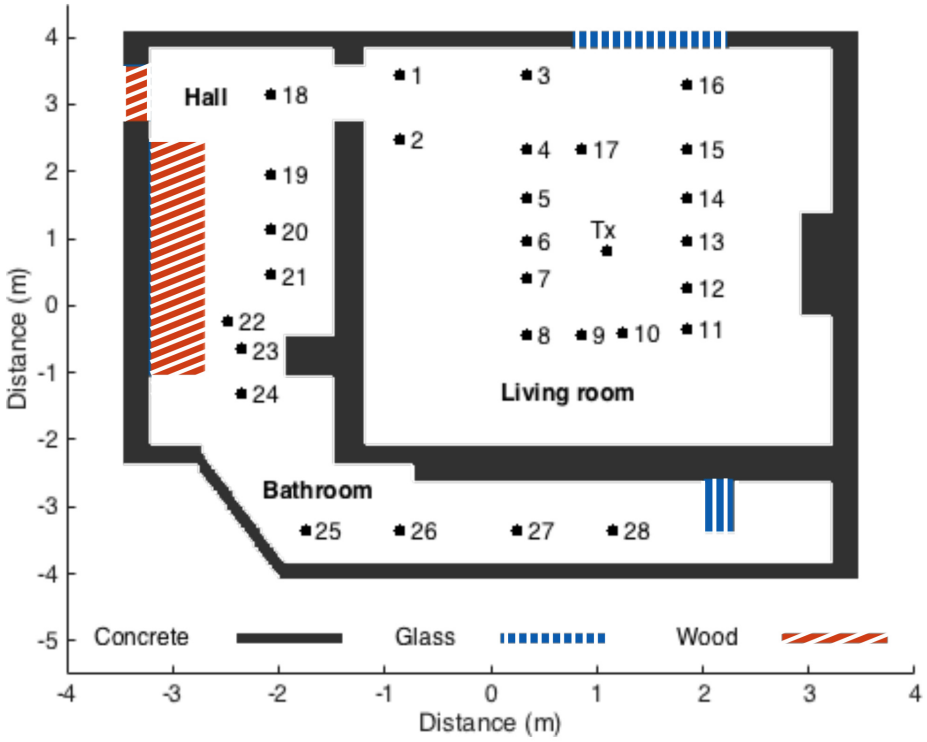

Figure 5.7: 2D depiction of a single storey portion of a house. Received power measurements were taken at the 28 receiver locations shown. The transmitter was kept constant throughout the measurement campaign. Small clutter such as a coffee table, book cabinet and chairs have been neglected in the model but are present in the measurement environment. The stairs located on the left hand side of the building are modelled as a solid block of wood.

Table 5.3: Parameters used to characterise the materials for the house in Figure 5.7.

Material	ϵ_r	μ_r	σ
Concrete	4.4	1	0.01
Glass	4.8	1	0
Wood	2.2	1	0
Stone	4.0	1	0.1
Tile	12	1	0
Plaster	2.5	1	0

The measurement campaign used two LSR 900 MHz omnidirectional dipole antennas operating at 915MHz and an Anritsu MS2651B spectrum analyser to measure the received signal strength. At each receiver location shown in Figure 5.7 five measurements were taken; one at the receiver location and the remaining four at the corners of a $\lambda \times \lambda$ square centred on the receiver location. These five measurement values were averaged to remove some of the effects of fast fading on the results.

5.3.1.2 Indoor Propagation Modelling

The 2D VEFIE is applied to the problem shown in Figure 5.7 and solved for the received power within it, which can be seen in Figure 5.8. The incident field is described by a line source radiating at 915MHz[1], which is commonly used in 2D problems instead of a dipole. The VEFIE is discretised at a rate of $\frac{\lambda}{10}$ which produces 57,200 unknowns. It is solved with the BiCGSTAB method enhanced with the FFT, reduced operator and block Jacobi preconditioner. It takes 4.63 seconds to solve the VEFIE to an error tolerance of 10^{-3}.

To validate the VEFIE for indoor propagation modelling it is compared against the measurements in Figure 5.9. The VEFIE results are averaged over a $\lambda \times \lambda$ box centred on the receiver location to remove some of the effects of fast fading, similarly to the averaging applied to the measurements. We can see there is a poor agreement between the mean power level of the measurements and the VEFIE in Figure 5.9a. This is primarily because there has been no effort made to match the transmit power of the 2D VEFIE to the transmit power in the measurement campaign.

[1] A broadband signal with a narrow channel width can be approximated by a single frequency simulation but for a wider channel response a full frequency sweep is required.

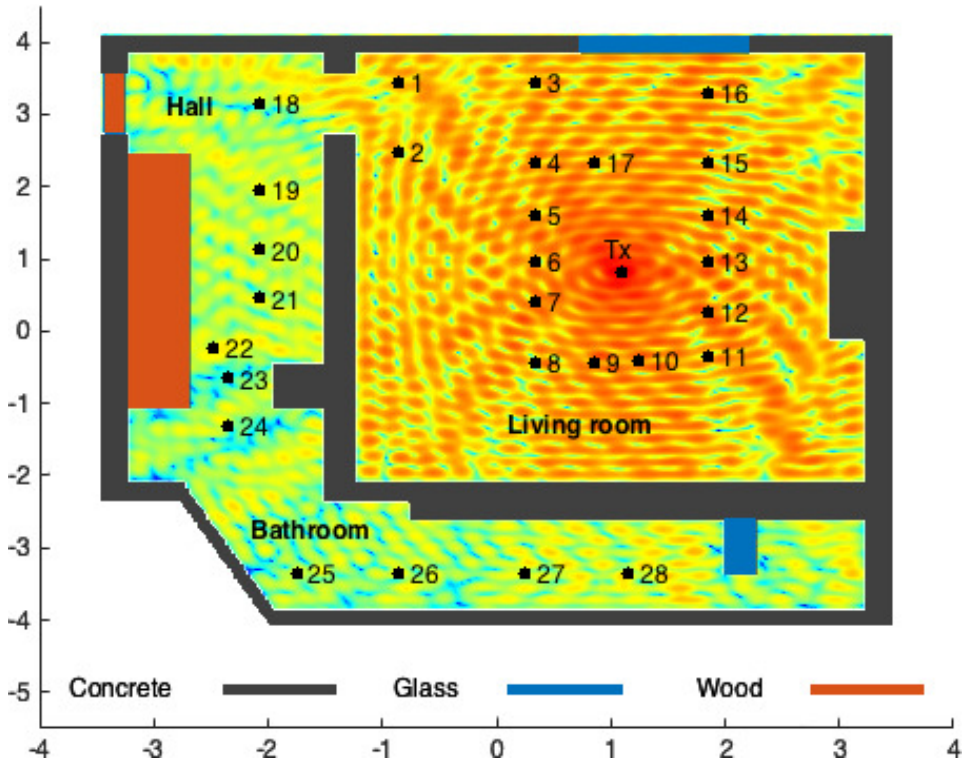

Figure 5.8: Received power for the house shown in Figure 5.7 computed by the VEFIE at 915MHz.

In the 2D VEFIE simulation the fields produced by the transmit antenna are modelled using a line source given by

$$E_z^i(\mathbf{r}) = H_0^{(2)}(k_0|\mathbf{r}|)$$

which assumes the fields are constant in the third dimension, the z dimension. Whereas, in the measurements a 3D vertical dipole was used which produces fields according to

$$\mathbf{E}^i(\mathbf{r}) \cong \hat{\boldsymbol{\theta}} \jmath\omega\mu_0 \frac{Il}{4\pi|\mathbf{r}|} e^{-\jmath k_0|\mathbf{r}|} \sin\theta$$

where I the current flowing in the dipole was 1mW and l its length was $\frac{\lambda}{2}$ corresponding to a half-wavelength dipole. The line source can't accurately approximate the fields close to the dipole due to its doughnut-like shape. The fields produced by the line source decay as $\sqrt{\frac{1}{|r|}}$ whereas those produced by the dipole decay as $\frac{1}{|r|}$. Thus, a choice was made not to attempt any matching of the transmit power for the 2D VEFIE as it would rely on measurement results and remove the fully deterministic nature of the 2D VEFIE. The 3D VEFIE and 2D to 3D models are investigated in Chapters 6 and 7 which do not experience this problem.

By applying a shift[2] to the 2D VEFIE results so that the mean error with the measurements is 0dB a very good agreement is achieved as shown in Figure 5.9a. However, without matching the transmit power the 2D VEFIE is able to capture the path loss characteristics of the environment very well which can be seen in Figure 5.9b. The path loss results do not require a correction because path loss is computed in dB by

$$PL = P_t - P_r \tag{5.19}$$

where P_t is the transmitted power and P_r is the received power. In this thesis, path loss is considered as a relative quantity independent of the absolute transmitted power whereas the average level of received power is dependent on the transmitted power and won't match if the transmitted powers aren't matched. The root mean square (RMS) error and standard deviation of error (Std. Dev.)[3] of the VEFIE against the measurements is shown in Table 5.4. It can be seen that the 2D VEFIE is able to model the path loss characteristics well.

[2] The shift adds the mean error between the 2D VEFIE and measurement results to the 2D VEFIE results so that the mean error between them is zero.

[3] If the RMS error is the same as the Std. Dev. then the mean error between two results is zero.

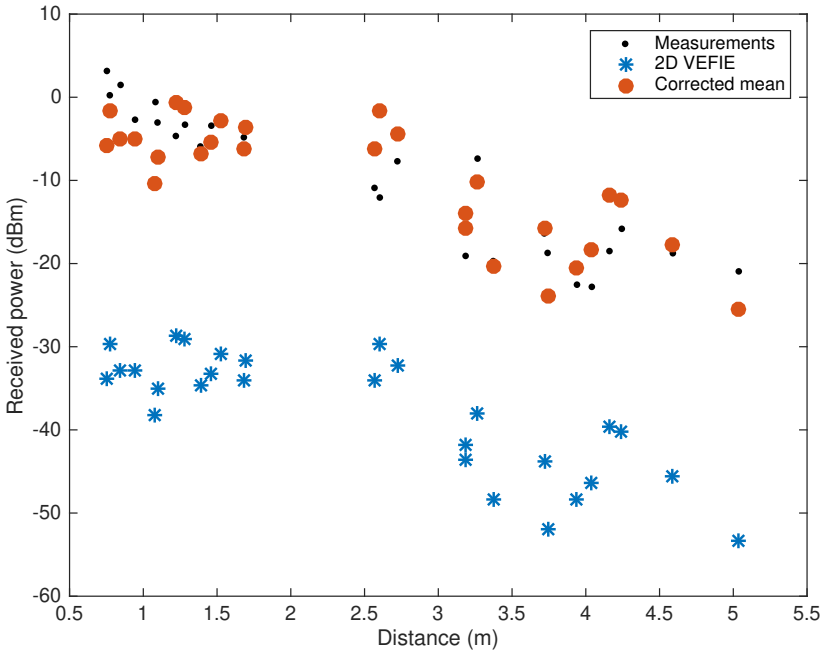

(a) Received power.

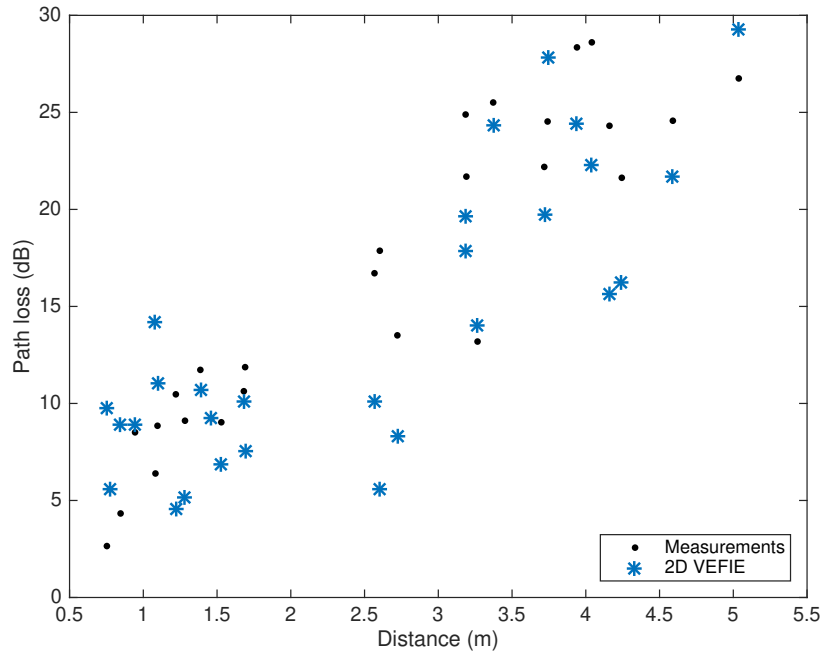

(b) Path loss.

Figure 5.9: Comparison of the VEFIE and measurements taken at the receiver locations shown in Figure 5.7.

Table 5.4: RMS error and standard deviation of the 2D VEFIE compared with measurements.

Quantity	**RMS Error**	**Std. Dev.**
Received power	28.25 dB	4.65 dB
Received power with 0dB mean correction	4.57 dB	4.65 dB
Path loss	4.96 dB	4.65 dB

5.3.1.3 Statistical and empirical model analysis

Empirical path loss models are one of the most common methods used for indoor propagation because they are extremely simple to apply. The most commonly used is the log-normal shadowing model, which has the form

$$PL(d) = PL(d_0) + 10n\log_{10}(\frac{d}{d_0}) + X_\sigma + F \tag{5.20}$$

and is also described in (2.1). $PL(d)$ is the path loss in dB at a distance d from the transmitter, $PL(d_0)$ is the known path loss at a reference distance d_0, n is a path loss exponent that depends on the propagation environment, X_σ represents shadow (or slow) fading, and F represents fast fading. Shadow fading is due to large objects and is primarily experienced when the receiver's line of sight (LOS) to the transmitter is obstructed. Fast fading occurs due to multipath effects in the environment and is affected by smaller objects in the environment. In the measurement campaign and VEFIE results in Figure 5.9 the effect of F is reduced due to the averaging process. A higher level of averaging would completely remove F and also partially or entirely remove the effect of X_σ.

The path loss model in (5.20) is normally parameterised by measurement campaigns but the VEFIE can be used instead. The values of $PL(d_0)$ and n are determined by finding the best fit using a least squares approach which produces values of 6.5602 and 2.1951 respectively, which are in line with typical values quoted in the literature [32]. The shading fading data, which is often modelled as normal (given that we are working with log values, or log-normal on a linear scale) is extracted by subtracting the mean path loss curve from the local mean path loss data. This data can be seen in Figure 5.10a. The resultant shadow fading data has a mean of 0.4298 and a standard deviation of 5.4177, again in accordance with values found in the literature [32]. To further validate the computed path loss model parameters and in particular

the shadow fading data its cumulative distribution function is compared to that of a normal variable in Figure 5.10b. An excellent agreement is achieved between the two demonstrating the ability to use the VEFIE to characterise statistical and empirical path loss models. The extracted path loss models are compared against the path loss VEFIE results and measurements in Figure 5.11 and Table 5.5. The mean path loss model is computed with $PL(d_0) + 10n\log_{10}(\frac{d}{d_0})$ in (5.20) where $PL(d_0)$ and n are given above. The mean path loss with random shadow fading data model adds random shadow fading data to the mean path loss model with the same mean and standard deviation found above.

Table 5.5: RMS error and standard deviation of the path loss 2D VEFIE results and extracted path loss model compared with measurements. The mean path loss model is computed by $PL(d_0) + 10n\log_{10}(\frac{d}{d_0})$ in (5.20) and the local mean path loss model by $PL(d_0) + 10n\log_{10}(\frac{d}{d_0}) + X_\sigma$ in (5.20).

Model	**RMS Error**	**Std. Dev.**
2D VEFIE - path loss	4.96 dB	4.65 dB
Mean path loss	3.91 dB	3.38 dB
Local mean path loss	7.69 dB	6.79 dB

Empirical path loss models have seen significant investigation in the literature [3]–[5], [32], [41], [44], [45], [57], [60], [63], [65], [66] and provide fast approximations for indoor propagation. The accuracy of the dual slope model, COST 231 multi-wall model and the adjusted Motley-Keenan model is examined against the VEFIE here. Other models exist like the average walls model and the partitioned model but they have been shown to be less accurate for indoor propagation modelling [60], [65].

Dual Slope Model The dual slope model has two distinct slopes; the first slope is for LOS regions whilst the second is for non line of sight (NLOS) regions. It states the path loss (in dB) at a point is given by

$$PL(d) = L_0 + \begin{cases} 10n_1\log_{10}(d) & 1m < d < d_{bp} \\ 10n_1\log_{10}(d_{bp}) + 10n_2\log_{10}(\dfrac{d}{d_{bp}}) & d \geq d_{bp} \end{cases} \tag{5.21}$$

where d_{bp} is the breakpoint between the LOS and NLOS regions and n_1 and n_2 must be determined experimentally through measurements. L_0 is fitted to the measure-

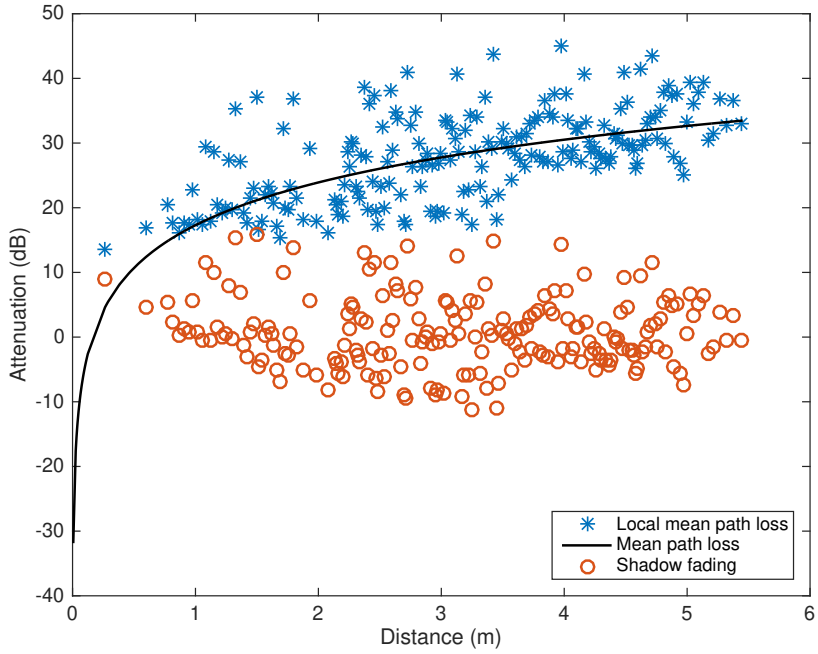

(a) Path loss data computed by the VEFIE. The local mean path loss corresponds to $PL(d_0) + 10n\log_{10}(\frac{d}{d_0}) + X_\sigma$ in (5.20) and the mean path loss is $PL(d_0) + 10n\log_{10}(\frac{d}{d_0})$.

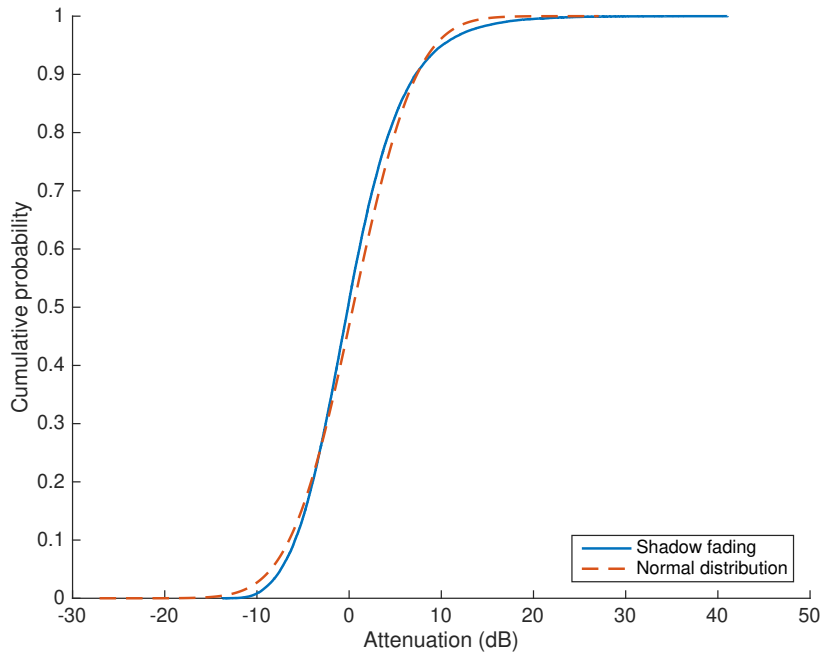

(b) Comparison of the cumulative distribution function of the extracted shadow fading data and a normal variable.

Figure 5.10: VEFIE data fitted to (5.20).

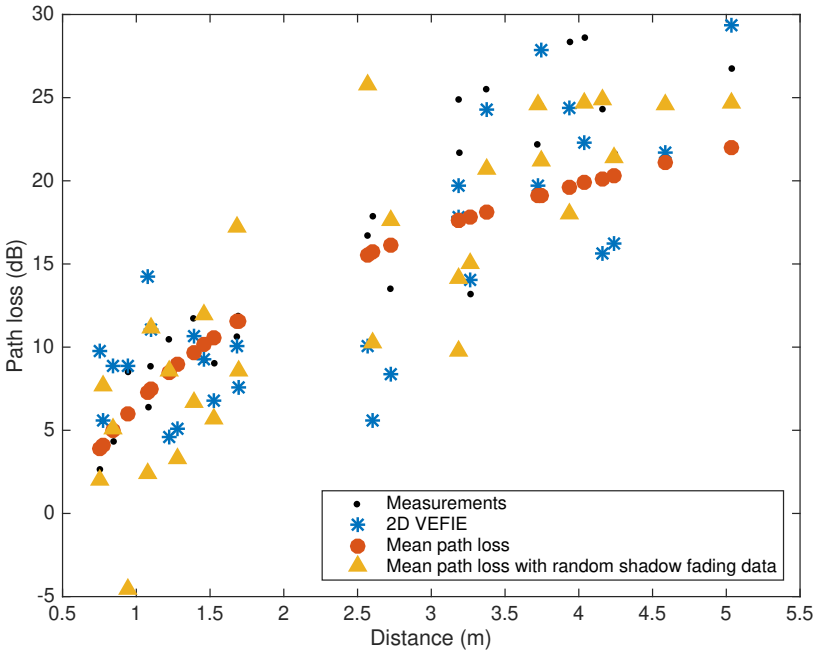

Figure 5.11: Comparison of the VEFIE and extracted path loss models against measurements. The mean path loss model is computed with $PL(d_0) + 10n\log_{10}(\frac{d}{d_0})$ in (5.20) where $PL(d_0) = 6.5602$ and $n = 2.1951$. The mean path loss with random shadow fading data model adds random shadow fading data to the mean path loss model with a mean of 0.4298 and standard deviation of 5.4177.

ments using a least squares approach and n_1 and n_2 are chosen to be 1.6 and 4 respectively as reported in [32] for in building LOS and NLOS propagation.

COST 231 Multi-Wall Model The single floor COST 231 multi-wall model represents the path loss as

$$PL(d) = L_0 + 20\log_{10}(d) + \sum_{i=1}^{H_w} h_{wi} L_{wi} \tag{5.22}$$

where d is the distance from the transmitter, H_w is the number of different types of walls, two being used in this work. h_{wi} is the number of walls of type L_{wi} obstructing the field and L_{wi} is 3.4dB for light walls (<10cm) and 6.9dB for heavy walls (>10cm). L_0 is fitted to the measurements similarly to that for the dual slope model.

Adjusted Motley-Keenan Model The adjusted Motley Keenan model calculates the path loss as

$$PL(d) = L_0 + 10n\log_{10}(d) + \sum_{i=1}^{H_w} h_i L_{0i} 2^{\log_3(\frac{e_i}{e_{0i}})} \tag{5.23}$$

where h_i is the number of walls of type i, L_{0i} is the loss in the reference wall of type i, e_{0i} is the thickness of the reference wall of type i and e_i is the actual thickness of the wall. H_w is the number of different walls. n must be determined experimentally by performing measurement campaigns. The reference values required for the adjusted Motley-Keenan model can be found in Table 5.6. L_0 and n are fitted to the measurements using a least squares approach.

Table 5.6: Reference values for Motley-Keenan model.

Wall	e_{0i} **(cm)**	L_{0i} **(dB)**
Plasterboard	12	2.5
Concrete	15	6.0

The RMS error and standard deviation of the dual slope model, the COST 231 multi-wall model and the adjusted Motley-Keenan model are shown in Table 5.7. It can be seen in Figure 5.12 the empirical models fit a curve through the measurement results with a few variations to account for NLOS areas. They do not include the fading information present in the 2D VEFIE. The dip in the COST 231 multi-wall

and adjusted Motley-Keenan models between 3m and 3.5m is because the points before and after the dip are in NLOS but the point where the dip occurs is in LOS. This isn't the capturing of fading information. It arises because of the format the data is displayed in. Each of the empirical models have to be fitted to the measurement results. They require L_0 to be determined experimentally. The Motley-Keenan model requires a measurement campaign to determine the value of n also. The VEFIE does not require measurement campaigns to be able to provide a good level of accuracy for path loss predictions but it does require knowledge of the environment, the scattering objects that are present and the electrical parameters used to characterise them, permittivity, permeability and conductivity. The VEFIE can also be used to produce angle of arrival and time domain information both of which are investigated next.

Table 5.7: RMS error and standard deviation of the VEFIE and popular empirical models compared with measurements.

Model	**RMS Error**	**Std. Dev.**
2D VEFIE - path loss	4.96 dB	4.65 dB
Dual slope	4.39 dB	3.51 dB
COST 231 multi-wall	2.81 dB	2.82 dB
Adjusted Motley-Keenan	6.37 dB	5.01 dB

5.3.1.4 Angle of arrival information

The VEFIE can leverage its computation of the fields for every point within the problem to compute angle of arrival information. From (3.56) the total field at any point is composed of the superposition of the incident field and a scaled contribution from every point within a scatterer. This information can be broken down into the description shown in Figure 5.13 where the power received versus angle for the receiver location (0.35, 3.43) in Figure 5.7 is shown. The angle, $\theta = 0$, is chosen such that the incident field arrives from this angle. The VEFIE is capable of providing detailed information at each angle down to a limit defined by the discretisation rate because every electromagnetic interaction is inherent within it.

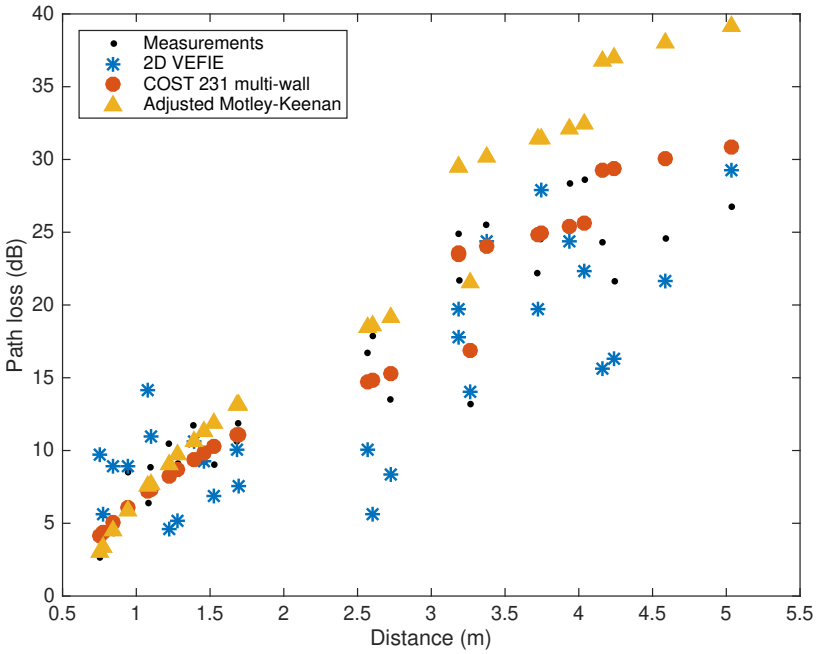

Figure 5.12: Comparison of the VEFIE and popular empirical models against measurements.

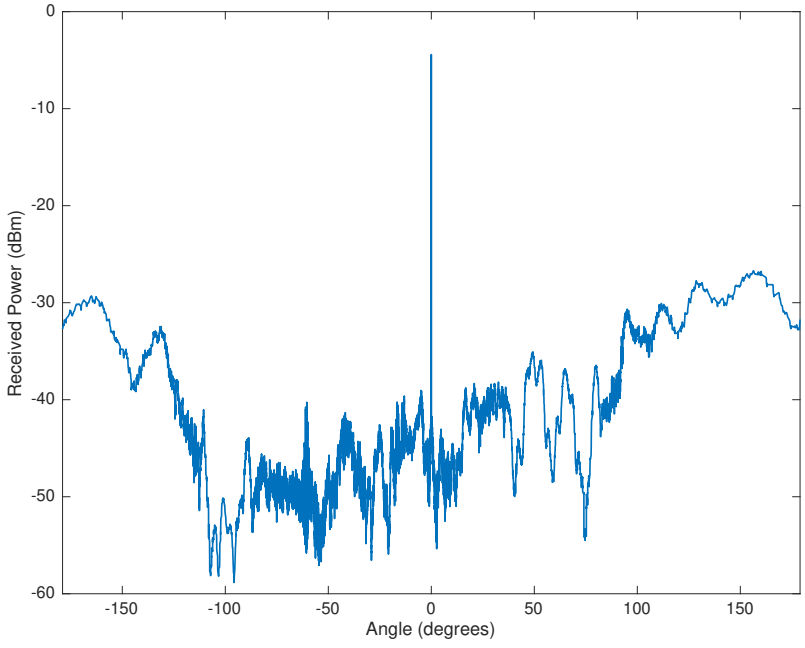

Figure 5.13: Received power with angle at (0.35, 3.43) in Figure 5.7. $\theta = 0$ is chosen such that the incident field arrives at that angle.

5.3.1.5 Time domain information

The VEFIE as described is a frequency domain method but it can be used to generate time domain information. To do so the VEFIE must be solved independently over a large frequency range as shown in Figure 5.14. This information is then transformed from the frequency domain to the time domain using the inverse Fourier transform to give the power delay profile (PDP) in Figure 5.15. The VEFIE solution at each frequency is independent of the solution at neighbouring frequencies and produces information about the field for all points within the problem domain. This enables time domain predictions in the form of PDPs to be computed for any point within the problem domain without any extra overhead after it has been solved at each frequency of interest. Here, the VEFIE has been applied to Figure 5.7 and solved over the frequency range from 10MHz to 3GHz with a frequency spacing of 10MHz producing information at 300 discrete frequencies. The information for the point (-0.86, 2.48) has been extracted and is shown in Figure 5.14. This information is windowed with a Blackman-Harris window to reduce some of the effects of aliasing due to the discrete data set and inverse Fourier transformed to produce the PDP in Figure 5.15. As a simple validation of this approach Geometrical Optics (GO) is used to determine when pulses are expected to arrive in the PDP by considering reflections and diffractions with a travel time of

$$\tau = \frac{R}{c_0}$$

where R is the distance travelled by the wave and c_0 is the speed of light which is assumed to be the speed electromagnetic waves travel through air. With this approach the time for the LOS pulse to arrive as well as reflections and diffractions can be computed. Some of these are overlaid on Figure 5.15 and show an excellent agreement with the VEFIE data. It is important to note the VEFIE produces more detailed information than GO can as it inherently includes all the interactions of electromagnetic waves on their surrounding environment. Alternative approaches like the time domain VEFIE [167], [168] exist but it is considerably more complex and has seen very little investigation in the literature.

As with all modelling approaches based on the VEFIE, time domain modelling also suffers from numerical inaccuracies. The transformation with the Fourier transform introduces aliasing into the time domain predictions as well as the numerical inaccuracies introduced in the frequency domain due to the discretisation and finite error tolerance the VEFIE is solved to. Aliasing is introduced in the time domain predic-

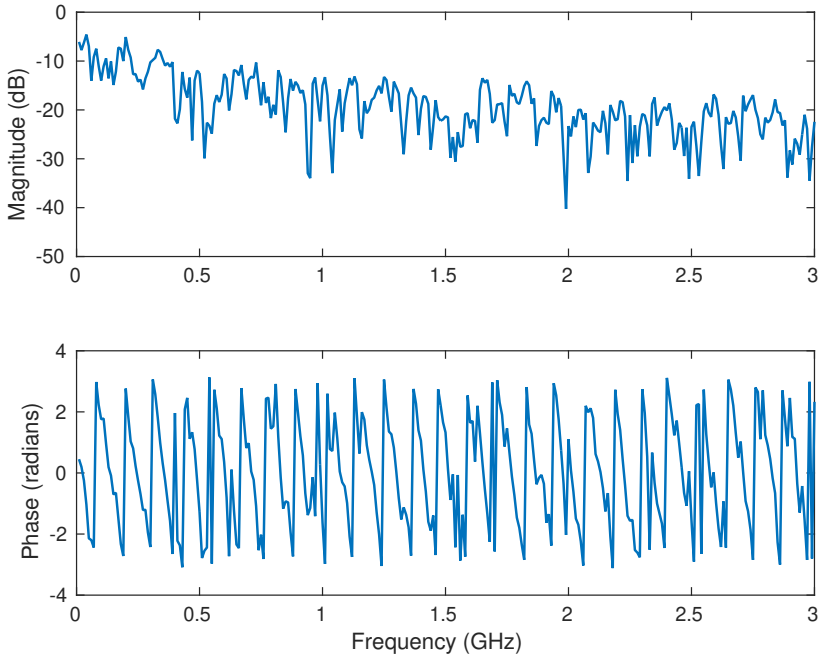

Figure 5.14: Electric field computed at (-0.86, 2.48) in Figure 5.7 from 10MHz to 3GHz with a frequency spacing of 10MHz with the VEFIE.

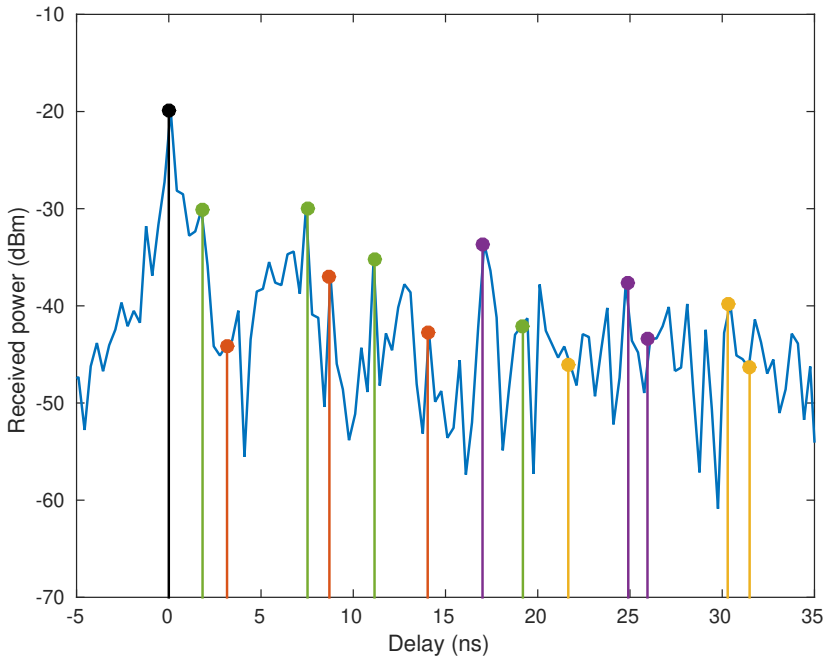

Figure 5.15: Power delay profile computed from the frequency domain VEFIE data in Figure 5.14. The LOS pulse is shown in black, first order reflections are in green, first order diffractions are in red, a first order reflection followed by a first order diffraction is shown in yellow and second order reflections are shown in purple.

tions because of the finite bandwidth and resolution used. There is a direct relationship between the bandwidth of the frequency domain data and the resolution of the PDP given by

$$t_s \propto \frac{1}{B} \tag{5.24}$$

where t_s is the sample time in the time domain and B is the bandwidth in the frequency domain. The length of the time domain signal is related to the number of points in the frequency domain (or frequency spacing) by

$$T \propto \frac{1}{N_f} \tag{5.25}$$

where T is the total length of time for the time domain signal and N_f is the number of frequencies computed in the frequency domain. The Figures 5.16 to 5.19 are used to illustrate the relationships in (5.24) and (5.25).

Figure 5.16 shows two signals; one signal with a bandwidth of 2GHz from 10MHz to 2.01GHz and another with a bandwidth of 1GHz from 0.51GHz to 1.51GHz. Both signals have a frequency spacing of 10MHz. The PDPs in Figure 5.17 are computed using the 2GHz and 1GHz bandwidth signals depicted in Figure 5.16. The two results show a poor agreement with each other. The average sense of the envelope is matched relatively well but the specific peaks and troughs within the PDPs are not matched accurately. The accuracy of the 1GHz bandwidth signal significantly degrades further along the time axis. Figure 5.18 shows two signals; the 10MHz signal has a frequency spacing of 10MHz and a bandwidth from 20MHz to 3GHz whereas the 20MHz signal has a frequency spacing of 20MHz and the same bandwidth. The PDPs shown in Figure 5.19 are computed using the 10MHz and 20MHz signals in Figure 5.18. The effect of aliasing can clearly be seen at the start and end of the 20MHz signal where the noise level is higher preceding the LOS pulse and this also affects the end of the signal by slightly increasing its power level above that of the 10MHz signal. The PDPs show an excellent agreement for around 30ns from the LOS pulse. These results demonstrate that to accurately capture the envelope of the time domain signal a large bandwidth is required in the frequency domain whereas the spacing does not play a crucial role up to a specific time. However, if a long time domain signal is required a small frequency domain resolution is necessary.

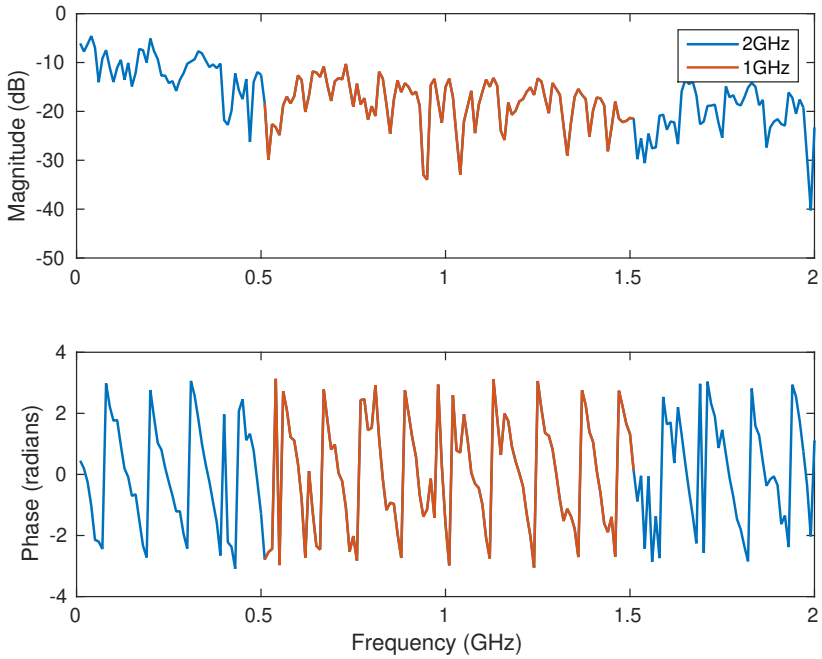

Figure 5.16: Depiction of a 2GHz and 1GHz bandwidth. The 2GHz bandwidth is from 10MHz to 2.01GHz and the 1GHz bandwidth is from 0.51GHz to 1.51GHz. Both signals have a frequency spacing of 10MHz. The two results shown here are used to compute the PDPs shown in Figure 5.17.

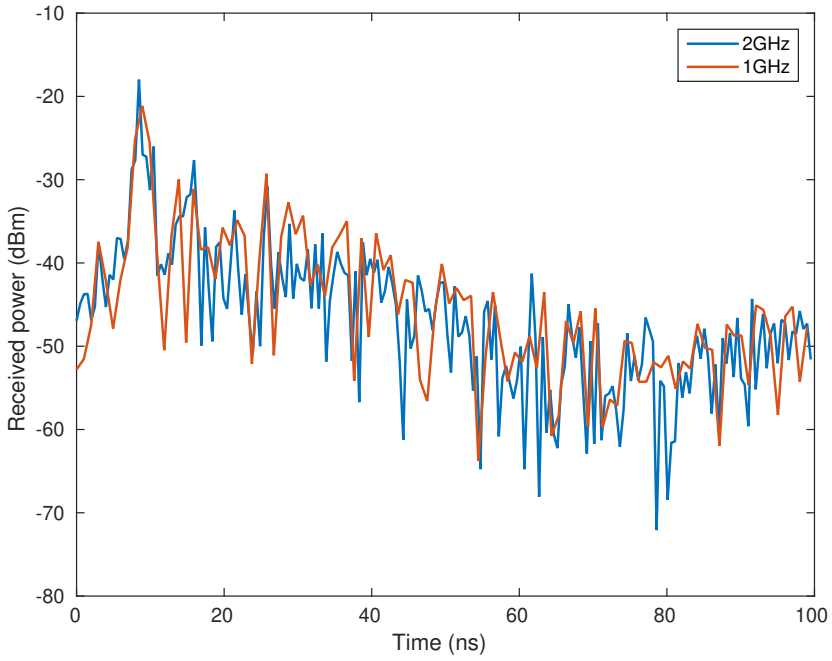

Figure 5.17: Illustration of the effect of a finite bandwidth in the frequency domain on the computation of time domain PDPs using the inverse Fourier transform. The frequency domain data used to compute these PDPs is shown in Figure 5.16. Both signals have the same frequency spacing of 10MHz but due to their different bandwidths (2GHz vs 1GHz) they have a different time domain spacing because of the relationship in (5.24).

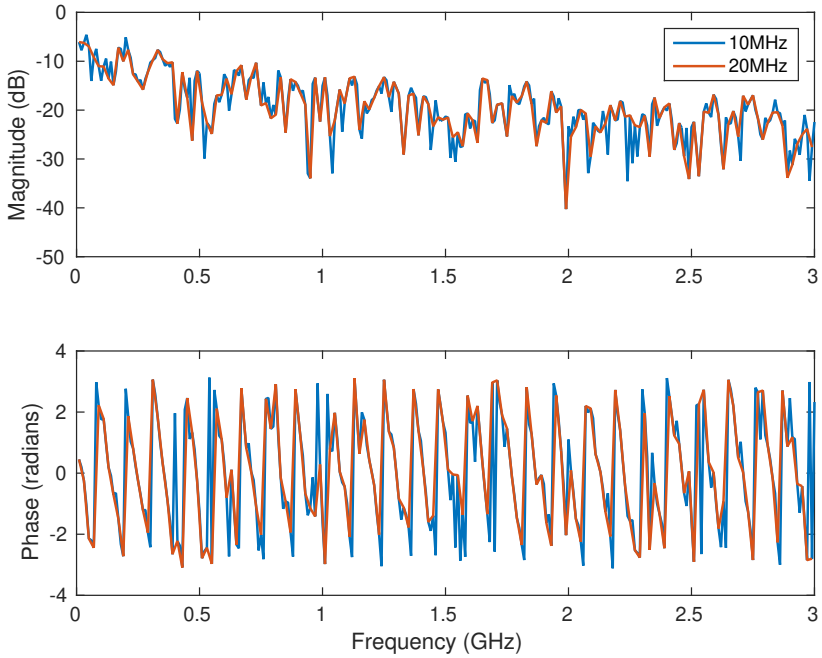

Figure 5.18: The 10MHz signal has a frequency spacing of 10MHz, whereas, the 20MHz signal has a frequency spacing of 20MHz. Both signals have a bandwidth from 20MHz to 3GHz. The 20MHz signal has 150 samples but the 10MHz signal has 299 samples. These signals are used to compute the PDPs shown in Figure 5.19.

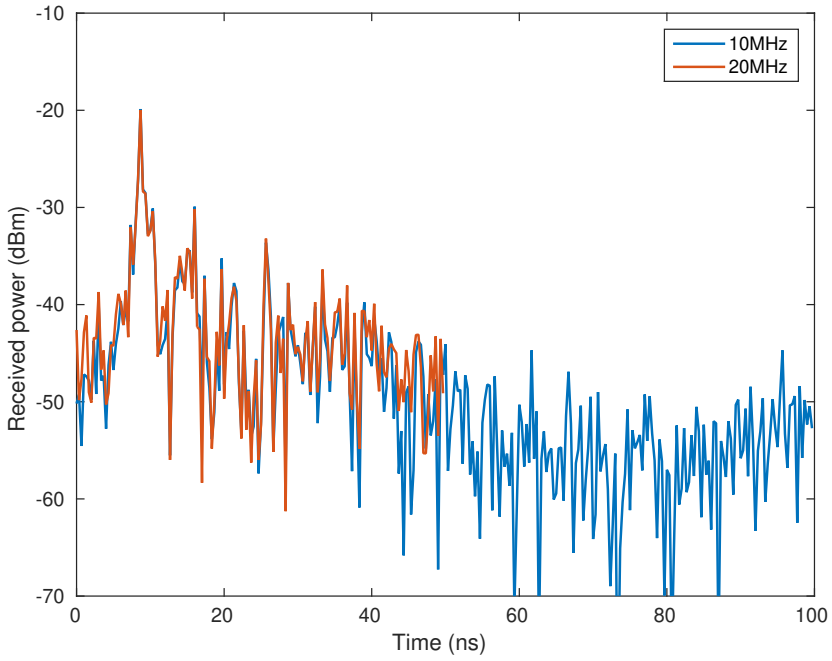

Figure 5.19: Illustration of the effect of a finite number of frequency samples in the frequency domain on the computation of time domain PDPs using the inverse Fourier transform. The frequency domain data used to compute these PDPs is shown in Figure 5.18. Both signals have a bandwidth from 20MHz to 3GHz. The 20MHz signal produces a PDP with approximately half the length of the 10MHz signal due to the relationship in (5.25).

5.3.2 Comparison with 3D ray tracing

In order to determine the viability of the VEFIE as an indoor propagation model it should be compared against the most popular deterministic model, ray tracing. The VEFIE has already been shown to be more efficient than the SEFIE, to match path loss measurements accurately and to be able to provide more information than statistical or empirical models. The 2D VEFIE is compared against GO and the Uniform Theory of Diffraction (UTD) which underpin most ray tracing models before being compared against a 3D ray tracing model developed by Kenny and Nuallain [152] that considers up to 3rd order reflections and transmissions but does not consider diffraction or diffuse scattering.

The 2D VEFIE is compared against GO and UTD (GO/UTD) for the problem described by Figure 5.20. The problem consists of a 5m $\times$ 5m 2D block positioned in the bottom left corner of a free space region of size 10m $\times$ 10m. The block is characterised by $\epsilon_r = 5$, $\mu_r = 1$ and $\sigma = 0.5$. The problem is illuminated by a line source radiating at 1GHz positioned at (-5, 3) for both the 2D VEFIE and 2D GO/UTD model. The agreement between the 2D VEFIE and GO/UTD is excellent as shown in Figure 5.21.

The 2D VEFIE is compared against the 3D ray tracing model for the environment shown in Figure 5.7. The incident field is modelled as a full three-dimensional dipole in the ray tracing model and its transmit power is matched to that of the measurements whilst the 2D VEFIE models the transmitter as a line source and does not match the transmit power. The 3D ray tracing model is, as expected, more accurate than the 2D VEFIE model as seen in Figure 5.22 and Table 5.8. However, despite the transmitted power in the ray tracing model being the same as the measurement campaign the mean power of the ray tracing predictions does not match the mean received power of the measurements as shown in Figure 5.22a. A correction similar to the 2D VEFIE is required for the ray tracing predictions to force the mean error to be 0dB. Both the mean corrected VEFIE and ray tracing received power results agree well with the measurements as shown in Figure 5.22a as do the path loss results in Figure 5.22b. The 3D ray tracing model produces a lower RMS error and standard deviation for the path loss results as shown in Table 5.8. The 3D VEFIE and 2D to 3D models in Chapters 6 and 7 are developed to remove the need for the mean error correction in the 2D VEFIE.

The 2D VEFIE model is more efficient than the 3D ray tracing model. The runtime of the 2D VEFIE and ray tracing is shown in Table 5.8. Both models are executed on a laptop with a Core *i*5-5250U CPU and 8GB RAM. The VEFIE model has 57,200

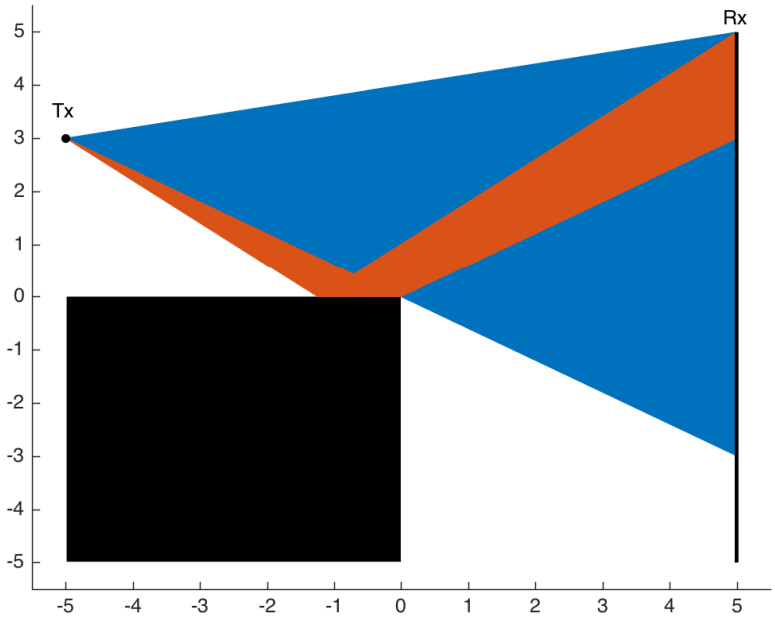

Figure 5.20: Problem scenario for comparison of GO/UTD with the 2D VEFIE. The models are compared along the black line. The direct ray path is illuminated in blue whilst the reflected ray path is shown in red. Non illuminated paths represent the region where only diffracted rays are present.

Table 5.8: Runtime, RMS error and standard deviation of the VEFIE and ray tracing compared with measurements.

		Received power		Path loss	
Model	**Runtime**	**RMS Error**	**Std. Dev.**	**RMS Error**	**Std. Dev.**
2D VEFIE	6.5s	28.25 dB	4.65 dB	4.96 dB	4.65 dB
Ray tracing	415s	7.85 dB	2.54 dB	2.50 dB	2.54 dB

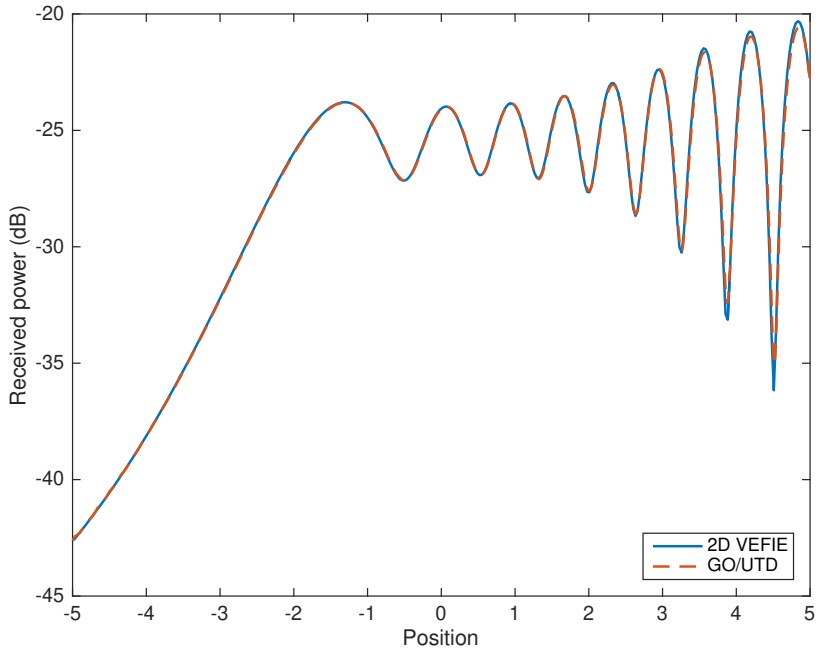

Figure 5.21: Comparison of the VEFIE and UTD for the problem shown in Figure 5.20.

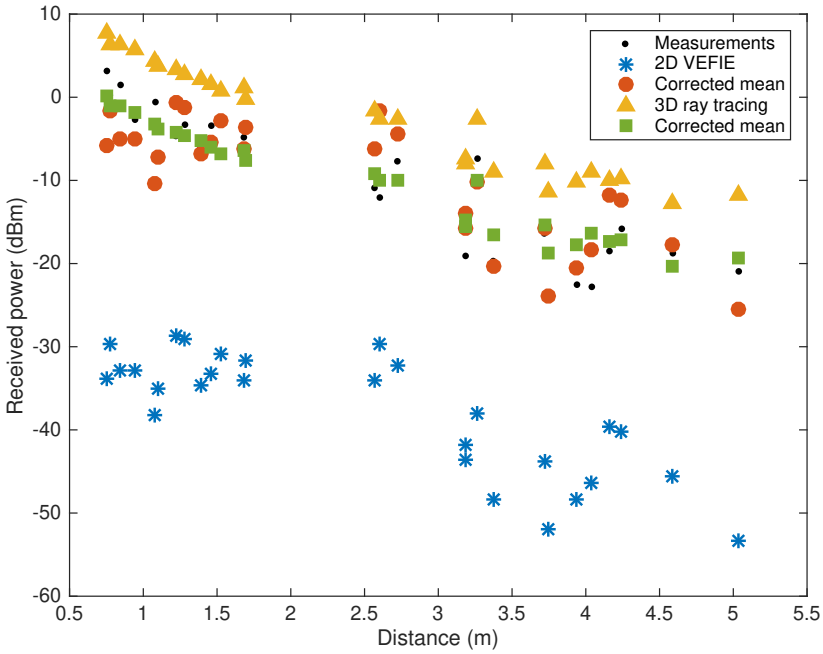

(a) Received power.

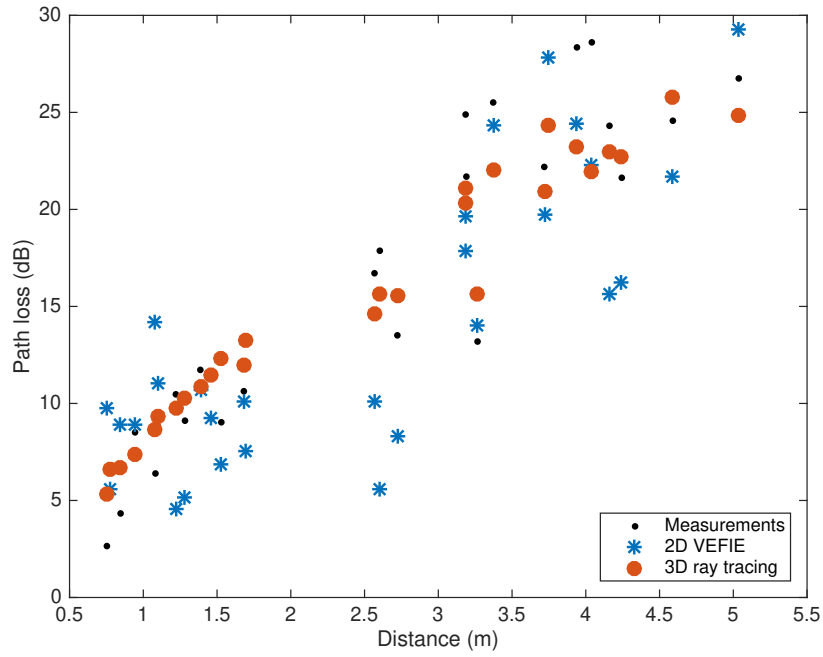

(b) Path loss.

Figure 5.22: Comparison of the VEFIE and ray tracing against measurements taken at the receiver locations shown in Figure 5.7.

unknown values to be computed. The ray tracing model computes the 3D fields for the plane perpendicular to the centre of the dipole, similarly to the 2D VEFIE. 53,463 receiver locations are used in the ray tracing model. The VEFIE is executed in MATLAB and takes advantage of parallelisation whilst the ray tracing model is written in C++ without parallelisation. The 2D VEFIE model is over 60 times faster than the 3D ray tracing model and computes the fields at slightly more points too.

5.3.3 Computational complexities

The efficiency and applicability of the methods described in Chapter 4 are investigated for the Mie series problem described by Figure 5.2. The problem is discretised at a rate of $\frac{\lambda}{10}$ which results in 48,400 unknown values to be solved. Each of the iterative solvers in Chapter 4 are applied to solve the problem and their convergence rates are shown in Figures 5.23 and 5.24. Only the CG-NE and BiCGSTAB methods converge to an error tolerance less than 10^{-2}. The CGS method converges to an error tolerance of $10^{-1.9}$ in 136 iterations but after that its solution diverges possibly due to the issues with rounding errors due to the squaring operation described in Section 4.2.3. The CG method does not converge as expected because it is only applicable to real symmetric positive definite problems which typical indoor propagation problems are not. The BiCG method does not converge and this is likely because it does not guarantee minimisation of the residual error.

The CG-NE, CGS, and BiCGSTAB methods all converge to a solution. Although in the case of the CGS it eventually diverges after reaching an error tolerance of $10^{-1.9}$. Table 5.9 shows the number of iterations each method requires to converge to an error tolerance of $10^{-1.9}$ and 10^{-6}. The average time for a single iteration of each method is shown in Figure 5.25. Overall, it can be seen that each method takes a similar length of time per iteration and, thus, the overriding factor for their total computation time and efficiency is their convergence rate. Each solver requires a similar computation time per iteration because there are two matrix vector multiplications required within each iteration for them which is the major time component per iteration. The BiCGSTAB method performs better than the CG-NE method as shown in Table 5.9, whilst the CGS method performs well to $10^{-1.9}$ before it diverges.

Section 4.3.3 demonstrates that a reduced operator can be used within iterative solvers to ignore the extra unknowns present in the VEFIE that arise by using the electric field as the primary unknown. In Figures 5.26 and 5.27 the effect of the re-

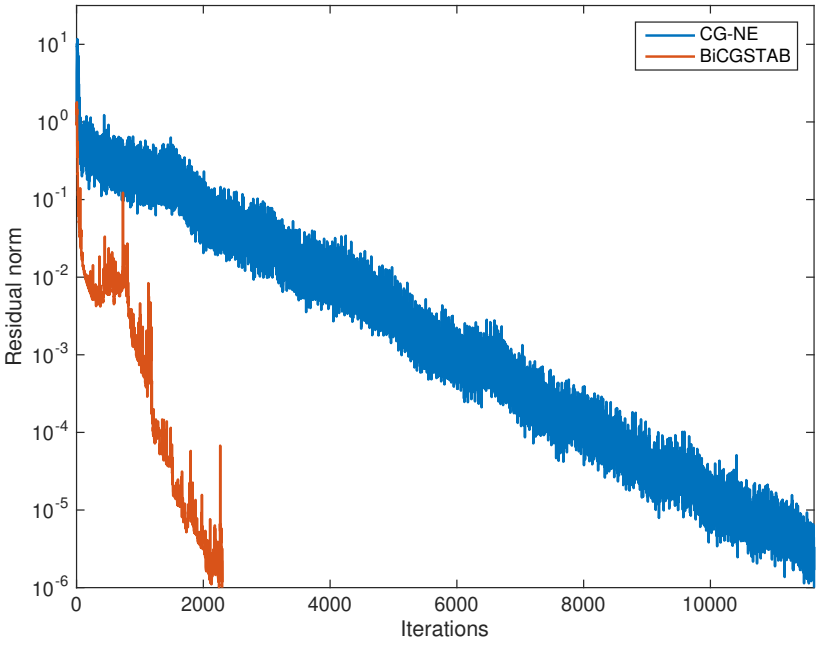

Figure 5.23: Convergence rate of the CG-NE and BiCGSTAB methods. The CG-NE converges to an error tolerance of 10^{-6} in 11,635 iterations and the BiCGSTAB method requires 2,298 iterations.

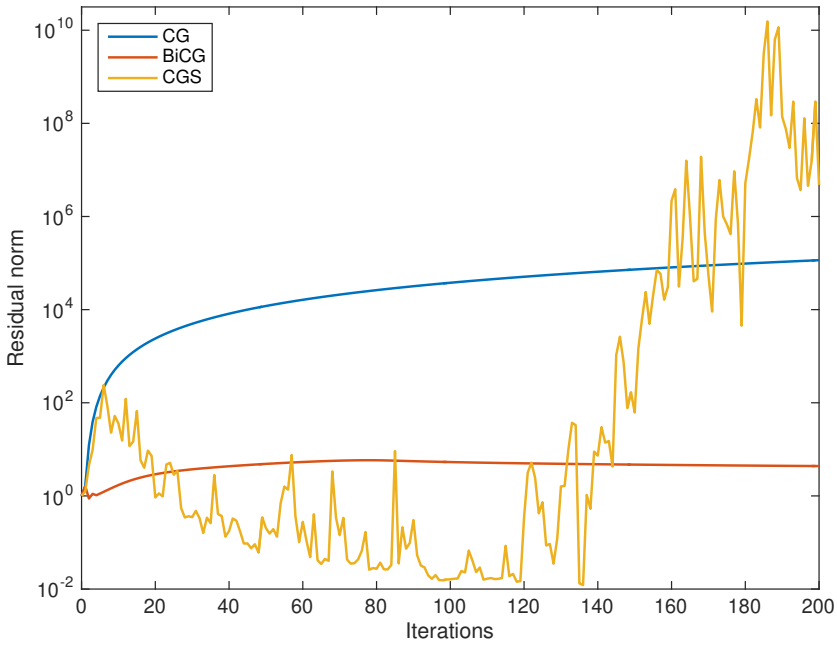

Figure 5.24: Convergence rate of the CG, BiCG and CGS methods. The three iterative solvers all diverge and never reach an error tolerance below 10^{-2}.

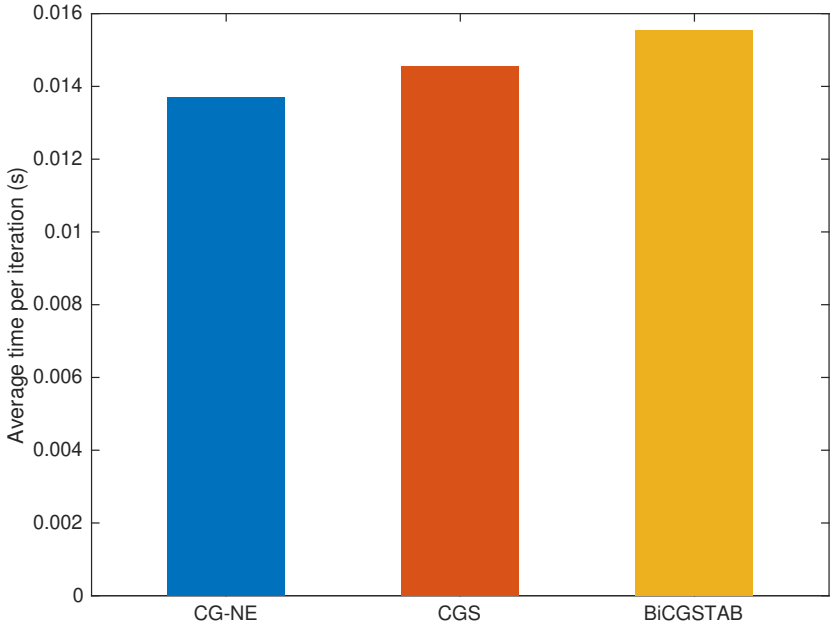

Figure 5.25: Average time to compute a single iteration within several iterative solvers for the problem described in Section 5.2.2.

Table 5.9: Number of iterations and runtime of iterative solvers to reach a given error tolerance.

	$10^{-1.9}$		10^{-6}	
	Iterations	**Runtime**	**Iterations**	**Runtime**
CG-NE	2,659	36.22s	11,635	159.46s
CGS	136	2.08s		
BiCGSTAB	115	1.74s	2,298	35.72s

duced operator on the number of iterations it takes for the CG-NE and BiCGSTAB methods, respectively, to converge to an error tolerance of 10^{-6} is shown. It can be seen from Figure 5.26 that the reduced operator has a significant effect on the CG-NE method reducing the number of iterations it takes to reach 10^{-6} from 11,635 to 5,120. The reduced operator does not have as large an effect on the BiCGSTAB method as shown in Figure 5.27. It reduces the number of iterations required to reach 10^{-6} from 2,298 to 2,039, an 11% reduction as opposed to the 56% reduction observed in the CG-NE method. The additional time to compute an iteration with the reduced operator is negligible over the case without it as shown in Figure 5.28. In fact it is slightly lower because the added sparsity can be exploited to marginally speed up some computations.

Preconditioning is described in Section 4.3 as a means to improve the convergence rate of iterative solvers. However, it was found that for the problem described in Section 5.2.2 using a block Jacobi preconditioner with the CG-NE method causes it to diverge and it offers no improvement to the BiCG and CGS methods. Thus, the application of the preconditioner will only be examined with respect to the BiCGSTAB method. The convergence rate of the BiCGSTAB without and with the preconditioner is shown in Figure 5.29. With the preconditioner the BiCGSTAB converges to an error tolerance of $10^{-5.9}$ in 460 iterations. After this it begins to diverge and eventually breaks down after 1,076 iterations. The unpreconditioned BiCGSTAB converges to $10^{-5.9}$ in 2,102 iterations. The preconditioner offers a reduction of 49% in the number of iterations, much better than the reduced operator, but unlike the reduced operator it greatly affects the time to compute a single iteration as shown in Figure 5.30a. The use of the preconditioner triples the time it takes to compute a single iteration with the BiCGSTAB method but due to the large reduction in number of iterations required the total time to reach a solution is much faster with the preconditioner than without,

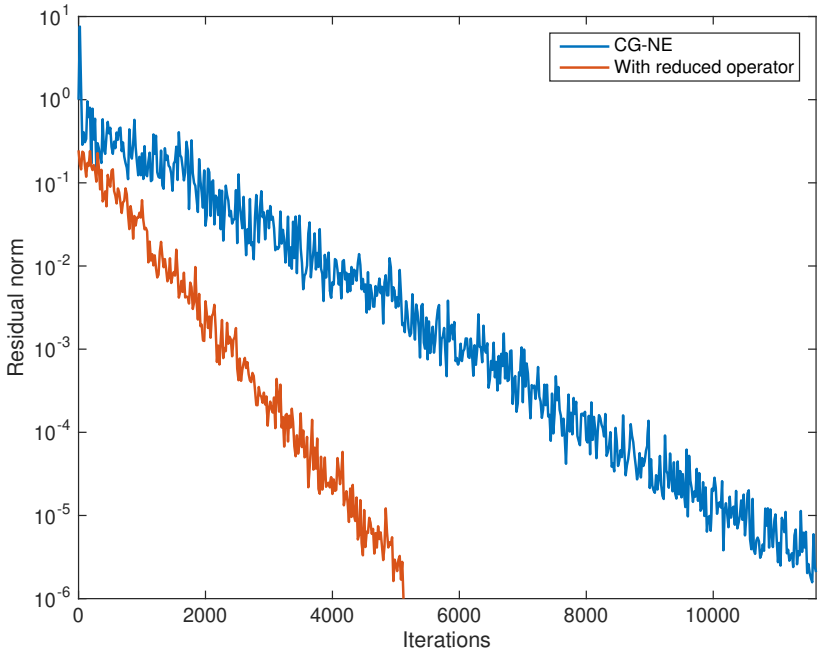

Figure 5.26: Convergence rate of CG-NE method. The CG-NE converges to an error tolerance of 10^{-6} in 11,635 iterations. With the reduced operator it converges in 5,120 iterations.

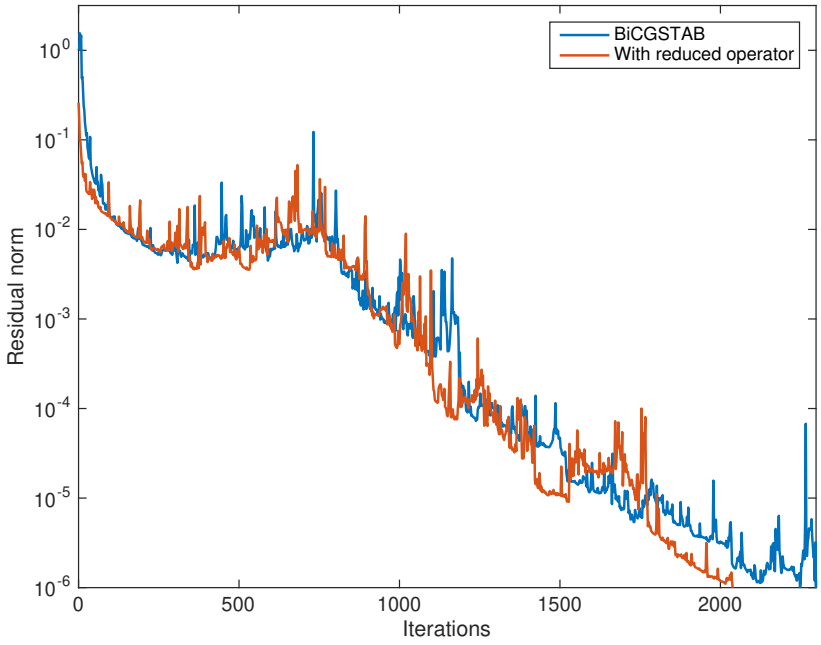

Figure 5.27: Convergence rate of BiCGSTAB method. The BiCGSTAB converges to an error tolerance of 10^{-6} in 2,298 iterations. With the reduced operator it converges in 2,039 iterations.

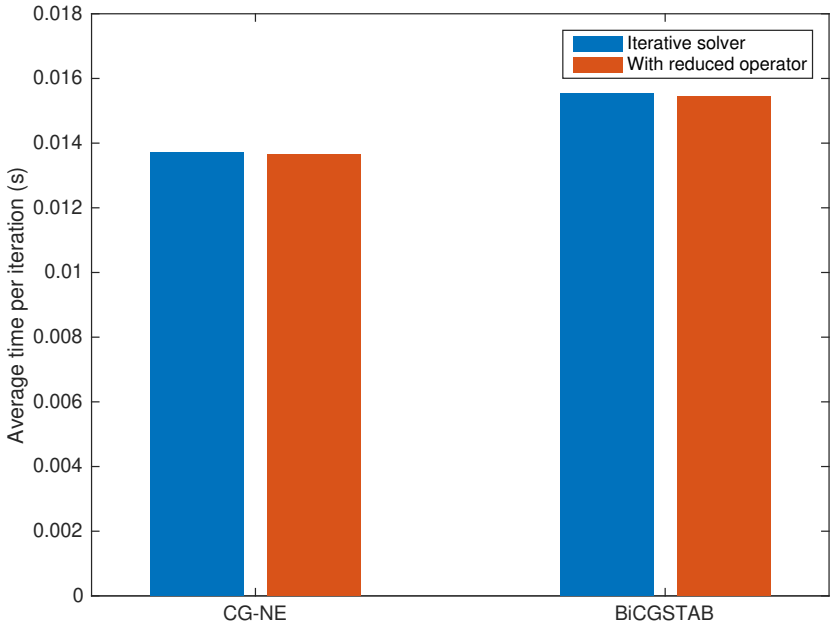

Figure 5.28: Average time to compute a single iteration within the CG-NE and BiCG-STAB methods.

which can be seen in Figure 5.30b. The reasons for the divergence of the BiCGSTAB with preconditioner are beyond the scope of this thesis but a possible reason could be due to implementation specific computations that cause floating point rounding error to propagate.

The reduced operator and preconditioner both improve the convergence rate and runtime of the iterative solution. Figure 5.31 examines the convergence rate of the BiCGSTAB method with the reduced operator and preconditioner applied together. The number of iterations and runtime for the various BiCGSTAB approaches are shown in Table 5.10. It can be clearly seen that the best approach is to use both the reduced operator and the preconditioner with the BiCGSTAB method. The main advantage of this approach is that the reduced operator can be used to reduce the size of the preconditioner which results in less computations and faster time to compute a single iteration, which can be seen in Figure 5.32a. Even though the time to compute a single iteration is still greater than without the preconditioner because the combined approach requires so few iterations it is much faster than the other approaches, which can be seen in Figure 5.32b. The reduced operator and preconditioner offer a 83% reduction in iterations over using the reduced operator only and a 85% reduction over the standard BiCGSTAB.

Table 5.10: Number of iterations and runtime of BiCGSTAB to reach a given error tolerance.

	$10^{-5.9}$		10^{-6}	
	Iterations	**Runtime**	**Iterations**	**Runtime**
BiCGSTAB	2,102	32.70s	2,298	35.72s
With reduced operator	1,990	30.73s	2,039	31.51s
With preconditioner	460	23.05s		
With reduced operator and preconditioner	346	9.50s	351	9.67s

5.4 Conclusions

2D integral equations have been examined for indoor propagation modelling. The SEFIE and VEFIE are briefly described. The VEFIE solution is validated against the analytical Mie series solution for scattering from a dielectric cylinder. Then the SEFIE

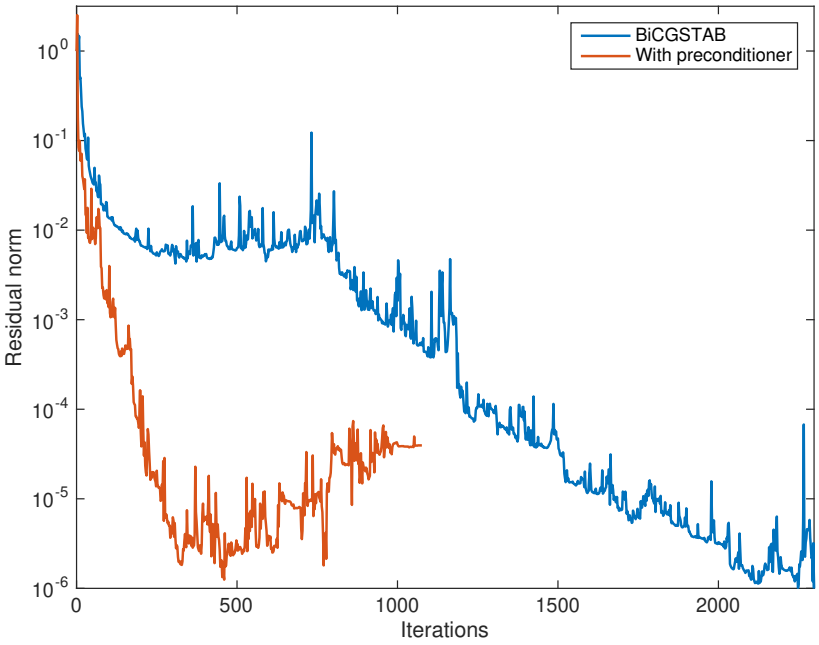

Figure 5.29: Convergence rate of BiCGSTAB method. The BiCGSTAB converges to an error tolerance of 10^{-6} in 2,298 iterations. With the preconditioner it converges to an error tolerance of $10^{-5.9}$ in 460 iterations after which it diverges and eventually breaks down.

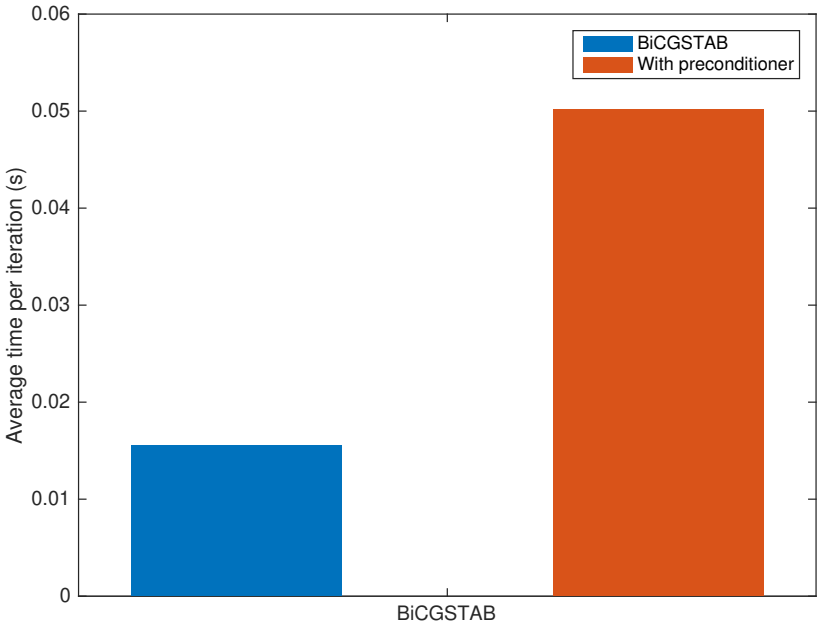

(a) Average time to compute a single iteration within the BiCGSTAB method.

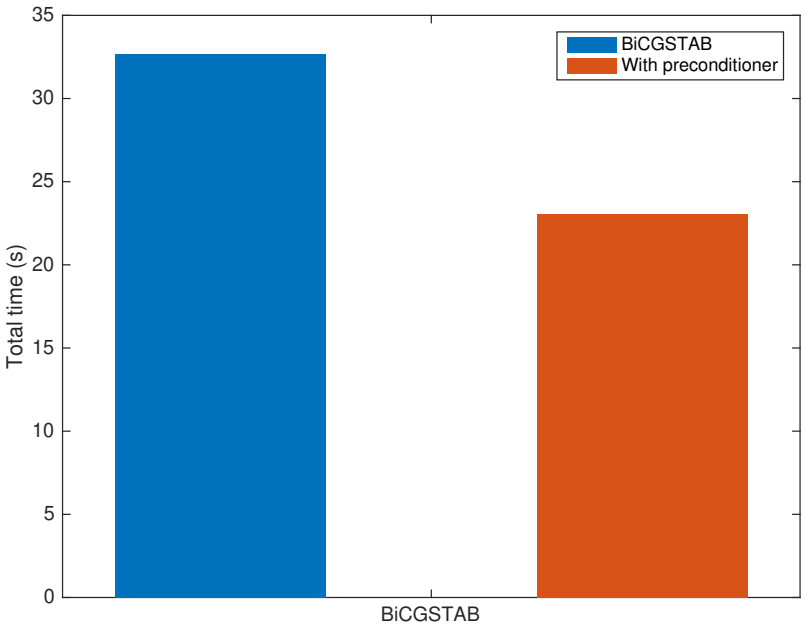

(b) Total time to converge to $10^{-5.9}$ for the BiCGSTAB method.

Figure 5.30: Comparison of the average time per iteration and total time of the BiCGSTAB method.

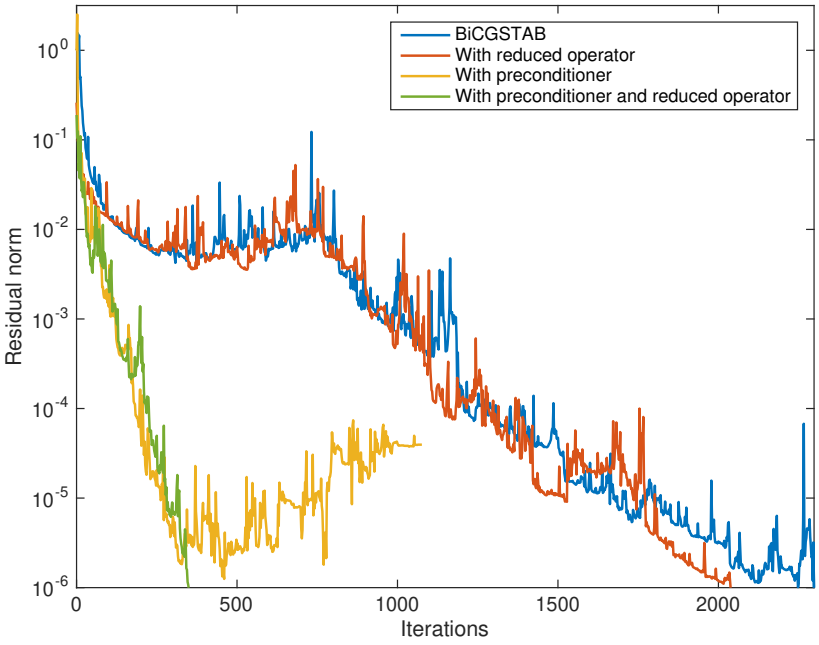

Figure 5.31: Convergence rate of the BiCGSTAB method. The BiCGSTAB converges to an error tolerance of 10^{-6} in 2,298 iterations. With the reduced operator and preconditioner it converges in 351 iterations.

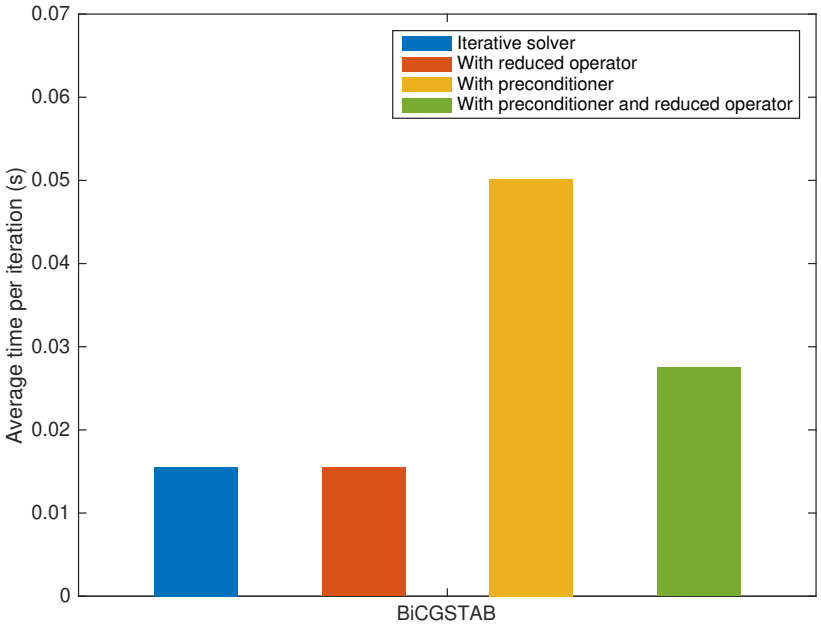

(a) Average time to compute a single iteration within the BiCGSTAB method.

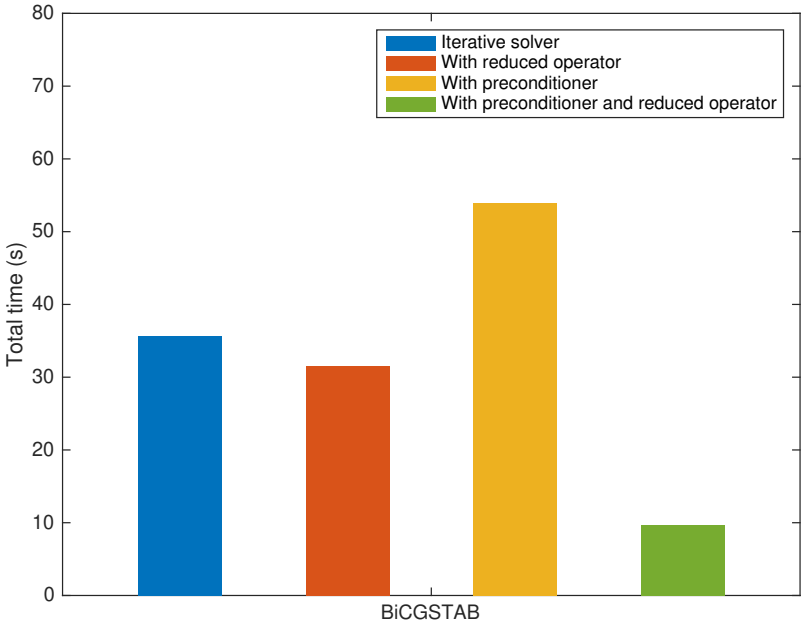

(b) Total time to converge to $10^{-5.9}$ for the BiCGSTAB method.

Figure 5.32: Comparison of the average time per iteration and total time of the BiCGSTAB.

and VEFIE are applied to a realistic 2D indoor propagation environment and shown to yield similar results as expected. However, the convergence rate and runtime of the VEFIE is considerably better than that of the SEFIE. Thus, it is used as the basis for an indoor propagation model in this chapter and extended to 3D in the next.

The propagation modelling capabilities of the VEFIE are investigated for the frequency and time domains. It is also shown how the VEFIE can compute angle of arrival information. The VEFIE is compared against popular empirical models where it shows a high level of accuracy and can produce more detail. It is compared against ray tracing too where it is shown it produces good predictions considerably faster. Lastly, the computational complexities and convergence properties of the iterative solvers, reduced operator and block Jacobi preconditioner described in Chapter 4 are examined. It is shown that the BiCGSTAB method accelerated with the reduced operator and preconditioner is the most efficient approach to solve the VEFIE.

Chapter 6

3D volume integral equation for indoor propagation

6.1 Introduction

The 2D Volume Electric Field Integral Equation (VEFIE) was examined in Chapter 5 for indoor propagation modelling, in this chapter the 3D VEFIE is investigated. A discretised form of the 3D VEFIE derived in Chapter 3 is solved using the BiCGSTAB method enhanced with the Fast Fourier Transform (FFT) and reduced operator. The 3D VEFIE is validated against the Mie series for scattering from a dielectric sphere before it is compared against measurements for a realistic indoor propagation environment. A comparison between ray tracing based on Geometrical Optics (GO) against the 3D VEFIE is presented.

6.2 3D volume integral equation

A propagation model based on the 3D VEFIE solves Maxwell's equations in a numerically exact fashion[1]. Therefore, it should be able to provide the high level of accuracy being sought after and required for next generation communications technology. The 2D VEFIE has been shown to be a good method for indoor propagation modelling in Chapter 5. However, its accuracy is limited because of its 2D nature but due to the efficiency it can be solved with its extension to three dimensions is a logical approach for improving accuracy. For these reasons, the 3D VEFIE is used here for indoor propagation modelling.

[1] By numerically exact it is meant that the only errors introduced are those introduced by the discretisation process and tolerance level used in the iterative solver.

The 3D VEFIE is derived from Maxwell's equations by applying the volumetric equivalence principle. It can be written as (3.54)

$$\mathbf{E}(\mathbf{r}) = \mathbf{E}^i(\mathbf{r}) + k_0^2 \left(1 + \frac{1}{k_0^2}\nabla\nabla\cdot\right) \int_V G(\mathbf{r},\mathbf{r}')\chi(\mathbf{r}')\mathbf{E}(\mathbf{r}')d\mathbf{r}'$$

Its derivation is presented in Section 3.2. A weak-form discretisation is applied to the 3D VEFIE because it weakens the effect of the singularity present in the integral. Its application is demonstrated in Section 3.4.1 along with the method of moments (MoM). The MoM results in a matrix equation of $3N$ linearly independent simultaneous equations that can be solved to predict the electric field throughout the environment to which it has been applied to. The resultant matrix equation has the form (3.95)

$$\mathbf{V} = \mathbf{Ze}$$

where $\mathbf{Z}$ is (3.96)

$$\mathbf{Z} = \mathbf{I} - k_0^2\Delta v\mathbf{GD} - \Delta v\mathbf{HGD}$$

Similarly to the 2D VEFIE, the matrix equation resulting from the discretised 3D VEFIE can be solved by direct matrix inversion but this is prohibitive due to the large memory requirements of the VEFIE. The system matrix of the VEFIE is of size $3N \times 3N$ where N the size of the problem is given by $N = N_xN_yN_z$ where N_x is the number of discretisations in the x direction and similarly for N_y and N_z. The factor of 3 is due to the need to independently compute the x, y and z components of the electric field, whereas in 2D only a single component is needed. Thus, the discretised form of the 3D VEFIE is solved with an iterative technique, namely the BiCGSTAB method. The FFT and reduced operator are used to speed up its solution. The Toeplitz nature of $\mathbf{G}$ requires only 1 row or column to be stored, $\mathbf{D}$ can be stored as a single vector because it is a diagonal matrix and $\mathbf{H}$ can be implemented within the solver as a function of $\mathcal{O}(N)$ complexity. These benefits reduce the storage requirements of $\mathbf{Z}$ from $\mathcal{O}(N^2)$ to $\mathcal{O}(N)$ and the cost of multiplying $\mathbf{Z}$ with $\mathbf{e}$ from $\mathcal{O}(N^2)$ to $\mathcal{O}(N\log N)$ using the FFT.

6.2.1 Validation against Mie series

The analytical Mie series is employed to validate the 3D VEFIE before it is applied to indoor propagation problems. The Mie series theory is described by Stratton and

Bohren et al. in [222], [223]. The Mie series computes the electric field at any point interior or exterior to a dielectric sphere illuminated by a plane wave. To validate the VEFIE, consider a homogeneous dielectric 3D sphere in free space irradiated by an impinging plane wave propagating in the z direction as shown in Figure 6.1. The sphere has radius a and is characterised by its permittivity, permeability and conductivity, ϵ, μ and σ respectively. The total field at a point exterior to the sphere in free space can be expressed as

$$\mathbf{E}^t(\mathbf{r}) = \mathbf{E}^i(\mathbf{r}) + \mathbf{E}^s(\mathbf{r}) \tag{6.1}$$

The incident field is formulated as

$$\mathbf{E}^i(\mathbf{r}) = \sum_{n=1}^{\infty} \jmath^n \frac{2n+1}{n(n+1)} \left(\mathbf{m}_{o1n}^{(1)} - \jmath \mathbf{n}_{e1n}^{(1)} \right) \tag{6.2}$$

where $\mathbf{m}_{o1n}^{(1)}$ and $\mathbf{n}_{e1n}^{(1)}$ are given by

$$\begin{aligned} \mathbf{m}_{o1n}^{(1)} &= \frac{1}{\sin\theta} \cos\phi P_n^1(\cos\theta) J_n(\rho)\ \hat{\theta} \\ &\quad - \sin\phi \frac{dP_n^1(\cos\theta)}{d\theta} J_n(\rho)\ \hat{\phi} \end{aligned} \tag{6.3}$$

$$\begin{aligned} \mathbf{n}_{e1n}^{(1)} &= \frac{J_n(\rho)}{\rho} \cos\phi n(n+1) P_n^1(\cos\theta)\ \hat{r} \\ &\quad + \cos\phi \frac{\partial P_n^1(\cos\theta)}{\partial\theta} \frac{1}{\rho} \frac{d}{d\rho} \left[\rho J_n(\rho)\right]\ \hat{\theta} \\ &\quad - \sin\phi \frac{P_n^1(\cos\theta)}{\sin\theta} \frac{1}{\rho} \frac{d}{d\rho} \left[\rho J_n(\rho)\right]\ \hat{\phi} \end{aligned} \tag{6.4}$$

where $J_n()$ is the spherical Bessel function of the first kind of order n. $\rho = k_0 r$ and r is the distance from the centre of the sphere to the point the fields are being evaluated at. $P_n^1()$ represents the Legendre function of degree n and order 1. $\hat{r}$, $\hat{\theta}$ and $\hat{\phi}$ are unit vectors in the direction of increasing r, θ and ϕ. The scattered field external to the sphere is given by

$$\mathbf{E}^s(\mathbf{r}) = \sum_{n=1}^{\infty} \jmath^n \frac{2n+1}{n(n+1)} \left(\jmath a_n \mathbf{n}_{e1n}^{(3)} - b_n \mathbf{m}_{o1n}^{(3)} \right) \tag{6.5}$$

where $\mathbf{m}_{o1n}^{(3)}$ and $\mathbf{n}_{e1n}^{(3)}$ are obtained by replacing the spherical Bessel function in (6.3) and (6.4) with the spherical Hankel function of the first kind, $H_n^{(1)}()$ and order n. a_n

and b_n are given by

$$a_n = \frac{\mu_0 v^2 J_n(vx)[xJ_n(x)]' - \mu_d J_n(x)[vxJ_n(vx)]'}{\mu_0 v^2 J_n(vx)[xH_n^{(1)}(x)]' - \mu_d H_n^{(1)}(x)[vxJ_n(vx)]'} \tag{6.6}$$

$$b_n = \frac{\mu_d J_n(vx)[xJ_n(x)]' - \mu_0 J_n(x)[vxJ_n(vx)]'}{\mu_d J_n(vx)[xH_n^{(1)}(x)]' - \mu_0 H_n^{(1)}(x)[vxJ_n(vx)]'} \tag{6.7}$$

where $v = \frac{k_d}{k_0}$ and $x = k_0 a$. $'$ denotes differentiation with respect to the argument of the Bessel or Hankel function. The total field internal to the sphere is given by

$$\mathbf{E}^t(\mathbf{r}) = \sum_{n=1}^{\infty} \jmath^n \frac{2n+1}{n(n+1)} \left(c_n \mathbf{m}_{o1n}^{(1)} - \jmath d_n \mathbf{n}_{e1n}^{(1)} \right) \tag{6.8}$$

where c_n and d_n are given by

$$c_n = \frac{\mu_d J_n(x)[xH_n^{(1)}(x)]' - \mu_d H_n^{(1)}(x)[xJ_n(x)]'}{\mu_d J_n(vx)[xH_n^{(1)}(x)]' - \mu_0 H_n^{(1)}(x)[vxJ_n(vx)]'} \tag{6.9}$$

$$d_n = \frac{\mu_d v J_n(x)[xH_n^{(1)}(x)]' - \mu_d v H_n^{(1)}(x)[xJ_n(x)]'}{\mu_d v^2 J_n(vx)[xH_n^{(1)}(x)]' - \mu_d H_n^{(1)}(x)[vxJ_n(vx)]'} \tag{6.10}$$

The Mie series and VEFIE are compared for a 3D sphere of radius $a = 0.5$m, with $\epsilon_r = 4$, $\mu_r = 1$ and $\sigma = 0.01$ at 700MHz. The VEFIE discretises a 2m $\times$ 2m $\times$ 2m region centred around the sphere at a rate of $\frac{\lambda}{20}$ leading to $N = 804,357$ unknowns to be computed. The discretisation rate of $\frac{\lambda}{20}$ is used to accurately capture the curvature of the sphere because pulse basis functions are used in the discretisation process which results in a structure like that shown in Figure 3.4 and also to reduce numerical inaccuracies so an accurate validation can be performed. The infinite Mie series is truncated to 200 terms. The total electric field at a point external to the sphere is computed by the VEFIE and Mie series. A very good agreement is achieved between both the real and imaginary parts of the x, y and z components shown in Figure 6.2.

6.3 Numerical results

The indoor propagation modelling capabilities of the 3D VEFIE are examined here. The 3D VEFIE is compared against measurements and the 2D VEFIE. Some results comparing the 3D VEFIE against a 3D ray tracing model are presented also.

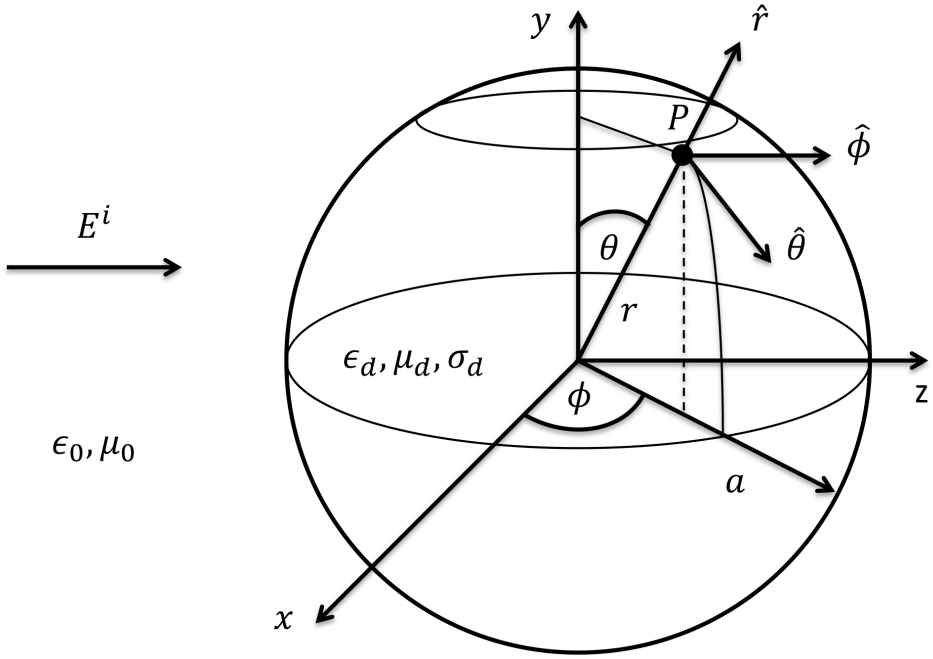

Figure 6.1: Incident plane wave impinging dielectric sphere for Mie series problem.

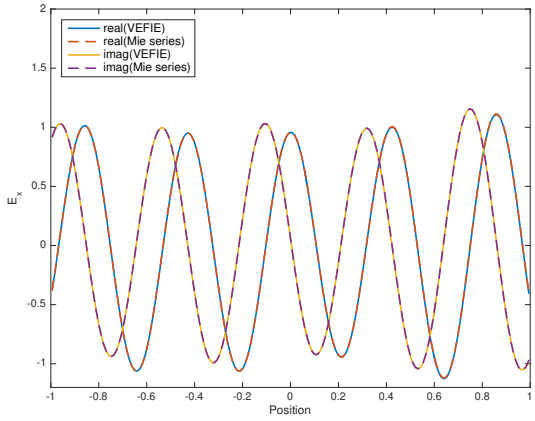

(a) Comparison of x component.

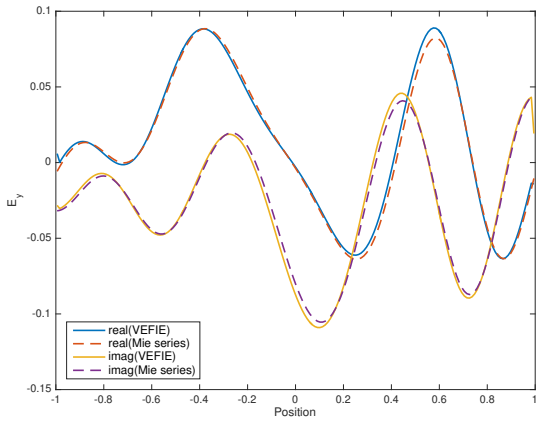

(b) Comparison of y component.

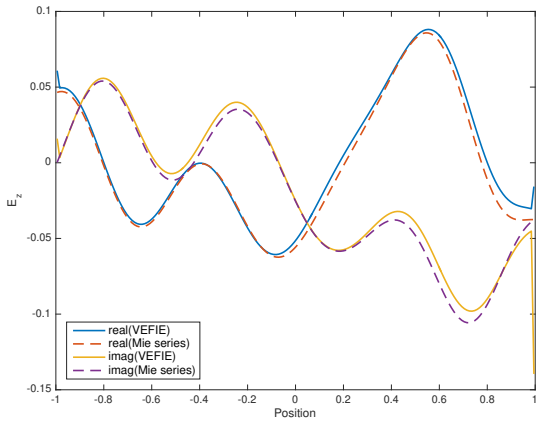

(c) Comparison of z component.

Figure 6.2: Comparison of real and imaginary components of VEFIE and Mie series for the problem in Figure 6.1.

6.3.1 Indoor propagation modelling

The 2D VEFIE has been shown to be an efficient method for indoor propagation modelling in Section 5.3. However, the 2D VEFIE is not able to accurately predict the received power of an indoor wireless communications system. A large mean error arises between the 2D VEFIE and measurement results because it is difficult to match the transmitted power when the transmit antennas are not the same. The power in the 2D VEFIE also decays as $\frac{1}{R}$, whereas in reality (for the measurements) and in the 3D VEFIE it decays as $\frac{1}{R^2}$ where R represents the distance from the transmitter. This is another source of error in the 2D VEFIE results that can be alleviated by using a full 3D model. The 3D VEFIE is compared against the 2D VEFIE and measurements here.

To recap, received power measurements were taken in the 6.95m $\times$ 8.2m $\times$ 2.95m portion of the house depicted in Figure 6.3. The floors in the house are wood, stone and tile and the ceiling is a thin layer of plaster throughout. The electrical parameters used for the materials are shown in Table 6.1. Small objects in the house have been neglected in the model but are implicitly present in the measurement environment. The discrepancies between the model and measurement environment will introduce a source of error in the results.

Table 6.1: Parameters used to characterise the materials for the house in Figure 6.3.

Material	ϵ_r	μ_r	σ
Concrete	4.4	1	0.01
Glass	4.8	1	0
Wood	2.2	1	0
Stone	4.0	1	0.1
Tile	12	1	0
Plaster	2.5	1	0

The 3D VEFIE is applied to this problem and the received power is computed throughout the environment. This can be seen in Figure 6.4. The incident field is produced by a vertically oriented Hertzian dipole radiating at 915MHz, which matches the transmit antenna used in the measurement campaign. The 3D VEFIE is discretised at a rate of $\frac{\lambda}{10}$ which produces 4,865,133 unknowns but because the $\nabla\nabla\cdot$ operator in (3.54) is computed with a central difference the problem domain must be padded with a layer of free space unknowns, which increases the size of the problem to 5,058,735,

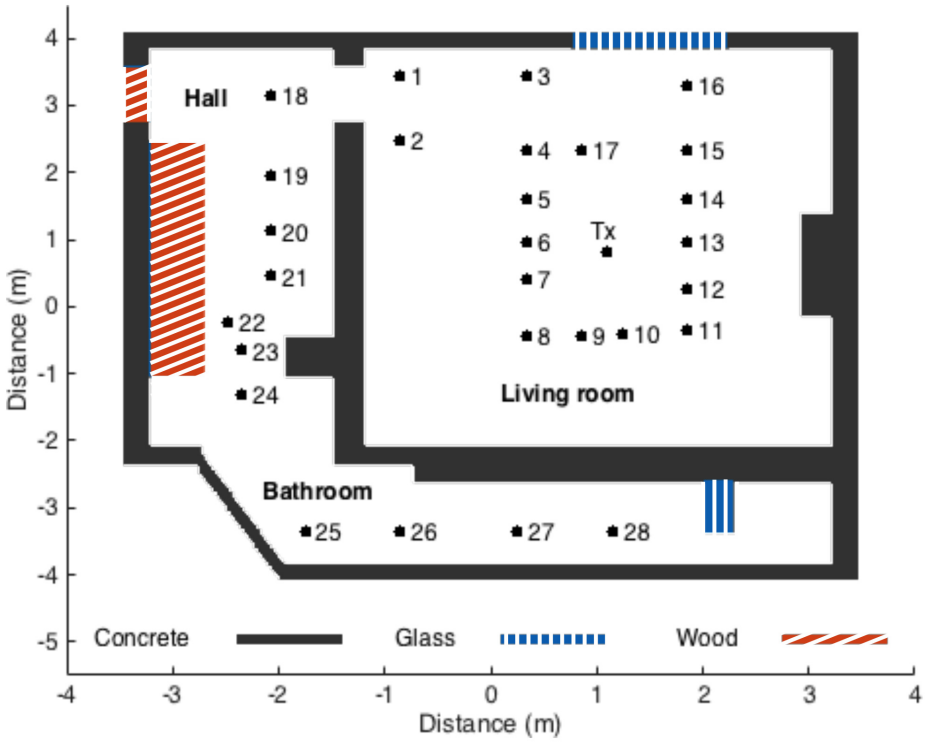

Figure 6.3: 2D depiction of a single storey portion of a house. Received power measurements were taken at the 28 receiver locations shown. The transmitter was kept constant throughout the measurement campaign.

an increase of 193,602 unknowns to be computed. It takes 19 hours and 28 minutes to solve the 3D VEFIE to an error tolerance of 10^{-3}.

The 3D VEFIE is compared against measurements in Figure 6.5 to validate it for indoor propagation modelling. The VEFIE results are averaged over a $\lambda \times \lambda$ box centred on the receiver location. We can see there is a very good agreement between the 3D VEFIE and measurements for both the received power and path loss comparison. The 3D VEFIE is able to predict the received power very accurately without any corrections whereas the 2D VEFIE is not. The discrepancies between the 3D VEFIE and measurements are likely due to errors introduced due to the numerical solution and the differences between the actual propagation environment and the simulated propagation environment. Both the 3D and 2D VEFIE are able to capture the path loss characteristics of the environment very well without any corrections being applied as shown in Figure 6.5b. The runtime, RMS error and standard deviation of the VEFIEs against measurements is shown in Table 6.2. It can be seen that the 3D VEFIE is more accurate than the 2D VEFIE but at the expense of a significant increase in runtime. These results form the basis for the development of the 2D to 3D models in Chapter 7 which attempt to utilise the efficiency of the 2D VEFIE to develop a full 3D model that can achieve an accuracy closer to the 3D VEFIE.

Table 6.2: Root mean square (RMS) error and standard deviation of the VEFIE compared with measurements.

		Received power		**Path loss**	
Model	**Runtime**	**RMS Error**	**Std. Dev.**	**RMS Error**	**Std. Dev.**
3D VEFIE	19.5hrs	3.68 dB	3.67 dB	3.11 dB	3.67 dB
2D VEFIE	4.63s	28.25 dB	4.65 dB	4.96 dB	4.65 dB

6.3.2 Statistical and empirical model analysis

The most common empirical path loss model for indoor propagation is described and parameterised in Section 5.3.1.3 with the 2D VEFIE. The parameterised values using both the 3D VEFIE and 2D VEFIE are shown in Table 6.3. The only significant difference between the 2D VEFIE and the 3D VEFIE is for n where the 3D VEFIE fits a value of 4.1747 but the 2D VEFIE fits 2.1951. This difference is likely due to the data from the full 3D environment being used instead of a single 2D plane. It could also be

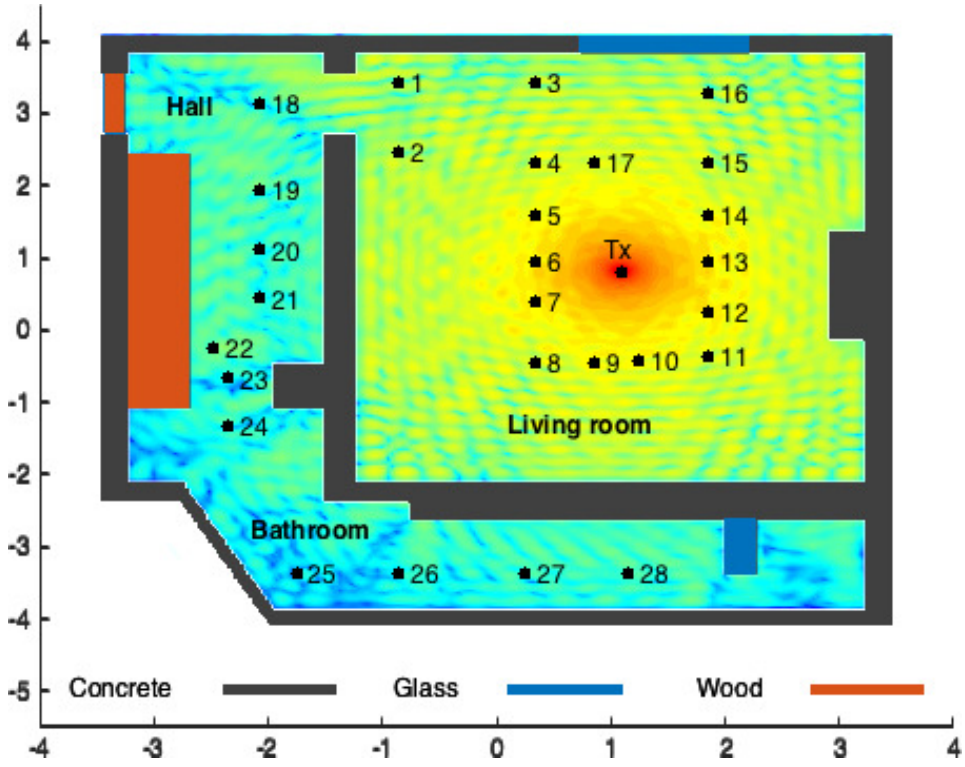

Figure 6.4: Received power for the house shown in Figure 6.3 computed by the VEFIE.

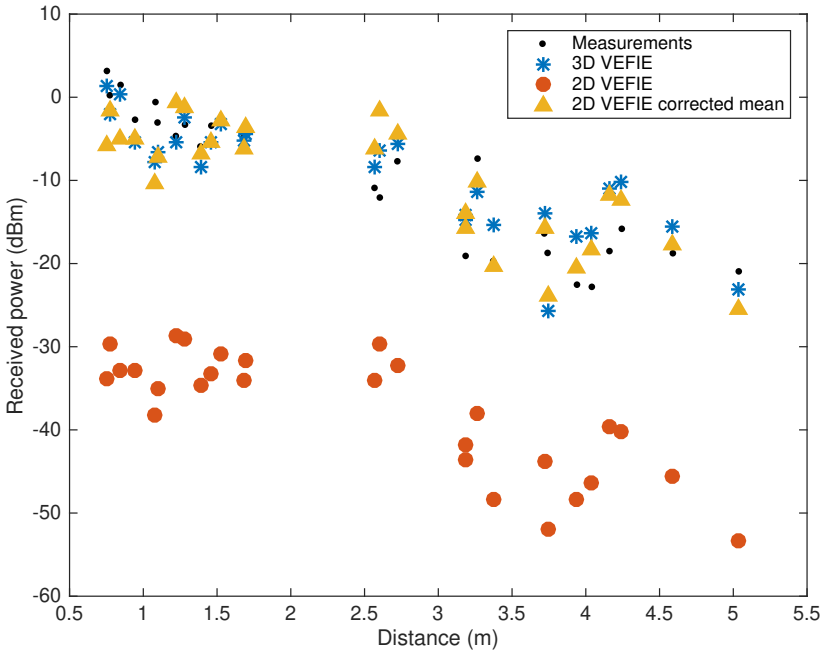

(a) Received power.

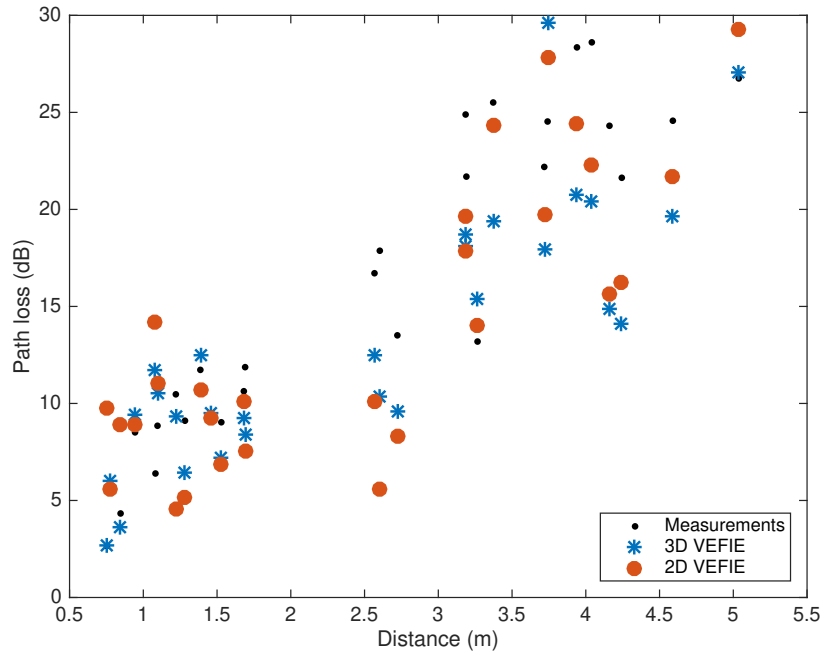

(b) Path loss.

Figure 6.5: Comparison of the VEFIE and measurements taken at the receiver locations shown in Figure 6.3.

caused by the difference in decay of the power in the 3D and 2D VEFIEs, $\frac{1}{R^2}$ versus $\frac{1}{R}$. Along with Figures 5.11 and 6.6 and Table 6.4 it shows that, although the 3D VEFIE is well able to model received power and path loss at a point, characterising empirical models is better done by the 2D VEFIE, at least for this scenario. This analysis points towards some of the main issues with statistical and empirical models, the difficulty in characterising them and their lack of a basis on the underlying physics of the problem.

Table 6.3: Parameterised values of log-normal shadowing path loss model.

		X_σ	
Model	n	**Mean**	**Std. Dev.**
3D VEFIE	4.1747	0.3174	6.6598
2D VEFIE	2.1951	0.4298	5.4177

Table 6.4: RMS error and standard deviation of the VEFIE and extracted path loss models compared with measurements. The mean path loss models are computed with the corresponding parameters from Table 6.4.

	Path loss		**Mean path loss**	
Model	**RMS Error**	**Std. Dev.**	**RMS Error**	**Std. Dev.**
3D VEFIE	3.11 dB	3.67 dB	6.25 dB	4.53 dB
2D VEFIE	4.96 dB	4.65 dB	3.91 dB	3.38 dB

In Section 5.3.1.3 the 2D VEFIE is compared against the dual slope model, COST 231 multi-wall model and the adjusted Motley-Keenan model. The empirical models are compared against the 2D and 3D VEFIEs in Figure 6.7 and Table 6.5 where it can be seen that the 3D VEFIE provides a high degree of accuracy. It produces a lower RMS error and standard deviation than all of the models except the COST 231 multi-wall model as well as being able to track the fading of the measurements.

6.3.3 Comparison against ray tracing

Ray tracing is the most common deterministic model for indoor propagation. It is based primarily on GO. GO defines the electromagnetic interactions for reflections

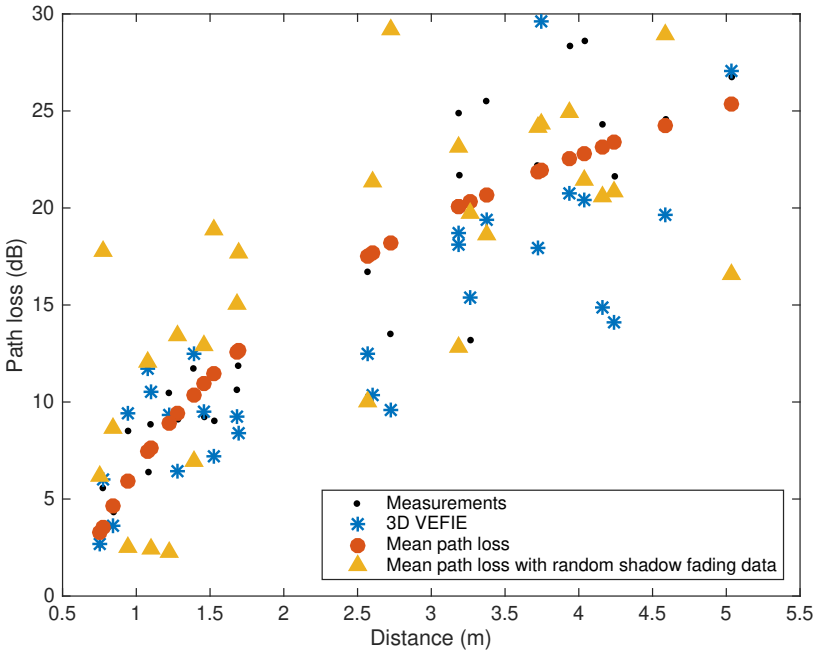

Figure 6.6: Comparison of the 3D VEFIE and extracted path loss models against measurements.

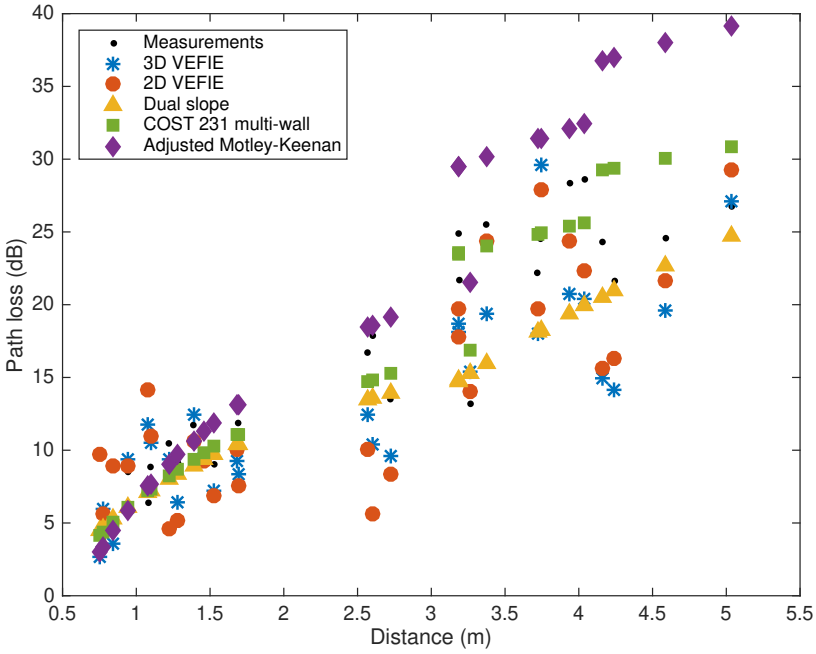

Figure 6.7: Comparison of the VEFIE and popular empirical models against measurements.

Table 6.5: Root mean square (RMS) error and standard deviation of the VEFIE and popular empirical models compared with measurements.

Model	**RMS Error**	**Std. Dev.**
3D VEFIE	3.11 dB	3.67 dB
2D VEFIE	4.96 dB	4.65 dB
Dual slope	4.39 dB	3.51 dB
COST 231 multi-wall	2.81 dB	2.82 dB
Adjusted Motley-Keenan	6.37 dB	5.01 dB

and transmissions. Here the 3D VEFIE is compared against GO before being compared against a full 3D ray tracing model that considers up to 3rd order reflections and transmissions only.

Figure 6.8 details a comparison of GO and the 3D VEFIE. A concrete like slab of size 2.5m $\times$ 5m $\times$ 2m is positioned in a free space region of size 5m $\times$ 5m $\times$ 2m. It has $\epsilon_r = 4$, $\mu_r = 1$ and $\sigma = 0.04$. A dipole radiating at 700MHz is positioned at (-2, 0). A good agreement is observed between GO and the 3D VEFIE in Figures 6.9 and 6.10. The models do not agree close to the edges of the slab where diffraction effects are present but further away from the edges, particularly in Figure 6.10, a very good agreement is observed between GO and the 3D VEFIE. This lays the basis for a full comparison between the 3D VEFIE and the 3D ray tracing model. The VEFIE based methods, unlike ray tracing, do not consider the incident and reflection shadow boundaries differently to any other region, thus, there is no specific requirement to analyse the VEFIEs accuracy for these reasons. A comparison between the 2D VEFIE and UTD is presented in Section 5.3.2.

The 2D VEFIE is compared against a 3D ray tracing model in Section 5.3.2. The results demonstrate that both models require their mean power to be corrected against the measurements in order to accurately predict the received power but they are capable of accurately predicting path loss within the building without a correction. The 2D VEFIE is significantly quicker than the 3D ray tracing model but it is less accurate. In Figure 6.11 and Table 6.6 the 3D VEFIE is compared against the 2D VEFIE and ray tracing for the same problem. The 3D VEFIE is the only model that does not require a correction to be able to accurately predict the received power measurements. It is less accurate than the ray tracing model for path loss prediction based on the RMS and standard deviation error values shown in Table 6.6. All of the models are ex-

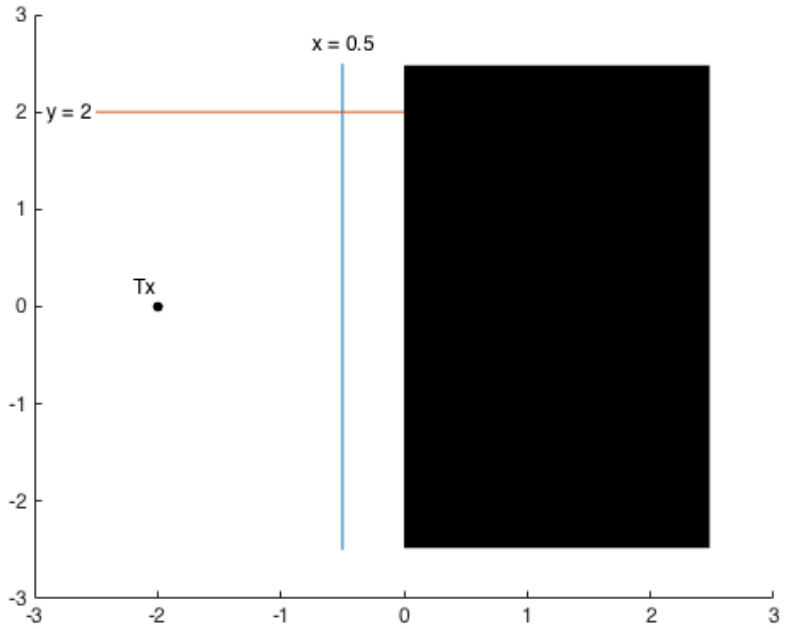

Figure 6.8: Problem scenario to compare reflections computed by the 3D VEFIE and ray tracing. The black slab is of size 2.5m $\times$ 5m $\times$ 2m and is in a free space region of size 5m $\times$ 5m $\times$ 2m. It is characterised by $\epsilon_r = 4$, $\mu_r = 1$ and $\sigma = 0.04$. The coloured x and y lines are used for comparison.

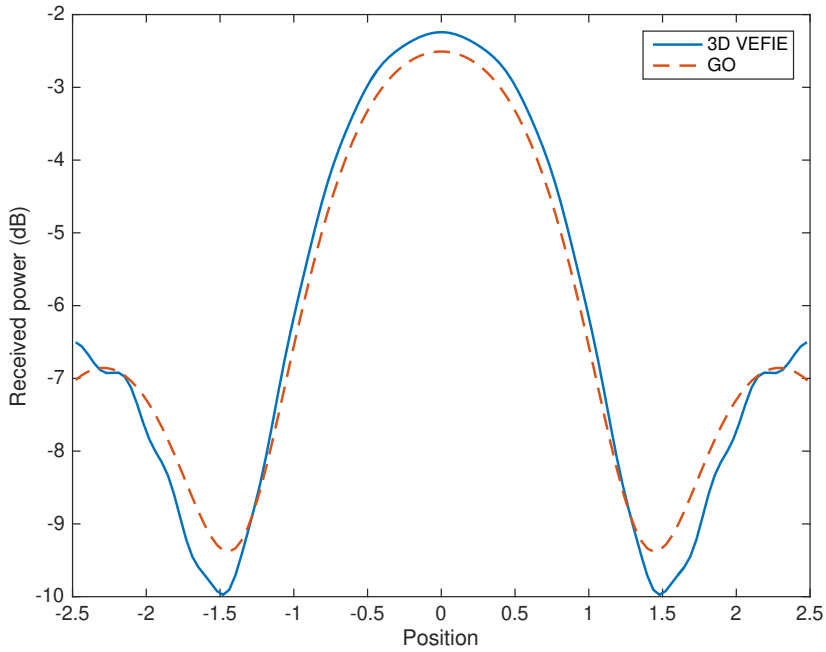

Figure 6.9: Comparison of VEFIE and ray tracing along the line $x = -0.5$ in Figure 6.8.

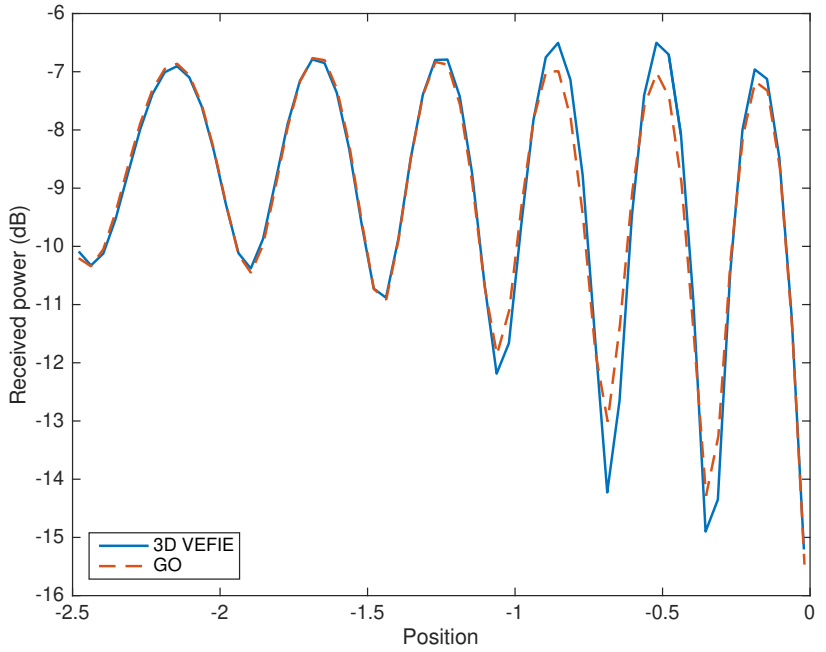

Figure 6.10: Comparison of VEFIE and ray tracing along the line $y = 2$ in Figure 6.8.

ecuted on a laptop with a Core *i*5-5250U CPU and 8GB RAM. The VEFIE models are implemented in MATLAB and make use of its built-in parallelisation whereas the ray tracing model is implemented in C++ without parallelisation. The 2D VEFIE model has 57,200 unknown values to compute, the 3D VEFIE computes 5,058,735 unknown values and the ray tracing model computes the fields at 53,463 receiver locations. The 3D VEFIE is the slowest model despite only being solved to an error tolerance of 0.2 instead of 0.001. The comparison of the received power and path loss in Figure 6.11 and Table 6.6 uses 3D VEFIE results solved to an error tolerance of 0.001, the same as the 2D VEFIE and all of the other results presented in this thesis.

Table 6.6: Runtime, RMS error and standard deviation of the 3D and 2D VEFIEs and ray tracing compared with measurements. The 3D VEFIE is solved to an error tolerance of 0.2, instead of the usual 0.001, to determine its runtime only.

		Received power		**Path loss**	
Model	**Runtime**	**RMS Error**	**Std. Dev.**	**RMS Error**	**Std. Dev.**
3D VEFIE	4305s	3.68 dB	3.67 dB	3.11 dB	3.67 dB
2D VEFIE	6.5s	28.25 dB	4.65 dB	4.96 dB	4.65 dB
Ray tracing	415s	7.85 dB	2.54 dB	2.50 dB	2.54 dB

6.4 Conclusions

The 3D VEFIE is examined here for indoor propagation modelling. The 3D VEFIE is briefly described and validated against the analytical Mie series solution for scattering from a dielectric sphere. The 3D VEFIE is applied to a realistic indoor propagation environment and compared against measurements were it demonstrates a very good agreement. Its ability to characterise a log-normal shadowing empirical propagation model is examined and contrasted with the 2D VEFIE. The 3D VEFIE is compared against other popular empirical models. Lastly, the 3D VEFIE is compared against GO for an idealised problem where a good agreement is achieved before being compared against a full 3D ray tracing model for an indoor propagation problem. The 3D VEFIE can accurately predict received power measurements without any corrections that are required by ray tracing but it is significantly slower than ray tracing. This helps form the basis for the development of the 2D to 3D models in the following

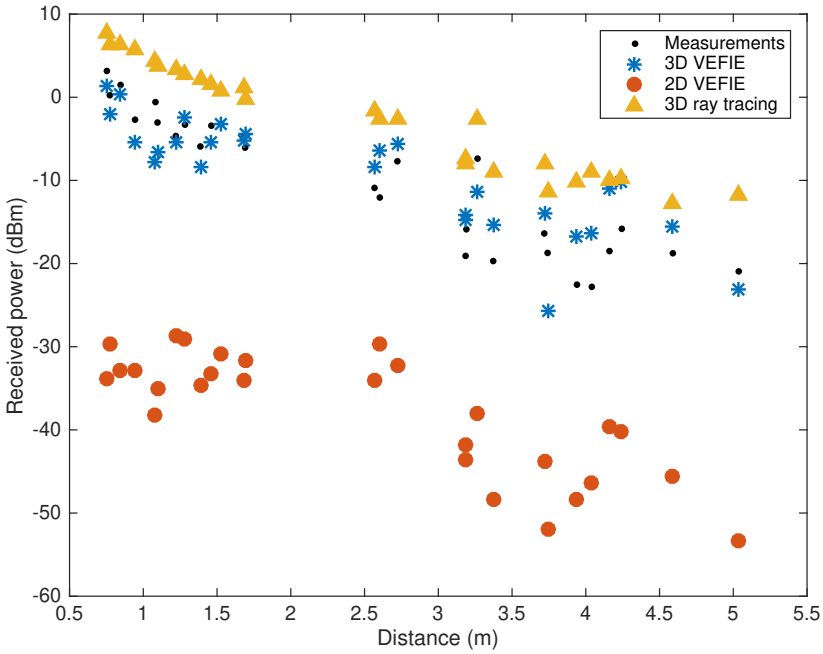

(a) Received power.

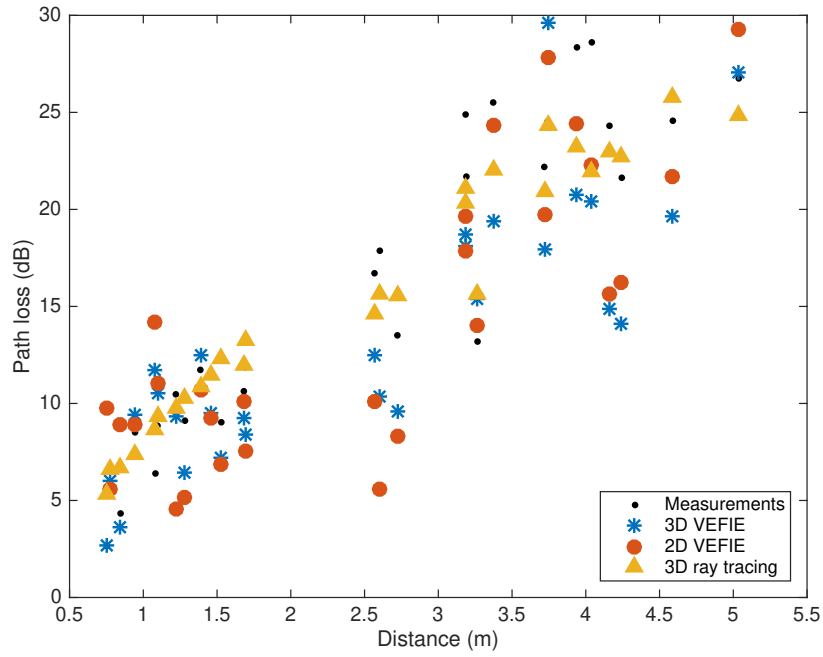

(b) Path loss.

Figure 6.11: Comparison of the 3D and 2D VEFIEs and ray tracing against measurements taken at the receiver locations shown in Figure 6.3.

chapter which aim to be able to provide a similar level of accuracy to the 3D VEFIE but utilising the efficiency of the 2D VEFIE.

Chapter 7

Efficient 2D to 3D VEFIE modelling approaches

7.1 Introduction

In Chapter 5 the 2D Volume Electric Field Integral Equation (VEFIE) is presented for indoor propagation modelling. However, it is difficult for it to make accurate received power predictions without correcting the mean error against measurements for a few reasons. In 2D a different antenna radiation pattern is simulated because power decays as $\frac{1}{R}$ for the 2D VEFIE whereas in reality it decays as $\frac{1}{R^2}$ where R is the distance from the transmitter to the receiver. The 3D VEFIE is used in Chapter 6 to develop a more accurate propagation model. In the 3D VEFIE the modelled antenna radiation pattern is correct and power decays correctly according to $\frac{1}{R^2}$ for both the incident and scattered fields. It is shown that the 3D VEFIE can produce accurate received power predictions without any corrections but it is extremely slow. Moreover, the 2D VEFIE is a much more efficient approach for indoor propagation modelling and if its predictions can be corrected to account for the radiation pattern of the antenna and 3D propagation mechanisms it would prove to be a very useful method for indoor propagation modelling. This leads to the development of efficient models based on 2D VEFIE simulations that are able to produce more accurate 3D propagation predictions than the 2D VEFIE.

The models presented here are called 2D to 3D models and three different approaches are investigated. The 2D to 3D modelling approaches are compared against each other before the most accurate approach is chosen and validated against the 3D VEFIE. This model is then used for indoor propagation modelling where it is compared against measurements in the frequency and time domains. Due to the effi-

ciency of the 2D to 3D modelling approach accurate time domain predictions can be made which are infeasible with the 3D VEFIE due to its long runtime. The 2D to 3D model is shown to be accurate for line of sight (LOS) and non line of sight (NLOS) and compare favourably against empirical and statistical models and ray tracing both in terms of efficiency and accuracy.

7.2 2D to 3D model

The solution of the 3D VEFIE is quite computationally expensive when compared with the 2D formulation for two reasons. Firstly, the solution of the 3D VEFIE requires the computation of three field components, x, y and z, as opposed to the single z component in the 2D transverse magnetic (TM) case. Secondly, assuming that N_x, N_y and N_z are the number of discretisations in the x, y and z-directions respectively, the total number of discretisations required grows as $N_x N_y N_z$ instead of $N_x N_y$ for the two-dimensional problem. This shows that a more computationally efficient approach would be to develop a model based on the 2D VEFIE and correct its solution to account for three-dimensional propagation. Three approaches based on the 2D VEFIE are examined here. The first technique is a simple heuristic correction applied to the solution of the 2D VEFIE. The second method averages the solution of two 2D VEFIE simulations that use the 2D and 3D Green's functions. To derive the 2D VEFIE from the 3D VEFIE the z dimension is assumed to extend from $-\infty$ to $+\infty$. The third 2D to 3D approach removes this approximation and uses a finite integration of the third dimension in the 2D VEFIE.

7.2.1 Heuristic correction method

There are several differences between the 2D and 3D forms of the VEFIE. The main difference as described above is the rate of decay of power. This is present in the both the incident and scattered fields. For instance, the fields produced by a vertical Hertzian dipole in spherical coordinates are given by

$$\mathbf{E}^i(\mathbf{r}) \cong \hat{\boldsymbol{\theta}} \jmath\omega\mu_0 \frac{Il}{4\pi|\mathbf{r}|} e^{-\jmath k_0|\mathbf{r}|} \sin\theta \tag{7.1}$$

where I is the current flowing in the dipole and l is its length. l is commonly $\frac{\lambda}{2}$ or $\frac{\lambda}{4}$ corresponding to a half or quarter-wavelength dipole. (7.1) is the far-field repres-

entation of a Hertzian dipole, it can be used as a good approximation for the fields produced by a Hertzian dipole providing $k_0|\mathbf{r}| \gg 1$ which is kept true for the cases investigated here. In 2D a line source is commonly used which produces fields given by

$$E_z^i(\mathbf{r}) = \frac{1}{4\jmath} H_0^{(2)}(k_0|\mathbf{r}|) \tag{7.2}$$

(7.2) can be expanded using the large argument approximation of the zeroth order Hankel function to give

$$E_z^i(\mathbf{r}) \approx \sqrt{\frac{2\jmath}{\pi k_0|\mathbf{r}|}} e^{-\jmath k_0|\mathbf{r}|} \tag{7.3}$$

The main difference between (7.1) and (7.3) is

$$\sqrt{\frac{1}{|\mathbf{r}|}}$$

this is also present in the difference between the 2D and 3D Green's functions in (3.46) and (3.49),

$$G(\mathbf{r}) = \frac{1}{4\jmath} H_0^{(2)}(k_0|\mathbf{r}|) \approx \frac{1}{4\jmath} \sqrt{\frac{2\jmath}{\pi k_0|\mathbf{r}|}} e^{-\jmath k_0|\mathbf{r}|}$$

$$G(\mathbf{r}) = \frac{e^{-\jmath k_0|\mathbf{r}|}}{4\pi|\mathbf{r}|}$$

respectively, when the zeroth order Hankel function is expanded using its large argument approximation.

$$\sqrt{\frac{2}{\pi k_0}}$$

is also present in the differences between incident and scattered fields. Thus, a partial correction for both fields can be computed by multiplying the solution of the 2D VEFIE (the total field, E_z) by

$$\sqrt{\frac{k_0}{2\pi|\mathbf{r}|}} \tag{7.4}$$

It should be noted that the fields produced by a Hertzian dipole in 3D and a line source in 2D have been examined here but the correction in (7.4) is not specific to the incident fields and is instead specific to the differences between 2D and 3D as shown in the Green's functions. The remaining elements of the heuristic correction model are specific to a Hertzian dipole and line source.

There are several differences between the field representations in (7.1) and (7.3) that have not been accounted for with (7.4). By examining (7.1) and (7.3) it has been found that a reasonable correction for the total field computed by the 2D VEFIE for the plane perpendicular to the centre of axis of the dipole ($\theta = \frac{\pi}{2}$) is given by

$$\frac{\beta}{\sqrt{|\mathbf{r}|}} \tag{7.5}$$

where

$$\beta = \frac{\omega \mu_0 I l}{4} \sqrt{\frac{k_0}{2\pi}} \tag{7.6}$$

The base correction for the solution of the 2D VEFIE is, thus, given by

$$E_z^{(3)}(\mathbf{r}_{x,y,z}) \approx \beta \frac{E_z^{(2)}(\mathbf{r}_{x,y})}{|\mathbf{r}_{x,y,z}|} \tag{7.7}$$

where $E_z^{(3)}(\mathbf{r}_{x,y,z})$ is the z component of the corrected 3D fields, $E_z^{(2)}(\mathbf{r}_{x,y})$ is the solution of the 2D VEFIE assumed to be the plane perpendicular to the centre of axis of the dipole, $\mathbf{r}_{x,y,z}$ is the position in three-dimensional space and $\mathbf{r}_{x,y}$ is the corresponding position in two-dimensional space where z is set equal to the height of the transmitter denoting the fields are computed for the plane $\theta = \frac{\pi}{2}$. The fields for planes where $\theta \neq \frac{\pi}{2}$ can be approximated by splitting the scenarios into those points that have LOS of the transmitter and those that do not (NLOS). For points in LOS, the 3D fields can be approximated by

$$E_z^{(3)}(\mathbf{r}_{x,y,z}) \approx \beta \frac{E_z^{(2)}(\mathbf{r}_{x,y})}{|\mathbf{r}_{x,y,z}|} \sin(\gamma) \tag{7.8}$$

where

$$\gamma = \tan^{-1}\left(\frac{\sqrt{x_a^2 + y_a^2}}{|z_a|}\right) \tag{7.9}$$

and x_a, y_a and z_a are the distances in the x, y and z-directions to the point $\mathbf{r}_{x,y,z}$ from the transmitter. $\sin(\gamma)$ applies a correction based on the radiation pattern of the dipole. It has been found that points in NLOS regions can be better approximated by

$$E_z^{(3)}(\mathbf{r}_{x,y,z}) \approx \alpha + \beta \frac{E_z^{(2)}(\mathbf{r}_{x,y})}{|\mathbf{r}_{x,y,z}|} \sin(\gamma) \tag{7.10}$$

than (7.8) up to a height of 1.5m where α has been experimentally determined as

$$\alpha = \frac{|z_a|}{10} \qquad \text{for } |z_a| \leq 1.5 \tag{7.11}$$

$E_z^{(3)}(\mathbf{r}_{x,y,z})$ is a good approximation for the total field in three dimensions as the dominant component of the field is the z component. Heights greater than 1.5m have not been thoroughly investigated due to the presence of floors and ceilings in typical indoor environments which will have an effect on the scattered field that can't simply be accounted for by the shift given by α. The heuristic correction inherently assumes that the geometry of the propagation environment is invariant in the z dimension. This correction could be extended to analyse multifloor environments by combining 2D simulations in a 2.5D approach similar to those presented in [31], [120].

7.2.2 Average Green's model

Simulating the propagation of electromagnetic fields with the 2D VEFIE instead of the 3D VEFIE introduces errors. The main differences between the two formulations are in the representation of the incident field, the Green's function and the $\nabla\nabla\cdot$ operation. The average Green's model attempts to eliminate some of these potential inaccuracies.

The approximated fields computed by the average Green's model is based on the solution of two 2D simulations and an accurate representation of the incident field in three dimensions. From Chapter 3 the discretised form of the 2D VEFIE is given by (3.76)

$$\mathbf{v} = \mathbf{Ze}$$

where $\mathbf{v}$ is a known vector containing the values of the incident field at the centre of each discretised cell, $\mathbf{e}$ is an unknown vector containing the values of the z component of the electric field at the same locations and $\mathbf{Z}$ is given by (3.77)

$$\mathbf{Z} = \mathbf{I} - \mathbf{GD}$$

$\mathbf{I}$ is the identity matrix, $\mathbf{G}$ represents the 2D Green's function, (3.49), and $\mathbf{D}$ is the contrast (3.55). $\mathbf{G}$ and $\mathbf{D}$ are evaluated at the centres of the discretised cells. In typical 2D VEFIE simulations $\mathbf{v}$ is represented as the fields being produced by a line source which is a 2D source whose power decays as $\frac{1}{R}$. The average Green's model instead

of using a line source to model the incident field uses the fields produced by the correct 3D radiation pattern which for the analysis here will be assumed to be a Hertzian dipole producing fields given by (7.1). The equation for the fields produced by the correct 3D incident field is evaluated for the plane perpendicular to its centre of axis $\theta = \frac{\pi}{2}$, i.e. with $z = 0$, only. The z component of the resultant fields is then subsequently taken and used in the 2D VEFIE simulations as the 2D VEFIE was derived for the TM case. This reduces one source of error in the 2D VEFIE over its 3D counterpart. The other main source of error in the 2D VEFIE over the 3D formulation that the average Green's model attempts to alleviate is in the differing Green's functions.

The average Green's model approximates the total electric field in three dimensions as

$$\mathbf{E}_z^{(3)} = \alpha \mathbf{E}_z^{(2)V} + \beta \mathbf{E}_z^{(2)VG} \tag{7.12}$$

where α and β are constants[1]. $\mathbf{E}_z^{(2)V}$ is the solution of the following 2D VEFIE problem

$$\mathbf{v}^{(3)} = \mathbf{Z}\mathbf{E}_z^{(2)V} \tag{7.13}$$

where $\mathbf{v}^{(3)}$ represents the z component of the fields produced by the 3D antenna evaluated for the plane $z = 0$ as described above. $\mathbf{E}_z^{(2)VG}$ is the solution of the following 2D VEFIE problem

$$\mathbf{v}^{(3)} = \mathbf{Z}^G \mathbf{E}_z^{(2)VG} \tag{7.14}$$

where $\mathbf{Z}^G$ is given by

$$\mathbf{Z}^G = \mathbf{I} - k_0^2 \mathbf{G}^{(3)} \mathbf{D} \tag{7.15}$$

where $\mathbf{G}^{(3)}$ is the 3D Green's function evaluated for points in the plane $z = 0$. $\mathbf{Z}$ in (7.13) is the same as that in the normal 2D VEFIE. Similarly to the heuristic correction, $\mathbf{E}_z^{(3)}$is a good approximation for the total field in three dimensions because the dominant component in three dimensions is the z component.

The average Green's model improves on the standard 2D VEFIE for two main reasons. Firstly, the representation of the incident field is closer to the correct representation. Secondly, the use of the 3D Green's function and averaging applied with the 2D Green's function reduces the error in the scattered field. The solution of (7.13) with the 2D Green's function implicitly assumes the total electric field at all points over the entire z axis from $-\infty$ to $+\infty$ is invariant. This results in an overestimation of the scattered field when compared with the 3D VEFIE. On the other hand, the solution

[1] α and β equal to $\frac{1}{2}$ has been found to produce a good agreement with the 3D VEFIE.

of (7.14) solves the 3D VEFIE assuming the z axis is one cell high which produces an underestimation of the scattered field. The averaging of the two results in (7.12) produces fields that demonstrate a much better agreement with the 3D VEFIE than the standard 2D VEFIE. This can be seen in Figure 7.2 where the solutions of (7.12) to (7.14), ($\mathbf{E}_z^{(3)}$, $\mathbf{E}_z^{(2)V}$, and $\mathbf{E}_z^{(2)VG}$), are compared against the 3D VEFIE for the scenario described by Figure 7.1. (7.12) is called "Average Green's", (7.13) is called "2D Green's" and (7.14) is called "3D Green's" in Figure 7.2.

7.2.3 Finite integration model

The average Green's model attempts to partially correct for the errors introduced in the 2D VEFIE due to the use of the 2D Green's function instead of the 3D formulation. However, it requires two simulations. The finite integration model presented here attempts to produce a model with a similar level of accuracy as the average Green's model but in a single simulation. The 2D Green's function is derived from the 3D Green's function by integrating over the invariant dimension from $-\infty$ to $+\infty$ (in this thesis the z dimension is used). The finite integration model begins with the 2D VEFIE and replaces the 2D Green's function with the 3D Green's function integrated between limits defined by the geometry of the environment, specifically the height of the environment. As with the average Green's model, the incident field used in the simulation for the finite integration model is the z component of the radiation pattern of the 3D antenna evaluated for the plane $z = 0$.

The finite integration model begins with the premise that the main error between the 2D and 3D VEFIE is due to the infinite integration in the z axis. Therefore, it builds in a finite integration along the z axis. The finite integration model takes the 2D VEFIE given by (3.56)

$$E_z(\mathbf{r}) = E_z^i(\mathbf{r}) + k_0^2 \int_S G(\mathbf{r}, \mathbf{r}')\chi(\mathbf{r}')E_z(\mathbf{r}')d\mathbf{r}'$$

and replaces the 2D Green's function $G(\mathbf{r}, \mathbf{r}')$ with

$$\int_{h_b}^{h_a} \frac{e^{-\jmath k\sqrt{\rho^2+z^2}}}{4\pi\sqrt{\rho^2+z^2}} dz \tag{7.16}$$

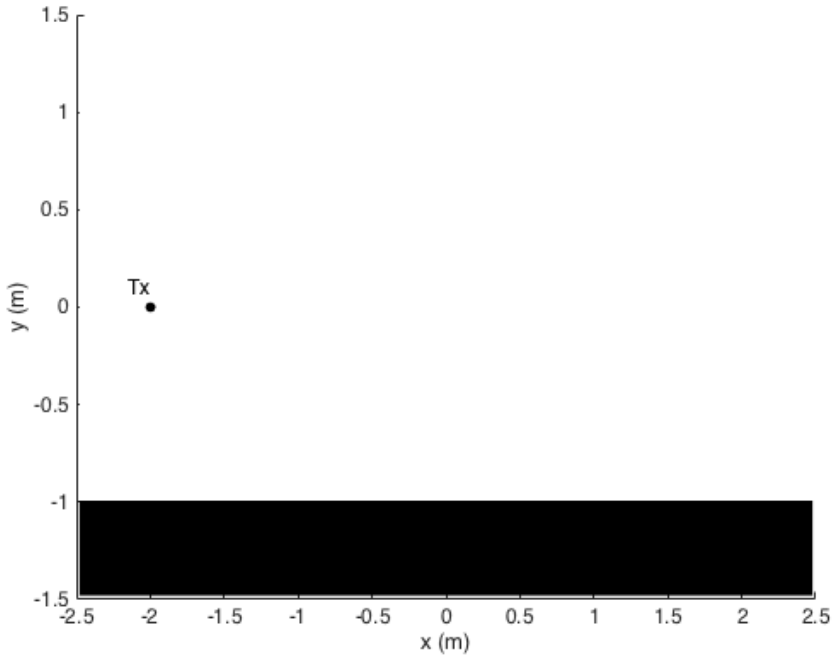

Figure 7.1: Simple slab scenario used to analyse the effect of the 2D and 3D Green's functions in the average Green's model and the accuracy of all of the 2D to 3D models. The scenario consists of a slab of size 5m $\times$ 0.5m $\times$ 2m positioned in a free space region of size 5m $\times$ 3m $\times$ 2m with a dipole radiating at 700MHz placed at (-2, 0, 0). The slab material has a relative permittivity of 4.4 and a conductivity of 0.01.

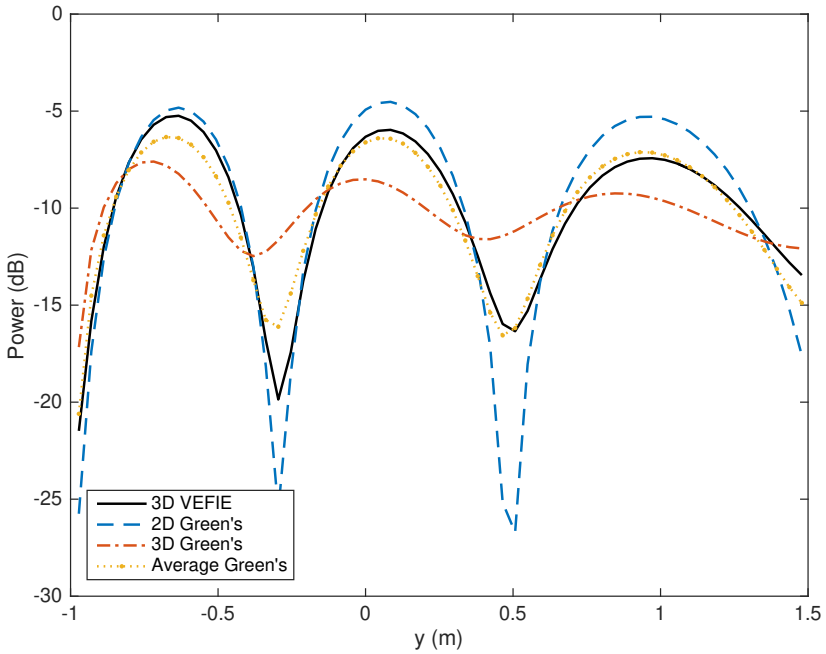

(a) $x = 1$.

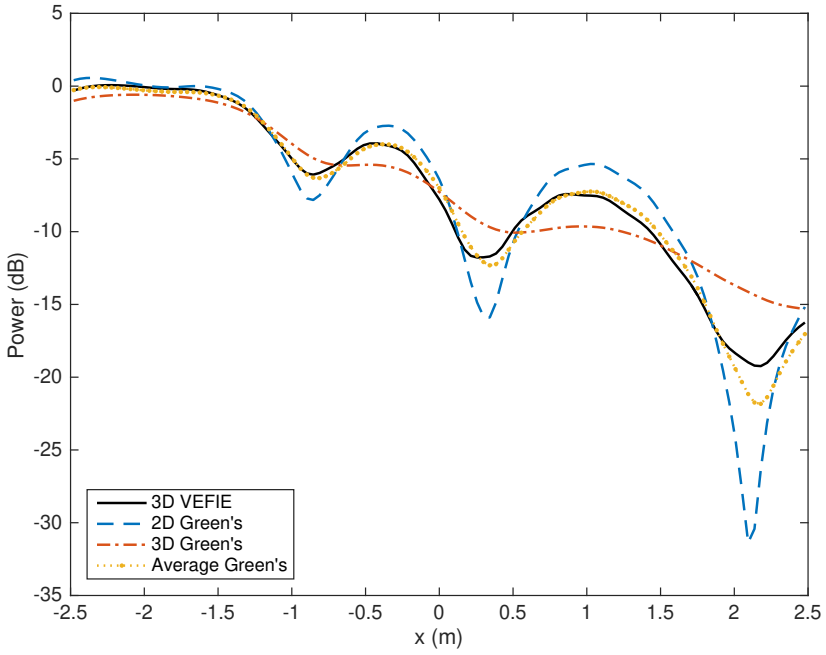

(b) $y = 1$.

Figure 7.2: Comparison showing the overestimation and underestimation effects in the average Green's model.

to give

$$E_z(\mathbf{r}) = E_z^i(\mathbf{r}) + k_0^2 \int_S \left(\int_{h_b}^{h_a} \frac{e^{-jk\sqrt{\rho^2+z^2}}}{4\pi\sqrt{\rho^2+z^2}} dz \right) \chi(\mathbf{r}') E_z(\mathbf{r}') d\mathbf{r}' \tag{7.17}$$

where $z = 0$ is defined as the plane perpendicular to the centre of the 3D antenna and h_a and h_b are the heights above and below this plane in the 3D environment governed by its geometry. $h_b \leq 0$ and $h_a \geq 0$. For example, if the environment being modelled has a height of 2m and the transmitter is located 1m above the bottom surface then $h_a = 1$ and $h_b = -1$. In the finite integration model the geometry of the environment is assumed constant in the z dimension up to the limits h_a and h_b. $\frac{e^{-jk\sqrt{\rho^2+z^2}}}{4\pi\sqrt{\rho^2+z^2}}$ from (7.16) is the 3D Green's function, (3.46), assuming no variance in the geometry in z where $\sqrt{\rho^2+z^2}$ is the distance in three-dimensional space. It can be shown that (7.16) reduces to the 2D Green's function (3.49) if $h_a = \infty$ and $h_b = -\infty$ [145].

7.2.4 Model analysis

The accuracy and runtime of the 2D to 3D models will be analysed against the 3D VEFIE. The heuristic correction, average Green's and finite integration 2D to 3D models are compared against the 3D VEFIE for the slab scenario shown in Figure 7.1. The comparison of the 2D to 3D models and the 3D VEFIE for the slab scenario can be seen in Figure 7.3 where the models are compared for two lines, $x = 1$ and $y = 1$. It is clear from this comparison that the finite integration model is the least accurate. It is more accurate than the 2D VEFIE which can be seen in Table 7.1 where the RMS error and standard deviation of the models is shown. The heuristic correction and average Green's models are more accurate than the finite integration model and 2D VEFIE. They are also quicker than the finite integration model. As the finite integration model has demonstrated the worst performance in terms of runtime and accuracy it will not be analysed further. The remaining scenarios will analyse the heuristic correction and average Green's models only.

The heuristic correction and average Green's models will be compared against the 3D VEFIE for a slightly more complex scenario that contains some NLOS regions shown in Figure 7.4. A comparison of the fields along two lines is shown in Figure 7.5 where it can be seen that the heuristic correction model is slightly more accurate than the average Green's model. This is further demonstrated in Table 7.2 where it can be seen that the heuristic correction model produces a lower RMS error and standard deviation than the average Green's model. It is also slightly faster than the average

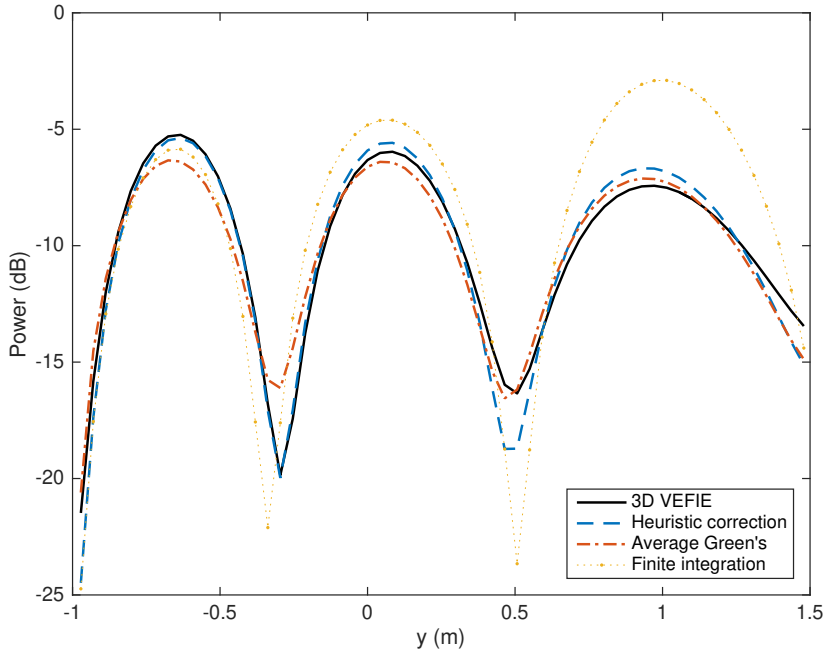

(a) $x = 1$.

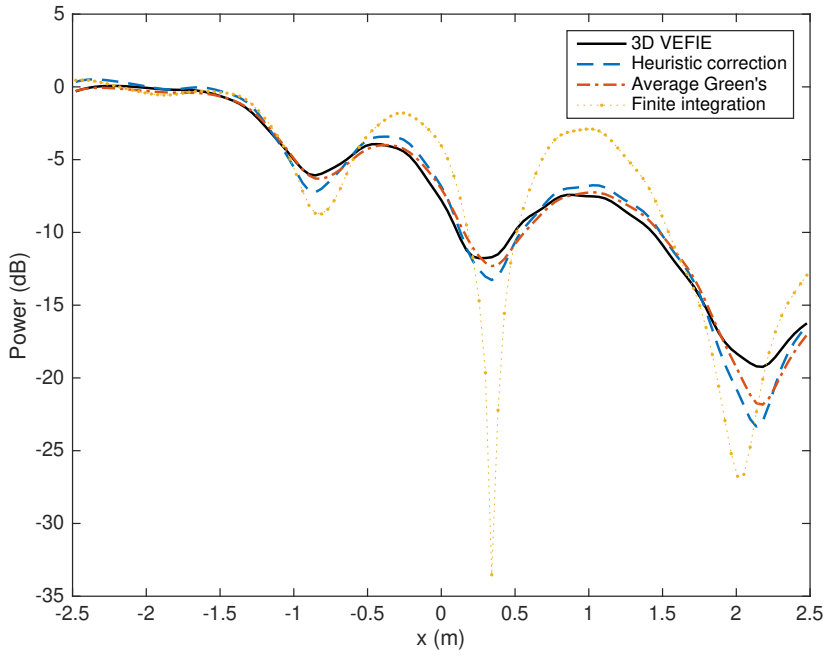

(b) $y = 1$.

Figure 7.3: Comparison of the heuristic correction, average Green's and finite integration 2D to 3D models against the 3D VEFIE for the scenario shown in Figure 7.1.

Table 7.1: Runtime and accuracy of the 2D to 3D models compared against the 2D and 3D VEFIE. The RMS error and standard deviation are calculated for the entire free space region for the scenario in Figure 7.1.

Model	**Runtime**	**RMS Error**	**Std. Dev.**
3D VEFIE	11.62 mins		
2D VEFIE	4.68 secs	11.03 dB	3.27 dB
Heuristic correction	4.68 secs	0.85 dB	0.85 dB
Average Green's	4.83 secs	0.76 dB	0.76 dB
Finite integration	7.38 secs	2.68 dB	2.65 dB

Green's model.

Table 7.2: Runtime and accuracy measurements of the heuristic correction and average Green's 2D to 3D models compared against the 2D and 3D VEFIE. The RMS error and standard deviation are calculated for the entire free space region for the scenario in Figure 7.4.

Model	**Runtime**	**RMS Error**	**Std. Dev.**
3D VEFIE	11.59 mins		
2D VEFIE	5.92 secs	10.71 dB	3.63 dB
Heuristic correction	5.92 secs	1.73 dB	1.73 dB
Average Green's	6.08 secs	2.58 dB	2.58 dB

A realistic building geometry is shown in Figure 7.6 and it is used to further analyse the accuracy of the heuristic correction and average Green's 2D to 3D models. Their comparison can be found in Figure 7.7 and Table 7.3 where again it is found that the heuristic correction model provides a higher level of accuracy and is quicker. The heuristic correction model is simpler to implement too as it requires a single unmodified simulation of the 2D VEFIE whereas the average Green's model requires two simulations where the Green's function is modified in one. Thus, the ability of the heuristic correction 2D to 3D model to be used for propagation modelling will be examined in Sections 7.2.5 and 7.3.

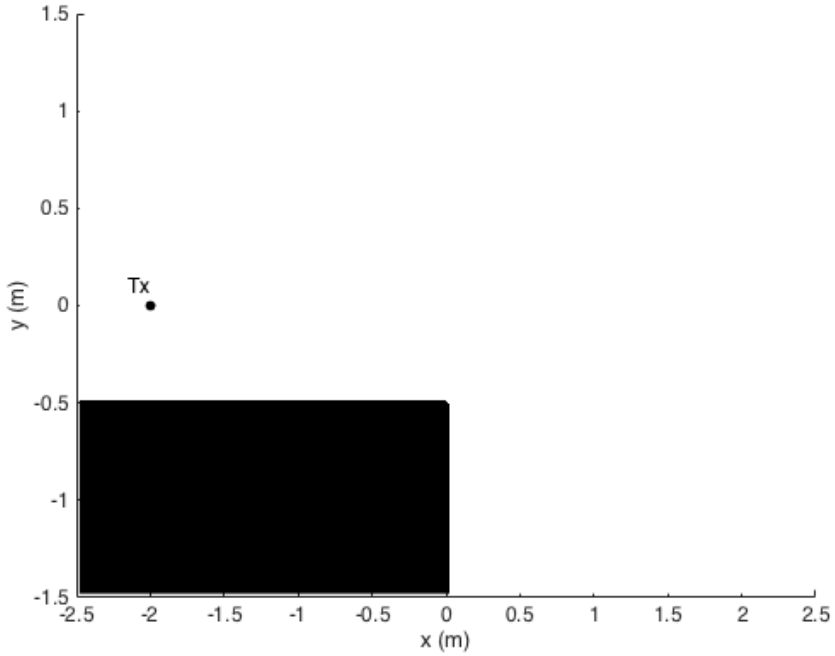

Figure 7.4: Simple block scenario used to analyse the accuracy of the 2D to 3D models. A block of size 2.5m $\times$ 1m $\times$ 2m is positioned in a free space region of size 5m $\times$ 3m $\times$ 2m with a dipole radiating at 700MHz placed at (-2, 0, 0). The block material has a relative permittivity of 4.4 and a conductivity of 0.01.

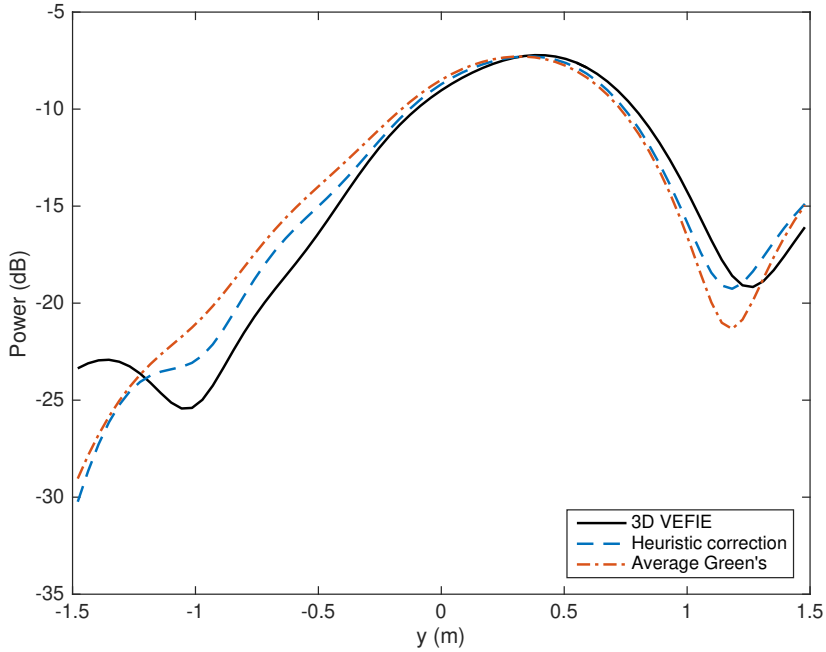

(a) $x = 1.5$.

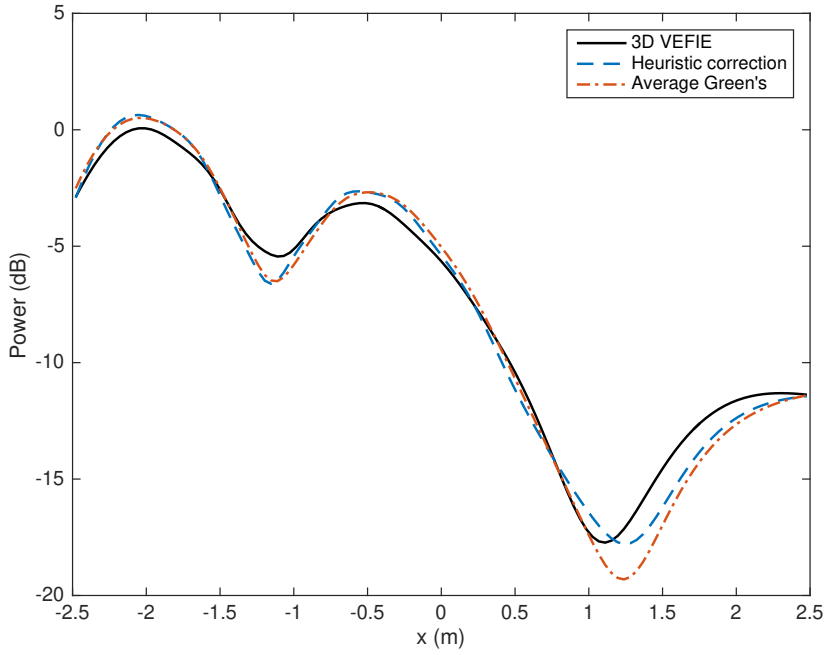

(b) $y = 1$.

Figure 7.5: Comparison of the heuristic correction and average Green's 2D to 3D models against the 3D VEFIE for the scenario shown in Figure 7.4.

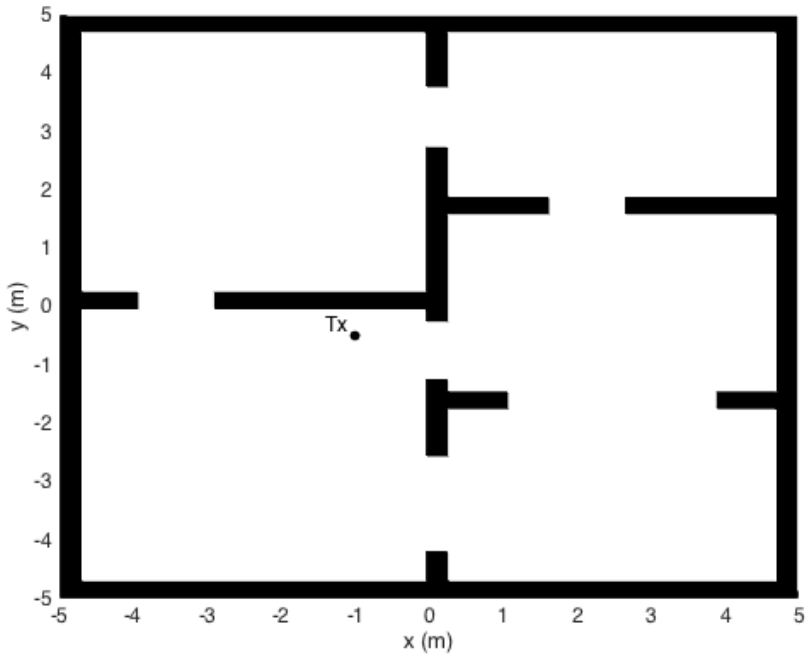

Figure 7.6: Building scenario used to analyse the accuracy of the 2D to 3D models. The building is of size 10m $\times$ 10m $\times$ 3m. A vertical dipole radiating at 700MHz is placed at (-1, -0.5, 0). The building material has a relative permittivity of 4.4 and a conductivity of 0.01.

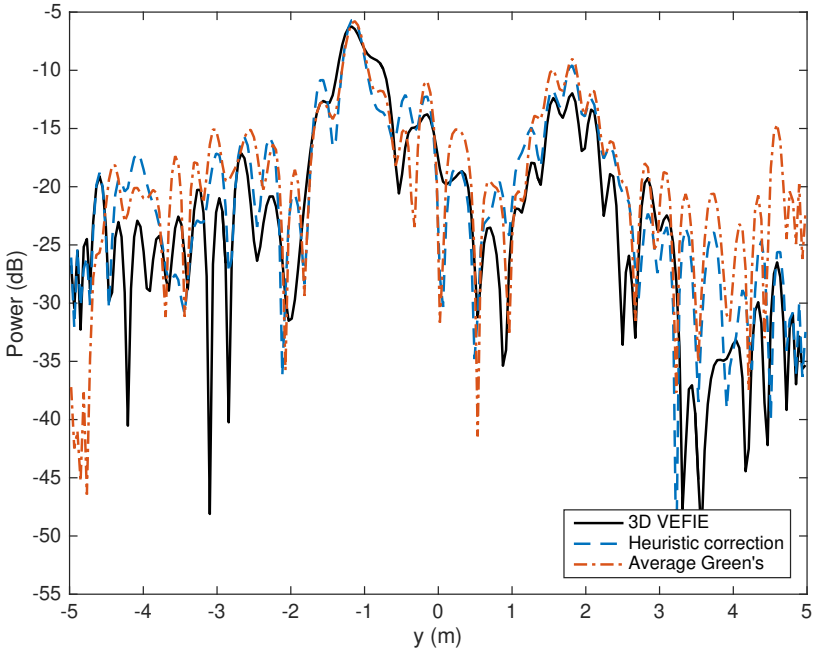

(a) x = 2.5.

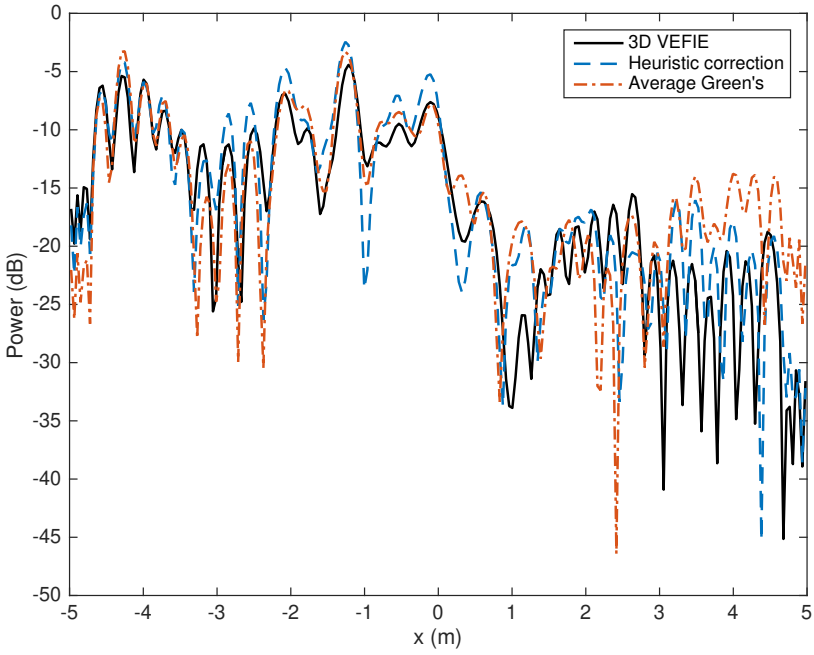

(b) y = -3.5.

Figure 7.7: Comparison of the heuristic and hybrid 2D to 3D models against the 3D VEFIE for the scenario shown in Figure 7.6.

Table 7.3: Runtime and accuracy measurements of the heuristic correction and average Green's 2D to 3D models compared against the 2D and 3D VEFIE. The RMS error and standard deviation are calculated for the entire free space region for the scenario in Figure 7.6.

Model	**Runtime**	**RMS Error**	**Std. Dev.**
3D VEFIE	181.31 mins		
2D VEFIE	68.81 secs	8.26 dB	4.86 dB
Heuristic correction	68.82 secs	4.25 dB	4.10 dB
Average Green's	73.99 secs	5.28 dB	4.93 dB

7.2.5 Further validation of heuristic correction against 3D VEFIE

Consider a cube of size 2m $\times$ 2m $\times$ 2m consisting of a concrete-like material defined by $\epsilon_r = 4$, $\mu_r = 1$ and $\sigma = 0.01$ positioned in free space with its top left edge located at $(-0.5, 1.5)$ and centred in the z-direction, i.e. it extends from $z = -1$ to $z = 1$, as shown in Figure 7.8. The transmitter is located at $(-1.5, 2, 0)$. Figure 7.9 demonstrates a comparison between the 2D to 3D model and the 3D and 2D VEFIE at a frequency of 1.2GHz along the z axis from $z = -1.5$ to $z = 1.5$. The LOS results are located at $(-2, -1, z)$, whilst the NLOS results are for the location $(2, -1, z)$. The RMS error and standard deviation for the results in Figure 7.9 can be found in Table 7.4.

Table 7.4: Averaged accuracy of the 2D to 3D model and 2D VEFIE against the 3D VEFIE for the results in Figure 7.9.

	LOS		**NLOS**	
	RMS Error	**Std. Dev.**	**RMS Error**	**Std. Dev**
2D VEFIE	7.80 dB	2.58 dB	16.66 dB	5.34 dB
2D to 3D	3.06 dB	1.87 dB	2.61 dB	2.60 dB

The 2D to 3D model produces a propagation model that is capable of accurate and efficient predictions in the frequency and time domains. It is valid over a wide frequency range due to its derivation from the full 3D VEFIE. Figure 7.10 and Table 7.5 demonstrate the effectiveness of the 2D to 3D model over a frequency range from 500MHz to 1.5GHz for the same problem described by Figure 7.8. Figure 7.10 compares the 2D to 3D model against the 3D VEFIE and 2D VEFIE at the points $(-2, -1, 0)$, $(2, -1, 0)$, $(-2, -1, -1)$ and $(2, -1, 1)$. The average RMS error and standard deviation

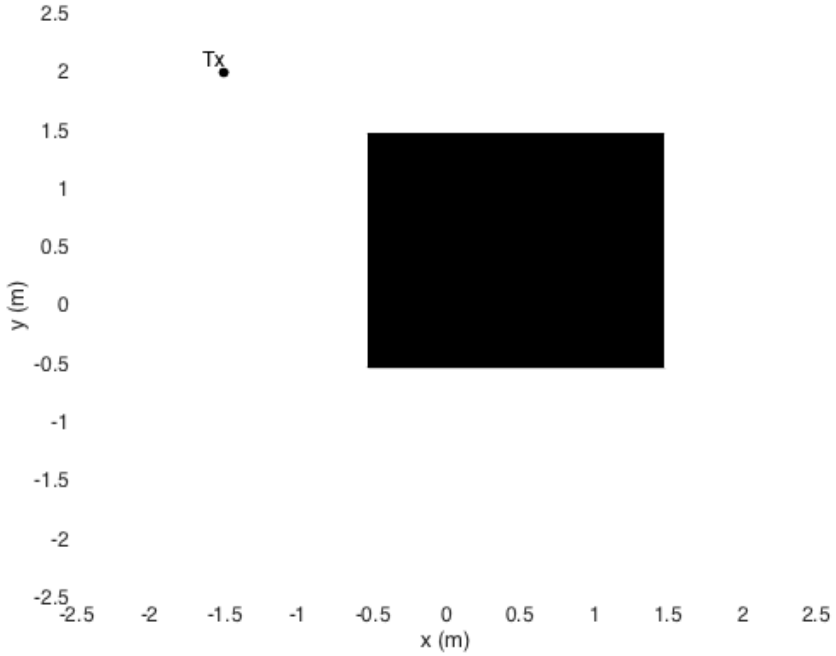

Figure 7.8: Cube scenario used to analyse the accuracy of the heuristic correction 2D to 3D model. A cube of size 2m $\times$ 2m $\times$ 2m is positioned in a free space region of size 5m $\times$ 5m $\times$ 3m with a dipole radiating at 700MHz placed at (-1.5, 2, 0). The cube material has a relative permittivity of 4 and a conductivity of 0.01.

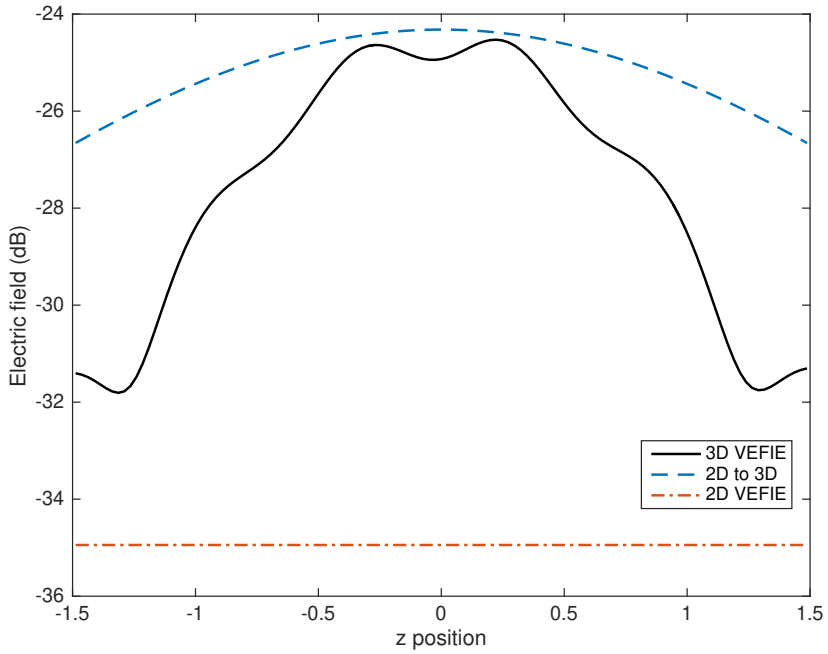

(a) Line of sight.

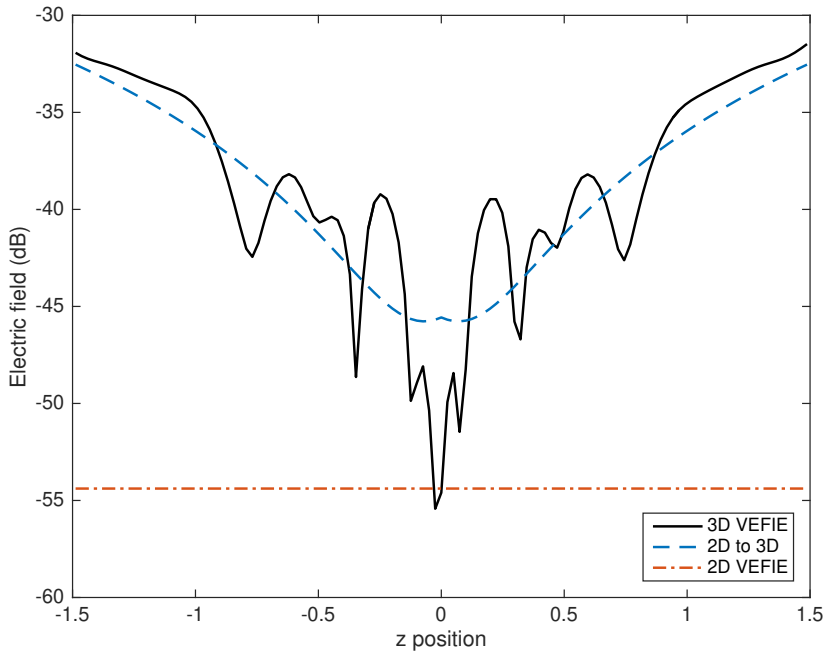

(b) Non line of sight.

Figure 7.9: Comparison of the 2D to 3D model against the 3D and 2D VEFIE. The LOS results are at $(-2, -1, z)$ and the NLOS results are at $(2, -1, z)$.

for all of these results including results at $(-2,-1,1)$ and $(2,-1,-1)$ are shown in Table 7.5. These results include points in LOS, NLOS, points in the same plane as the transmitter and points in a plane $1m$ above and below the transmitter but in each case the 2D to 3D model provides a much better agreement with the 3D VEFIE than the 2D VEFIE.

Table 7.5: Averaged accuracy of the 2D to 3D model and 2D VEFIE against the 3D VEFIE for the results in Figure 7.10 including results at $(-2,-1,1)$ and $(2,-1,-1)$ also.

	LOS		**NLOS**	
	RMS Error	**Std. Dev.**	**RMS Error**	**Std. Dev**
2D VEFIE	9.65 dB	2.95 dB	19.32 dB	5.51 dB
2D to 3D	2.44 dB	2.45 dB	3.14 dB	3.00 dB

7.2.6 2D to 3D model limitations

The 2D to 3D models are limited in the information they can provide as they are based on the 2D VEFIE. The main limitation is that only the z component of the electric field can be computed because TM polarisation is assumed. The heuristic correction in Section 7.2.1 is limited to a dipole but works well for other omni-directional antennas that have a similar radiation pattern to a dipole as shown in Section 7.3.1.3. The average Green's and finite integration models in Sections 7.2.2 and 7.2.3 are only capable of making predictions in a 2D plane perpendicular to the centre of axis of a three-dimensional antenna.

7.3 Results

The heuristic correction 2D to 3D model is compared against the 3D and 2D VEFIEs for indoor propagation problems. The runtime and accuracy of the 2D to 3D model is compared against the 3D and 2D VEFIE for typical environments. It is shown how the 2D to 3D model takes the advantages from the 2D VEFIE and the 3D VEFIE to produce a propagation model capable of making rapid frequency and time domain predictions.

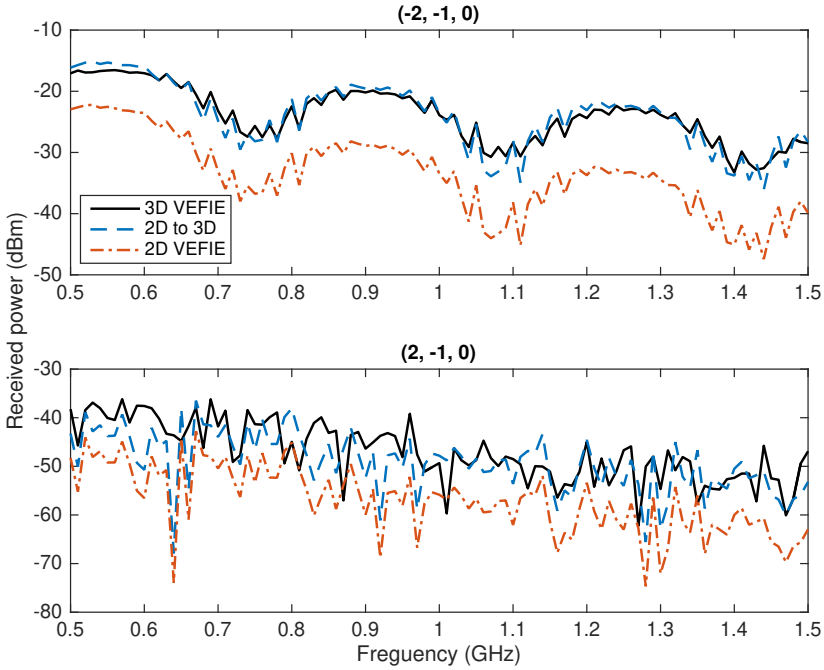

(a) In plane.

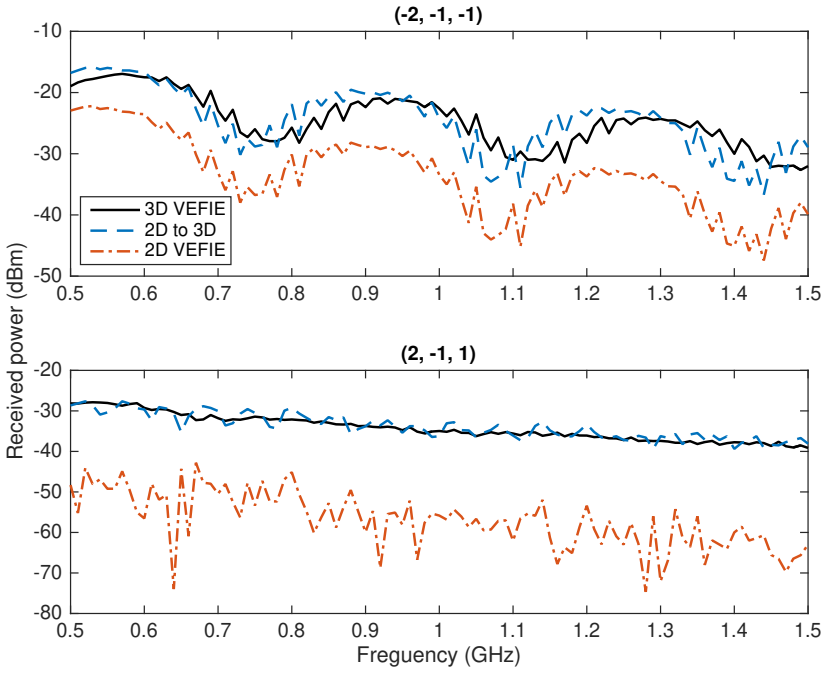

(b) Off plane.

Figure 7.10: Comparison of the 2D to 3D model against the 3D and 2D VEFIE over a frequency range from 500MHz to 1.5GHz with a spacing of 10MHz.

7.3.1 In-building propagation modelling

The 2D VEFIE has been shown to be an efficient method for indoor propagation modelling in Section 5.3. The 3D VEFIE was examined to make accurate received power predictions but it is very slow as shown in Section 6.3. Thus, the 2D to 3D model was developed and is applied to examine propagation modelling in buildings.

7.3.1.1 Measurement campaigns

The 2D to 3D model will be applied to several different environments where measurement campaigns have been performed. The first scenario is the same as that in Section 5.3.1.1 which was used to examine the use of the 2D and 3D VEFIE for indoor propagation modelling. This campaign took received power measurements at 28 locations in a 6.95m $\times$ 8.2m $\times$ 2.95m portion of a house shown in Figure 7.11 that consists of 6 different materials characterised by the parameters in Table 7.6.

Table 7.6: Parameters used to characterise the materials for the house in Figure 7.11.

Material	ϵ_r	μ_r	σ
Concrete	4.4	1	0.01
Glass	4.8	1	0
Wood	2.2	1	0
Stone	4.0	1	0.1
Tile	12	1	0
Plaster	2.5	1	0

The second measurement campaign measured the complex channel transfer function for the room shown in Figure 7.12. The size of the room is 3.35m $\times$ 6.1m. It is made up of four different materials, namely concrete, glass, wood and metal. The electrical parameters used to model these are shown in Table 7.7. These are based on values reported by Meissner et. al in [224] and averaged values from the literature for wood and metal (assumed to be aluminium). Only the 2D VEFIE and heuristic correction 2D to 3D model are applied to this building, therefore, the height, floor and ceiling are neglected for modelling purposes. There are also tables on the right hand side of the room that are neglected which will introduce a source of error. Skycross SMT-3TO10M UWB antennas and custom made coin antennas which both have an

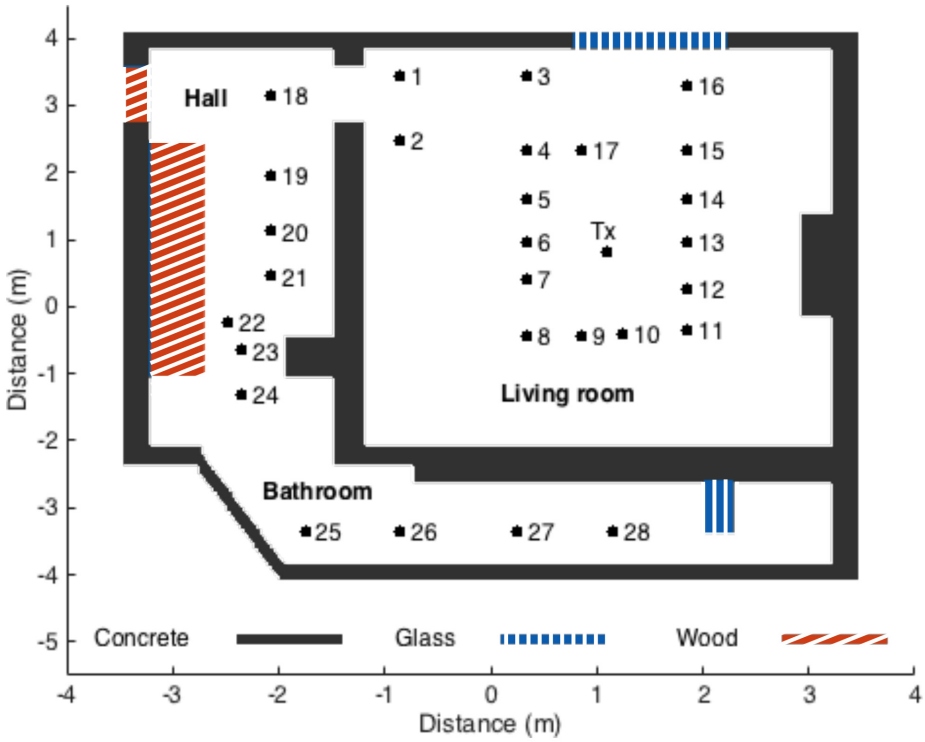

Figure 7.11: 2D depiction of a single storey portion of a house. Received power measurements were taken at the 28 receiver locations shown. The transmitter was kept constant throughout the measurement campaign.

approximately uniform azimuthal radiation pattern and zeros in the pattern at +/- 90° elevation angle [225] were used. The complex channel transfer function over the frequency range from 3.1GHz to 10.6GHz was measured using a Rohde and Schwarz ZVA-24 vector network analyser [225].

Table 7.7: Material parameters used to characterise the room in Fig. 7.12.

Material	ϵ_r	μ_r	σ
Concrete	6.0	1	0.08
Glass	5.5	1	0
Wood	2.2	1	0
Metal	1.7	1	3×10^7

7.3.1.2 Frequency domain analysis

The 2D and 3D VEFIE have been applied to the propagation problem defined by the house in Figure 7.11. A comparison of the 2D and 3D VEFIE against the measurement results is shown in Figure 7.13 for both received power and path loss predictions. The root mean square (RMS) error and standard deviation between the 2D and 3D VEFIE and measurements are shown in Table 7.8. The 3D VEFIE agrees very well with the measurement results. However, it is clear from Figure 7.13 and Table 7.8 that the 2D VEFIE is not able to make accurate received power predictions for 3D propagation.

Table 7.8: Root mean square (RMS) error and standard deviation of the 2D and 3D VEFIE and 2D to 3D model compared with measurements.

		Received power		**Path loss**	
Model	**Runtime**	**RMS Error**	**Std. Dev.**	**RMS Error**	**Std. Dev.**
3D VEFIE	19.5hrs	3.68 dB	3.67 dB	3.11 dB	3.67 dB
2D VEFIE	4.63s	28.25 dB	4.65 dB	4.96 dB	4.65 dB
2D to 3D	4.63s	4.33 dB	4.09 dB	4.69 dB	4.09 dB

The heuristic correction 2D to 3D model presented in Section 7.2.1 is also compared against the 2D and 3D VEFIE and measurements in Figure 7.13 and Table 7.8. It can clearly be seen that the 2D to 3D model provides a significant improvement over the 2D VEFIE for received power predictions. It also provides a slight improvement for

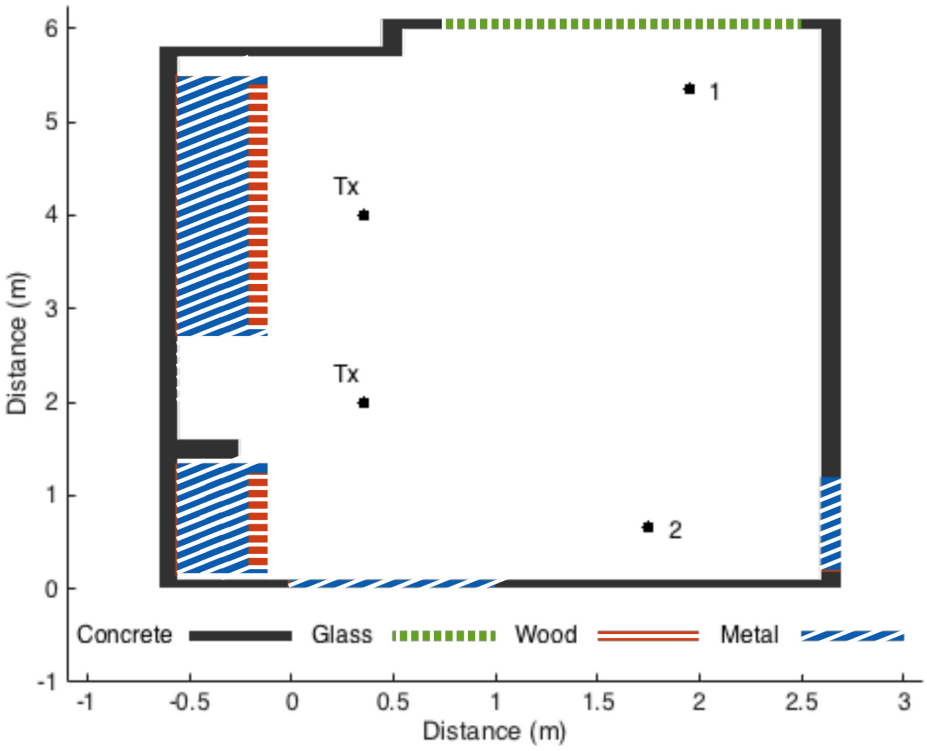

Figure 7.12: A laboratory room. The complex channel transfer function was measured at the two receiver locations from 3.1GHz to 10.6GHz at 5MHz increments for both of the transmitter locations.

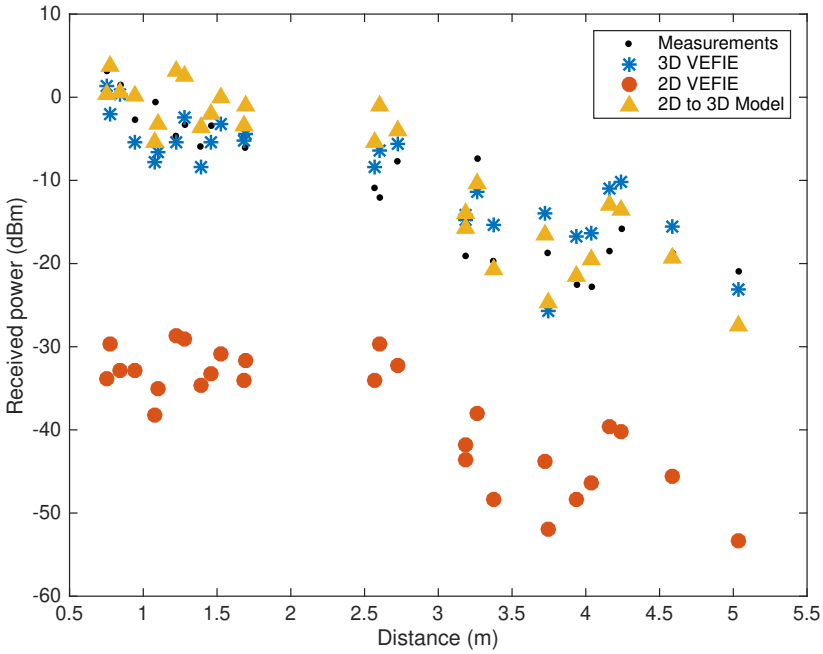

(a) Received power.

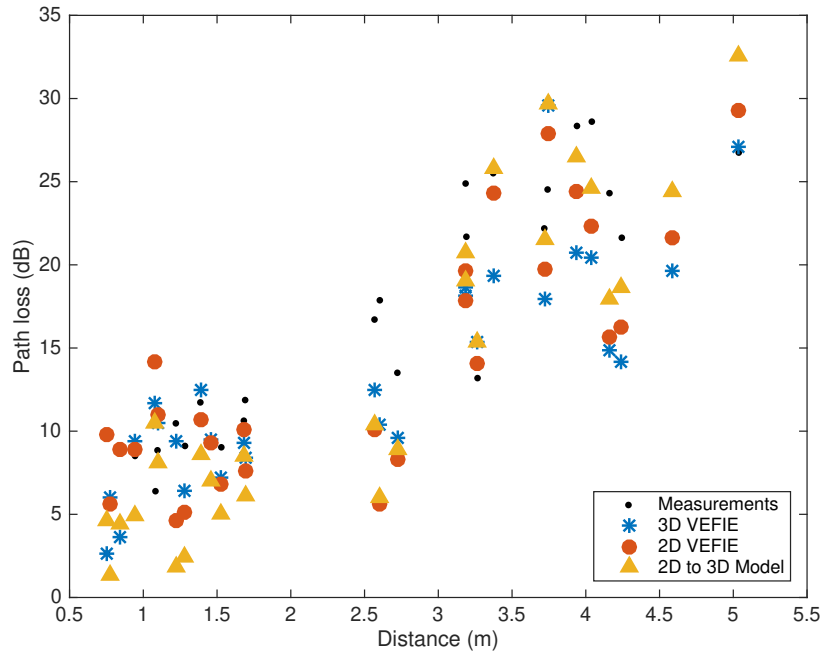

(b) Path loss.

Figure 7.13: Comparison of the 2D and 3D VEFIE, 2D to 3D model and measurements taken at the receiver locations shown in Figure 7.11.

path loss predictions as shown in Table 7.8. The full 3D VEFIE solution is more accurate than the 2D to 3D model. However, the main advantage of the 2D to 3D model is its significantly quicker runtime, 4.63 seconds as opposed to 19.5 hours for the full 3D VEFIE. It should be noted that the runtime of the 2D to 3D model is dependant on the efficiency of the visibility algorithm used to determine whether points are in LOS or NLOS regions. Here, the visibility is known for the 28 receiver points and thus the additional time to compute the 2D to 3D model over the 2D VEFIE is negligible.

Indoor environments typically contain many NLOS regions so it is important that an indoor propagation model is able to perform well in both LOS and NLOS cases. Conventional empirical models typically break down and lose accuracy for NLOS scenarios. The RMS error and standard deviation for LOS and NLOS regions for the 2D to 3D model and the 2D and 3D VEFIE are shown in Table 7.9. It can be seen that the 2D to 3D model's accuracy does not degrade for NLOS regions. This is further demonstrated in Figure 7.14 where the 2D to 3D model and 2D and 3D VEFIE are compared against the measurements for LOS and NLOS regions, respectively.

Table 7.9: RMS error and standard deviation of the 2D and 3D VEFIE and the 2D to 3D model for LOS and NLOS regions.

	Received Power			
	LOS		**NLOS**	
	RMS Error	**Std. Dev.**	**RMS Error**	**Std. Dev.**
3D VEFIE	3.01 dB	2.96 dB	5.03 dB	4.26 dB
2D VEFIE	29.10 dB	5.08 dB	26.89 dB	3.81 dB
2D to 3D	4.65 dB	4.07 dB	3.77 dB	3.94 dB
	Path Loss			
	LOS		**NLOS**	
	RMS Error	**Std. Dev.**	**RMS Error**	**Std. Dev.**
3D VEFIE	3.01 dB	2.96 dB	6.26 dB	4.26 dB
2D VEFIE	5.05 dB	5.08 dB	4.82 dB	3.81 dB
2D to 3D	5.13 dB	4.07 dB	3.92 dB	3.94 dB

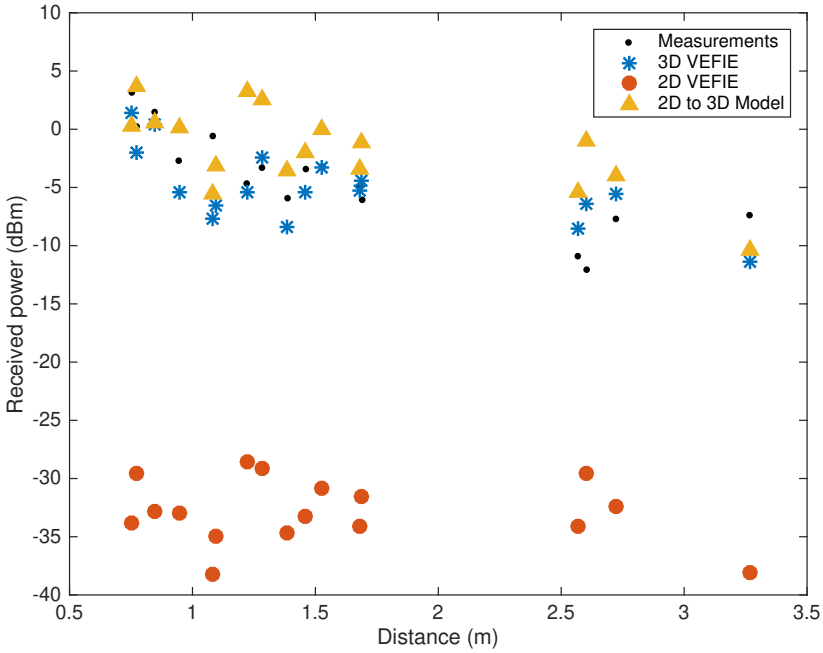

(a) Line of sight.

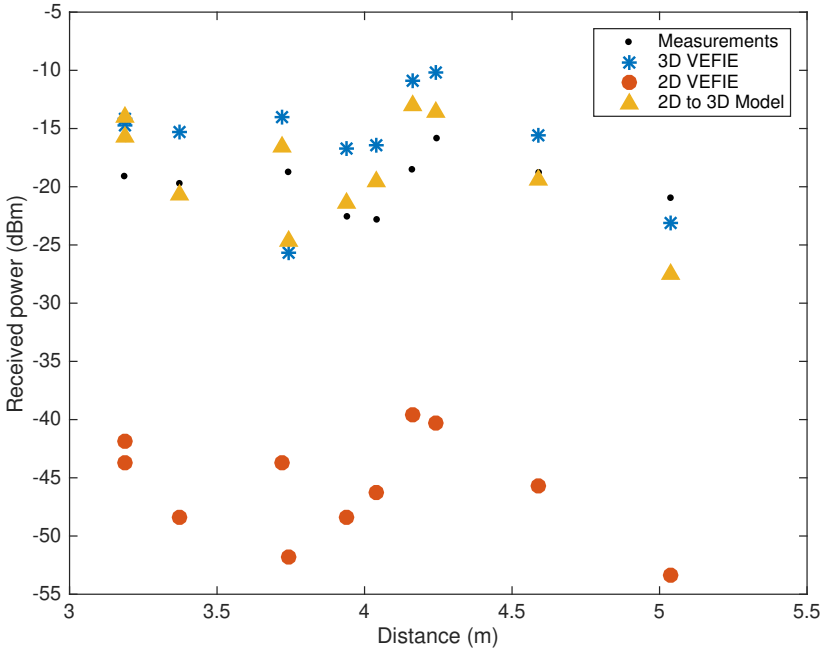

(b) Non line of sight.

Figure 7.14: Comparison of the 2D and 3D VEFIE, 2D to 3D model and measurements for LOS and NLOS at the receiver locations shown in Figure 7.11 Receivers 1 - 17 are in LOS and 18 - 28 are in NLOS.

7.3.1.3 Time domain modelling

An indoor propagation model should be capable of predicting the radio channel in both the frequency and time domains accurately and efficiently. The 2D to 3D model presented has been shown to work well for frequency domain predictions. It was demonstrated in Section 5.3.1.5 how time domain predictions can be computed using the frequency domain 2D VEFIE method. Now, the 2D to 3D model will be used to compute accurate 3D time domain predictions in the form of PDPs and be compared against measurements for the scenario shown in Figure 7.12. The 2D VEFIE is applied to this scenario for the separate transmitter locations shown, $(0.35, 2)$ and $(0.35, 4)$ and solved from 3.1GHz to 10.6GHz at 5MHz increments. The 2D to 3D model is applied to the resultant 2D VEFIE data, and an example of this can be seen in Figure 7.15, to compute 3D predictions. The 2D to 3D data is then inverse Fourier transformed to generate PDPs that can be compared with the measurements.

The inverse Fourier transform is applied to the data in Figure 7.15 for the transmitter located at (0.354, 2) and (0.354, 4) and the receiver located at (1.95, 5.35) and (1.75, 0.65), four in total, to compute a PDP such as those shown in Figure 7.16. In Figure 7.16 the 2D to 3D model is compared against the measurement results where it can be seen that except for the noise preceding the initial pulse a good agreement is achieved. The average RMS error and standard deviation for all transmitter and receiver pairs for the 2D to 3D model and 2D VEFIE is shown in Table 7.10. The 2D to 3D model is also able to accurately predict the mean delay and RMS delay spread of the environment as shown in Table 7.11.

Table 7.10: Average RMS error and standard deviation for all transmitter and receiver pairs.

	RMS Error	**Std. Dev.**
2D to 3D	9.33 dB	9.30 dB
2D VEFIE	28.40 dB	9.30 dB

The 2D to 3D time domain modelling approach produces a large amount of data. In the frequency domain analysis, the data from the VEFIE and measurement campaign was averaged over a box of size $\lambda \times \lambda$ to remove some of the effects of fast fading. Here, by applying a 10-point moving average filter, which corresponds to a delay of 1ns, a much clearer picture of the signal can be seen in Figure 7.17.

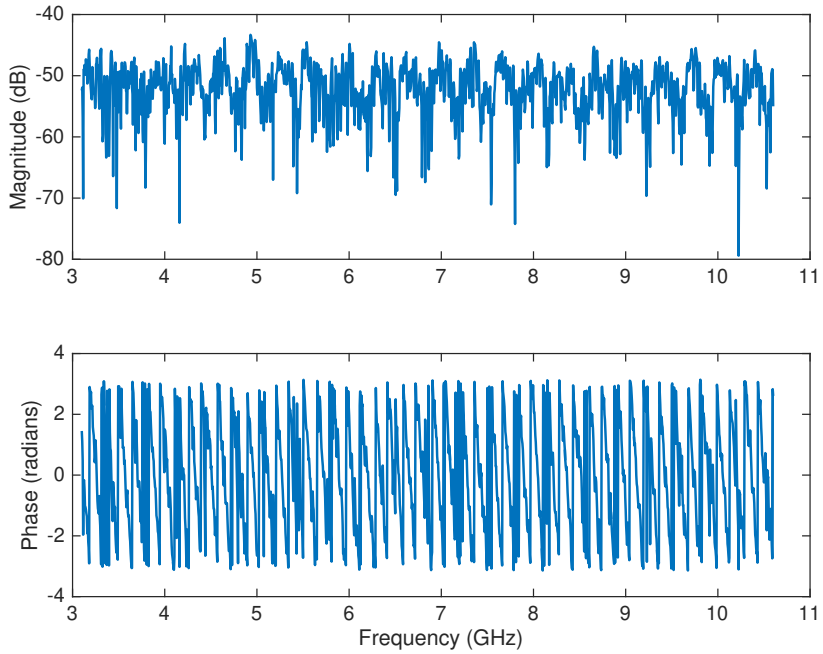

Figure 7.15: Illustration of the complex channel transfer function data computed by the 2D to 3D model for the second receiver location, at (1.75, 0.65). The transmitter was located at (0.354, 2).

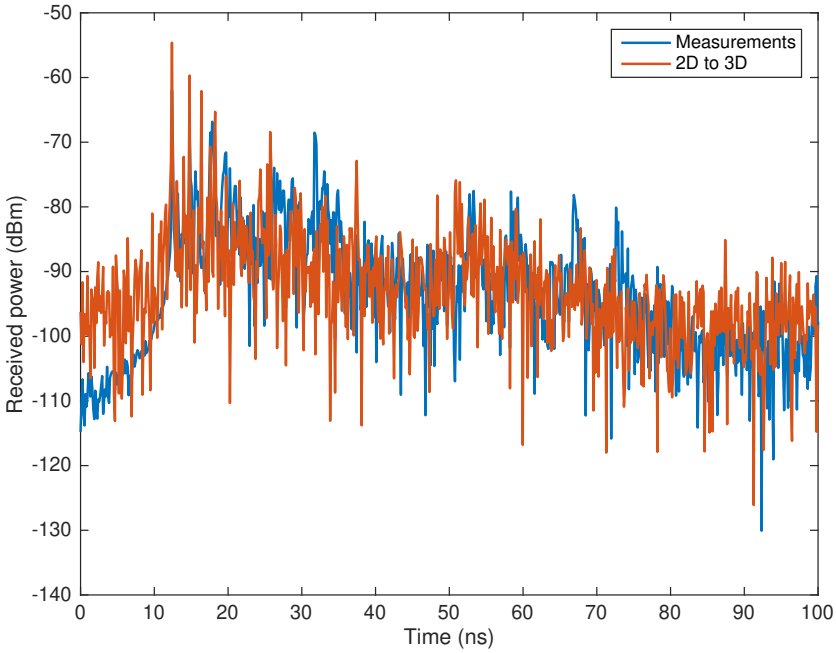

(a) Rx = (1.95, 5.35).

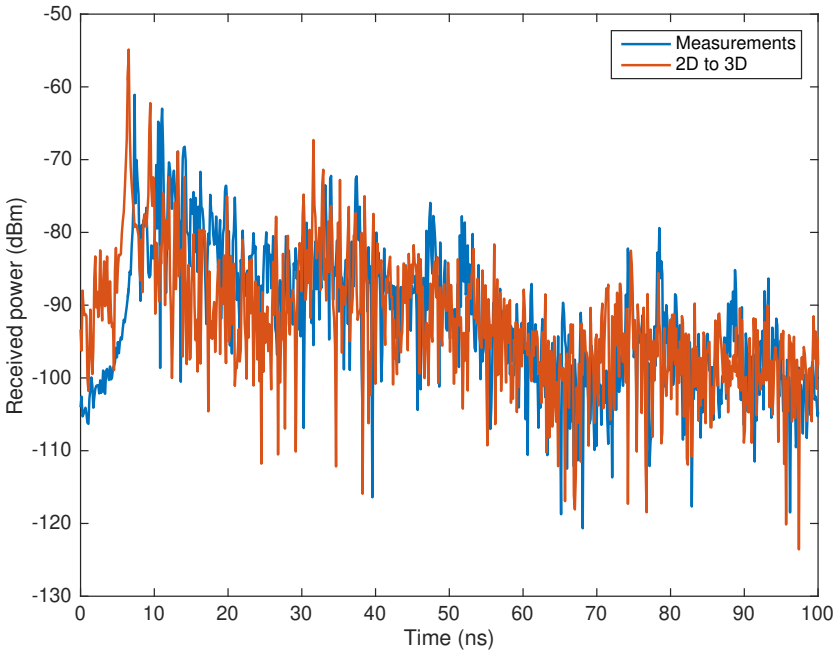

(b) Rx = (1.75, 0.65).

Figure 7.16: Comparison of the PDPs computed by the 2D to 3D model and measurements for receivers (1.95, 5.35) and (1.75, 0.65). The transmitter is located at (0.35, 2).

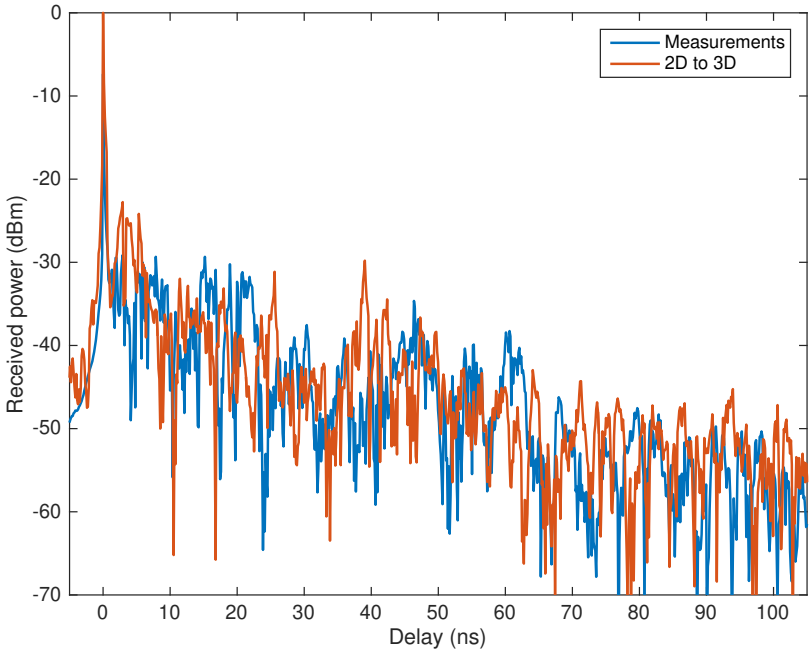

(a) Rx = (1.95, 5.35).

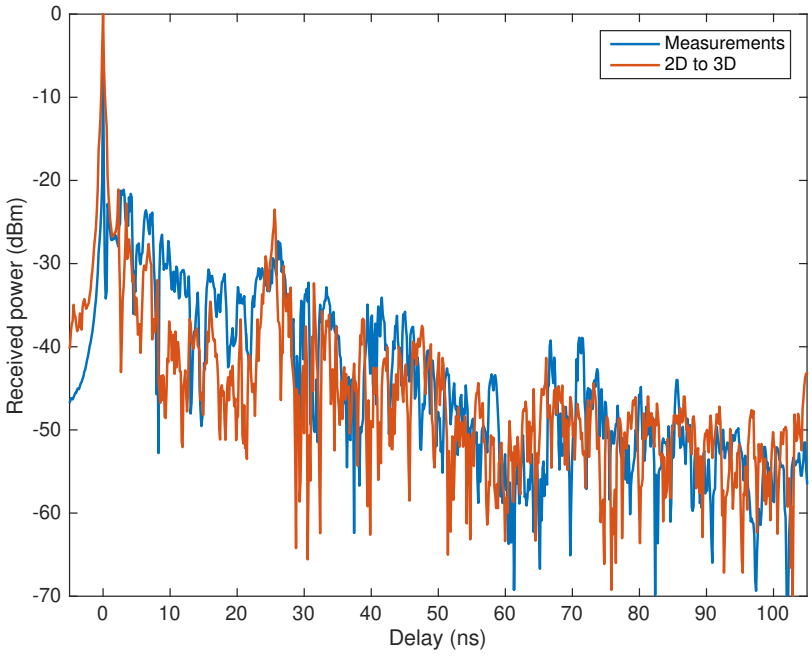

(b) Rx = (1.75, 0.65).

Figure 7.17: Comparison of the PDPs computed by the 2D to 3D model and measurements for receivers (1.95, 5.35) and (1.75, 0.65). The transmitter is located at (0.35, 2). A moving average filter has been applied to both data sets.

Table 7.11: Average mean delay and RMS delay spread for all transmitter and receiver pairs.

	Mean Delay	**RMS Delay Spread**
Measurements	51.46 ns	28.28 ns
2D to 3D	52.40 ns	28.30 ns
2D VEFIE	53.05 ns	28.21 ns

7.3.2 Statistical and empirical model analysis

7.3.2.1 Frequency domain analysis

In Section 6.3.2 the 2D and 3D VEFIE are compared against the dual slope model, COST 231 multi-wall model and the adjusted Motley-Keenan model. The dual slope model and COST 231 multi-wall model achieve a higher level off accuracy against the measurements than the Motley-Keenan model. The 2D to 3D model is shown to be more accurate than the 2D VEFIE in Section 7.3.1. Thus, the dual slope model and the COST 231 multi-wall model are compared against the 2D to 3D model and 3D VEFIE in Figure 7.18 and Table 7.12. It can be seen from Table 7.12 that the empirical models produce a lower RMS error and standard deviation than the 2D to 3D model but as explained in Section 5.3.1.3 the empirical models require a measurement campaign to characterise them. The 2D to 3D model does not.

Table 7.12: RMS error and standard deviation of the VEFIE and popular empirical models compared with measurements.

Model	**RMS Error**	**Std. Dev.**
3D VEFIE	3.11 dB	3.67 dB
2D to 3D	4.69 dB	4.09 dB
Dual slope	4.39 dB	3.51 dB
COST 231 multi-wall	2.81 dB	2.82 dB

As mentioned in Section 7.3.1 an important consideration for indoor propagation models is their ability to make accurate predictions in both LOS and NLOS regions. The results in Figure 7.18 are broken down into LOS and NLOS regions in Figure 7.19 where it can be seen that the accuracy of the empirical models degrades for NLOS regions over LOS. This can be seen more clearly in Table 7.13 where the RMS error

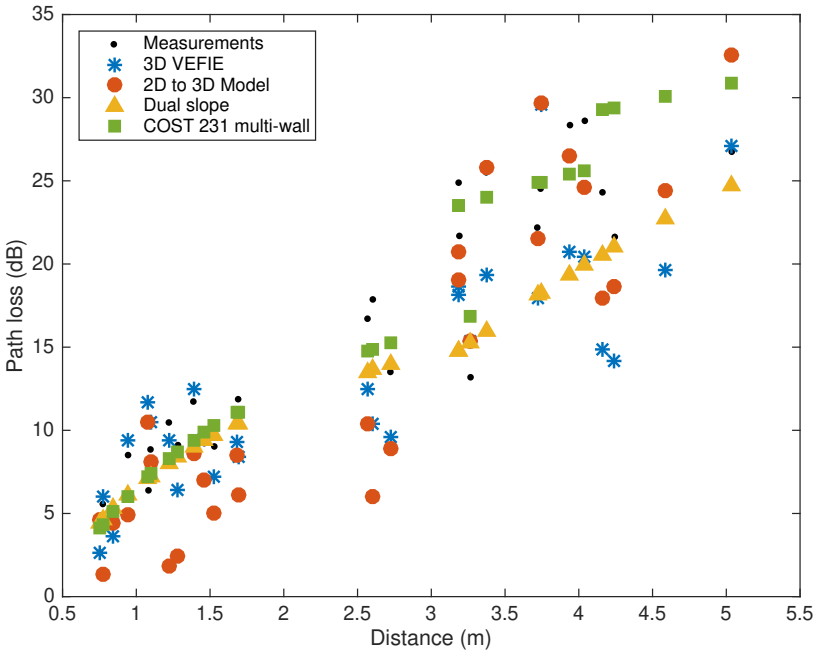

Figure 7.18: Comparison of the 3D VEFIE, heuristic correction 2D to 3D model and popular empirical models ability to model path loss against measurements for the scenario shown in Figure 7.11.

and standard deviation for each model is broken down into LOS and NLOS regions. The empirical models produce a very high level of accuracy in LOS regions as they are primarily developed for these regions but their accuracy degrades significantly for NLOS regions.

Table 7.13: RMS error and standard deviation of the 2D and 3D VEFIE, the 2D to 3D model and popular empirical models for LOS and NLOS regions.

	LOS		**NLOS**	
	RMS Error	**Std. Dev.**	**RMS Error**	**Std. Dev.**
3D VEFIE	3.01 dB	2.96 dB	6.26 dB	4.26 dB
2D to 3D	5.13 dB	4.07 dB	3.92 dB	3.94 dB
Dual slope	1.93 dB	1.83 dB	6.58 dB	3.40 dB
COST 231 multi-wall	1.81 dB	1.84 dB	3.88 dB	3.67 dB

7.3.2.2 Time domain analysis

The dual slope and COST 231 multi wall models produce path loss predictions but do not provide phase or multipath information, thus, they can't be used to make time domain predictions unlike the VEFIE. A simple time domain model based on reverberation theory is compared against the 2D to 3D heuristic correction and measurements in Figure 7.20 for the scenario shown in Figure 7.12. The reverberation theory model tracks the overall trend of the measurements but lacks a significant amount of detail. It also lacks accuracy in characterising the environment based on its mean delay and RMS delay spread as shown in Table 7.14.

Table 7.14: Average mean delay and RMS delay spread for all transmitter and receiver pairs.

	Mean Delay	**RMS Delay Spread**
Measurements	51.46 ns	28.28 ns
2D to 3D	52.40 ns	28.30 ns
Reverberation theory	57.73 ns	35.98 ns

The analysis in Sections 7.3.2.1 and 7.3.2.2 demonstrates the need for deterministic models to produce accurate predictions for indoor propagation. The VEFIE and 2D

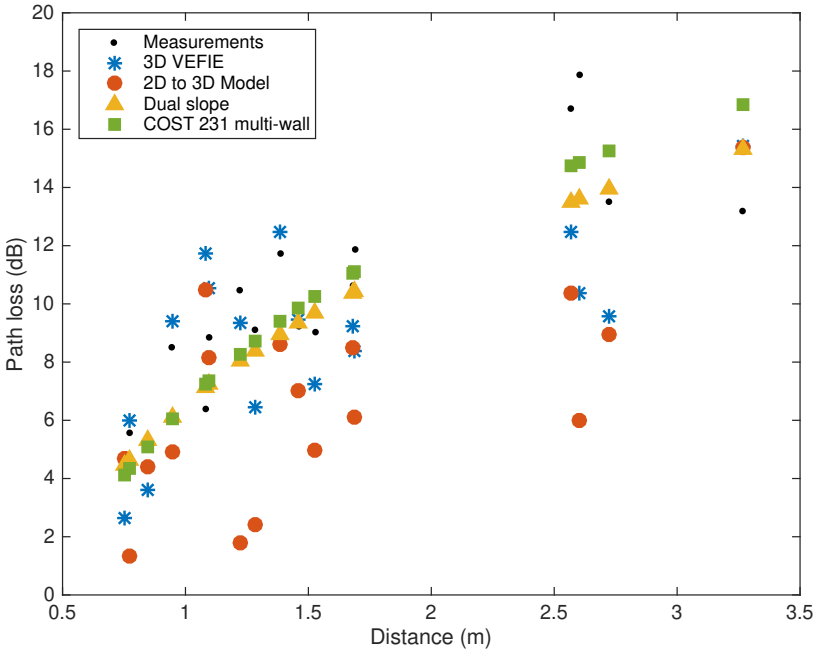

(a) Line of sight. Receivers 1 - 17 in Figure 7.11.

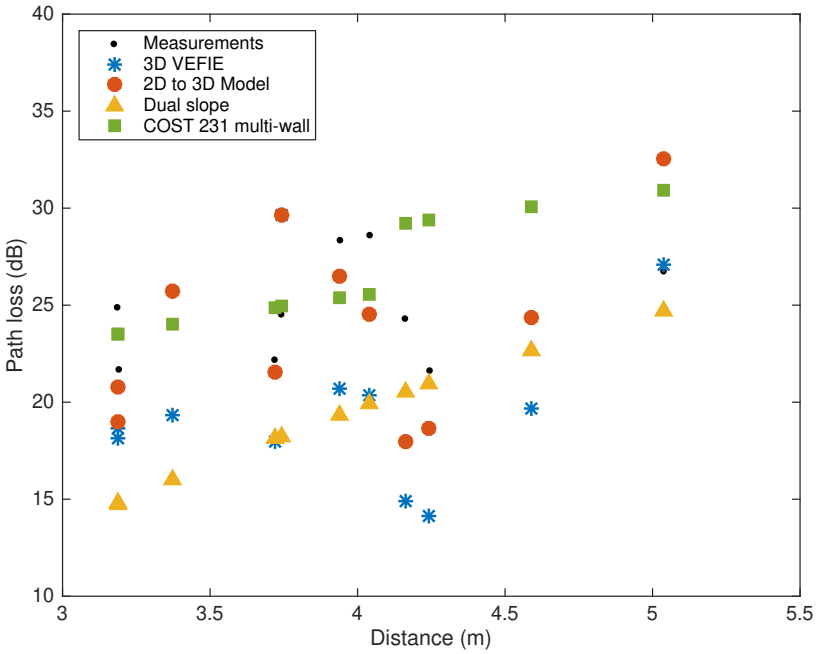

(b) Non line of sight. Receivers 18 - 28 in Figure 7.11.

Figure 7.19: Comparison of the 3D VEFIE, heuristic correction 2D to 3D model and popular empirical models ability to model path loss against measurements for LOS and NLOS at the receiver locations in Figure 7.11.

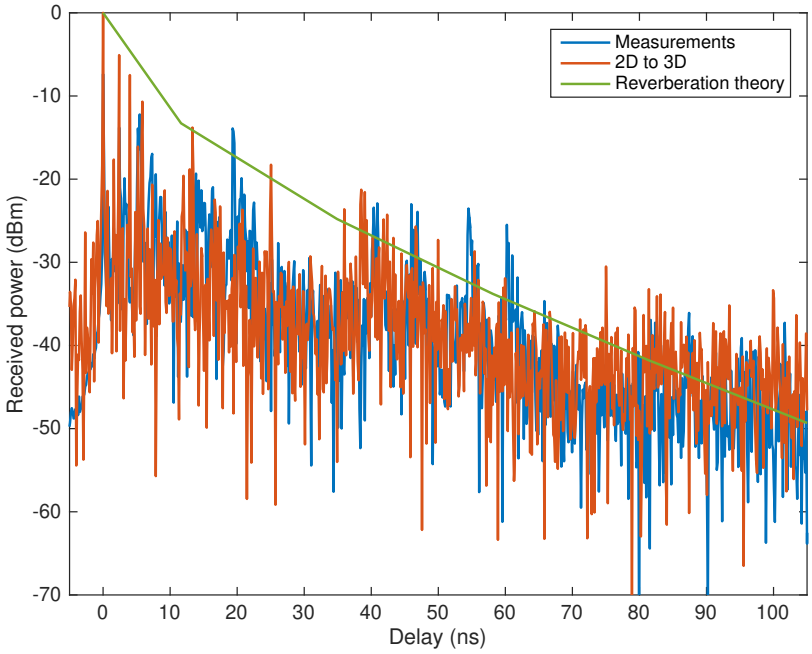

(a) Rx = (1.95, 5.35).

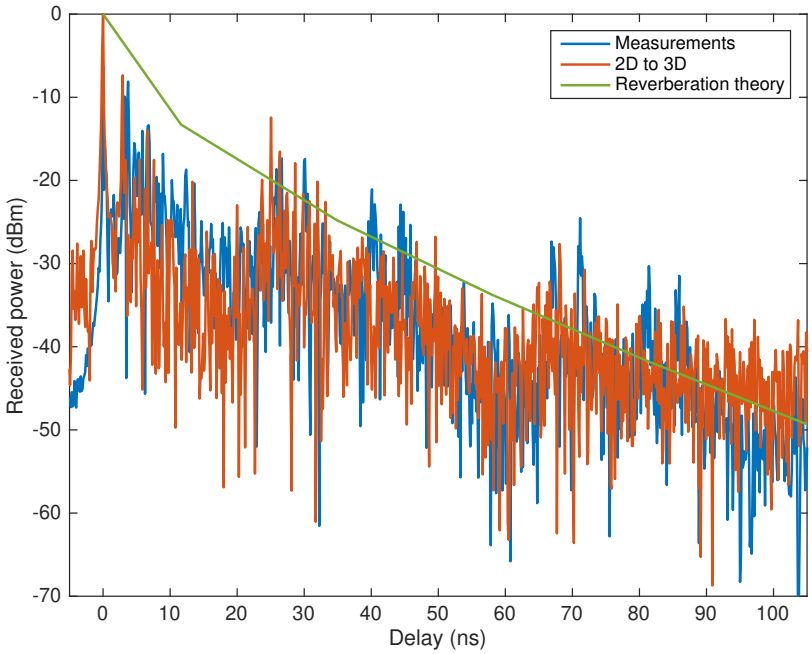

(b) Rx = (1.75, 0.65).

Figure 7.20: Comparison of the PDPs computed by the 2D to 3D model, reverberation theory and measurements for receivers (1.95, 5.35) and (1.75, 0.65). The transmitter is located at (0.35, 2).

to 3D models don't require measurement campaigns but they do require information about the environment geometry and material composition which should be easier to acquire in the future than it will be to perform measurement campaigns due to the use of 3D CAD tools and the trend towards point-clouds to generate the geometry of 3D environments. This will provide a greater level of accuracy for deterministic models whilst empirical and statistical methods won't be able to provide a higher level of accuracy without more detailed and comprehensive measurement campaigns. The next section examines the accuracy of the heuristic correction model against ray tracing.

7.3.3 Comparison against ray tracing

In Section 5.3.2 it is shown that the 2D VEFIE is much faster than the 3D ray tracing model and that neither model is able to make accurate received power predictions. The 3D ray tracing model produces a higher level of accuracy for path loss predictions than the 2D VEFIE. It also produces a higher level of accuracy than the 3D VEFIE for path loss predictions and in a quicker time frame, which can be seen in Section 6.3.3. In Figure 7.21 the 2D to 3D model is compared against the same 3D ray tracing model for the scenario shown in Figure 7.11. The 2D to 3D heuristic correction is faster than the 3D ray tracing model as shown in Table 7.15. As shown in Table 7.15 the ray tracing model is more accurate for path loss predictions in this case. However, the 2D to 3D model is better for received power predictions.

Table 7.15: Runtime, RMS error and standard deviation of the 2D to 3D model, 3D VEFIE and ray tracing compared with measurements. The 3D VEFIE is solved to an error tolerance of 0.2, instead of the usual 0.001, to determine its runtime only.

		Received power		**Path loss**	
Model	**Runtime**	**RMS Error**	**Std. Dev.**	**RMS Error**	**Std. Dev.**
3D VEFIE	4305s	3.68 dB	3.67 dB	3.11 dB	3.67 dB
2D to 3D	6.5s	4.33 dB	4.09 dB	4.69 dB	4.09 dB
Ray tracing	415s	7.85 dB	2.54 dB	2.50 dB	2.54 dB

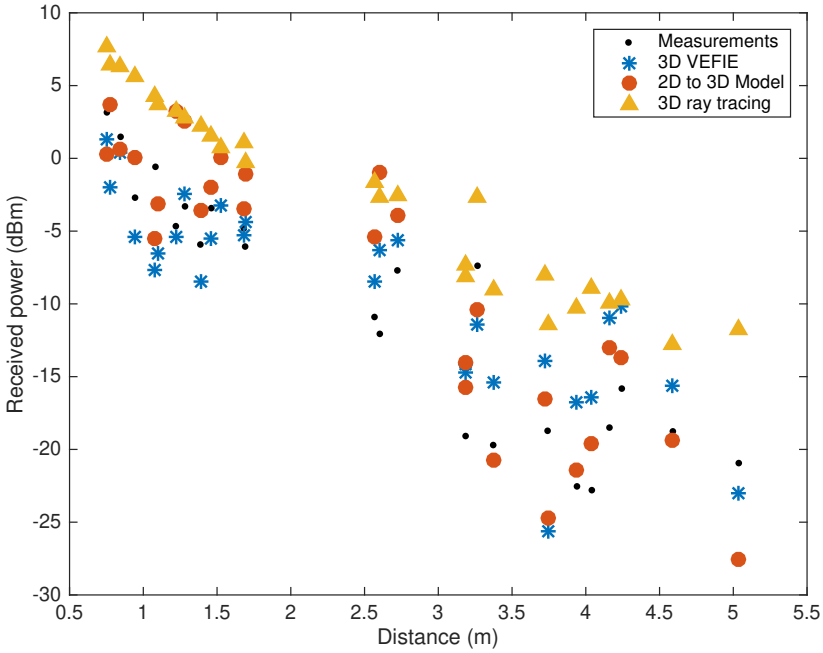

(a) Received power.

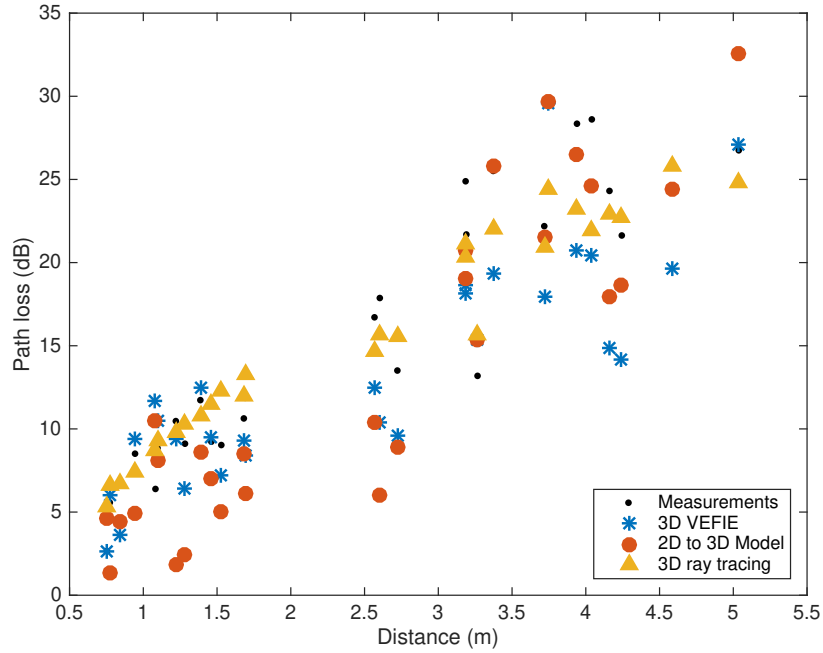

(b) Path loss.

Figure 7.21: Comparison of the 3D VEFIE, heuristic correction 2D to 3D model and ray tracing ability to model path loss against measurements for the scenario shown in Figure 7.11.

7.4 Conclusions

2D to 3D models are presented here to produce accurate and efficient indoor propagation models. The 2D to 3D models are compared against each other before the heuristic correction model is validated against the 3D VEFIE for frequency and time domain predications. The heuristic correction 2D to 3D model is applied to realistic indoor propagation environments. Its efficiency is demonstrated over the 3D VEFIE and it is shown how it provides nearly the same accuracy as the 3D VEFIE. The accuracy of the 2D to 3D model is examined in both the frequency and time domains and is also compared against empirical and statistical models where it shows a good level of accuracy. Lastly, the heuristic correction 2D to 3D model is compared against a full 3D ray tracing model which it is faster than.

Chapter 8

Conclusions

The focus of this thesis is on the use of full-wave techniques to model radio wave propagation in buildings. An overview of propagation modelling and the most common methods used for indoor propagation modelling is presented in Chapter 2. A strong focus is put on the most commonly used full-wave methods. The advantages and disadvantages of the various methods are contrasted. Hybrid methods combining the advantages of several different types of methods are discussed also. A general description of statistical and empirical models as well as ray optical techniques was also provided in this chapter.

Maxwell's equations which underpin the propagation of electromagnetic waves are described in Chapter 3. The two most common full-wave methods for solving Maxwell's equations for indoor propagation, Finite Difference Time Domain (FDTD) and the Method of Moments (MoM), are briefly explained. The full-wave propagation models presented in this thesis are based on the Volume Electric Field Integral Equation (VEFIE) which is derived from Maxwell's equations in this chapter also. The MoM is applied to the VEFIE and it results in a matrix equation that can be solved numerically.

The matrix equation obtained after applying the MoM to the VEFIE is typically very large for the problems found in propagation modelling. Therefore, it is usually prohibitive to solve it by direct matrix inversion. Iterative solvers can be employed instead. Chapter 4 delivers a description of Krylov iterative solvers along with an explanation of preconditioning and fast matrix-vector multiplication techniques. The matrix-vector multiplication techniques are specific to computational electromagnetics problems as they depend on the Green's function but the preconditioning techniques are generic to linear algebra problems. This chapter also mentions some considerations that are required when implementing these methods numerically and in

parallel.

Chapters 5 to 7 report on the use of the VEFIE in 2D and 3D as an indoor propagation modelling tool. Chapter 5 details the use of the 2D VEFIE, whilst Chapter 6 uses the 3D VEFIE. Novel modifications to the 2D VEFIE designed to produce accurate 3D predictions in a fraction of the time it takes for a full 3D VEFIE solution are presented in Chapter 7. The 2D and 3D VEFIE are discretised using the MoM. The resulting matrix equation is solved using the BiCGSTAB method which is primarily accelerated by using the Fast Fourier Transform (FFT) and a reduced operator.

In Chapter 5 the 2D VEFIE is employed to model the propagation of electromagnetic waves in buildings. The 2D VEFIE is validated against the analytical Mie series solution for scattering from a dielectric cylinder before it is compared against a surface integral equation, the Surface Electric Field Integral Equation (SEFIE) in order to determine the most efficient integral equation formulation for indoor propagation. The 2D VEFIE whilst requiring significantly more unknowns than the surface equation converges much more rapidly and reaches a more accurate solution in a faster runtime. The 2D VEFIE is then used to model indoor propagation in both the frequency and time domains. It is capable of producing accurate path loss predictions but suffers when predicting the received power due to its 2D nature. A comparison is also made against a 3D ray tracing model. An examination of the computational efficiencies of the methods described in Chapter 4 applied to the 2D VEFIE is also presented.

In Chapter 6 the 2D VEFIE is extended to three dimensions and the 3D VEFIE is adopted for in building propagation. The 3D VEFIE is validated against the analytical Mie series solution for scattering from a dielectric sphere. It is employed as an indoor propagation model where it shows a high level of accuracy compared with popular empirical models and 3D ray tracing but it suffers from a very long runtime.

The extremely long runtime of the 3D VEFIE led to the development of 2D to 3D methods in Chapter 7. The 2D to 3D methods are enhancements to the 2D VEFIE designed to improve its accuracy and make accurate 3D predictions. They are faster than the 3D VEFIE as they are based on the 2D VEFIE. Results presented in this chapter demonstrate that the heuristic correction method is the best and it is validated over a wide range of frequencies against the 3D VEFIE. It is shown how the 2D to 3D model is capable of providing a high level of accuracy in both the frequency and time domains. Comparisons are again made against popular empirical and statistical models as well as 3D ray tracing.

8.1 Future work

In terms of future work there are a few avenues that can be pursued further. The first is the use of the VEFIE for providing angle of arrival (AoA) information. The AoA results presented in this thesis have not been compared against measurements or another model to validate that they are correct and the right procedure is being used to generate them. This is the only quantity presented in this thesis that has not been compared against measurement results as they are quite difficult to obtain.

Secondly, the 3D VEFIE model is quite slow and memory intensive. It is currently implemented in MATLAB. Future work could investigate implementing it in a compiled language like C or C++ to reduce its memory requirements and computational burden. The use of parallelisation and advantages of vectorisation should also be examined. Supercomputers and GPGPUs provide a large benefit over conventional computers for performing large computations. Their use could also be investigated to improve the runtime of the 3D VEFIE.

The 2D to 3D models presented in Chapter 7 require more exploration. Currently, the models do not provide information about the x and y components of the electric field in three dimensions. One possible avenue of investigation is the use of the x and y components of the incident field and Born series [226] to compute predictions for them. The 2D to 3D models could also benefit from taking a different approach, instead of solving for the 2D free space fields and then correcting these, they could solve for 2D fields in scatterers, correct these for 3D propagation and then the fields in free space can be computed by a single integration with the 3D VEFIE over the fields in the scatterers. This may be able to produce a more accurate 3D representation of the fields.

In power delay profiles (PDPs) computed by the VEFIE a large noise floor is experienced that is not found in measurement data. This needs further investigation in order to determine its cause, which may be due to the 2D to 3D model or the lack of accurate knowledge of the propagation environment. One such method that may be able to eliminate this is the Hilbert transform which imposes causality in the time domain on a frequency domain signal. Coupling the Hilbert transform with the time shifting property of the Fourier transform could effectively eliminate the noise floor.

The VEFIE is a frequency domain method. In order to produce time domain predictions it must be solved at a large number of independent frequencies. This is extremely time consuming and eliminates the ability to use the full 3D VEFIE. Fast

frequency sweep techniques like asymptotic waveform evaluation (AWE) [227], [228] should be further investigated to speed up this computation. They were briefly examined but simple implementations were found not to converge or produce meaningful results and thus were omitted from this thesis.

Appendix A

Embedding a Discrete Linear Convolution in a Circular Convolution - An Extension from One Dimension to Two and Three Dimensions

In Section 4.4.1 the process of computing a one-dimensional discrete linear convolution by the Fast Fourier Transform (FFT) to reduce its complexity is described. Here, the extension of this process, whereby the linear convolution is first embedded in a circular convolution, is briefly described for two and three dimensions. The circular convolution is then computed using the 2D and 3D FFT and inverse FFT

$$e = \mathcal{F}_N^{(2)-1}\{\mathcal{F}_N^{(2)}(f)\mathcal{F}_N^{(2)}(g)\} \tag{A.1}$$

$$e = \mathcal{F}_N^{(3)-1}\{\mathcal{F}_N^{(3)}(f)\mathcal{F}_N^{(3)}(g)\} \tag{A.2}$$

where $\mathcal{F}_N^{(2)}$ and $\mathcal{F}_N^{(3)}$ are the 2D and 3D N point DFT with inverses $\mathcal{F}_N^{(2)-1}$ and $\mathcal{F}_N^{(3)-1}$.

A two-dimensional discrete convolution is an operation of the form

$$e_{pq} = \sum_{n=0}^{N-1}\sum_{m=0}^{M-1} f_{nm}g_{p-n,q-m} \qquad \begin{Bmatrix} p \\ q \end{Bmatrix} = 0, 1, \ldots, \begin{Bmatrix} N-1 \\ M-1 \end{Bmatrix} \tag{A.3}$$

or in matrix form

$$\begin{bmatrix} \mathbf{E}_0 \\ \mathbf{E}_1 \\ \mathbf{E}_2 \\ \vdots \\ \mathbf{E}_{M-1} \end{bmatrix} = \begin{bmatrix} \mathbf{G}_0 & \mathbf{G}_{-1} & \mathbf{G}_{-2} & \cdots & \mathbf{G}_{1-M} \\ \mathbf{G}_1 & \mathbf{G}_0 & \mathbf{G}_{-1} & \cdots & \mathbf{G}_{2-M} \\ \mathbf{G}_2 & \mathbf{G}_1 & \mathbf{G}_0 & \cdots & \mathbf{G}_{3-M} \\ \vdots & \vdots & \vdots & \ddots & \vdots \\ \mathbf{G}_{M-1} & \mathbf{G}_{M-2} & \mathbf{G}_{M-3} & \cdots & \mathbf{G}_0 \end{bmatrix} \begin{bmatrix} \mathbf{F}_0 \\ \mathbf{F}_1 \\ \mathbf{F}_2 \\ \vdots \\ \mathbf{F}_{M-1} \end{bmatrix} \tag{A.4}$$

where each element of the $M \times M$ block Toeplitz matrix in (A.4) is itself a Toeplitz matrix of the form depicted in (4.44) and each $\mathbf{E}_m$ and $\mathbf{F}_m$ are of length N. If the elements $\mathbf{G}_m$ repeat with period M, so that

$$\mathbf{G}_{m-M} = \mathbf{G}_m \qquad m = 1, 2, \ldots, M-1 \tag{A.5}$$

and the elements within $\mathbf{G}_M$ repeat with period N as described for the 1D case then this too is a circular discrete convolution. Otherwise, it is a linear discrete convolution problem. The 2D linear convolution problem of size $N \times M$ can be embedded into a circular convolution problem by extending each element $\mathbf{G}_m$ to repeat with period $2N-1$ as in the 1D case, extending $\mathbf{g}$ so that it repeats with period $2M-1$, padding $\mathbf{f}$ with zeros to size $2N-1 \times 2M-1$ and increasing the summation limits to $2N-2$ and $2M-2$. Then, (A.3) and (A.4) can be efficiently computed using the FFT by (A.1).

A three-dimensional discrete convolution is an operation of the form

$$e_{pqr} = \sum_{n=0}^{N-1} \sum_{m=0}^{M-1} \sum_{o=0}^{O-1} f_{nmo} g_{p-n,q-m,r-o} \qquad \begin{Bmatrix} p \\ q \\ r \end{Bmatrix} = 0, 1, \ldots, \begin{Bmatrix} N-1 \\ M-1 \\ O-1 \end{Bmatrix} \tag{A.6}$$

or in matrix form

$$\begin{bmatrix} \mathbf{E}_0 \\ \mathbf{E}_1 \\ \mathbf{E}_2 \\ \vdots \\ \mathbf{E}_{O-1} \end{bmatrix} = \begin{bmatrix} \mathbf{G}_0 & \mathbf{G}_{-1} & \mathbf{G}_{-2} & \cdots & \mathbf{G}_{1-O} \\ \mathbf{G}_1 & \mathbf{G}_0 & \mathbf{G}_{-1} & \cdots & \mathbf{G}_{2-O} \\ \mathbf{G}_2 & \mathbf{G}_1 & \mathbf{G}_0 & \cdots & \mathbf{G}_{3-O} \\ \vdots & \vdots & \vdots & \ddots & \vdots \\ \mathbf{G}_{O-1} & \mathbf{G}_{O-2} & \mathbf{G}_{O-3} & \cdots & \mathbf{G}_0 \end{bmatrix} \begin{bmatrix} \mathbf{F}_0 \\ \mathbf{F}_1 \\ \mathbf{F}_2 \\ \vdots \\ \mathbf{F}_{O-1} \end{bmatrix} \tag{A.7}$$

where each element of the $O \times O$ block Toeplitz matrix in (A.7) is itself a Toeplitz matrix of the form depicted in (A.4) and each $\mathbf{E}_o$ and $\mathbf{F}_o$ are of size $N \times M$. If the

elements $\mathbf{G}_o$ repeat with period O, so that

$$\mathbf{G}_{o-O} = \mathbf{G}_o \qquad o = 1, 2, \ldots, O-1 \tag{A.8}$$

and the elements within $\mathbf{G}_o$ repeat as described for the 2D case then this too is a circular discrete convolution. Otherwise, it is a linear discrete convolution problem. A 3D linear convolution problem of size $N \times M \times O$ can be embedded in a circular convolution problem of size $2N-1 \times 2M-1 \times 2O-1$ by following the same procedure as the extension from 1D to 2D. Then, (A.6) and (A.7) can be efficiently computed using the FFT by (A.2)

Bibliography

[1] J. Zhang, G. De la Roche *et al.*, *Femtocells: Technologies and deployment*. Wiley Online Library, 2010.

[2] S. Saunders and A. Aragón-Zavala, *Antennas and propagation for wireless communication systems*. John Wiley & Sons, 2007, p. 546.

[3] G. F. Pedersen, *COST 231-Digital mobile radio towards future generation systems*. EU, 1999.

[4] A. J. Motley and J. M. P. Keenan, 'Personal communication radio coverage in buildings at 900 MHz and 1700 MHz', *Electronics Letters*, vol. 24, no. 12, pp. 763–764, Jun. 1988.

[5] A. G. M. Lima and L. F. Menezes, 'Motley-Keenan model adjusted to the thickness of the wall', in *SBMO/IEEE MTT-S International Conference on Microwave and Optoelectronics, 2005.*, Jul. 2005, pp. 180–182.

[6] T. S. Rappaport, S. Y. Seidel and K. Takamizawa, 'Statistical channel impulse response models for factory and open plan building radio communicate system design', *IEEE Transactions on Communications*, vol. 39, no. 5, pp. 794–807, May 1991.

[7] D. B. Davidson, *Computational electromagnetics for RF and microwave engineering*. Cambridge University Press, 2010.

[8] J. W. Schuster and R. J. Luebbers, 'Comparison of GTD and FDTD predictions for UHF radio wave propagation in a simple outdoor urban environment', in *Antennas and Propagation Society International Symposium, 1997. IEEE., 1997 Digest*, vol. 3, Jul. 1997, 2022–2025 vol.3.

[9] F. S. de Adana, O. G. Blanco, I. G. Diego, J. P. Arriaga and M. F. Catedra, 'Propagation model based on ray tracing for the design of personal communication systems in indoor environments', *IEEE Transactions on Vehicular Technology*, vol. 49, no. 6, pp. 2105–2112, Nov. 2000.

[10] W. S. Ament, 'Toward a theory of reflection by a rough surface', *Proceedings of the IRE*, vol. 41, no. 1, pp. 142–146, Jan. 1953.

[11] V. Degli-Esposti, F. Fuschini, E. M. Vitucci and G. Falciasecca, 'Measurement and modelling of scattering from buildings', *IEEE Transactions on Antennas and Propagation*, vol. 55, no. 1, pp. 143–153, 2007.

[12] Y. Lostanlen and G. Gougeon, 'Introduction of diffuse scattering to enhance ray-tracing methods for the analysis of deterministic indoor UWB radio channels', in *Electromagnetics in Advanced Applications, 2007. ICEAA 2007. International Conference on*, Sep. 2007, pp. 903–906.

[13] V. Degli-Esposti, 'A diffuse scattering model for urban propagation prediction', *IEEE Transactions on Antennas and Propagation*, vol. 49, no. 7, pp. 1111–1113, Jul. 2001.

[14] Y. Cocheril and R. Vauzelle, 'A new ray-tracing based wave propagation model including rough surfaces scattering', *Progress In Electromagnetics Research*, vol. 75, pp. 357–381, 2007.

[15] J. Jürvelüinen and K. Haneda, 'Sixty gigahertz indoor radio wave propagation prediction method based on full scattering model', *Radio Science*, vol. 49, no. 4, pp. 293–305, Apr. 2014.

[16] J. Pascual-Garcia, M. T. Martinez-Ingles, J. M. M. Garcia-Pardo, J. V. Rodriguez and L. J. Llácer, 'Using tuned diffuse scattering parameters in ray tracing channel modeling', in *2015 9th European Conference on Antennas and Propagation (EuCAP)*, May 2015, pp. 1–4.

[17] J. Pascual-García, J. M. Molina-García-Pardo, M. T. Martínez-Inglés, J. V. Rodríguez and N. Saurín-Serrano, 'On the importance of diffuse scattering model parameterization in indoor wireless channels at mm-wave frequencies', *IEEE Access*, vol. 4, pp. 688–701, 2016.

[18] V. Degli-Esposti, D. Guiducci, A. de'Marsi, P. Azzi and F. Fuschini, 'An advanced field prediction model including diffuse scattering', *IEEE Transactions on Antennas and Propagation*, vol. 52, no. 7, pp. 1717–1728, Jul. 2004.

[19] M.-L. Zhai, W.-Y. Yin, Z. (Chen, H. Nie and X.-H. Wang, 'Modeling of ultra-wideband indoor channels with the modified leapfrog ADI-FDTD method', *International Journal of Numerical Modelling: Electronic Networks, Devices and Fields*, vol. 28, no. 1, pp. 50–64,

[20] A. Alighanbari and C. D. Sarris, 'Rigorous and efficient time-domain modeling of electromagnetic wave propagation and fading statistics in indoor wireless channels', *IEEE Transactions on Antennas and Propagation*, vol. 55, no. 8, pp. 2373–2381, Aug. 2007.

[21] C.-P. Lim, J. L. Volakis, K. Sertel, R. W. Kindt and A. Anastasopoulos, 'Indoor propagation models based on rigorous methods for site-specific multipath environments', *IEEE Transactions on Antennas and Propagation*, vol. 54, no. 6, pp. 1718–1725, Jun. 2006.

[22] G. de la Roche and J. M. Gorce, 'A 3D formulation of MR-FDPF for simulating indoor radio propagation', in *2006 First European Conference on Antennas and Propagation*, Nov. 2006, pp. 1–6.

[23] G. de la Roche, J. M. Gorcey and J. Zhang, 'Optimized implementation of the 3D MR-FDPF method for indoor radio propagation predictions', in *2009 3rd European Conference on Antennas and Propagation*, Mar. 2009, pp. 2241–2245.

[24] X. Tu, H. Hu, Z. Lai, J. M. Gorce and J. Zhang, 'Performance comparison of MR-FDPF and ray launching in an indoor office scenario', in *2013 Loughborough Antennas Propagation Conference (LAPC)*, Nov. 2013, pp. 424–428.

[25] C. C. Lu, 'Indoor radio-wave propagation modeling by multilevel fast multipole algorithm', *Microwave and Optical Technology Letters*, vol. 29, no. 3, pp. 168–175, 2001.

[26] T. S. Rappaport, S. Sun, R. 5zus, H. Zhao, Y. Azar, K. Wang, G. N. Wong, J. K. Schulz, M. Samimi and F. Gutierrez, 'Millimeter wave mobile communications for 5G cellular: It will work!', *IEEE Access*, vol. 1, pp. 335–349, 2013.

[27] J. D. Parsons and P. J. D. Parsons, 'The mobile radio propagation channel', 1992.

[28] F. Fuschini, E. M. Vitucci, M. Barbiroli, G. Falciasecca and V. Degli-Esposti, 'Ray tracing propagation modeling for future small-cell and indoor applications: A review of current techniques', *Radio Science*, vol. 50, no. 6, pp. 469–485,

[29] G. K. Theofilogiannakos, T. V. Yioultsis and T. D. Xenos, 'An efficient hybrid parabolic equation - integral equation method for the analysis of wave propagation in highly complex indoor communication environments', *Wireless Personal Communications*, vol. 43, no. 2, pp. 495–510, Oct. 2007.

[30] K. S. Butterworth, K. W. Sowerby and A. G. Williamson, 'Base station placement for in-building mobile communication systems to yield high capacity and efficiency', *IEEE Transactions on Communications*, vol. 48, no. 4, pp. 658–669, Apr. 2000.

[31] A. C. M. Austin, M. J. Neve and G. B. Rowe, 'Modeling propagation in multifloor buildings using the FDTD method', *IEEE Transactions on Antennas and Propagation*, vol. 59, no. 11, pp. 4239–4246, Nov. 2011.

[32] T. S. Rappaport *et al.*, *Wireless communications: principles and practice*. prentice hall PTR New Jersey, 1996, vol. 2.

[33] P. Bernardi, M. Cavagnaro, S. Pisa and E. Piuzzi, 'SAR distribution and temperature increase in an anatomical model of the human eye exposed to the field radiated by the user antenna in a wireless LAN', *IEEE Transactions on Microwave Theory and Techniques*, vol. 46, no. 12, pp. 2074–2082, Dec. 1998.

[34] F. Mazhar, M. G. Khan and B. Sällberg, 'Precise indoor positioning using UWB: A review of methods, algorithms and implementations', *Wireless Personal Communications*, vol. 97, no. 3, pp. 4467–4491, Dec. 2017.

[35] I. Bisio, F. Lavagetto, M. Marchese, M. Pastorino and A. Randazzo, 'Training-less fingerprinting-based indoor positioning algorithms with smartphones using electromagnetic propagation models', in *2012 IEEE International Conference on Imaging Systems and Techniques Proceedings*, Jul. 2012, pp. 190–194.

[36] M. R. Mahfouz, C. Zhang, B. C. Merkl, M. J. Kuhn and A. E. Fathy, 'Investigation of high-accuracy indoor 3-D positioning using UWB technology', *IEEE Transactions on Microwave Theory and Techniques*, vol. 56, no. 6, pp. 1316–1330, Jun. 2008.

[37] J. Kulmer, E. Leitinger, P. Meissner, S. Hinteregger and K. Witrisal, 'Cooperative localization and tracking using multipath channel information', in *2016 International Conference on Localization and GNSS (ICL-GNSS)*, Jun. 2016, pp. 1–6.

[38] P. Meissner, E. Leitinger, M. Lafer and K. Witrisal, 'Real-time demonstration of multipath-assisted indoor navigation and tracking (MINT)', in *2014 IEEE International Conference on Communications Workshops (ICC)*, Jun. 2014, pp. 144–149.

[39] L. Yang and G. B. Giannakis, 'Ultra-wideband communications: An idea whose time has come', *IEEE Signal Processing Magazine*, vol. 21, no. 6, pp. 26–54, Nov. 2004.

[40] X. Shen, M. Guizani, H. H. Chen, R. C. Qiu, A. F. Molisch and L. B. Milstein, 'Guest editorial ultra-wideband wireless communications - theory and applications', *IEEE Journal on Selected Areas in Communications*, vol. 24, no. 4, pp. 713–716, Apr. 2006.

[41] T. K. Sarkar, Z. Ji, K. Kim, A. Medouri and M. Salazar-Palma, 'A survey of various propagation models for mobile communication', *IEEE Antennas and Propagation Magazine*, vol. 45, no. 3, pp. 51–82, Jun. 2003.

[42] A. F. Molisch, *Wireless communications*. John Wiley & Sons, 2012, vol. 34.

[43] A. Valcarce, G. D. L. Roche and J. Zhang, 'A GPU approach to FDTD for radio coverage prediction', in *Communication Systems, 2008. ICCS 2008. 11th IEEE Singapore International Conference on*, Nov. 2008, pp. 1585–1590.

[44] V. Degli-Esposti, G. Falciasecca, F. Fuschini and E. M. Vitucci, 'A meaningful indoor path-loss formula', *IEEE Antennas and Wireless Propagation Letters*, vol. 12, pp. 872–875, 2013.

[45] D. Plets, W. Joseph, K. Vanhecke, E. Tanghe and L. Martens, 'Simple indoor path loss prediction algorithm and validation in living lab setting', *Wireless Personal Communications*, vol. 68, no. 3, pp. 535–552, Feb. 2013.

[46] J. Weng, X. Tu, Z. Lai, S. Salous and J. Zhang, 'Modelling the mmWave channel based on intelligent ray launching model', in *Antennas and Propagation (EuCAP), 2015 9th European Conference on*, IEEE, 2015, pp. 1–4.

[47] F. S. De Adana, O. G. Blanco, I. G. Diego, J. P. Arriaga and M. F. Cátedra, 'Propagation model based on ray tracing for the design of personal communication systems in indoor environments', *IEEE Transactions on Vehicular Technology*, vol. 49, no. 6, pp. 2105–2112, 2000.

[48] K. Belbase, M. Kim and J.-i. Takada, 'Study of propagation mechanisms and identification of scattering objects in indoor multipath channels at 11 GHz', in *Antennas and Propagation (EuCAP), 2015 9th European Conference on*, IEEE, 2015, pp. 1–4.

[49] A. Alighanbari and C. D. Sarris, 'Parallel time-domain full-wave analysis and system-level modeling of ultrawideband indoor communication systems', *IEEE Transactions on Antennas and Propagation*, vol. 57, no. 1, pp. 231–240, Jan. 2009.

[50] L. Azpilicueta, F. Falcone and R. 1aswamy, 'A hybrid ray launching-diffusion equation approach for propagation prediction in complex indoor environments', *IEEE Antennas and Wireless Propagation Letters*, vol. 16, pp. 214–217, 2017.

[51] L.-R. Harris, T. Hikage and T. Nojima, 'Using large-scale FDTD method to obtain precise numerical estimation of indoor wireless local area network office environment', *IEICE transactions on fundamentals of electronics, communications and computer sciences*, vol. 92, no. 9, pp. 2177–2183, 2009.

[52] A. Valcarce, G. de la Roche, L. Nagy, J. F. Wagen and J. M. Gorce, 'A new trend in propagation prediction', *IEEE Vehicular Technology Magazine*, vol. 6, no. 2, pp. 73–81, Jun. 2011.

[53] A. Laner, A. Bahr and I. Wolff, 'FDTD simulations of indoor propagation', in *Proceedings of IEEE Vehicular Technology Conference (VTC)*, Jun. 1994, 883–886 vol.2.

[54] Y. Wang, S. Safavi-Naeini and S. K. Chaudhuri, 'A hybrid technique based on combining ray tracing and FDTD methods for site-specific modeling of indoor radio wave propagation', *IEEE Transactions on Antennas and Propagation*, vol. 48, no. 5, pp. 743–754, May 2000.

[55] M. Hata, 'Empirical formula for propagation loss in land mobile radio services', *IEEE Transactions on Vehicular Technology*, vol. 29, no. 3, pp. 317–325, Aug. 1980.

[56] P. Harley, 'Short distance attenuation measurements at 900 MHz and 1.8 GHz using low antenna heights for microcells', *IEEE Journal on Selected Areas in Communications*, vol. 7, no. 1, pp. 5–11, Jan. 1989.

[57] A. Neskovic, N. Neskovic and G. Paunovic, 'Modern approaches in modeling of mobile radio systems propagation environment', *IEEE Communications Surveys Tutorials*, vol. 3, no. 3, pp. 2–12, Mar. 2000.

[58] A. A. M. Saleh and R. Valenzuela, 'A statistical model for indoor multipath propagation', *IEEE Journal on Selected Areas in Communications*, vol. 5, no. 2, pp. 128–137, Feb. 1987.

[59] Q. Spencer, M. Rice, B. Jeffs and M. Jensen, 'A statistical model for angle of arrival in indoor multipath propagation', in *1997 IEEE 47th Vehicular Technology Conference. Technology in Motion*, vol. 3, May 1997, 1415–1419 vol.3.

[60] C. B. Andrade and R. P. F. Hoefel, 'IEEE 802.11 WLANs: A comparison on indoor coverage models', in *CCECE 2010*, May 2010, pp. 1–6.

[61] K.-W. Cheung, J. H. M. Sau and R. D. Murch, 'A new empirical model for indoor propagation prediction', *IEEE Transactions on Vehicular Technology*, vol. 47, no. 3, pp. 996–1001, Aug. 1998.

[62] S. Shellhammer, 'Overview of ITU-R P. 1238-1, propagation data and prediction methods for planning of indoor radiocommunication systems and radio lan in the frequency band 900 MHz to 100 GHz', *doc.: IEEE802*, pp. 15–00, 2000.

[63] C. L. Holloway, M. G. Cotton and P. McKenna, 'A model for predicting the power delay profile characteristics inside a room', *IEEE Transactions on Vehicular Technology*, vol. 48, no. 4, pp. 1110–1120, Jul. 1999.

[64] G. Steinböck, T. Pedersen, B. H. Fleury, W. Wang and R. Raulefs, 'Distance dependent model for the delay power spectrum of in-room radio channels', *IEEE Transactions on Antennas and Propagation*, vol. 61, no. 8, pp. 4327–4340, Aug. 2013.

[65] D. C. Karia, T. Potdar, B. K. Lande and R. D. Daruwala, 'Modeling of indoor radio propagation channel for IEEE 802.11b/g', in *International Conference on Next Generation Networks*, Sep. 2010, pp. 1–6.

[66] Y. F. Solahuddin and R. Mardeni, 'Indoor empirical path loss prediction model for 2.4 GHz 802.11n network', in *2011 IEEE International Conference on Control System, Computing and Engineering*, Nov. 2011, pp. 12–17.

[67] K. A. Remley, H. R. Anderson and A. Weisshar, 'Improving the accuracy of ray-tracing techniques for indoor propagation modeling', *IEEE Transactions on Vehicular Technology*, vol. 49, no. 6, pp. 2350–2358, Nov. 2000.

[68] R. K. Arora and J. R. Wait, 'Refraction theories of radio wave propagation through the troposphere - a review', *Radio Science*, vol. 13, no. 3, pp. 599–600, May 1978.

[69] S. Grubisic, W. P. Carpes, C. B. Lima and P. Kuo-Peng, 'Ray-tracing propagation model using image theory with a new accurate approximation for transmitted rays through walls', *IEEE Transactions on Magnetics*, vol. 42, no. 4, pp. 835–838, Apr. 2006.

[70] J. B. Keller, 'Geometrical theory of diffraction', *JOSA*, vol. 52, no. 2, pp. 116–130, 1962.

[71] R. G. Kouyoumjian and P. H. Pathak, 'A uniform geometrical theory of diffraction for an edge in a perfectly conducting surface', *Proceedings of the IEEE*, vol. 62, no. 11, pp. 1448–1461, 1974.

[72] R. Luebbers, 'Finite conductivity uniform GTD versus knife edge diffraction in prediction of propagation path loss', *IEEE Transactions on Antennas and Propagation*, vol. 32, no. 1, pp. 70–76, Jan. 1984.

[73] R. J. Luebbers, 'Comparison of lossy wedge diffraction coefficients with application to mixed path propagation loss prediction', *IEEE Transactions on Antennas and Propagation*, vol. 36, no. 7, pp. 1031–1034, Jul. 1988.

[74] ——, 'A heuristic UTD slope diffraction coefficient for rough lossy wedges', *IEEE Transactions on Antennas and Propagation*, vol. 37, no. 2, pp. 206–211, Feb. 1989.

[75] W. S. Ament, 'Toward a theory of reflection by a rough surface', *Proceedings of the IRE*, vol. 41, no. 1, pp. 142–146, Jan. 1953.

[76] H. R. Anderson, 'A second generation 3-D ray-tracing model using rough surface scattering', in *Proceedings of Vehicular Technology Conference - VTC*, vol. 1, Apr. 1996, 46–50 vol.1.

[77] F. Villanese, W. G. Scanlon, N. E. Evans and E. Gambi, 'Hybrid image/ray-shooting UHF radio propagation predictor for populated indoor environments', *Electronics Letters*, vol. 35, no. 21, pp. 1804–1805, Oct. 1999.

[78] S.-H. Chen and S.-K. Jeng, 'An SBR/image approach for radio wave propagation in indoor environments with metallic furniture', *IEEE Transactions on Antennas and Propagation*, vol. 45, no. 1, pp. 98–106, Jan. 1997.

[79] A. S. Glassner, 'Space subdivision for fast ray tracing', *IEEE Computer Graphics and Applications*, vol. 4, no. 10, pp. 15–24, Oct. 1984.

[80] F. A. Agelet, F. P. Fontan and A. Formella, 'Fast ray tracing for microcellular and indoor environments', *IEEE Transactions on Magnetics*, vol. 33, no. 2, pp. 1484–1487, Mar. 1997.

[81] G. Tiberi, S. Bertini, A. Monorchio, F. Giannetti and G. Manara, 'Computationally efficient ray-tracing technique for modelling ultrawideband indoor propagation channels', *IET Microwaves, Antennas Propagation*, vol. 3, no. 3, pp. 395–401, Apr. 2009.

[82] B. S. Lee, A. R. Nix and J. P. McGeehan, 'A spatio-temporal ray launching propagation model for UMTS pico and microcellular environments', in *IEEE VTS 53rd Vehicular Technology Conference, Spring 2001. Proceedings*, vol. 1, 2001, 367–371 vol.1.

[83] Z. Lai, G. De La ROCHE, N. Bessis, P. Kuonen, G. Clapworthy, D. Zhou and J. Zhang, 'Intelligent ray launching algorithm for indoor scenarios.', *Radioengineering*, vol. 20, no. 2, 2011.

[84] Z. Lai, N. Bessis, G. de la Roche, P. Kuonen, J. Zhang and G. Clapworthy, 'A new approach to solve angular dispersion of discrete ray launching for urban scenarios', in *2009 Loughborough Antennas Propagation Conference*, Nov. 2009, pp. 133–136.

[85] L. Azpilicueta, M. Rawat, K. Rawat, F. M. Ghannouchi and F. Falcone, 'A ray launching-neural network approach for radio wave propagation analysis in complex indoor environments', *IEEE Transactions on Antennas and Propagation*, vol. 62, no. 5, pp. 2777–2786, May 2014.

[86] R. Tahri, D. Fournier, S. Collonge, G. Zaharia and G. E. Zein, 'Efficient and fast gaussian beam-tracking approach for indoor-propagation modeling', *Microwave and Optical Technology Letters*, vol. 45, no. 5, pp. 378–381,

[87] J. Tan, Z. Su and Y. Long, 'A full 3-D GPU-based beam-tracing method for complex indoor environments propagation modeling', *IEEE Transactions on Antennas and Propagation*, vol. 63, no. 6, pp. 2705–2718, Jun. 2015.

[88] P. Lyu, X. Xu, S. Yan and Z. Ren, '60 GHz indoor propagation with time-domain geometric-optics', *IEEE Transactions on Magnetics*, vol. 52, no. 3, pp. 1–4, Mar. 2016.

[89] A. Lauer, I. Wolff, A. Bahr, J. Pamp, J. Kunisch and I. Wolff, 'Multi-mode FDTD simulations of indoor propagation including antenna properties', in *1995 IEEE 45th Vehicular Technology Conference. Countdown to the Wireless Twenty-First Century*, vol. 1, Jul. 1995, 454–458 vol.1.

[90] G. D. Kondylis, F. D. Flaviis, G. J. Pottie and T. Itoh, 'A memory-efficient formulation of the finite-difference time-domain method for the solution of Maxwell equations', *IEEE Transactions on Microwave Theory and Techniques*, vol. 49, no. 7, pp. 1310–1320, Jul. 2001.

[91] Z. Sayegh, M. Latrach, F. Costen, G. E. Zein and G. Zaharia, 'Numerical modeling of human effect on indoor propagation', in *2013 13th Mediterranean Microwave Symposium (MMS)*, Sep. 2013, pp. 1–4.

[92] M. L. Zhai, W. Y. Yin and Z. Chen, 'Modelling of electromagnetic propagation characteristics in indoor wireless communication systems using the LOD-FDTD method', in *2013 Proceedings of the International Symposium on Antennas Propagation*, vol. 02, Oct. 2013, pp. 701–704.

[93] C.-N. Kuo, V. A. Thomas, S. T. Chew, B. Houshmand and T. Itoh, 'Small signal analysis of active circuits using FDTD algorithm', *IEEE Microwave and Guided Wave Letters*, vol. 5, no. 7, pp. 216–218, Jul. 1995.

[94] A. Taflove, S. C. Hagness *et al.*, 'Computational electrodynamics: The finite-difference time-domain method', *Norwood, 2nd Edition, MA: Artech House, l995*, 1995.

[95] V. Van and S. K. Chaudhuri, 'A hybrid implicit-explicit FDTD scheme for nonlinear optical waveguide modeling', *IEEE Transactions on Microwave Theory and Techniques*, vol. 47, no. 5, pp. 540–545, May 1999.

[96] K. Yee, 'Numerical solution of initial boundary value problems involving Maxwell's equations in isotropic media', *IEEE Transactions on Antennas and Propagation*, vol. 14, no. 3, pp. 302–307, May 1966.

[97] A. Bayliss, M. Gunzburger and E. Turkel, 'Boundary conditions for the numerical solution of elliptic equations in exterior regions', *SIAM Journal on Applied Mathematics*, vol. 42, no. 2, pp. 430–451, 1982.

[98] B. Engquist and A. Majda, 'Absorbing boundary conditions for numerical simulation of waves', *Proceedings of the National Academy of Sciences*, vol. 74, no. 5, pp. 1765–1766, 1977.

[99] R. L. Higdon, 'Numerical absorbing boundary conditions for the wave equation', *Mathematics of computation*, vol. 49, no. 179, pp. 65–90, 1987.

[100] Z.-F. Liao, K.-l. Huang, B.-p. Yang and Y.-F. YUAN, 'A transmitting boundary for transient wave analyses', *Science in China Series A-Mathematics, Physics, Astronomy & Technological Science*, vol. 27, no. 10, pp. 1063–1076, 1984.

[101] O. M. Ramahi, 'The concurrent complementary operators method for FDTD mesh truncation', *IEEE Transactions on Antennas and Propagation*, vol. 46, no. 10, pp. 1475–1482, 1998.

[102] Y. Mao, A. Z. Elsherbeni, S. Li and T. Jiang, 'Non-uniform surface impedance absorbing boundary condition for FDTD method', in *Antennas and Propagation (EUCAP), 2017 11th European Conference on*, IEEE, 2017, pp. 516–519.

[103] B. Wei, S.-q. Zhang, F. Wang and D. Ge, 'A novel UPML FDTD absorbing boundary condition for dispersive media', *Waves in Random and Complex Media*, vol. 20, no. 3, pp. 511–527, 2010.

[104] B. Abdulkareem, J.-P. Bérenger, F. Costen, R. Himeno and H. Yokota, 'An operator absorbing boundary condition for the absorption of electromagnetic waves in dispersive media', *IEEE Transactions on Antennas and Propagation*, 2018.

[105] J.-P. Berenger, 'A perfectly matched layer for the absorption of electromagnetic waves', *Journal of computational physics*, vol. 114, no. 2, pp. 185–200, 1994.

[106] J. P. Berenger, 'Improved PML for the FDTD solution of wave-structure interaction problems', *IEEE Transactions on Antennas and Propagation*, vol. 45, no. 3, pp. 466–473, Mar. 1997.

[107] J. A. Roden and S. D. Gedney, 'Convolution PML (CPML): An efficient FDTD implementation of the CFS–PML for arbitrary media', *Microwave and Optical Technology Letters*, vol. 27, no. 5, pp. 334–339,

[108] J. Shibayama, M. Muraki, J. Yamauchi and H. Nakano, 'Efficient implicit FDTD algorithm based on locally one-dimensional scheme', *Electronics Letters*, vol. 41, no. 19, pp. 1046–1047, Sep. 2005.

[109] E. L. Tan, 'Unconditionally stable LOD-FDTD method for 3-D Maxwell's equations', *IEEE Microwave and Wireless Components Letters*, vol. 17, no. 2, pp. 85–87, Feb. 2007.

[110] F. Zhen, Z. Chen and J. Zhang, 'Toward the development of a three-dimensional unconditionally stable finite-difference time-domain method', *IEEE Transactions on Microwave Theory and Techniques*, vol. 48, no. 9, pp. 1550–1558, Sep. 2000.

[111] A. Valcarce, G. De La Roche, Á. Jüttner, D. López-Pérez and J. Zhang, 'Applying FDTD to the coverage prediction of WiMAX femtocells', *EURASIP J. Wirel. Commun. Netw.*, vol. 2009, 3:1–3:13, Feb. 2009.

[112] U. T. Virk, K. Haneda, V. M. Kolmonen, J. F. Wagen and P. Vainikainen, 'Full-wave characterization of indoor office environment for accurate coverage analysis', in *Electromagnetics in Advanced Applications (ICEAA), 2013 International Conference on*, Sep. 2013, pp. 1197–1200.

[113] A. Y. Rykshin, V. V. Scherbinin and I. P. Molostov, 'NVIDIA CUDA technology application to numerical simulation of electromagnetic pulse scattering by dual layered structure', in *Control and Communications (SIBCON), 2015 International Siberian Conference on*, May 2015, pp. 1–4.

[114] G. Y. Delisle and L. Talbi, 'Multipath impulse response modelling for indoor channel using TD-BEM', *Canadian Journal of Electrical and Computer Engineering*, vol. 22, no. 2, pp. 55–61, Apr. 1997.

[115] B. D. Backer, F. Olyslager and D. D. Zutter, 'An integral equation approach to the prediction of indoor wave propagation', *Radio Science*, vol. 32, no. 5, pp. 1833–1850,

[116] R. W. Kindt and J. L. Volakis, 'Array decomposition-fast multipole method for finite array analysis', *Radio Science*, vol. 39, no. 2, 2004.

[117] B. Chopard, P. O. Luthi and J. F. Wagen, 'Lattice Boltzmann method for wave propagation in urban microcells', *IEE Proceedings - Microwaves, Antennas and Propagation*, vol. 144, no. 4, pp. 251–255, Aug. 1997.

[118] W. J. R. Hoefer, 'The transmission-line matrix method - theory and applications', *IEEE Transactions on Microwave Theory and Techniques*, vol. 33, no. 10, pp. 882–893, Oct. 1985.

[119] J. M. Gorce, K. Jaffres-Runser and G. de la Roche, 'Deterministic approach for fast simulations of indoor radio wave propagation', *IEEE Transactions on Antennas and Propagation*, vol. 55, no. 3, pp. 938–948, Mar. 2007.

[120] G. de la Roche, X. Gallon, J. m. Gorce and G. Villemaud, '2.5D extensions of the frequency domain parflow algorithm for simulating 802.11b/g radio coverage in multifloored buildings', in *IEEE Vehicular Technology Conference*, Sep. 2006, pp. 1–5.

[121] J. M. Gorce, E. Jullo and K. Runser, 'An adaptive multi-resolution algorithm for 2D simulations of indoor propagation', in *Twelfth International Conference on Antennas and Propagation, 2003 (ICAP 2003). (Conf. Publ. No. 491)*, vol. 1, Mar. 2003, 216–219 vol.1.

[122] H. Inanoglu and E. Topuz, 'Hybrid representations for indoor propagation modeling', in *Proceedings of 1997 Wireless Communications Conference*, Aug. 1997, pp. 215–219.

[123] N. Noori and H. Oraizi, 'Evaluation of MIMO channel capacity in indoor environments using vector parabolic equation method', *Progress In Electromagnetics Research*, vol. 4, pp. 13–25, 2008.

[124] A. Hrovat, G. Kandus and T. Javornik, 'A survey of radio propagation modeling for tunnels', *IEEE Communications Surveys Tutorials*, vol. 16, no. 2, pp. 658–669, Feb. 2014.

[125] G. R. Hadley, 'Wide-angle beam propagation using Padé approximant operators', *Opt. Lett.*, vol. 17, no. 20, pp. 1426–1428, Oct. 1992.

[126] ——, 'Multistep method for wide-angle beam propagation', *Opt. Lett.*, vol. 17, no. 24, pp. 1743–1745, Dec. 1992.

[127] F. N. B. Magno, J. F. de Souza, K. Cozzolino, J. C. Costa and G. P. d. S. Cavalcante, 'A model for radio propagation loss prediction in buildings using wide-angle parabolic equations', in *2009 SBMO/IEEE MTT-S International Microwave and Optoelectronics Conference (IMOC)*, Nov. 2009, pp. 491–495.

[128] G. K. Theofilogiannakos, T. D. Xenos and T. V. Yioultsis, 'A hybrid parabolic equation - integral equation technique for wave propagation modeling of indoor communications', *IEEE Transactions on Magnetics*, vol. 45, no. 3, pp. 1112–1115, Mar. 2009.

[129] G. S. Baron, E. Fiume and C. D. Sarris, 'Graphics hardware accelerated multiresolution time-domain technique: Development, evaluation and applications', *IET Microwaves, Antennas Propagation*, vol. 2, no. 3, pp. 288–301, Apr. 2008.

[130] P. N. Zakharov, R. A. Dudov, E. V. Mikhailov, A. F. Korolev and A. P. Sukhorukov, 'Finite integration technique capabilities for indoor propagation prediction', in *2009 Loughborough Antennas Propagation Conference*, Nov. 2009, pp. 369–372.

[131] P. N. Zakharov, E. V. Mikhailov, A. A. Potapov, A. F. Korolev and A. P. Sukhorukov, 'Comparative analysis of ray tracing, finite integration technique and empirical models using ultra-detailed indoor environment model and measurements', in *2009 3rd IEEE International Symposium on Microwave, Antenna, Propagation and EMC Technologies for Wireless Communications*, Oct. 2009, pp. 169–176.

[132] M. Thiel and K. Sarabandi, 'A hybrid method for indoor wave propagation modeling', *IEEE Transactions on Antennas and Propagation*, vol. 56, no. 8, pp. 2703–2709, Aug. 2008.

[133] J. Leung and C. D. Sarris, 'Hybrid FDTD/waveguide theory for indoor hallway propagation modeling', in *2009 IEEE Antennas and Propagation Society International Symposium*, Jun. 2009, pp. 1–4.

[134] A. Skarlatos, R. Schuhmann and T. Weiland, 'Coupling of finite integration technique and ray tracing', in *IEEE Antennas and Propagation Society International Symposium*, vol. 4, Jul. 2001, 318–321 vol.4.

[135] M. Porebska, T. Kayser and W. Wiesbeck, 'Verification of a hybrid ray-tracing/FDTD model for indoor ultra-wideband channels', in *2007 European Conference on Wireless Technologies*, Oct. 2007, pp. 169–172.

[136] A. C. M. Austin, N. Sood, J. Siu and C. D. Sarris, 'Application of polynomial chaos to quantify uncertainty in deterministic channel models', *IEEE Transactions on Antennas and Propagation*, vol. 61, no. 11, pp. 5754–5761, Nov. 2013.

[137] V. Mohtashami and A. A. Shishegar, 'Effects of inaccuracy of material permittivities on ray tracing results for site- specific indoor propagation modeling', in *2013 IEEE-APS Topical Conference on Antennas and Propagation in Wireless Communications (APWC)*, Sep. 2013, pp. 1172–1175.

[138] ——, 'Effects of geometrical uncertainties on ray tracing results for site-specific indoor propagation modeling', in *2013 IEEE-APS Topical Conference on Antennas and Propagation in Wireless Communications (APWC)*, Sep. 2013, pp. 836–839.

[139] ——, 'Sensitivity analysis of ray tracing to the geometrical description of the environment', *IET Microwaves, Antennas Propagation*, vol. 10, no. 11, pp. 1225–1234, 2016.

[140] J. Järveläinen, M. Kurkela and K. Haneda, 'Impacts of room structure models on the accuracy of 60 GHz indoor radio propagation prediction', *IEEE Antennas and Wireless Propagation Letters*, vol. 14, pp. 1137–1140, 2015.

[141] CUDA NVIDIA, *Programming guide*, 2010.

[142] W. C. Chew, E. Michielssen, J. Song and J.-M. Jin, *Fast and efficient algorithms in computational electromagnetics*. Artech House, Inc., 2001.

[143] C. A. Balanis, *Advanced engineering electromagnetics*. John Wiley & Sons, 1999.

[144] D. Fleisch, *A student's guide to Maxwell's equations*. Cambridge University Press, 2008.

[145] A. F. Peterson, S. L. Ray and R. Mittra, *Computational methods for electromagnetics*. IEEE press New York, 1998, vol. 2.

[146] W. C. Gibson, *The method of moments in electromagnetics*. CRC press, 2014.

[147] R. F. Harrington, 'The method of moments in electromagnetics', *Journal of Electromagnetic waves and Applications*, vol. 1, no. 3, pp. 181–200, 1987.

[148] M. Kline, 'An asymptotic solution of Maxwell's equations', *Communications on Pure and Applied Mathematics*, vol. 4, no. 2-3, pp. 225–262, 1951.

[149] R. K. Luneburg and M. Herzberger, *Mathematical theory of optics*. Univ of California Press, 1964.

[150] M. Kline, 'Electromagnetic theory and geometrical optics', AIR FORCE CAMBRIDGE RESEARCH LABS LG HANSCOM FIELD MASS, Tech. Rep., 1962.

[151] A. S. Glassner, *An introduction to ray tracing*. Elsevier, 1989.

[152] E. M. Kenny and E. O. Nuallain, 'Convex space building discretization for ray-tracing', *IEEE Transactions on Antennas and Propagation*, vol. 65, no. 5, pp. 2578–2591, May 2017.

[153] H. Ling, R.-C. Chou and S.-W. Lee, 'Shooting and bouncing rays: Calculating the RCS of an arbitrarily shaped cavity', *IEEE Transactions on Antennas and propagation*, vol. 37, no. 2, pp. 194–205, 1989.

[154] B. R. Levy and J. B. Keller, 'Diffraction by a smooth object', *Communications on pure and applied mathematics*, vol. 12, no. 1, pp. 159–209, 1959.

[155] R. Kouyoumjian, P. Pathak and W. Burnside, 'A uniform GTD for the diffraction by edges, vertices and convex surfaces', *Theoretical Methods for Determining the Interaction of Electromagnetic Waves with Structures*, 1981.

[156] D. A. McNamara and C. Pistotius, 'Introduction to the uniform geometrical theory of diffraction', *Artech House Microwave Library*, 1990.

[157] H.-T. Chou and T.-H. Lee, 'Asymptotic high frequency methods', in *Novel Technologies for Microwave and Millimeter - Wave Applications*. Boston, MA: Springer US, 2004, pp. 425–460.

[158] K. Zheng, H. Luo, Z. Mu, J. Li and G. Wei, 'Parallel TSS-FDTD method for analyzing underwater low-frequency electromagnetic propagation', *IEEE Antennas and Wireless Propagation Letters*, vol. 15, pp. 1217–1220, 2016.

[159] A. Lauer, W. Simon and A. Wien, 'FDTD XPU technology on systems with non uniform computer memory (NUMA) architecture', in *2016 10th European Conference on Antennas and Propagation (EuCAP)*, Apr. 2016, pp. 1–4.

[160] R. J. Adams and G. S. Brown, 'A combined field approach to scattering from infinite elliptical cylinders using the method of ordered multiple interactions', *IEEE Transactions on Antennas and Propagation*, vol. 47, no. 2, pp. 364–375, Feb. 1999.

[161] J. C. West, 'Integral equation formulation for iterative calculation of scattering from lossy rough surfaces', *IEEE Transactions on Geoscience and Remote Sensing*, vol. 38, no. 4, pp. 1609–1615, Jul. 2000.

[162] A. Taflove and M. E. Brodwin, 'Numerical solution of steady-state electromagnetic scattering problems using the time-dependent Maxwell's equations', *IEEE Transactions on Microwave Theory and Techniques*, vol. 23, no. 8, pp. 623–630, Aug. 1975.

[163] P. H. Harms, J.-F. Lee and R. Mittra, 'A study of the nonorthogonal FDTD method versus the conventional FDTD technique for computing resonant frequencies of cylindrical cavities', *IEEE Transactions on Microwave Theory and Techniques*, vol. 40, no. 4, pp. 741–746, 1992.

[164] R. Schuhmann and T. Weiland, 'A stable interpolation technique for FDTD on non-orthogonal grids', *International Journal of Numerical Modelling: Electronic Networks, Devices and Fields*, vol. 11, no. 6, pp. 299–306, 1998.

[165] 5. K. Chaudhari, 'Non-conventional discretization grid based FDTD for EM wave propagation in magnetized plasma metallic photonic crystal', *Progress In Electromagnetics Research*, vol. 49, pp. 211–219, 2016.

[166] R. F. Harrington, *Field computation by moment methods*. Wiley-IEEE Press, 1993.

[167] C. C. Su, 'The three-dimensional algorithm of solving the electric field integral equation using face-centered node points, conjugate gradient method, and FFT', *IEEE Transactions on Microwave Theory and Techniques*, vol. 41, no. 3, pp. 510–515, Mar. 1993.

[168] R. S. M. and S. T. K., 'Implicit solution of time-domain integral equations for arbitrarily shaped dielectric bodies', *Microwave and Optical Technology Letters*, vol. 21, no. 3, pp. 201–205,

[169] S. Rao, D. Wilton and A. Glisson, 'Electromagnetic scattering by surfaces of arbitrary shape', *IEEE Transactions on Antennas and Propagation*, vol. 30, no. 3, pp. 409–418, May 1982.

[170] D. Schaubert, D. Wilton and A. Glisson, 'A tetrahedral modeling method for electromagnetic scattering by arbitrarily shaped inhomogeneous dielectric bodies', *IEEE Transactions on Antennas and Propagation*, vol. 32, no. 1, pp. 77–85, Jan. 1984.

[171] I. S. Gradshteyn and I. M. Ryzhik, *Table of integrals, series, and products*. Academic press, 2014.

[172] J. Richmond, 'Scattering by a dielectric cylinder of arbitrary cross section shape', *IEEE Transactions on Antennas and Propagation*, vol. 13, no. 3, pp. 334–341, 1965.

[173] P. Zwamborn and P. M. Van Den Berg, 'The three dimensional weak form of the conjugate gradient FFT method for solving scattering problems', *IEEE Transactions on Microwave Theory and Techniques*, vol. 40, no. 9, pp. 1757–1766, 1992.

[174] Z. Q. Zhang, Q. H. Liu, C. Xiao, E. Ward, G. Ybarra and W. T. Joines, 'Microwave breast imaging: 3-D forward scattering simulation', *IEEE Transactions on Biomedical Engineering*, vol. 50, no. 10, pp. 1180–1189, 2003.

[175] A. M. Davie and A. J. Stothers, 'Improved bound for complexity of matrix multiplication', *Proceedings of the Royal Society of Edinburgh Section A: Mathematics*, vol. 143, no. 2, pp. 351–369, 2013.

[176] R. W. Farebrother, *Linear least squares computations*. Marcel Dekker, Inc., 1988.

[177] J. R. Shewchuk *et al.*, *An introduction to the conjugate gradient method without the agonizing pain*, 1994.

[178] V. Eijkhout, 'A bluffers' guide to iterative methods for systems of linear equations', May 2014.

[179] A. Greenbaum, *Iterative methods for solving linear systems*. Siam, 1997, vol. 17.

[180] H. A. Van der Vorst, *Iterative Krylov methods for large linear systems*. Cambridge University Press, 2003, vol. 13.

[181] J. C. West and J. M. Sturm, 'On iterative approaches for electromagnetic rough-surface scattering problems', *IEEE Transactions on Antennas and Propagation*, vol. 47, no. 8, pp. 1281–1288, Aug. 1999.

[182] J.-Y. Lee and R. A. Scholtz, 'Ranging in a dense multipath environment using an UWB radio link', *IEEE Journal on Selected Areas in Communications*, vol. 20, no. 9, pp. 1677–1683, Dec. 2002.

[183] S. Yu, Z. Deng, J. Jiao, S. Jiang, J. Mo and F. Xu, 'The multipath fading channel simulation for indoor positioning', in *China Satellite Navigation Conference (CSNC) 2016 Proceedings: Volume II*, Springer, 2016, pp. 341–347.

[184] M. Fakharzadeh, S. Jafarlou and A. Tabibiazar, 'Indoor multipath channel measurement at 60 GHz', in *2014 IEEE Antennas and Propagation Society International Symposium (APSURSI)*, Jul. 2014, pp. 1169–1170.

[185] Y. Saad, *Iterative methods for sparse linear systems*. siam, 2003, vol. 82.

[186] H. P. Decell Jr, 'An application of the Cayley-Hamilton theorem to generalized matrix inversion', *SIAM review*, vol. 7, no. 4, pp. 526–528, 1965.

[187] R. Fletcher, 'Conjugate gradient methods for indefinite systems', in *Numerical analysis*, Springer, 1976, pp. 73–89.

[188] C. C. Paige and M. A. Saunders, 'Solution of sparse indefinite systems of linear equations', *SIAM journal on numerical analysis*, vol. 12, no. 4, pp. 617–629, 1975.

[189] R. Barrett, M. W. Berry, T. F. Chan, J. Demmel, 6. Donato, J. Dongarra, V. Eijkhout, R. Pozo, C. Romine and H. Van der Vorst, *Templates for the solution of linear systems: building blocks for iterative methods*. Siam, 1994, vol. 43.

[190] H. A. Van der Vorst, 'Bi-CGSTAB: A fast and smoothly converging variant of Bi-CG for the solution of nonsymmetric linear systems', *SIAM Journal on scientific and Statistical Computing*, vol. 13, no. 2, pp. 631–644, 1992.

[191] P. Sonneveld, 'CGS, a fast Lanczos-type solver for nonsymmetric linear systems', *SIAM journal on scientific and statistical computing*, vol. 10, no. 1, pp. 36–52, 1989.

[192] G. H. Golub and C. F. Van Loan, *Matrix computations*. JHU Press, 2012, vol. 3.

[193] A. M. Bruaset, *A survey of preconditioned iterative methods*. CRC Press, 1995, vol. 328.

[194] M. Benzi, 'Preconditioning techniques for large linear systems: A survey', *Journal of computational Physics*, vol. 182, no. 2, pp. 418–477, 2002.

[195] J. Song, C.-C. Lu and W. C. Chew, 'Multilevel fast multipole algorithm for electromagnetic scattering by large complex objects', *IEEE Transactions on Antennas and Propagation*, vol. 45, no. 10, pp. 1488–1493, Oct. 1997.

[196] M. Bruning, P. Benner, A. Bunse-Gerstner, R. Bunger, J. Reiter and J. Ritter, 'A sparse approximate inverse preconditioner for the method of moments accelerated with the multilevel fast multipole method', in *IEEE Antennas and Propagation Society International Symposium*, vol. 2, 2002, 602–605 vol.2.

[197] X. M. Pan and X. Q. Sheng, 'Sparse approximate inverse preconditioner for multiscale dynamic electromagnetic problems', *Radio Science*, vol. 49, no. 11, pp. 1041–1051, Nov. 2014.

[198] T. Malas and L. Gurel, 'Scalable parallelization of the sparse-approximate-inverse (SAI) preconditioner for the solution of large-scale integral-equation problems', in *2009 IEEE Antennas and Propagation Society International Symposium*, Jun. 2009, pp. 1–4.

[199] M. T. Bettencourt, B. Zinser, R. E. Jorgenson and J. D. Kotulski, 'Performance portable sparse approximate inverse preconditioner for EFIE equations', in *2017 International Conference on Electromagnetics in Advanced Applications (ICEAA)*, Sep. 2017, pp. 1469–1472.

[200] J. Liu, Z. Li, H. Zhang and J. Su, 'The application of sparse approximate inverse preconditioner in the fast solution of volume-surface integral equation', in *2017 International Applied Computational Electromagnetics Society Symposium (ACES)*, Aug. 2017, pp. 1–2.

[201] E. Chow, 'A priori sparsity patterns for parallel sparse approximate inverse preconditioners', *SIAM Journal on Scientific Computing*, vol. 21, no. 5, pp. 1804–1822, 2000.

[202] M. J. Grote and T. Huckle, 'Parallel preconditioning with sparse approximate inverses', *SIAM Journal on Scientific Computing*, vol. 18, no. 3, pp. 838–853, 1997.

[203] E. Chow and Y. Saad, 'Approximate inverse preconditioners via sparse-sparse iterations', *SIAM Journal on Scientific Computing*, vol. 19, no. 3, pp. 995–1023, 1998.

[204] B. Carpentieri, L. Giraud and I. Duff, 'Some sparse pattern selection strategies for robust Frobenius norm minimization preconditioners in electromagnetism', SCAN-0005096, Tech. Rep., 2000.

[205] B. Carpentieri, I. S. Duff, L. Giraud and G. Sylvand, 'Combining fast multipole techniques and an approximate inverse preconditioner for large electromagnetism calculations', *SIAM Journal on Scientific Computing*, vol. 27, no. 3, pp. 774–792, 2005.

[206] K. W. Van Dongen, C. Brennan and W. M. Wright, 'Reduced forward operator for electromagnetic wave scattering problems', *IET Science, Measurement Technology*, vol. 1, no. 1, pp. 57–62, Jan. 2007.

[207] C.-C. Lu and W. C. Chew, 'Fast far field approximation for calculating the RCS of large objects', in *IEEE Antennas and Propagation Society International Symposium. 1995 Digest*, vol. 1, Jun. 1995, 22–25 vol.1.

[208] E. Bleszynski, M. Bleszynski and T. Jaroszewicz, 'AIM: Adaptive integral method for solving large-scale electromagnetic scattering and radiation problems', *Radio Science*, vol. 31, no. 5, pp. 1225–1251, Sep. 1996.

[209] J. L. Guo, J. Y. Li and Q. Z. Liu, 'Analysis of arbitrarily shaped dielectric radomes using adaptive integral method based on volume integral equation', *IEEE Transactions on Antennas and Propagation*, vol. 54, no. 7, pp. 1910–1916, Jul. 2006.

[210] Z. Q. Zhang and Q. H. Liu, 'A volume adaptive integral method (VAIM) for 3-D inhomogeneous objects', *IEEE Antennas and Wireless Propagation Letters*, vol. 1, pp. 102–105, 2002.

[211] W. C. Chew, T. J. Cui and J. M. Song, 'A FAFFA-MLFMA algorithm for electromagnetic scattering', *IEEE Transactions on Antennas and Propagation*, vol. 50, no. 11, pp. 1641–1649, Nov. 2002.

[212] C. Brennan and P. J. Cullen, 'Application of the fast far-field approximation to the computation of UHF pathloss over irregular terrain', *IEEE Transactions on Antennas and Propagation*, vol. 46, no. 6, pp. 881–890, Jun. 1998.

[213] J. Bolz, I. Farmer, E. Grinspun and P. Schröoder, 'Sparse matrix solvers on the GPU: Conjugate gradients and multigrid', *ACM transactions on graphics (TOG)*, vol. 22, no. 3, pp. 917–924, 2003.

[214] R. Helfenstein and J. Koko, 'Parallel preconditioned conjugate gradient algorithm on GPU', *Journal of Computational and Applied Mathematics*, vol. 236, no. 15, pp. 3584–3590, 2012.

[215] G. A. Gravvanis, C. K. Filelis-Papadopoulos and K. M. Giannoutakis, 'Solving finite difference linear systems on GPUs: CUDA based parallel explicit preconditioned biconjugate conjugate gradient type methods', *The Journal of Supercomputing*, vol. 61, no. 3, pp. 590–604, Sep. 2012.

[216] S. Xu, W. Xue, K. Wang and H. X. Lin, 'Generating approximate inverse preconditioners for sparse matrices using CUDA and GPGPU', *Journal of Algorithms & Computational Technology*, vol. 5, no. 3, pp. 475–500, 2011.

[217] R. Li and Y. Saad, 'GPU-accelerated preconditioned iterative linear solvers', *The Journal of Supercomputing*, vol. 63, no. 2, pp. 443–466, Feb. 2013.

[218] A. F. P. de Camargos, V. C. Silva, J. M. Guichon and G. Munier, 'Efficient parallel preconditioned conjugate gradient solver on GPU for FE modeling of electromagnetic fields in highly dissipative media', *IEEE Transactions on Magnetics*, vol. 50, no. 2, pp. 569–572, Feb. 2014.

[219] A. Dziekonski, A. Lamecki and M. Mrozowski, 'Jacobi and Gauss-Seidel preconditioned complex conjugate gradient method with GPU acceleration for finite element method', in *The 40th European Microwave Conference*, Sep. 2010, pp. 1305–1308.

[220] M. M. Dehnavi, D. M. Fernandez and D. Giannacopoulos, 'Enhancing the performance of conjugate gradient solvers on graphic processing units', *IEEE Transactions on Magnetics*, vol. 47, no. 5, pp. 1162–1165, May 2011.

[221] D. E. Lawrence and K. Sarabandi, 'Acoustic and electromagnetic wave interaction: Analytical formulation for acousto-electromagnetic scattering behavior of a dielectric cylinder', *IEEE Transactions on Antennas and Propagation*, vol. 49, no. 10, pp. 1382–1392, Oct. 2001.

[222] J. A. Stratton, *Electromagnetic theory*. John Wiley & Sons, 2007.

[223] C. F. Bohren and D. R. Huffman, *Absorption and scattering by a sphere*. Wiley Online Library, 1983.

[224] P. Meissner, M. Gan, F. Mani, E. Leitinger, M. Fröhle, C. Oestges, T. Zemen and K. Witrisal, 'On the use of ray tracing for performance prediction of UWB indoor localization systems', in *2013 IEEE International Conference on Communications Workshops (ICC)*, Jun. 2013, pp. 68–73.

[225] P. Meissner, E. Leitinger, S. Hinteregger, J. Kulmer, M. Lafer and K. Witrisal, *MeasureMINT UWB database, Graz University of Technology*, [Online] Available: www.spsc.tugraz.at/tools/UWBmeasurements, 2013.

[226] M. Born and E. Wolf, *Principles of optics: electromagnetic theory of propagation, interference and diffraction of light*. Elsevier, 2013.

[227] J. Gong and J. L. Volakis, 'AWE implementation for electromagnetic FEM analysis', *Electronics Letters*, vol. 32, no. 24, pp. 2216–2217, Nov. 1996.

[228] C. J. Reddy, M. D. Deshpande, C. R. Cockrell and F. B. Beck, 'Fast RCS computation over a frequency band using method of moments in conjunction with asymptotic waveform evaluation technique', *IEEE Transactions on Antennas and Propagation*, vol. 46, no. 8, pp. 1229–1233, Aug. 1998.

Publications

Journal

- I. Kavanagh and C. Brennan, 'Full Wave Indoor Propagation Modelling using the Volume Integral Equation', *Accepted for publication in IEEE Transactions on Antennas and Propagation Special Issue on Radio Wave Propagation*, 2018.
- I. Kavanagh and C. Brennan, 'Validation of a Volume Integral Equation Method for Indoor Propagation Modelling', *Submitted for publication in IET Microwaves, Antennas and Propagation Special Issue on LAPC 2017 (Invited Paper)*, 2018.

Conference

- I. Kavanagh, S. Hussain and C. Brennan, 'A Full Wave Propagation Model for Indoor Wireless Communications', *The 17th Research Colloquium on Communications and Radio Science into the 21st Century*, Dublin, 2014.
- V. Pham-Xuan, I. Kavanagh, M. Condon and C. Brennan, 'On comparison of integral equation approaches for indoor wave propagation,' *2014 IEEE-APS Topical Conference on Antennas and Propagation in Wireless Communications (APWC)*, Palm Beach, 2014, pp. 796-799.
- I. Kavanagh, V. Pham-Xuan, M. Condon and C. Brennan, 'A method of moments based indoor propagation model,' *2015 9th European Conference on Antennas and Propagation (EuCAP)*, Lisbon, 2015.
- I. Kavanagh and C. Brennan, 'Computationally efficient extension of a 2D integral equation propagation model to 3D,' *2015 International Conference on Electromagnetics in Advanced Applications (ICEAA)*, Turin, 2015, pp. 187-190.

- I. Kavanagh, 'Developing a method of moments based indoor propagation model,' *IEEE EUROCON 2015 - International Conference on Computer as a Tool (EUROCON)*, Salamanca, 2015.
- I. Kavanagh and C. Brennan, 'Preliminary comparison of 3D integral equation based indoor propagation model and ray tracing,' *2015 International Conference on Advanced Technologies for Communications (ATC)*, Ho Chi Minh City, 2015, pp. 350-354.
- I. Kavanagh and C. Brennan, 'A hybrid 2D to 3D full wave indoor propagation model,' *2016 International Conference on Electromagnetics in Advanced Applications (ICEAA)*, Cairns, QLD, 2016, pp. 748-751.
- I. Kavanagh, S. Hussain and C. Brennan, 'Comparison of 3D volume integral equation and ray tracing for indoor propagation modelling,' *2016 10th European Conference on Antennas and Propagation (EuCAP)*, Davos, 2016.
- I. Kavanagh and C. Brennan, 'Preliminary investigation of power delay profile computation from full wave frequency domain indoor propagation model,' *2017 11th European Conference on Antennas and Propagation (EUCAP)*, Paris, 2017, pp. 2242-2245.
- I. Kavanagh and C. Brennan, 'Volume integral equation based modelling of in building propagation,' *2017 International Conference on Electromagnetics in Advanced Applications (ICEAA)*, Verona, 2017, pp. 1498-1501.
- I. Kavanagh and C. Brennan, 'Analysis of full-wave 2D to 3D propagation models and ray tracing for indoor environments,' *Communications and Radio Science for a Smarter World, Royal Irish Academy Research Colloquium*, Dublin, 2017, pp.53-56.
- I. Kavanagh and C. Brennan, 'Validation of a volume integral equation method for indoor propagation modelling,' *Loughborough Antennas & Propagation Conference (LAPC 2017)*, Loughborough, 2017.

Technical Documents

- I. Kavanagh and C. Brennan, 'Path Loss Modelling for Indoor Environments using an Integral Equation Formulation', *COST ACTION (IC1004) in Cooperative*

Radio Communications for Green Smart Environments, Dublin, 2015.

- I. Kavanagh and C. Brennan, 'Indoor Propagation Modelling using the Volume Integral Equation', *COST ACTION (CA15104) in Inclusive Radio Communication Networks for 5G and Beyond (IRACON)*, Lisbon, 2017.

- I. Kavanagh and C. Brennan, 'Volume Integral Equation Based In-Building Propagation Modelling', *COST ACTION (CA15104) in Inclusive Radio Communication Networks for 5G and Beyond (IRACON)*, Graz, 2017.

- X. Lin, B. Ai, K. Guan, D. He, I. Kavanagh, C. Brennan, and Z. Zhong, 'Comparative Analysis of Ray-Tracing and Volume Electric Field Integral Equation for Indoor Propagation', *COST ACTION (CA15104) in Inclusive Radio Communication Networks for 5G and Beyond (IRACON)*, Nicosia, 2018.

- I. Kavanagh and C. Brennan, 'Power delay profile modelling in indoor environments using the VEFIE', *COST ACTION (CA15104) in Inclusive Radio Communication Networks for 5G and Beyond (IRACON)*, Cartegna, 2018.